A dissertation entitled

Numerical investigation of hybrid heat transfer enhancement techniques for a shell and tube latent heat storage unit

A Dissertation

Submitted in partial fulfilment of the requirements for

the award of the degree of

DOCTOR OF PHILOSOPHY

in

MECHANICAL ENGINEERING

By

AMUDHALAPALLI GOPI KRISHNA

(Roll No: 701929)

Supervisor

Dr. D. JAYA KRISHNA

(Professor)

Department of Mechanical Engineering

National Institute of Technology,

Warangal (TS), India.

September 2023

Thesis approval for Ph.D

This thesis entitled "**Numerical investigation of hybrid heat transfer enhancement techniques for a shell and tube latent heat storage unit"** is approved for the degree of Doctor of Philosophy.

Examiners

_____

_____

_____

Supervisor

(Dr. D. Jaya Krishna)
Professor,
Department of Mechanical Engineering,
National Institute of Technology, Warangal

Chairman

(Dr. V. Suresh Babu)
Professor and Head
Department of Mechanical Engineering,
National Institute of Technology, Warangal

NATIONAL INSTITUTE OF TECHNOLOGY- WARANGAL

CERTIFICATE

This is to certify that the thesis entitled "**Numerical investigation of hybrid heat transfer enhancement techniques for a shell and tube latent heat storage unit"** being submitted by **Amudhalapalli Gopi krishna (Roll No: 701929)** for the award of the degree of **Doctor of Philosophy (Ph.D.) in Mechanical Engineering** to the National Institute of Technology, Warangal, India, is a record of the bonafide research work carried out by him under my supervision. The thesis has fulfilled the requirements according to the regulations of this Institute and in my opinion has reached the standards for submission. The results embodied in the thesis have not been submitted to any other University or Institute for the award of any degree.

Date:

Prof. D. Jaya Krishna
Thesis Supervisor
Department of Mechanical Engineering,
National Institute of Technology, Warangal

Prof. V. Suresh Babu
Chairman, DSC & Head
Department of Mechanical Engineering,
National Institute of Technology, Warangal

DECLARATION

This is to certify that the work presented in the thesis entitled "**Numerical investigation of hybrid heat transfer enhancement techniques for a shell and tube latent heat storage unit"** is a bonafide work done by me under the supervision of Dr. D. Jaya Krishna (Professor, MED) and was not submitted elsewhere for award of any degree.

I declare that this written submission represents my ideas in my own words and where others' ideas or words have been included, I have adequately cited and referenced the original sources. I also declare that I have adhered to all principles of academic honesty and integrity and have not misrepresented or fabricated or falsified any idea/data/fact/source in my submission. I understand that any violation of the above will be a cause for disciplinary action by the Institute and can also evoke penal action from the sources which have thus not been properly cited or from whom proper permission has not been taken when needed.

Date: (Amudhalaplli Gopi krishna)

Place: Warangal Roll No. 701929

ACKNOWLEDGEMENT

I would like to express my sincere gratitude and it gives me an immense pleasure to acknowledge the people who were the part of this research work in plenty ways. It would not have been possible without close association with many people. I take this opportunity to extend my sincere gratitude and appreciation to all those who made this research work possible. First and foremost, I want to thank my thesis supervisor Prof. D. Jaya Krishna. He cultivated the seed of the research in me and inspired to apply this knowledge not only in laboratories but also in the personal life. His invaluable contributions of time and ideas during Ph.D. stay provide me wealthy in experiences, which is productive and stimulating in all aspects. His positive attitude at any diverse situations taught me how to tackles the hurdles at any stage with joy and enthusiasm. He provided me an excellent platform to nourish and grow my professional as well as personal life.

I wish to sincerely thank university authorities, Prof. Bidyadhar Subudhi, Director, National Institute of Technology, Warangal and other higher officials who gave me an opportunity to carry out research work.

I also sincerely acknowledge Prof. V Suresh Babu, Head, Mechanical Engineering Department, National Institute of Technology Warangal for his continuous support towards carrying out research work.

I wish to express my sincere and whole hearted thanks and gratitude to my doctoral scrutiny committee (DSC) members Prof. Madhu Murthy K, Mechanical Engineering Department, Prof. Veeresh Babu A, Mechanical Engineering Department, Prof. P.V. Suresh, Chemical Engineering Department, National Institute of Technology, Warangal for their kind help, encouragement and valuable suggestions for successful completion of research work.

I would like to extend my thanks to all the faculty members in the Department of Mechanical Engineering for their valuable suggestions and encouragement. I am also thankful to all the supporting and technical staff of the Department of Mechanical Engineering who has directly or indirectly helped during the course of my work.

I am thankful to all my senior and fellow research scholars especially, Dr. Lokesh Kalapala, Dr. Sandip khobragada, Dr. G. Uma Maheswararao, Dr.Mahesh, Mr. T. Markandeyulu, Mr. C. Raghu, Mr .A. Srikanth, Mr. Suprio, Mr. Nithin, Mr. V. Nagendra,

Ms. Sai Nandini , Ms. Rakshita, Ms. Sai Lakshimi, Mr. Raghav, Mr. M.Sandip, and many others for always standing by my side and sharing a great relationship as compassionate friends. I will always cherish the warmth shown by them.

I should thank all my friends Mr. P Avinash, Mr. N Sai Krishna, Mr. M Srinath, Mr. G Vivek, Mr. Rajesh, Mr. Phani, Mr. Sheshank, Mr. Preetham, Mr. Ch Sai krishna, Mr.Ch Shravan, Mr. Dinesh supporting me.

Last but not the least; In this auspicious moment, I owe my deepest regards family members and well-wishers for their eternal support and understanding of my goals and aspirations. My heartfelt regards go to my parents A Padma and A Sudhakar Rao. Finally, I would like to thank my sister Lakshmi Bhargavi for her moral support.

(Amudhalapalli Gopi Krishna)

Abstract

The depletion of the earth's environment due to the continuous emission of pollution and the increase in energy demand daily due to the increase in the population and lifestyle are important issues that need serious consideration for a better society. To overcome these issues, sustainable and cleaner methods for energy generation are necessary. Solar energy is a potential source of energy for a sustainable society. But solar energy is irregular in nature. Thermal energy storage (TES) systems play a crucial role in solving the demand and supply mismatch. Latent heat storage systems (LHSS) based on phase change materials (PCMs) are prominent techniques for storing thermal energy. These systems have higher energy storage density with less fluctuation in the temperature. Among various heat exchanger configurations, shell and tube type LHSS is chosen due to its minimal heat loss. The thermal performance of the LHSS significantly depends upon the heat transfer enhancement techniques. Usage of extended surfaces (fins), nanoparticles, metal foam, cascading, encapsulation, etc., are a few heat transfer enhancement techniques used in the literature. In the present work performance of the LHSS is analyzed with hybrid heat transfer enhancement techniques.

The present work is aimed to analyze the performance of the LHSS due to the usage of (a) Fins (radial, spiral and longitudinal) + GNP (graphene Nano platelets) nanoparticles, (b) metal foam (0.97, 0.95 and 0.93 porosity) + GNP nanoparticles and (c) cascaded metal foam (linearly and radially). The effect of the orientation is also considered in the present research work. To analyze the performance of the LHSS; melting time, solidification time, energy storage and release ratios and exergy efficiency during melting and solidification are considered. The performance of the LHSS is compared with pure PCM shell and tube heat exchanger. The influence of geometric parameters and HTF (heat transfer fluid) conditions on exergy efficiency is also analyzed. Numerical analysis is carried out for the melting and solidification process using ANSYS FLUENT.

Initially, the performance of the pure PCM shell and tube LHSS is carried out. The pure PCM shell and tube LHSS results are compared with the hybrid enhanced PCM shell and tube LHSS. The shell and tube LHSS dimensions are considered based on the optimized

geometries specified in the literature. Throughout the analysis of the hybrid enhanced LHSS, the dimensions of the shell and tube LHSS and inlet conditions of the HTF are the same.

The radius, pitch, and thickness of the radial fins are considered based on the optimal dimensions obtained from the literature. The same pitch is considered for the spiral finned heat exchanger, and ten fins are considered for the longitudinal finned heat exchanger. The thickness of spiral and longitudinal fins is selected such that PCM in all the finned LHSS is the same. GNP (graphene Nano platelets) nanoparticles are selected as they are compatible with PCM. The usage of fins + GNP nanoparticles resulted in a reduction of melting and solidification time. Maximum reduction of melting time and solidification time by 73.71% and 82.23% are noted in radial finned 1% volume GNP nanoparticle LHSS oriented vertically. Exergy efficiency during solidification has also improved on the usage of fins. The maximum exergy efficiency of 4.55% is noted in radial finned 1% volume GNP nanoparticle LHSS oriented at 45°. A minimum exergy efficiency of 0.715% is noted in pure PCM LHSS oriented horizontally during solidification. But the usage of fins + GNP nanoparticles reduced the energy storage ratio and exergy efficiency during melting. The energy storage ratio is reduced to 0.89 in 1% volume GNP nanoparticle radial fin LHSS inclined vertically compared to 0.992 in pure PCM LHSS inclined at 45°. Exergy efficiency during melting is reduced to 44.4% in 1% volume GNP nanoparticle radial fin LHSS inclined vertically compared to 76.16% in pure PCM LHSS oriented at 45°. Variation in energy release ratio is negligible using fins + GNP nanoparticles compared with pure PCM LHSS.

The metal foam + GNP nanoparticles LHSS analysis is performed considering 0.97, 0.95 and 0.93 porosity copper metal foams in combination with pure PCM, 0.5% and 1% vol fraction GNP nanoparticles. Dimensions of the shell and tube heat exchanger are kept the same as pure PCM shell and tube LHSS. The usage of metal foam + GNP nanoparticles improved melting time, solidification time, and exergy efficiency during solidification. Maximum reduction of melting and solidification time by 78.32 % and 91.75% are noted in 0.93 porosity metal foam 1% volume GNP nanoparticles LHSS oriented vertically. The maximum exergy efficiency of 10.5% is noted in 0.93 porosity metal foam 1% volume GNP nanoparticle LHSS oriented at 45° during solidification. As observed in fins + GNP nanoparticles, using metal foam + GNP nanoparticles also resulted in the reduction of energy storage ratio and exergy

efficiency during melting. The energy storage ratio is reduced to 0.88 using 0.93 porosity metal foam LHSS enhanced with 1% volume GNP nanoparticles oriented vertically. Whereas 0.992 is observed in pure PCM LHSS inclined at 45°. Exergy efficiency during melting is reduced to 46.28% on the usage of 0.93 porosity metal foam LHSS enhanced with 1% volume GNP nanoparticles oriented vertically compared to 76.16% in pure PCM LHSS oriented at 45°. Variation in energy release ratio is negligible due to the usage of metal foam + GNP nanoparticles compared with pure PCM LHSS.

Thermal performance analysis of the cascaded metal foam LHSS is carried out considering 0.93, 0.95 and 0.97 porosity copper metal foams. Metal foams are cascaded in both radial and linear manner. Cascaded metal foams improved melting/solidification rates and exergy efficiency during solidification. Maximum reduction of melting and solidification time by 76.17 % and 91.75% are noted in radial cascaded 0.93-0.95-0.97 LHSS. The maximum exergy efficiency of 9.22% is observed in radial cascaded 0.93-0.95-0.97 LHSS inclines at 45° compared to 0.715% in pure PCM LHSS oriented horizontally during solidification. Also, cascaded metal foams resulted in a reduction of energy storage ratio and exergy efficiency during melting. The energy storage ratio is reduced to 0.86 in linear cascaded 0.97-0.93-0.95 porosity metal foams LHSS oriented vertically. Exergy efficiency during melting is reduced to 45.4% on the usage of 0.97-0.93-0.95 porosity metal foam LHSS oriented vertically compared with 76.16% in pure PCM LHSS oriented at 45°.

The usage of hybrid techniques enabled an improvement in melting/solidification time and exergy efficiency during solidification. Although the energy storage ratio decreased, this decrease in energy storage is not due to improper usage of latent heat of the PCM but ineffective use of the PCM sensible heat. So the reduction in the energy storage ratio has little effect on the performance of LHSS. But the decline in exergy efficiency during melting is an important performance factor. Although improvement in exergy efficiency during solidification is observed, further improvement is necessary as maximum exergy efficiency is only 10.5%. This is a serious concern that limits the usage of LHSS. Using metal foam+ GNP nanoparticles has shown better thermal performance than the other two hybrid techniques. So machine learning model is developed to predict the transient variation of melt fraction in metal foam + GNP nanoparticles enhanced shell and tube LHSS.

Further study is carried out to analyze the effect on the phase change time and exergy efficiency during melting and solidification by varying porosity of metal foam, the volume fraction of GNP nanoparticles, length of the heat exchanger, the inlet temperature of HTF, length to diameter ratio (l/d) of shell and Reynolds number of HTF. l/d ratio of LHSS is varied such that amount of PCM in LHSS is the same as that in pure PCM LHSS. A significant improvement of 23.32% in exergy efficiency during solidification is obtained. It is observed that the l/d ratio of LHSS and the porosity of metal foam significantly affect the melting and solidification rates. Exergy efficiency during melting depends considerably on the HTF inlet temperature. Whereas exergy efficiency during solidification is noted to be significantly dependent on the Reynolds number of the HTF.

Keywords: Latent heat storage, PCM, GNP nanoparticles, Fins, Metal foam, Exergy efficiency

Contents

List of Figures

List of tables

NOMENCLATURE

Nomenclature:

c_p : specific heat (kJ/kg.K)

E : Energy (J)

Ex : exergy (J)

$\dot{E}x$: rate of exergy (J/sec)

g : acceleration due to gravity (m/sec^2)

h : enthalpy (J/kg)

k : thermal conductivity (W/m.K)

L : latent heat (J/kg)

$\dot{m}$: mass flow rate (kg/sec)

o : ambient

P : pressure (N/m^2)

Pr : Prandtl number

Ra : Rayleigh number

T : temperature (K)

t : time (sec)

V : velocity (m/sec)

Greek

α : thermal diffusivity (m^2/sec)

β : thermal expansion coefficient (K^{-1})

ρ : density (kg/m^3)

υ : kinematic viscosity (m^2/sec)

μ : viscosity (kg/m.sec)

ϕ : volume fraction of the additives

ε : porosity

Subscripts

avg : average

htf : heat transfer fluid

l : liquid

li : liquidus

np : nanoparticles

nepcm : nanoparticle enhanced phase change material

pcm : phase change materials

pm : porous media

s : solid

so : solidus

vol : volume

Abbreviations

GNP : Graphene Nano Platelets

HTF : Heat Transfer Fluid

LHSS : Latent Heat Storage System

NEPCM : Nanoparticle Enhanced Phase Change Material

NP : Nanoparticle

PCM : Phase Change Materials

Chapter 1

Introduction

Based on the statistical review of world energy, it was estimated that 85% of the world's total primary energy for the year 2018 was from fossil fuels [1]. Due to the continuous increase in population, the energy demand is also increasing, which leads to the usage of more fossil fuels. However, because of the environmental effects and depletion of fossil fuels, the usage of renewable energy sources becomes necessary. Renewable energy systems play an important role in producing clean energy and reducing greenhouse emissions. Among various available renewable energy sources, solar energy can be considered a promising option. Solar energy can be used to tap the energy in most parts of the world due to its availability, abundance and can be converted directly to both electrical and thermal energy. But one of the main limitations of solar energy is its discontinuous nature and the available energy depends upon the location, time, and climatic conditions [2]. This problem can be overcome by coupling solar collectors to energy storage units. Thermal energy storage (TES) systems can be coupled with conventional energy generation and solar collectors. The processes in TES are charging, storing, and discharging [2].

1.1 Thermal energy storage

TES can be further classified into sensible heat storage and latent heat storage. The temperature in sensible heat storage systems increases during energy storage and decreases during energy release. Whereas latent heat storage has the advantage of storing a large amount of energy almost at a constant temperature. Latent heat storage materials (LHSMs) change phase during storage and release of the heat due to which LHSMs are also cited as phase change materials (PCMs). It is estimated that sensible heat storage materials take 5 to 14 times more space when compared to latent heat storage materials (LHSMs) to store the same amount of thermal energy [3]. Due to very less change in specific volume during solid to liquid phase change and easy handling, solid–liquid PCMs are preferred over solid–gas and liquid–gas PCMs. The selection of a PCM depends upon phase change

temperature (which depends upon the operating temperature of the system), latent heat, thermal conductivity, specific heat, density, and thermal expansion coefficient.

1.2 Phase change materials

Phase change materials are termed as PCMs. PCMs at phase change temperature absorb and release a large amount of energy during the charging and discharging process. There are different types of PCMs such as organic, inorganic, and eutectics as shown in Fig 1.1. Details on the classifications of the PCMs are available in the literature with different melting/freezing points, thermal conductivity, and latent heat [4–8].

Because of its diverse advantages, PCM has attracted various applications. Table. 1.1 shows the summary of various applications based on the PCMs. Because of enormous applications, active research is being carried out on the development of different kinds of PCMs and a few available PCMs for low temperature applications are listed in Table 1.2.

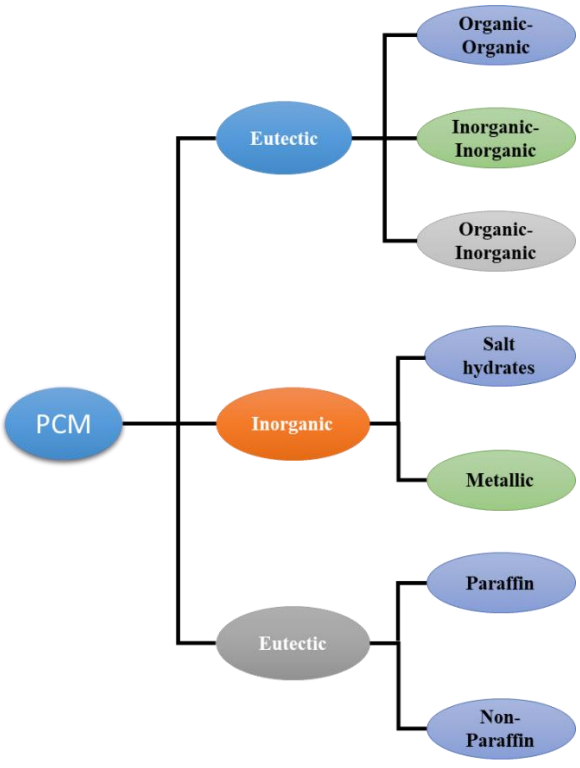

Fig 1.1 Classification of PCMs

Table 1.1 Summary of recent review papers on PCMs application

Ref.	Application	Contents
[9]	Solar water heater	Performance enhancement of solar water heater embedded with PCMs
[10]	Solar water heater	Improvement of heat transfer and utilization of PCMs in solar water heater
[11]	Solar water heater	Investigation of PCMs for solar and space heating applications
[12]	Thermal management	Batteries thermal management using PCMs
[13]	Thermal management	Li-ion batteries for vehicles integrated with PCMs
[14]	Thermal management	Introduced potential PCMs for thermal management system
[15]	Automobile industries	Use of PCMs in the automotive industries
[16]	Distillation system	Use of PCMs in the solar still for distillation
[17]	Heating and cooling of the building	Review of PCMs for heating and cooling of building application
[18]	Heating and cooling of the building	Role of PCMs in heating and cooling of buildings with hybrid application
[19]	Solar dryer	Role of PCMs in solar dryer application to improve the efficiency of agricultural products
[20]	Refrigeration	Investigation and recent development of PCMs in refrigeration system
[21]	Solar chimney	Review on the solar chimney associated with PCMs
[22]	Medical application	Use of PCMs in medical applications for thermal management
[23]	Textile	Implementation of PCMs in textile industries

Table 1.2 List of PCMs [24][25][26][11][27]

		Melting Point (°C)	Latent heat (kJ/kg)
Organic PCM	N-pentadecane	10	205
	Propyl palminate	19	186

	Paraffin C18	28	244
	Capric acid	36	152
	Medicinal paraffin	40-44	146
	Lauric acid	49	178
	Myristic acid	58	199
	Stearic acid	69.4	199
	Acetamide	81	241
Inorganic PCM	H_2SO_4	10.4	100
	P_4O_6	23.7	64
	$TiBr_4$	38.2	23
	$H4P_2O_6$	55	213
	$SbCl_3$	73.4	25
Eutectic PCM	$C_5H_5C_6H_5$+ $(C_6H_5)_2O$	12	97.9
	$C_{14}H_{28}O_2$+$C_{10}H_{20}O_2$	24	147.7
	Myristic acid + glycerol	31.96	154.3
	NH_2CONH_2+NH_4 NO_3	46	95
	Palmitic acid + glycerol	58.5	185.9
	Stearic acid + glycerol	63.45	149.4
	$AlCl_3$+NaCl+KCl	70	209
	$LiNO_3$ + NH_4NO_3+NaNO3	80.5	113

1.3 Scope of research work

TES is essential for the efficient tapping of solar energy for various applications. In this direction, a latent heat storage system (LHSS) has many advantages over other storage mediums. Therefore, to maximize the performance of LHSS, extensive research should be carried out. Though the PCMs have a wide range of applications, their usage is limited due to poor thermal conductivity, phase segregation, and super-cooling effect [28]. Several researchers suggested the usage of techniques like increase in the surface area[29][30],[31],[32] by using fins, the inclusion of nanoparticles[33][34], encapsulation[35], metal foam[36], cascading[3] and hybrid techniques[37] by combining the individual methods. The present work is focused on improving the performance of LHSS by employing hybrid techniques.

1.4 Organization of the thesis

In this thesis, the performance of shell and tube LHSS in the presence of various hybrid techniques is analyzed numerically during melting and solidification. The entire thesis is presented in 10 chapters.

Chapter 1 provides a brief introduction to TES and PCMs.

Chapter 2 presents the literature review on the various heat transfer enhancement techniques employed in the LHSS.

Chapter 3 presents the numerical methodology used in the present work.

Chapter 4 presents the performance of the pure PCM shell and tube LHSS.

Chapter 5 provides the effect of various types of fins, nanoparticles, and orientation on the performance of the PCM shell and tube LHSS.

Chapter 6 deals with the influence of metal foam, nanoparticles, and orientation on the performance of PCM shell and tube LHSS.

Chapter 7 provides the effect of cascaded metal foam and inclination on the performance of PCM shell and tube LHSS.

Chapter 8 deals with the machine learning model developed to predict the transient variation of melt fraction of PCM in metal foam and nanoparticle-enhanced PCM shell and tube LHSS.

Chapter 9 provides the influence on the exergy efficiency due to the design and flow parameters of heat transfer fluid (HTF) in PCM shell and tube LHSS.

Chapter 10 provides the major findings of the current research work and the scope for future work.

1.5 Closure

In this chapter, the need for thermal energy storage is highlighted. The advantages of latent heat storage compared with other storage methods are briefly discussed. Also, the type of PCMs for low temperature applications and various industrial applications based on PCMs are reviewed. As a concluding remark, an analysis of the influence of various hybrid heat transfer enhancement techniques on PCM shell and tube LHSS should be carried out.

Chapter 2

Literature review

2.1 Introduction

Effective utilization of the latent heat capacity of the phase change materials (PCMs) is essential to store a large amount of thermal energy. Latent heat storage systems (LHSS) are designed in such a way that they exhibit better energy storage/retrieval density and charging/discharging rate. The thermal performance of LHSS has a significant impact on the operating parameters, geometric design parameters and heat transfer enhancement techniques. The present chapter provides a brief literature review regarding the effect of operating parameters, geometric design parameters and heat transfer enhancement techniques.

2.2 Configurations of latent heat storage system (LHSS)

Configuration of the LHSS is a key factor to be considered. A thorough review of the literature on LHSS indicated that the most commonly used LHSS shapes are cylindrical and square cavities. Agyenim et al. [27] on reviewing the literature highlighted that more than 70% of works pertaining to LHSS is corresponding to the shell and tube heat exchangers. Due to minimal heat loss to the surroundings shell and tube heat exchanger is preferred. Also, shell and tube heat exchangers are considered to be promising for practical applications in terms of ease of fabrication and stability. Hence, S & T HX is chosen for current research work and most of the literature in the following section is related to shell and tube heat exchangers.

2.3 Effect of operational parameters on thermal performances of LHSS

Operational parameters of LHSS play a crucial role in the heat transfer between heat transfer fluid (HTF) and PCM. Hence, operational parameters affect the thermal performance of LHSS. Various studies were carried out to study the influence of parameters viz. flow rate of HTF, inlet temperature of HTF and orientation of LHSS on the charging/discharging process.

2.3.1 Effect of the flow rate of heat transfer fluid (HTF)

The flow rate of heat transfer fluid (HTF) is a very important factor which shows a significant effect on the performance of the LHSS. Focusing on the effect of different mass flow rates of HTF on the performance of LHSS first study was carried out by Cao and Faghri [38]. It was observed that increase in the mass flow rate of HTF, charging time decreased. Khan et al.[39],[40] on carrying out numerical analysis noted that the solidification process significantly depends on the flow rate of the HTF. Opposing this view Lu et al.[41] observed that melting time was inversely proportional to the flow rate of HTF and solidification time was observed to be independent of HTF flow rate. Kalapala and Devanuri[42] on carrying out numerical analysis observed that the influence of the mass flow rate of HTF is negligible. Shakrina et al.[43] on carrying numerical analysis observed that the flow rate of HTF showed a minimal effect during solidification than during melting. Mao et al.[44] reviled that HTF flow rate has minimal effect during melting. Panisilvam et al.[45] and Nguyen et al.[46] noted that the HTF flow rate has shown a minimal effect on the phase change process. Shen et al.[47] noted that as flow rates of HTF increase, energy efficiency also increases. Wang et al. [48] studied the influence of mass flow rate on energy storage and found that with the increase in the mass flow rate from 0.0015 to 0.015 kg/s energy storage was enhanced by 10 %. Contrary to this, Wang et al. [49] experimentally investigated the impact of mass flow rate on energy stored and reported that mass flow rate between 90 kg/h to 140 kg/h shows no difference in energy stored. Most of the studies revealed that the effect of the flow rate of HTF is insignificant or has shown a minor effect on charging/discharging time.

2.3.2 Inlet temperature of heat transfer fluid (HTF)

Khan et al.[39],[40] on carrying out numerical analysis and mentioned that the melting process significantly depends on the HTF inlet temperature. The rate of melting increased with an increase in the inlet temperature of HTF. In line with this Lu et al. [41] observed that melting time decreases with the increase in the inlet temperature. Similar results were observed by Kabria et al. [50]. In their study when HTF inlet temperature was varied from 77°C to 88°C during charging melting rate was noted to increase. In line with this, Avci and Yazici [51] noted that charging time was decreased by 25% when HTF temperature

was increased from 75°C to 85°C. Hosseini et al. [52] observed that with the increase in inlet temperature from 70 °C to 80 °C the charging time was noted to decrease by 37%. Esen et al.[53] investigated the influence of the HTF temperature on paraffin wax. The result indicated that when the inlet temperature of HTF is 50°C the melting time of PCM was 10 hr, whereas for 65°C the melt time decreased to 4 hr. Malik et al.[54] noted that phase change time was inversely proportional to temperature of HTF. From the literature it can be noted that inlet temperature of HTF has shown significant effect on the rate of phase change. All the studies revealed the same result, that with increase in the inlet temperature of HTF rate of melting increases i,e. melting time decreased.

2.3.3 Orientation

Along with the flow rate and inlet temperature of HTF orientation of LHSS is a vital parameter which affects the performance of the LHSS. The heat transport due to buoyancy-induced flow is observed to be dominant during the phase change process. The convective mode of heat transfer predominantly depends on the orientation of LHSS. So it is very important to analyse the effect of orientation on the thermal performance of a LHSS.

Seddegh et al.[55] numerically analyzed the orientation effect on both melting and solidification for vertical and horizontal LHSS. They noted that in the horizontal condition, the thermal transport was higher when compared to the vertical condition. Inline to Seddegh et al.[55] and Koush et al.[56] also reported similar results on carrying out experiments to study the effect of orientation on the performance of LHSS. They considered 0̊, 30̊, 60̊ and 90̊ angles. Siyabi et al.[57] analyzed melting behaviour and propagation of melt front profile of PCM along the axial and radial directions of the shell and tube heat exchanger. It was observed that the temperature gradient along the axial direction decreased with the change in orientation from 0̊ to 90̊. Kalapala and Krishna [58] performed energy and exergy analysis for 0̊, 30̊, 60̊ and 90̊ oriented LHSS and observed maximum exergy efficiency for vertical configuration.

On carrying out experimental and numerical analysis Kalapala and Devanuri [59] observed that in the case of a horizontally orientated radial fin heat exchanger, the time required to melt the top portion is less. The vertical configuration was observed to have lesser melting time and higher exergy efficiency. Borhani et al.[60] performed numerical analysis of the

spiral finned heat exchanger and mentioned that for vertical orientation a decrease in melting time of 56% is observed when compared with the horizontal heat exchanger. Bouzennada et al. [61] carried out a numerical study to check the thermal behaviour of PCM with 90°, 45° and 0° oriented finned LHSS. They noted that horizontally positioned LHSS has least melting time and vertically oriented LHSS has shown highest melting time. Mahdi et al. [62] reported that in LHSS influence of inclination is insignificant in the presence of fins. From the literature it can be noted that, there is an ambiguity in selecting the orientation of the LHSS. Therefore, it is necessary to study the effect of orientation on the performance of the LHSS.

2.4 Effect of geometric parameters on the thermal performance of latent heat energy storage system

Geometric parameters of PCM-based shell and tube heat exchanger i,e length, and the diameter of shell and tube play a significant role in the performance of the LHSS. So it is very important to study the effect of geometric parameters on the thermal performance of an LHSS.

On conducting numerical analysis, Wang et al.[48] observed that as the height and the radius of the shell increased, the energy efficiency decreased due to the increase in the ratio of pump/stored work. Kalapala and Devanuri[63] on carrying out a detailed review of several research works on shell and tube heat exchanger type LHSS concluded that the optimized ratio of shell diameter to tube diameter should be nearly 4. Trp et al.[64] carried out numerical studies to analyse the effect of shell diameter and length of the tube during the melting and solidification process. It was noted that LHSS has shown better performance when the ratio of length to shell diameter is kept at 3.2. From the literature optimized LHSS has a shell diameter to tube diameter ratio of 4 and length to shell diameter ratio of 3.2 nearly.

2.5 Heat transfer enhancement techniques

Although PCMs have various applications, their utilization is limited due to less thermal conductivity which results in long phase change times which further results in the decrease of energy storage[37]. In recent studies, many researchers focused on heat transfer

enhancement techniques in PCMs. These studies revealed that techniques like inserting extended surfaces (fins)[3] to heat transfer fluid (HTF) tube, the addition of nanoparticles[65],[66] to pure PCM, encapsulation[35] of PCM, insertion of metal foam[67] in PCM, cascading[68]of PCMs, usage of surface textures[69] on tube and hybrid techniques[37],[70]improved the performance of the LHSS. The literature review is mostly focused on fins, nanoparticles, metal foam and a combination of these techniques as these are chosen as the heat transfer enhancement technique in the current research work.

2.5.1 Employing of fins

The usage of fins is a well-known and effective approach to improving heat transfer rate. Surface area is increases due to the inclusion of fins, which results in an improved heat transfer rate. To increase the thermal effectiveness of PCM-based heat exchangers (HX), different types of fins such as radial or circular fins, longitudinal fins, spiral fins, pin fins and Y-shaped fins are used. Radial, longitudinal and spiral fins are the most commonly used fins in shell and tube heat exchangers. The following discussion is focused on radial, longitudinal and spiral fins used in LHSS.

Schematic of the radial/circular, spiral and longitudinal fins arrangement on heat transfer fluid (HTF) tube placed in shell and tube heat exchanger is shown in Fig.2.1. On conducting numerical analysis, Wang et al.[48] observed that as the height and the radius of the shell increased, the energy efficiency decreased due to the increase in the ratio of pump/stored work. They also suggested that the ratio of the pitch of fins to the radius of the tube should not exceed 4. Kalapala and Devanuri[29] carried out the numerical analysis on the radial finned shell and tube heat exchanger and gave a correlation for the optimized design of non-dimensional fin diameter and fin pitch. Kalapala and Devanuri[59] conducted experimental and numerical analysis on radial finned shell and tube HX. It was noted that in the case of a horizontal-orientated heat exchanger, the time required to melt at the top half portion is very less than compared to the bottom half portion. It was also observed that a vertically oriented heat exchanger has lesser melting time and higher exergy efficiency. Khan et al.[39],[40] noted that the inclusion of longitudinal fins escalated the rate of heat transfer in both the solidification and melting. It was mentioned that the melting process significantly depends on the HTF inlet temperature rather than the

flow rate, whereas the solidification process significantly depends on the flow rate of the HTF. Kazemi et al.[71] carried out a numerical analysis on two finned longitudinal fin PCM heat exchanger in horizontal orientation. It was observed that melting time decreased by placing both the fins at the bottom portion with an angle of 45° between them. Borhani et al.[60] studied the melting behaviour of spiral-finned PCM heat exchangers. A decrease in the melting time of 56% for the vertical orientation when compared with the horizontal was observed. Rozenfeld et al.[72] conducted experiments on a spiral-finned heat exchanger and observed that as the pitch of the fin decreased the melting time got decreased. Based on experiments Lu et al.[41] observed that melting time is inversely proportional to the temperature and flow rate of HTF. But the solidification time was observed to be independent of HTF mass flow rate. Agyenim et al.[73] carried out the experimental analysis on radial and longitudinal fin heat exchangers. The longitudinal finned heat exchanger showed better performance during melting and also reduced the sub-cooling effect during the solidification process. Tay et al.[74] observed that the radial fin heat exchanger performed better in comparison to the pin fin during the solidification due to its higher surface area. Soupart et al.[75] performed experimental analysis on radial and spiral fin heat exchangers. It was observed that irrespective of fin type the reduction in melting time was observed by 10 times when compared with heat exchanger without fins. Zhai et al.[76] carried out the numerical analysis on radial, longitudinal and mixed radial longitudinal finned PCM heat exchangers. It was observed that mixed types of fins showed superior performance than individual fins. It was also observed that with the decrease in pitch of the radial fins, the melting time got reduced. Luo et al.[77] performed numerical analysis on the combined fractal fin heat exchanger. It was noted that the usage of these fins could attain uniform temperature in the heat exchanger. Sciacovelli et al.[78] observed an increase in the performance of the heat exchanger during solidification with the usage of Y-shaped fins.

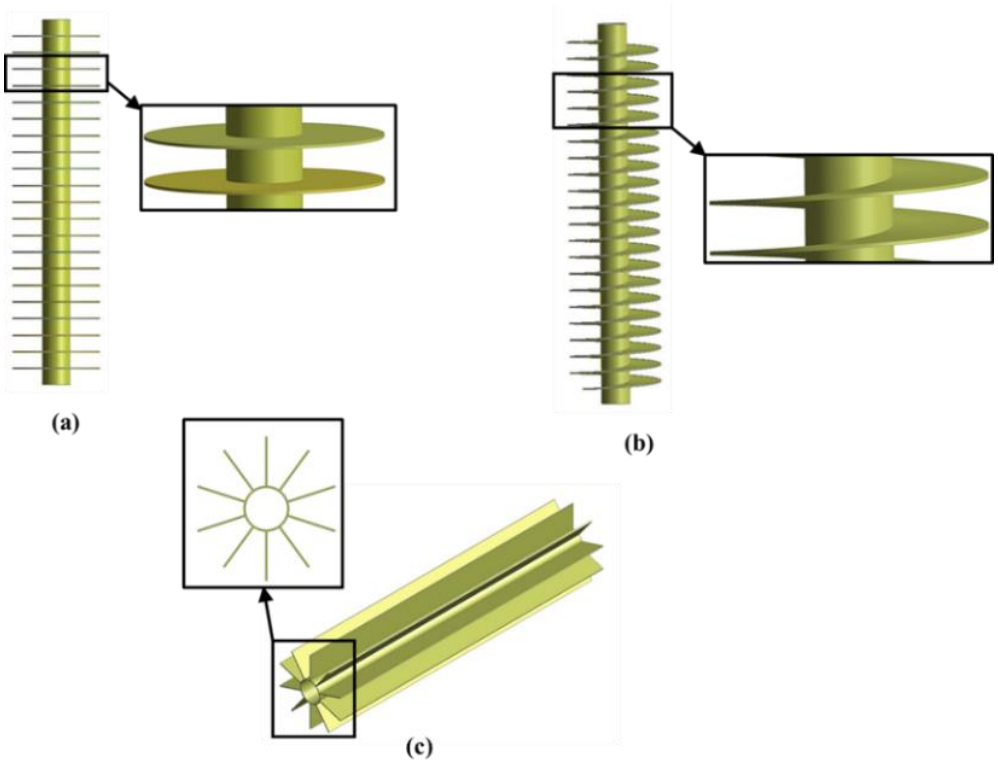

Fig 2.1 Configurations of (a) radial (b) spiral and (c) longitudinal fins

2.5.2 Dispersion of nanoparticle

Dispersion of nanoparticles improves the effective thermal conductivity of the PCM, thus increase in the heat transfer rate. Nanoparticles dispersed PCMs are termed nanoparticle enhanced PCMs (NEPCMs). The schematic of NEPCM based shell and tube heat exchanger is shown in Fig.2.2.

Das et al.[65],[33],[79] carried out the numerical analysis on nanodiamonds, single walled carbon nano tubes (SWCNT) and graphene nanoplatelets (GNPs) based PCM. It was observed that PCM with GNP nanoparticles showed better performance during melting. The melting time is minimal in horizontal orientation. On carrying out numerical analysis, Parsazadeh and Duan[80] observed that adding less amount of nanoparticles to PCM and HTF increased the rate of heat transfer and decreased the melting time. Alomair et al.[81] carried out the experimental and numerical analysis and observed that as the amount of nanoparticles increased the melting time got decreased. Khan et al.[82],[83] conducted the experimental and numerical analysis with various metal oxide and GNP nanoparticles and concluded that during the phase change process, GNPs showed better performance.

Amudhalapalli and Devanuri[66] on reviewing the literature concluded that among 44 different nanoparticles used to enhance the thermal conductivity of PCMs, GNP nanoparticles are best suitable for PCM-based LHSS.

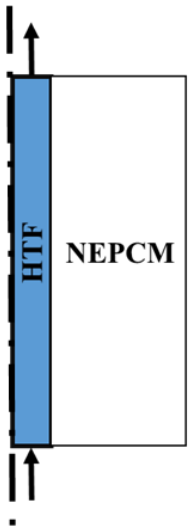

Fig 2.2 Axisymmetric view of Nanoparticle enhanced phase change materials in a shell and tube heat exchanger

2.5.3 Metal foam

Inserting the high thermal conductivity metal foam matrix in PCM enables to increase in the effective thermal conductivity of the PCM. This results in an increase in the heat transfer rate. A schematic of a metal foam based shell and tube heat exchanger is shown in Fig.2.3.

Zhao et al.[84] noted that usage of the metal foam increased the melting rate by 3-10 times and this depends upon the porosity of the metal foam. Alhusseny et al.[85] noticed that the usage of metal foam reduced both melting and solidification time by 50%. Esapoura et al.[86] and Sardaria et al.[87] on carrying out numerical analysis independently noted that the usage of metal foam in PCM reduced the phase change time. Zhang et al.[88] performed both numerical and experimental analysis on the usage of metal foam in PCM heat exchanger, this resulted in the reduction of convective effect but an increase in the heat transfer. Xu et al.[89] numerically examined the effect of copper, SiC, Nickel, and Al_2O_3 metal foams. Among the selected metal foams copper metal foam has shown better performance. Yang et al.[90] analyzed the effect of metal foam in the PCM and HTF

domains. Metal foam enabled to increase in the thermal response rate, thus melting time was decreased by 88.54%. Joshi et al.[91] on carrying out numerical analysis observed that usage of metal foam resulted in the reduction of melting time. Huang et al.[92] noticed that natural convection was suppressed if the heat was supplied in the direction of gravity when metal foam was used, also observed that with the increase in pore density effect of natural convection decreased. Zadeh et al.[93] on carrying out numerical analysis noted that usage of metal foam in PCM enables to increase in the charging power. Sardari et al.[94] on carrying out numerical analysis observed uniform temperature distribution within PCM when metal foam was used. Sardari et al.[95] observed that the usage of copper foam in PCM enabled to enhance the heat recovery by 73% when compared with pure PCM cases. Yao and Wu [96] noted that the usage of copper foam resulted in a high rate of phase change, higher rate of heat storage and temperature uniformity in heat exchanger. Chen et al.[97] noted that using copper metal foam in both PCM and HTF sides resulted in a decrease in overall melting and solidification time by 84.9%, whereas usage of metal foam only in PCM resulted in a reduction in overall melting and solidification time by only 40%.

Fig 2.3 Shell and tube heat exchanger with metal foam [98]

2.5.4 Encapsulation

This is another method to enhance the heat transfer rate of PCM by copulating with suitable material (coating /shell). Encapsulation PCM is classified into two main criteria i.e macro-encapsulation and micro-encapsulation based on shape or size. An encapsulation

shell larger than 1 mm is referred to as micro-encapsulation whereas encapsulation shells size smaller than 1 cm is macro-encapsulation. Macro-encapsulation is flexible in shape and size leading to a simple manufacturing process according to practical application. Using macro- encapsulation mechanical stability of the PCM system can be improved. In addition, micro-encapsulation increases the heat transfer rate due to a higher surface-to-volume ratio, homogenous PCM melting and solidification process carried out.

Xu et al.[99] experimentally investigated LHSS integrated with macro-encapsulated PCM during the charging and discharging process. They studied the effect of mass flow rate, the inlet temperature of HTF and orientation on the melting and solidification process. They observed that an increase in the HTF inlet temperature from 55°C to 60°C reduces the melting time by 42%. During solidification, reducing the inlet temperature from 35°C to 30°C solidification time was decreased by 52%. Similarly, by increasing the mass flow rate of HTF from 1.5 to 4.3 l/h, solidification and melting times were reduced by 14% and 13% respectively. Aziz et al.[100] experimentally and numerically studied the performance of encapsulated PCM in shell and tube heat exchangers. Three configurations of encapsulated PCM (with and without pin, with and without copper plating) were investigated. They observed that the encapsulated PCM with pin reduces the melting time by 27%, whereas copper coating decreases by 37% as compared to plain encapsulated PCM. He et al.[101] investigated the LHSS with and without encapsulated PCM. The result depicted that encapsulated PCM gave improved performance and extracted more energy from the PCM. Fang et al.[102] analyzed the temperature distribution at various radial positions and the progress of the solid-liquid interface for the thermal energy storage system. They investigated the effect of encapsulated particle fraction and PCM core fraction. They concluded that more encapsulation particle fraction leads to more accumulated energy by the PCM. However, a small difference in temperature profile and accumulated energy with different core fractions was observed. Amin et al.[103] studied the suitability of the Ɛ-NTU method for thermal energy storage systems with encapsulated PCM. An empirical correlation was evaluated to find out the effectiveness at a given mass flow rate. They observed that an increase in the mass flow rate decreased the effectiveness of LHSS. Lee et al.[104] studied the effect of capsule conduction and capsule outside convection on LHSS. They considered three models based on boundary conditions on the external surface of the

capsule i.e isothermal surface, constant temperature and natural convection. They concluded that constant temperature and convection boundary conditions outside the capsule resulted in a lower discharging rate than isothermal conditions alone. They also suggested that capsule material with low thermal conductivity should be preferable

2.5.5 Heat pipe

Phase Change materials based LHSS play a very important role in many applications such as air condensing, heating and waste heat recovery. However, the low thermal conductivity of PCM reduces and hinders thermal performance. LHSS embedded with heat pipe (HP) is commonly utilized in applications due to its ability to transfer heat over a large distance [105][106].

Sharifi et al.[107] investigated the influence of heat pipe (HP) on the melting process of PCM. The performance of a vertically positioned heat pipe with PCM was simulated. The result showed that the malting rate of PCM significantly improved due to HP. They also compared the HP, solid and hollow tube effects on the melting process. Out of all, HP provides the maximum melting rate. Shabgard et al.[108] analyzed the heat transfer process in the LHESS incorporated with HP. In their study, two cases were investigated with HP orientation. Case-1, PCM placed inside the shell side and HTF flow through the tube and Case-2, PCM placed inside the tube and HTF flow over the PCM. In case-1 orientation of HP shows negligible effect on energy storage whereas, in case-2 orientation of HP shows a significant influence on energy storage. They also observed that the effectiveness of LHSS was decreased by increasing HP wall thickness. Nityanandam and Pitchumani [109] numerically investigated the HP-assisted LHSS and evaluated the thermal performance with varying different parameters like length and radius of the HTF tube and flow rate of HTF. They observed that the melting rate of the PCM decreases with mass flow rate and length, while the same for increasing radius. They also carried out studies similar to Shabgard et al.[108] with the same case-1 and 2. Results indicated that case-1 showed more effectiveness and lower charging time as compared to case-2. Motahar et al.[110] experimentally investigated the influence of HP on the melting and solidification of PCM in shell and tube heat exchangers. A constant thermal reservoir was incubated to provide a constant temperature for the heating and cooling of PCM. They

observed that HP improved the heat transfer rate during the melting and solidification process.

Ebrahimi et al.[111] numerically investigated on the performance of LHSS with HP in shell and tube heat exchangers. The effect of parameters such as the number of tubes and angle of HP (0° to 90°) were studied. Results depicted that melting time reduce by 12% with increasing tubes from one to three. HP with 30° inclination reduces the melting time by 90% when compared to no heat pipe condition. Chopra et al.[112] experimentally investigated HP-embedded LHSS with and without PCM for the water heating system. Stearic acid was used as PCM. They observed that the thermal efficiency of LHSS with PCM-HP enhanced by 37.56% as compared to the without HP LHSS. Song et al.[113] optimized the HP parameter integrated with LHSS. The optimized parameter considered being the length of the condenser, the length of the evaporator and the length of PCM.

2.5.6 Hybrid heat transfer enhancement techniques

Few researchers analyzed the performance of the LHSS in which two or more individual heat transfer enhancement techniques are used. Singh et al.[114][115] on carrying out numerical analysis on GNP nanoparticle enhanced PCM in a radial finned shell and tube heat exchanger observed that a combined system of fins and 5% volume GNP nanoparticles resulted in reducing the melting time by 43%. Inline to this Lohrasbi et al.[116] also noted that combined usage of Y-shaped fins with nanoparticles has shown better thermal performance during melting. Sheikholeslami et al.[117] noted that the solidification process was accelerated by using both longitudinal fins and nanoparticles. A similar result was observed by the Hosseinzadeh et al.[118] on using the Y-shaped fins combined with the TiO_2 + CuO nanoparticles solidification process got accelerated. Khan et al.[119] bought down the charging time of 24.5 hours to 1.57, 1.33 and 1.02 hours by using the longitudinal, radial and wire wound fins with 5% GNP nanoparticles respectively.

On using both metal foam and nanoparticles charging time and discharging time are reduced by 96.11% and 96.23% respectively when compared with pure PCM heat exchanger, discharging time decreased with decreasing porosity, while pore density had no effect on phase change rate. Senobari et al.[120] carried out an experimental analysis on

metal foam and nanoparticles with PCM in a cylindrical container heated from the bottom. It was noted that LHSS with metal foam and nanoparticles has shown better performance than LHSS with only metal foam. Lei et al.[121] examined copper metal foam and aluminium nanoparticles enhanced LHSS. Uniform distribution of temperature was observed on the usage of metal foam. The solidification time was lower by 81.2% with the usage of 0.94 porosity metal form when compared to the heat exchanger with 0.1% volume nanoparticles in PCM. It was also observed that the usage of nanoparticles and metal foam increased the exergy efficiency. Mahdia et al.[122] carried out a numerical analysis on RT 50,55,60 with Al_2O_3 nanoparticles and aluminium metal foam and noted that usage of both metal foam and nanoparticles resulted in the reduction of solidification time. Mahdi and Nsofor [123] noticed that a decrease in metal foam porosity reduced the effect of nanoparticles. Combined usage of metal foam and nanoparticles exhibited the least solidification time. Zhao et al.[124] on carrying out experimental analysis of copper foam and expanded graphite in $NaNO_3$ observed that the natural convective effect is suppressed but the overall performance of the system was improved. It was also observed that both metal foam and expanded graphite improved the thermal performance of the LHSS. Jethelah et al.[125] carried out an experimental analysis on coconut oil as PCM with CuO nanoparticles and aluminium metal foam. Combined usage of nanoparticles and metal foam improved the performance of the heat exchanger and resulted in uniform temperature distribution. Lia et al.[126] on carrying out numerical analysis of PCM with copper metal foam and copper nanoparticles noted that the usage of nanoparticles and metal foam enabled the reduction of the melting and solidification time. Ghalambaz et al.[127] also noted that the usage of nanoparticles and metal foam enhance the performance of shell and tube heat exchanger.

Abandani and Ganji [128] reduced the melting time by 88% using the 0.95 porosity copper metal foam, a further reduction in melting time by 11.6% was noted by using cascaded 0.96-0.94 porosity metal foam. Similarly Sardari et al.[129] observed an 85% decrease in melting time on the usage of metal foam and a further decrease of 3.5% melting time on the usage of cascaded metal foam. Wang et al.[130] carried out experiments on aluminium gradient porous media in LHSS. It was noted that melting time was decreased by 37.6% and observed uniform temperature distribution in the heat exchanger. Pu et al.[131] noted

that the usage of cascaded PCM and cascaded metal foam in the radial direction in the PCM shell and tube heat exchanger enhanced the performance of the heat exchanger. It was also observed that heat exchangers in which porosity decreases along the radial direction from tube to shell have shown better melting performance.

2.6 Observation from literature review

- Several parameters influence the performance of the LHSS. An ambiguity exists in the selection of the orientation angle of the LHSS.
- In most of the numerical studies, the 2D computational domain of shell and tube heat exchanger was considered to analyze the thermal performance of LHSS.
- Most of the studies were carried out for the melting (charging) process of LHSS.
- Almost all the researchers analyzed the performance of the LHSS only based on the phase change time and energy stored.
- The usage of hybrid heat transfer techniques has shown better thermal performance than individual heat transfer techniques.

2.7 Research gaps

- To analyze the performance of the LHSS, phase change time and energy analysis are not sufficient. Exergy analysis is also an important parameter to be considered to analyze the performance of the LHSS. Very less amount of the studies were carried on the exergy efficiency of LHSS.
- Comparison studies of radial, spiral and longitudinal fin PCM shell and tube heat exchanger with GNP nanoparticle enhanced PCM considering the effect of orientation during melting and solidification were not carried out.
- Thermal performance analysis of PCM-based shell and tube heat exchanger enhanced with copper metal foam and GNP nanoparticles considering the effect of inclination was not performed.
- Three-dimensional studies were not presented comparing the thermal performance of shell and tube heat exchangers enhanced with radial and linear cascaded copper metal foams.

- Selection of the best hybrid heat transfer enhancement technique for PCM shell and tube heat exchanger is to be carried out.
- The effect of geometrical and heat transfer fluid parameters on the exergy efficiency is yet to be investigated.

2.8 Objectives

The following objectives are framed based on the above literature and research gaps.

1. Performance analysis of the shell and tube heat exchanger with nanoparticle enhanced phase change material (NEPCM) with different types of fins.
2. Performance analysis of the shell and tube heat exchanger with NEPCM and metal foam.
3. Performance analysis of the phase change materials (PCM) based shell and tube heat exchanger with the cascaded porous media.
4. Parametric study of PCM-based shell and tube heat exchanger studying the effect on exergy efficiency during melting and solidification.

Overall, the present study analyzes the influence of hybrid heat transfer enhancement techniques on the thermal performance of shell and tube LHSS during melting and solidification.

2.9 Closure

A comprehensive literature review on various factors which affects the thermal performance of a shell and tube LHSS is discussed. Various heat transfer enhancement techniques are analyzed. The objectives for the current research work are framed by thoroughly identifying the research gaps. To achieve the proposed objectives, numerical analysis is needed, the details of which are discussed in the next chapter.

Chapter 3

Numerical methodology

In chapter 2, various works pertaining to heat transfer enhancement techniques in phase change materials (PCMs) based LHSS units were discussed and depending on the research gaps, various objectives are framed. The details of the numerical methodology adopted for nanoparticle enhanced PCM (NEPCM) and porous media + PCM in the simulations are discussed in this current chapter. Various parameters used to compare the performance of the heat exchangers are presented in the current chapter.

3.1 Numerical procedure

In the present work melting and solidification analysis of PCM based shell and tube heat exchanger with hybrid heat transfer enhancement techniques is carried out. PCM + nanoparticles + fins, PCM+ nanoparticles + metal foam and PCM + cascaded metal foam techniques are used to enhance the performance of the PCM based shell and tube heat exchanger. The performance of these heat exchangers is compared with pure PCM shell and tube heat exchangers.

3.1.1 Numerical modeling of phase change

To model the behavior of the mushy zone region enthalpy-porosity technique is used, in which the mushy zone region is considered as porous media. ANSYS FLUENT is used to solve the governing equations. The finite volume method is considered for the computational domain. For pressure-velocity coupling, the PISO methodology is used. To handle the pressure, the PRESTO methodology is used and a second order upwind scheme is used to discretize momentum and energy equations. The convergence criteria for continuity, momentum, and energy equations are kept as 10^{-6}, 10^{-6}, and $10^{-8,}$ respectively.

To model the melting and solidification process, the following assumptions are made.

- Thermal contraction and expansion of tube, fins, metal foam, and nanoparticles are neglected.
- Adiabatic wall boundary condition is applied on the surface of the shell.
- PCM in both states is considered to be isotropic and homogeneous.

- Variation in the density of PCM in the liquid state, which results in the natural convection, is incorporated into the governing equations by using the Boussinesq approximation.
- The flow of liquid PCM and HTF are incompressible, unsteady, laminar, and Newtonian

The governing equations are:

Continuity equation:

$$\frac{\partial \rho}{\partial t} + \nabla.\left(\rho \vec{V}\right) = 0 \tag{3.1}$$

Momentum equation:

$$\rho \frac{\partial \vec{V}}{\partial t} + \rho \vec{V}.\left(\nabla.\vec{V}\right) = -\nabla P + \mu \nabla^2 \vec{V} + \rho \vec{g} \beta \Delta T + A\vec{V} \tag{3.2}$$

Energy equation:

$$\rho \frac{\partial h}{\partial t} + \rho \nabla.\left(h.\vec{V}\right) = \frac{k}{c_p} \nabla^2 h + S_h \tag{3.3}$$

In the Eqn.3.2 "A" is defined such that it imitates the flow in the porous media and is given as

$$A = -C \frac{(1-\epsilon)^2}{\epsilon^3 + b} \tag{3.4}$$

"*C*" is a mushy zone constant that influences the rate of heat transfer and thermal hydraulics of PCM during phase change. The value of the "*C*" is taken as 10^6 [132]. "ϵ" is the porosity which is equal to the liquid fraction. "b" is a constant which is given to avoid the zero in denominator.

"S_h" in Eqn.3.3 is the source term in the energy equation and is given as

$$S_h = \frac{\partial(\rho \Delta h)}{\partial t} + \vec{V}.\left(\rho \vec{V} \Delta h\right) \tag{3.5}$$

If phase change occurs isothermally, the first term in the above equation vanishes, and Δh depends on temperature *(Δh =f (T)). f (T)* is given as

For melting *f(T)* is given as

$$f(T) = \begin{cases} 0 & T < T_{so} \\ \frac{L(T-T_{so})}{(T_{li}-T_{so})} & T_{so} \leq T \leq T_{li} \\ L & T > T_{li} \end{cases} \quad (3.6)$$

For solidification *f(T)* is given as

$$f(T) = \begin{cases} 0 & T > T_{li} \\ \frac{L(T_{li}-T)}{(T_{li}-T_{so})} & T_{li} \geq T \geq T_{so} \\ L & T < T_{so} \end{cases} \quad (3.7)$$

3.1.2 Initial and boundary conditions

Initial and boundary conditions during melting and solidifications are as follows.

3.1.2.1 Melting process

- The temperature at the inlet and volume flow rate of HTF are 353K and 1.4LPM.
- The outlet condition of fluid is considered as "outflow".
- The initial temperature of PCM is 300K.
- Adiabatic condition is given to the outer surface of the shell.

3.1.2.2 Solidification process

- The temperature at the inlet and volume flow rate of HTF are 300K and 1.4LPM.
- The outlet condition of fluid is considered as "outflow".
- The initial temperature of PCM is 353K.
- Adiabatic condition is given at the outer surface of the shell.

3.1.3 Thermophysical properties of NEPCM

Variation in the specific heat capacity, density, coefficient of thermal expansion, and latent heat of NEPCM is calculated by using a mixture of the component technique[82]. To calculate the viscosity, the Krieger-Dougherty model is used[65]. By considering the interfacial thermal boundary resistance between PCM and nanoparticles the effective thermal conductivity of NEPCM is calculated by using the effective medium theory[65].

Density:

$$\rho_{nepcm} = (1-\varphi)\rho_{pcm} + \varphi\rho_{np} \quad (3.8)$$

Heat capacity

$$\left(\rho c_p\right)_{nepcm} = (1-\varphi)\left(\rho c_p\right)_{pcm} + \varphi\left(\rho c_p\right)_{np} \tag{3.9}$$

Latent heat:

$$\rho_{nepcm} L_{nepcm} = (1-\varphi)(\rho L)_{pcm} \tag{3.10}$$

Thermal expansion coefficient:

$$\rho_{nepcm}\beta_{nepcm} = (1-\varphi)(\rho\beta)_{pcm} + \varphi(\rho\beta)_{np} \tag{3.11}$$

Viscosity:

$$\mu_{nepcm} = \mu_{pcm}\left(1 - \frac{\varphi}{\varphi_{max}}\right)^{-A\varphi_{max}} \tag{3.12}$$

"A" and φ_{max} are intrinsic viscosity and maximum packing factor which are influenced by the shape of nanoparticles. Packing factors for spherical, 1D and 2D materials are 0.632, 0.268, and 0.382 respectively[65]. The intrinsic viscosity for GNP is 9.87(dL/g).

Thermal conductivity:

$$k_{nepcm} = k_{pcm}\left[\frac{3+\varphi[2\lambda_{xx}(1-L_{xx})+\lambda_{zz}(1-L_{zz})]}{3-\varphi[2\lambda_{xx}L_{xx}+\lambda_{zz}L_{zz}]}\right] \tag{3.13}$$

Where

$$L_{xx} = \frac{a^2}{2(a^2-1)} + \frac{a}{2(1-a^2)^{3/2}}\cos^{-1} a \tag{3.14}$$

$$L_{zz} = (1-2L_{xx}) \tag{3.15}$$

$$\lambda_{xx} = \frac{k_{f,xx}-k_{pcm}}{K_{pcm}+L_{xx}\left(k_{f,xx}-k_{pcm}\right)} \tag{3.16}$$

$$\lambda_{zz} = \frac{k_{f,zz}-k_{pcm}}{k_{pcm}+L_{zz}\left(k_{f,zz}-k_{pcm}\right)} \tag{3.17}$$

$$k_{f,ii} = \frac{k_{np}}{1+\gamma L_{ii}\left({}^{k_{np}}/_{k_{pcm}}\right)} \tag{3.18}$$

$$\gamma = (1+2a)\frac{R_{bd}k_{pcm}}{d_{np}} \qquad \text{for } a \le 1 \tag{3.19}$$

L_{xx}, L_{yy}, *and* L_{zz} are geometric parameters that depend upon the aspect ratio of nanoparticles. $k_{f,xx}$ and $k_{f,zz}$ are equivalent thermal conductivity. k_{np} and R_{bd} are the thermal conductivity of nanoparticles and thermal boundary resistance between nanoparticles and PCM which is in the order of 10^8 m^2 K^{-1} W^{-1} [65].

3.1.4 Parameters of metal foam

Pore density, porosity and diameter of the metal foam ligament are important parameters required to obtain the characteristics of the metal foam. Ligament diameter 'd_l' is estimated by Eqn.3.20.

$$\frac{d_l}{d_p} = 1.18\sqrt{\frac{1-\varepsilon}{3\pi}}\left(\frac{1}{1-e^{-(1-\varepsilon)/0.04}}\right) \tag{3.20}$$

Where the diameter of pore 'd_p' is given by Eqn.3.21.

$$d_p = \frac{0.0254}{\omega} \tag{3.21}$$

Where 'ω' is pore density (PPI)

The other parameters are the permeability of metal foam 'K' and inertial coefficient 'C_f' are given in Eqns.3.22 and 3.23 respectively.

$$\frac{K}{d_p^2} = 0.00073(1-\varepsilon)^{-0.224}\left(\frac{d_l}{d_p}\right)^{-1.11} \tag{3.22}$$

$$C_f = 0.00212(1-\varepsilon)^{-0.132}\left(\frac{d_l}{d_p}\right)^{-1.63} \tag{3.23}$$

The effective thermal conductivity of PCM with metal foam 'k_{pcm}' and effective thermal conductivity of metal foam 'k_{pm}' are given in Eqns.3.24 and 3.25 [121].

$$k_{eff,pcm} = \frac{\sqrt{2}}{2(M_A+M_B+M_C+M_D)} \qquad \text{where } k_{pm} = 0 \tag{3.24}$$

$$k_{eff,pm} = \frac{\sqrt{2}}{2(M_A+M_B+M_C+M_D)} \qquad \text{where } k_{pcm} = 0 \tag{3.25}$$

Where:

$$M_A = \frac{4\sigma}{(2a^2+\pi\sigma(1-a))k_{pm}+(4-2a^2-\pi\sigma(1-a))k_{pcm}} \tag{3.26}$$

$$M_B = \frac{(a-2\sigma)^2}{\left((a-2\sigma)a^2k_{pm}\right)+(2a-4\sigma-(a-2\sigma)a^2)k_{pcm}} \tag{3.27}$$

$$M_C = \frac{\left(\sqrt{2}-2a\right)^2}{2\pi\sigma^2\left(1-2a\sqrt{2}\right)k_{pm}+2\left(\sqrt{2}-2a-\pi\sigma^2\left(1-2a\sqrt{2}\right)\right)k_{pcm}} \tag{3.28}$$

$$M_D = \frac{2a}{a^2k_{pm}+(4-a^2)k_{pcm}} \tag{3.29}$$

$$\sigma = \sqrt{\frac{\sqrt{2}\left(2-5/8a^3\sqrt{2}-2\varepsilon\right)}{\pi\left(3-4a\sqrt{2}-a\right)}} \tag{3.30}$$

Where 'a' = 0.339; 'ε' is the porosity of metal foam and '$k_{eff,pcm}$' is the thermal conductivity of PCM in the presence of metal foam.

In the present study, the heat transfer coefficient 'h_{sf}' between porous media and PCM is estimated using Churchill and Chu correlation [123][91]. Metal foam ligaments are considered to be smooth cylinders. The heat transfer coefficient is given as

$$h_{sf} = \frac{k_{pcm}}{d_f}\left(0.6 + \frac{0.387Ra^{1/6}}{\left[1+\left(\frac{0.599}{Pr}\right)^{9/27}\right]^{8/27}}\right)^2 \tag{3.31}$$

Where

$$Pr = \left(\frac{\mu c_p}{k}\right)_{pcm} \tag{3.32}$$

$$Ra = \frac{g\beta|T_{pm}-T_{pcm}|d_l^3}{(\alpha\vartheta)_{pcm}} \quad (3.33)$$

The specific surface area between metal foam and PCM 'A_{sf}' is given as

$$A_{sf} = \frac{3\pi d_l\left(1-e^{-(1-\varepsilon)/0.04}\right)}{\left(0.59d_p\right)^2} \quad (3.34)$$

In the present work, a non-thermal equilibrium approach is used to model the heat transfer interaction between PCM and metal foam. To model the heat transfer interaction between PCM and metal foam continuity and momentum equations remain the same as shown in Eqns.3.1 and 3.2 but instead of one energy equation, two separate equations are used. Eqns.3.35 and 3.36 are energy equations of metal foam and PCM respectively.

PCM:

$$\varepsilon\left(\rho c_p\right)_{pcm}\left(\frac{\partial T}{\partial t} + V.\nabla T_{pcm}\right) + \varepsilon\rho_{pcm}\frac{\partial(\Delta h)}{\partial t} = k\nabla^2 T_{pcm} + h_{sf}A_{sf}\left(T_{pcm} - T_{pm}\right) + s_h \quad (3.35)$$

Porous media (metal foam):

$$(1-\varepsilon)\left(\rho c_p\right)_{pm}\left(\frac{\partial T_{pm}}{\partial t}\right) = k\nabla^2 T_{pm} + h_{sf}A_{sf}\left(T_{pm} - T_{pcm}\right) \quad (3.36)$$

3.2 Parameter definition

In this study to compare the performance of various heat exchangers melting time, solidification time, exergy efficiency, energy storage (energy absorbed by PCM during melting) and energy release (energy released by PCM during solidification) ratios are considered. Both melting time and solidification time are obtained from the numerical simulations.

3.2.1 Energy storage and release ratios

The energy storage ratio is given as the ratio of energy stored to the maximum amount of energy that LHSS can store. During melting, energy is stored (E_{st}) and during solidification, energy is released (E_r). The equations are given as

$$E_{st} = \begin{cases} c_{p,s}(T_{avg} - T_{ini}) & T_{avg} < T_{so} \\ c_{p,s}(T_{so} - T_{ini}) + L\left(\frac{T_{avg}-T_{so}}{T_{li}-T_{so}}\right) & T_{so} \le T_{avg} \le T_{li} \\ c_{p,s}(T_{so} - T_{ini}) + L + c_{p,l}(T_{avg} - T_l) & T_{avg} > T_{li} \end{cases} \quad (3.37)$$

$$E_r = \begin{cases} c_{p,l}(T_{ini} - T_{avg}) & T_{avg} > T_{li} \\ c_{p,l}(T_{ini} - T_{li}) + L\left(\frac{T_{avg}-T_{li}}{T_{li}-T_{so}}\right) & T_{so} \le T_{avg} \le T_{li} \\ c_{p,l}(T_{ini} - T_{li}) + L + c_{p,s}(T_{so} - T_{avg}) & T_{avg} < T_{so} \end{cases} \quad (3.38)$$

During melting, the energy storage ratio (ε_{st}) is given as Eqn.3.40. Here E_{st} and E_{ms} are the energy stored and the maximum amount of energy that LHSS can store.

$$E_{ms} = c_{p,s}(T_{so} - T_{ini}) + L + c_{p,l}(T_{htf} - T_{li}) \quad (3.39)$$

$$\varepsilon_{st} = \frac{E_{st}}{E_{ms}} \quad (3.40)$$

During solidification, the energy release ratio (ε_r) is given as Eqn.3.42. Here E_r and E_{mr} are the energy release and the maximum amount of energy that LHSS can release.

$$E_{mr} = c_{p,s}(T_{so} - T_{htf}) + L + c_{p,l}(T_{ini} - T_{li}) \quad (3.41)$$

$$\varepsilon_r = \frac{E_r}{E_{mr}} \quad (3.42)$$

3.2.2 Exergy

Exergy is the quality of the energy available. Exergy relations during melting and solidification are given below.

During melting

$$E\dot{x}_{in} = \dot{m}_{htf} C_{p,htf} \left[(T_{in} - T_{out}) - T_o ln\left(\frac{T_{in}}{T_{out}}\right)\right] \quad (3.43)$$

$$\dot{Ex}_{st} = \dot{E}_{st}\left[1 - \frac{T_o}{T_{avg}}\right] \quad (3.44)$$

$$\eta_{Ex,m} = \frac{\dot{Ex}_{st}}{\dot{Ex}_{in}} \times 100 \quad (3.45)$$

Where $\dot{Ex}_{in}$ is exergy given by HTF, $\dot{Ex}_{st}$ is exergy stored, $\eta_{Ex,m}$ is exergy efficiency during melting, T_{in} is inlet temperature and T_{out} is the outlet temperature of HTF.

During solidification

$$\dot{Ex}_r = \dot{E}_r\left[1 - \frac{T_o}{T_{avg}}\right] \quad (3.46)$$

$$\dot{Ex}_{out} = \dot{m}_{htf} C_{p,htf}\left[(T_{out} - T_{in}) - T_o ln\left(\frac{T_{out}}{T_{in}}\right)\right] \quad (3.47)$$

$$\eta_{Ex,sol} = \frac{\dot{Ex}_{out}}{\dot{Ex}_r} \times 100 \quad (3.48)$$

Where $\dot{Ex}_r$ exergy released by PCM, $\dot{Ex}_{out}$ is exergy out to HTF, $\eta_{Ex,sol}$ is exergy efficiency during solidification and T_o is ambient temperature.

3.3 Closure

In the present chapter, numerical methodology followed to model PCM interaction with nanoparticles + fins, PCM interaction with porous media (metal foam) and PCM interaction with porous media + nanoparticles are discussed. Initial and boundary conditions used in simulations are presented. The parameters considered to analyze the performance of the LHSS are discussed in the current chapter.

Chapter 4

Numerical analysis of thermal transport for pure PCM in shell and tube heat exchanger

In chapter 3, numerical methodology and comparison parameters used to numerically simulate and analyze the heat exchangers are discussed. For numerical simulations, the shell and tube heat exchanger dimensions are fixed based on the optimal design parameters obtained from the literature. The analysis of pure PCM based shell and tube heat exchanger is carried out in the present chapter. The study gives an inference on the performance of the pure PCM shell and tube heat exchanger. The results of the pure PCM shell and tube heat exchanger are used to compare the performance of the PCM shell and tube heat exchangers, in which hybrid heat transfer enhancement techniques are used in the next chapters. The current chapter conducts melting and solidification analysis of pure PCM shell and tube heat exchanger.

4.1 Geometric parameters of shell and tube heat exchanger

Geometric parameters of the heat exchanger are selected considering the optimized geometric parameters in the literature. On reviewing the literature related to LHSS shell and tube heat exchanger, Kalpala and Devanuri [63] concluded that tube to shell diameter should be nearly 0.25. In the present work, this ratio is considered as 0.254. Trp et al.[64] observed that LHSS has shown better performance when the ratio of length to shell diameter is kept near 3.2. In the present study, this ratio is 3.33. The heat exchanger length, shell diameter and tube thickness are considered as 250mm, 75mm and 0.8mm, respectively. The schematic of the heat exchanger is shown in Fig. 4.1. Kalpala and Devanuri [42] noted that varying mass flow rate of HTF has an insignificant effect on the performance of the heat exchanger. The volume flow rate of HTF is fixed at 1.4 LPM[29]. Compatibility studies of organic PCMs with different metals carried out by Gaddala and Devanuri [133] revealed that stainless steel exhibited better compatibility with the PCM; as a result, the tube material is selected as stainless steel. Since lauric acid is suitable for heat storage applications, it is considered for the study. The thermophysical properties of lauric acid [134] are given in Table 4.1.

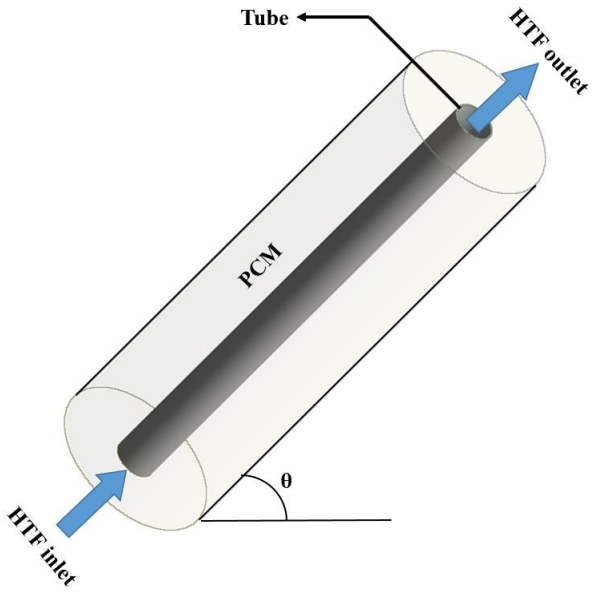

Fig 4.1 Schematic of PCM shell and tube heat exchanger

Table 4.1 Thermo physical Properties of Lauric acid[134]

Thermophysical properties	**Value**
Solidus temperature (K)	316.46
Liquidus temperature (K)	322.94
Latent heat (J/kg)	156827
Density (kg/m^3)	1051.2 (solid) 885.04 (liquid)
Thermal conductivity (W/m K)	0.227 (solid) 0.388 (liquid)
Specific heat (J/kg K)	1390 (solid) 1570 (liquid)
Thermal expansion coefficient (K^{-1})	0.000925
Viscosity (kg/m s)	0.00435

4.2 Results and discussion

4.2.1 Melting

4.2.1.1 Temperature distribution and melt fraction

Fig.4.2 shows the contours of temperature and melt fraction during melting for considered LHSS heat exchangers. Both the temperature and melt fraction contours indicate that the melted hot PCM is settling at the top portion of the heat exchanger due to the buoyancy effect. Initially, the amount of melted PCM is less in the vertically positioned heat exchanger than in the incline and horizontally positioned heat exchanger, but the maximum temperature is noted to be high in the vertically oriented heat exchanger. As time progresses, the temperature of the hot PCM settled at the top portion of the heat exchanger increases and reaches nearly the temperature of HTF. During the final stage of melting, unmelted PCM is noted to present at the bottom part of the heat exchanger, irrespective of the orientations of the heat exchangers. It infers that initially, heat transport took place towards the top portion of the heat exchanger due to natural convection and during the final stage, heat transport took place from the top portion to the bottom portion of the heat exchanger due to the conduction mode of heat transfer.

To better understand the effect of orientation during melting, transient variations of melt fraction and average temperature are analyzed. Fig.4.3 shows the transient variation of temperature and melt fraction of the LHSS considered. From Fig.4.3 (a), it can be noticed that at the initial stage of melting, variation in average temperature with time is the same for all the considered orientations of the heat exchanger. Whereas during the initial stage of melting, the rate of melting is less in the vertically oriented heat exchanger and is equal in the inclined (45°) and horizontally oriented heat exchanger. As time progresses, a sudden decrease in the rate of increase in the average temperature and melt fraction in horizontally oriented heat exchanger is noted. This is because PCM present at the top portion of the heat exchanger reached to a temperature nearly that of HTF temperature and heat transport to the bottom portion takes place from the top portion of the heat exchanger. PCM presented in the bottom portion which is to be melted due to the conduction mode of heat transfer is maximum in horizontally oriented heat exchanger followed by incline (45°) oriented heat exchanger, and least in vertically oriented heat

exchanger. As a result, on further melting, the rate of increase in the melting and average temperature decreases in the inclined (45°) heat exchanger. Although initially during melting, the rate of melting is less in case of the vertically oriented heat exchanger overall melting time is less, this is because during the final stage of the melting, heat transport took place due to the conductive mode of heat transfer. The amount of PCM which is to be melted due to the conductive mode of heat transfer is less in the case of the vertically oriented heat exchanger. The complete melting time of vertical, incline (45°) and horizontally oriented heat exchangers are 6505, 8065 and 8050 seconds, respectively. The average temperature at the end of melting for vertical, incline (45°) and horizontally oriented heat exchangers are 350.67, 352.4 and 347.05 K, respectively.

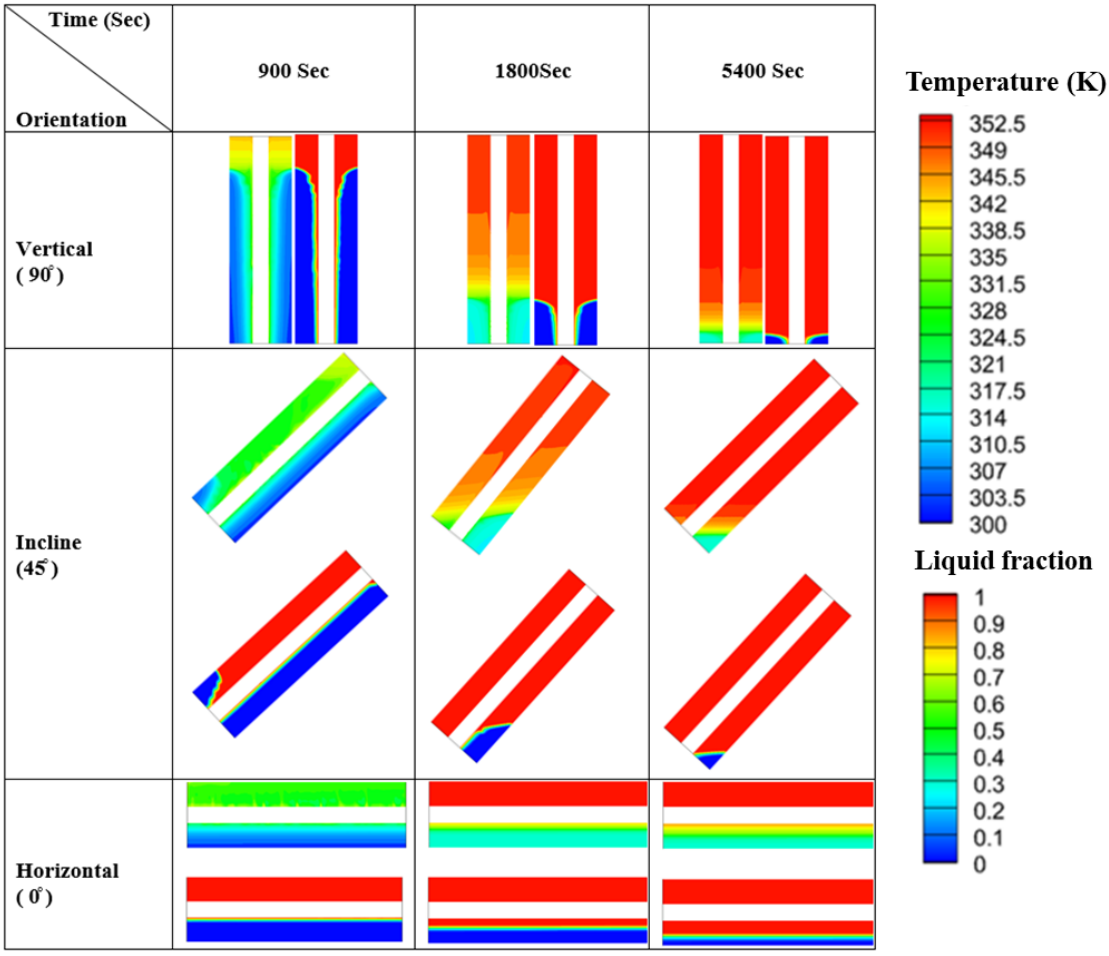

Fig 4.2 Temperature (left) and melt fraction (right) contours during melting

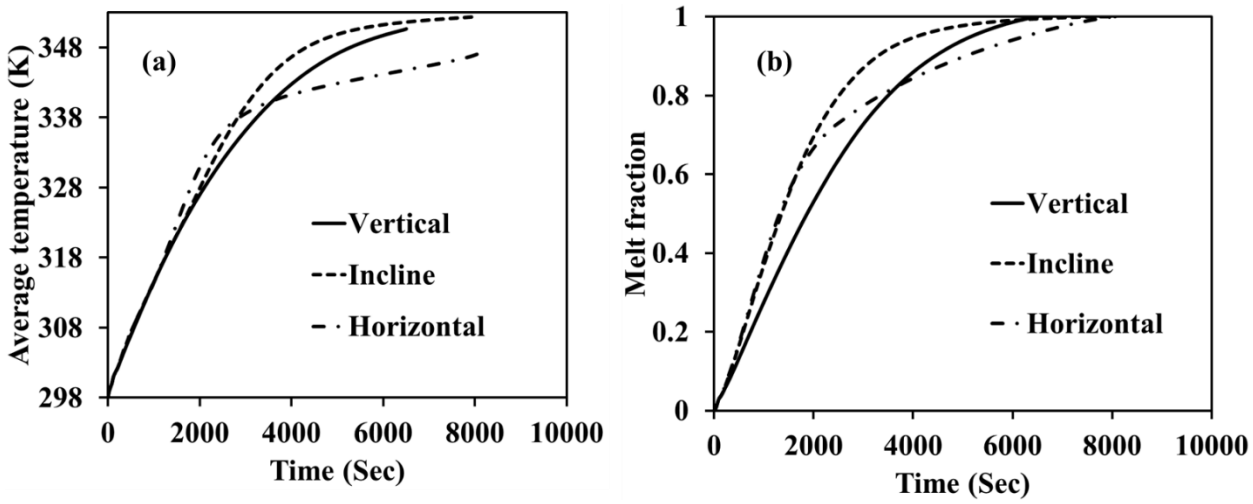

Fig 4.3 Average temperature and melt fraction evolution for heat exchangers during melting

4.2.1.2 Energy storage ratio

The amount of the energy stored is proportionate to the average temperature and is calculated by Eq.3.37. The energy storage ratio is given by Eqn.3.40. Fig.4.4 shows the transient variation of the energy storage ratio for the considered heat exchangers. It can be noted that irrespective of the orientation of the heat exchanger the energy storage ratio of considered LHSS can be divided into three stages. During the initial stage, the energy is absorbed in the form of sensible heat, due to this the rate of increase in the energy storage ratio is less. During the second stage, the energy is absorbed in the form of latent heat of the material. In this stage, a large amount of energy is stored with very less change in the temperature, a sharp rise in the energy storage ratio is noted in this stage. Until the completion of the second stage, the trend in energy storage ratio is the same in all heat exchangers irrespective of the orientation of the heat exchanger. This is because until the second stage average temperature of all LHSSs is the same. During the third stage of melting the energy storage again takes place in the form of sensible heat. As a result, the rate of energy storage is less. In this stage variation in the energy storage ratio is due to variation in the average temperature of LHSS. The energy storage ratio at the end of melting for vertical, incline (45°) and horizontally oriented heat exchangers are 0.98, 0.99 and 0.95 respectively. The energy storage ratio followed the trend of average temperature.

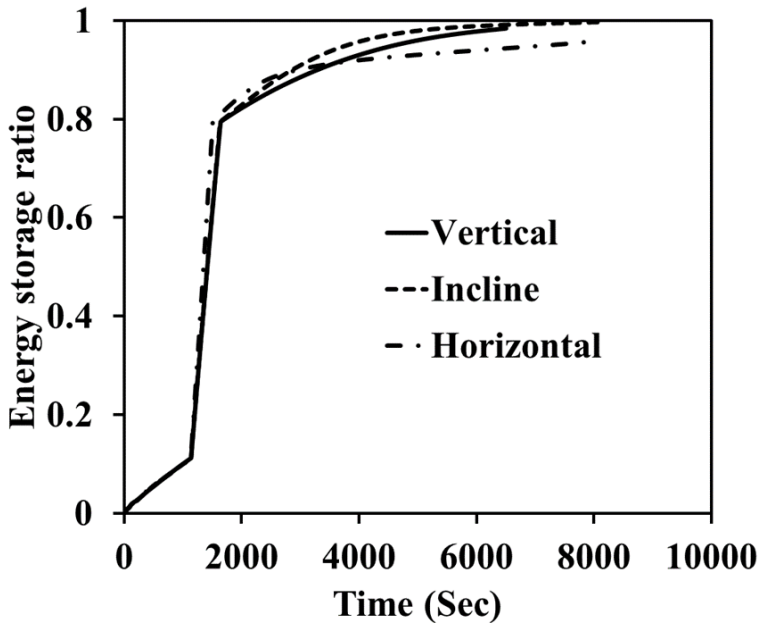

Fig 4.4 Energy storage ratio evolution for heat exchangers during melting

4.2.1.3 Exergy efficiency during melting

Exergy is the amount of available energy. Exergy efficiency represents the quality of the energy that can be retrieved. It depends upon the outlet and inlet temperatures of HTF and the PCM average temperature. Fig.4.5 shows the exergy efficiency of considered heat exchangers. It is observed that for all the considered cases exergy efficiency during the process of melting is observed to follow the trend of the average temperature of PCM. This is because as the process of melting progresses the average temperature of PCM increases which prompts an increase in the exergy efficiency with time. Throughout the melting process, the difference between the outlet and inlet temperature of HTF is very less, as a result, the exergy efficiency is dependent mostly on the average temperature of the PCM. Average exergy efficiency for vertical, incline (45°) and horizontally oriented heat exchangers are 67.55%, 76.16% and 70.88% respectively. Since the vertical heat exchanger is operated at high temperatures for less time its exergy efficiency is less when compared with other orientations of the heat exchanger and the inclined heat exchanger is operated at high temperatures for the highest time, thus resulting in the highest average exergy efficiency.

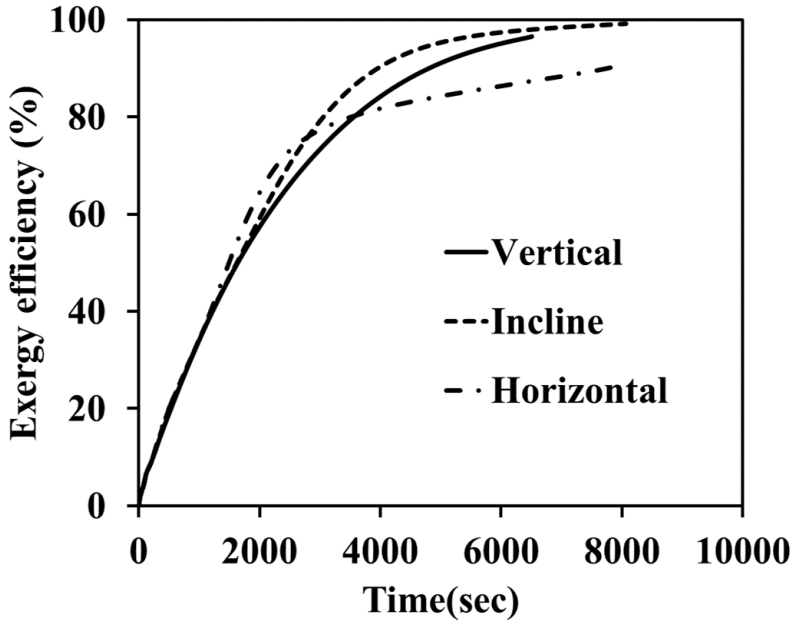

Fig 4.5 Exergy efficiency evolution for heat exchangers during melting

4.2.2 Solidification

4.2.2.1 Temperature distribution and melt fraction

Fig.4.6 shows the contours of temperature and melt fraction during solidification for the considered LHSS heat exchangers. It is observed that during the initial stage of solidification, the distribution of temperature is nearly uniform. This indicates that the solidification process is conduction dominant. But in liquid fraction contours, a small portion of liquid PCM at the top and near the shell surface of the heat exchanger can be noted. This is due to buoyancy force. In the case of the horizontal heat exchanger amount of liquid PCM settled at the top is more than the other orientations of the heat exchanger, at the same time maximum amount of the solidified PCM is present at the bottom section of the horizontally oriented heat exchanger than compared with other two. As time progress, the amount of the solidified PCM increases in the heat exchanger. A maximum amount of the solidified PCM is observed to be present at the bottom part of the heat exchanger. This is because of buoyancy force, which results in hot liquid PCM settling at the top portion of the heat exchanger. This phenomenon is observed even at the final stage of the solidification.

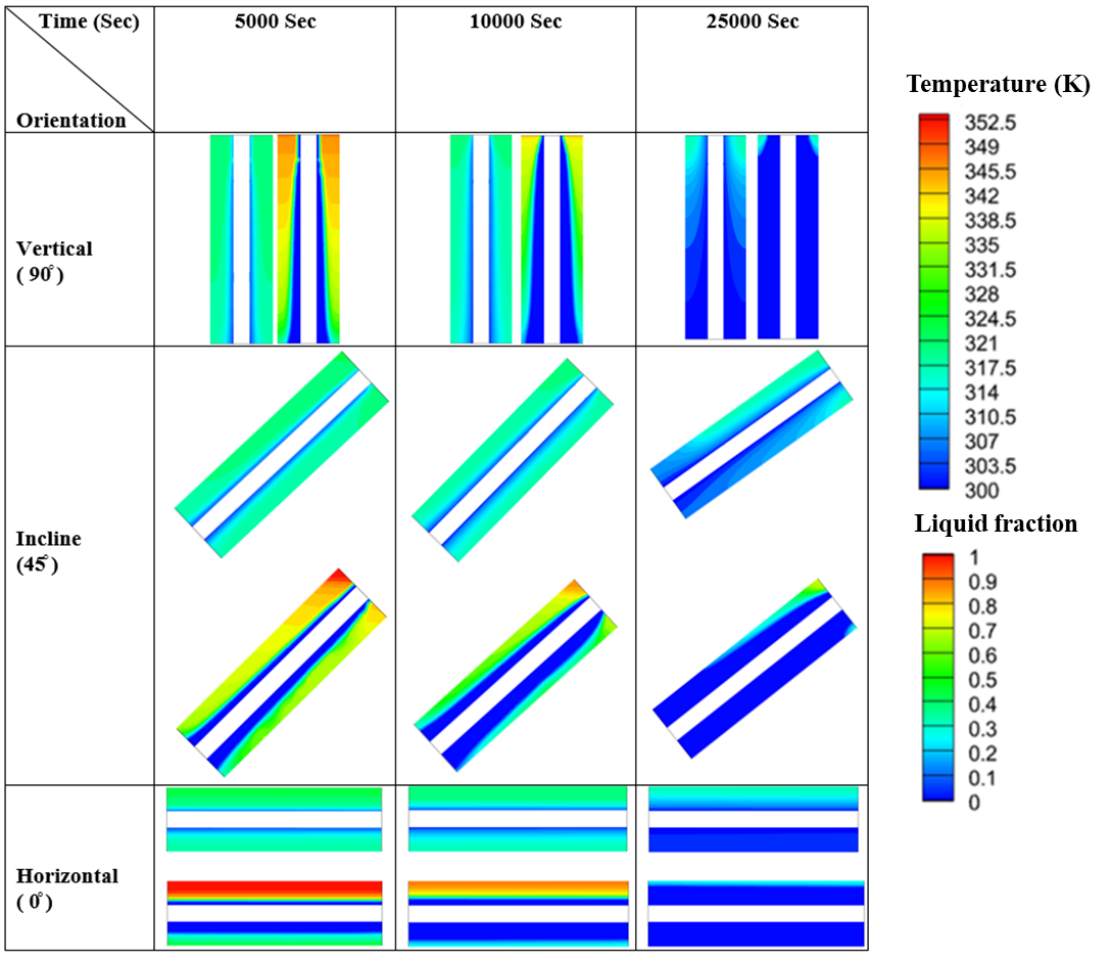

Fig 4.6 Temperature (left) and melt fraction (right) contours during solidification

To have better insight into the effect of orientation during solidification, transient variation of average temperature and melt fraction is analyzed. Fig.4.7 shows the transient variation of temperature and melt fraction of LHSS considered. From Fig.4.7 (a) it can be noticed that irrespective of the orientation of the heat exchanger, trends in the transient variation of average temperature and melt fraction are the same. This is because throughout the solidification process heat transfer is predominantly due to conduction. A rapid decrease in the temperature is noted during the initial stage of the solidification and reaches to liquids temperature of PCM although the melt fraction in this situation is greater than 0.8. This indicates that due to the conduction mode of heat transfer a uniform decrease in the temperature is noted in the LHSS heat exchanger. As time progresses decrease in the rate of temperature decreases due to a decrease in the temperature difference between the average temperature of LHSS and HTF. The complete

solidification time of vertical, incline (45°) and horizontal oriented heat exchangers are 29100, 30775 and 26675 seconds respectively. The average temperature at the end of solidification for vertical, incline (45°) and horizontal oriented heat exchangers are 300.74, 299.47 and 303.18 K respectively.

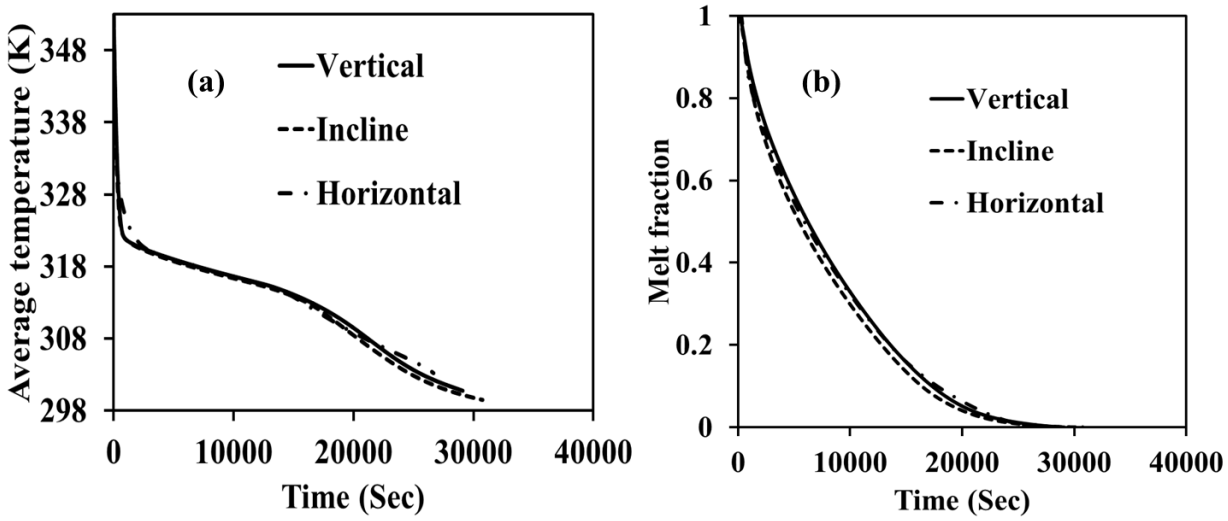

Fig 4.7 Temperature (left) and melt fraction (right) contours during solidification

4.2.2.2 Energy release ratio

The energy released by PCM is proportional to the difference between the initial temperature and the average temperature of the PCM. The energy release ratio is the energy given away by PCM to the maximum energy that PCM can release. Fig.4.8 shows the transient variation of the energy release ratio for the considered heat exchanger. It can be noted that irrespective of the orientation of the heat exchanger, the energy release ratio of considered LHSS can also be divided into three stages like energy storage ratio. The initial stage during which energy is released is in the form of sensible heat. The rate of energy ratio during the first stage is very high because of the rapid decrease in the temperature during the first stage of solidification. During the second stage, the energy is released in the form of the latent heat capacity of the material. In this stage, a large amount of energy is released for very less change in the temperature. During the third stage of solidification again the energy release takes place in the form of sensible heat and the rate of decrease in temperature is also less during this stage, as a result, the rate of energy release is less. From Fig.4.8 it can be observed that the orientation of the heat exchanger

has less effect on the energy release ratio during the solidification. The energy release ratio at the end of solidification for vertical, incline (45°), and horizontal oriented heat exchangers are 0.98, 0.99 and 0.96 respectively.

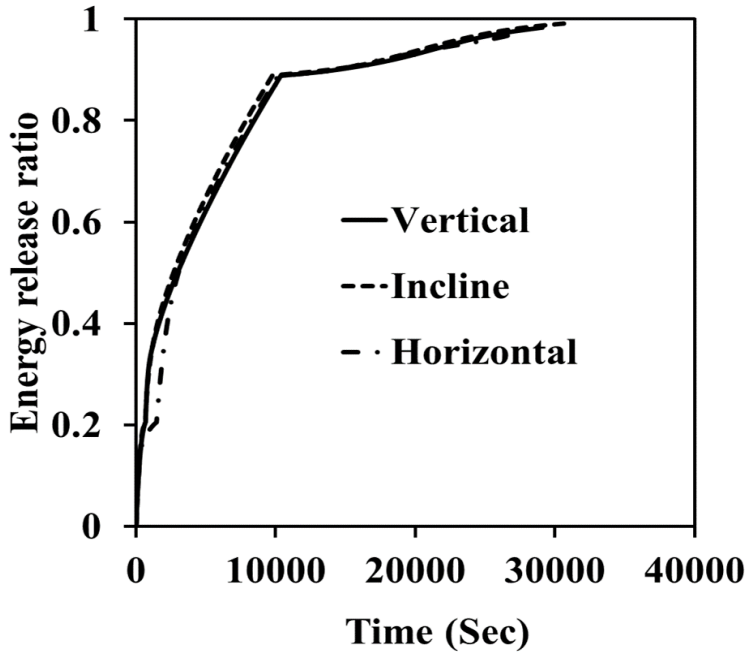

Fig 4.8 Energy storage ratio evolution for heat exchangers during melting

4.2.2.3 Exergy efficiency

Analysis of exergy efficiency during solidification is very important. It gives an insight into the quality of energy that can be recovered. Fig.4.9 shows the exergy efficiency for all considered heat exchangers. From Fig.4.9 it can be observed that exergy efficiency decreased with the progress of solidification. The PCM releases energy at a temperature that is much higher than the outlet temperature of the HTF, thus resulting in exergy destruction during the process of solidification. Initially, the difference in inlet and outlet temperatures of HTF is considerably high as a result exergy efficiency is high. Average exergy efficiency for vertical, incline (45°) and horizontally oriented heat exchangers during solidification are 0.59%, 0.61% and 0.72% respectively. The average exergy efficiency during solidification is very less. This indicates that the outlet temperature of HTF is very less when compared with the temperature at which PCM releases energy.

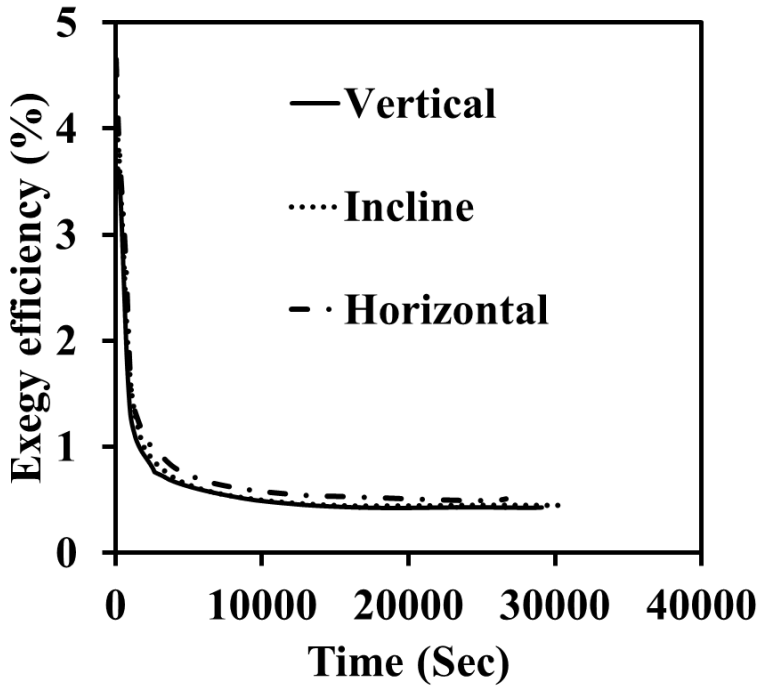

Fig 4.9 Exergy efficiency evolution for heat exchangers during solidification

4.3 Closure

In this chapter thermal performance of the pure PCM (Lauric acid) in shell and tube heat exchanger during both melting and solidification is investigated considering the effect of orientation. Performance comparison of the considered heat exchangers is carried out.

- During melting minimum of 6505 sec and a maximum of 8065 sec are noted in vertical and 45° oriented heat exchangers.
- The final average temperature of LHSS during melting has a minimal effect due to the orientation of the heat exchanger, thus resulting in a minimal effect on the final energy storage ratio.
- During melting, maximum average exergy efficiency and minimum average exergy efficiency of 76.16% and 67.55% are noted in 45° and vertically oriented heat exchangers.
- During solidification minimum of 26675 sec and a maximum of 30775 sec are noted in horizontal and 45° oriented heat exchangers.
- The final average temperature, final energy release ratio and exergy efficiency of LHSS during solidification have a minimal effect due to the orientation of the heat exchanger.

Chapter 5

Effect of fins – nanoparticles on the thermal performance of latent heat storage system

5.1 Introduction

The usage of fins and nanoparticles has shown a significant improvement in the melting and solidification of phase change materials (PCM). Analysis of the combined effect of the fins and nanoparticles further improves the performance of the latent heat energy storage systems (LHSS). On reviewing the literature, it was found that radial, spiral and longitudinal fins are the most commonly used fins to enhance the rate of heat transfer in LHSS and graphene nanoplatelets (GNPs) nanoparticles were found to show better compatibility with PCMs. Inclination studies on LHSS have shown contradicting results. Hence, in the present chapter melting and solidification performance of radial fins, spiral fins, and longitudinal fins in combination with nanoparticle-enhanced phase change materials (NEPCM) in a shell and tube heat exchanger is analyzed, and a comparison is made. GNPs are selected as nanoparticles in the present analysis because they lead to a high increase in the thermal conductivity of PCMs.

5.2 Physical model

The computational domains of radial, spiral and longitudinal finned shell and tube type LHSS is shown in Fig.5.1. To decide the geometric parameters for the hybrid fin-NEPCM-based shell and tube heat exchanger, the optimized parameters from the literature are considered. Kalapala and Devanuri[63] on reviewing several research works, concluded that the optimized ratio of shell to tube diameter should be nearly 4. Kaplala and Devanuri[29] gave the non-dimensional correlation for fin spacing and fin diameter by optimizing the melting time for radial finned LHSS heat exchanger. In the present study, the same pitch and diameter of fins are considered for radial and spiral finned LHSS heat exchangers. Rabienataj et al.[135] on conducting numerical analysis found that the optimal number of longitudinal fins is 10 considering the melting time for a shell and tube LHSS heat exchanger. Gaddala and Devanuri[133] on conducting compatibility studies with

different organic PCMs concluded that stainless steel showed better resistance to the corrosion effect.

The length of the heat exchanger, the inner diameter of the shell, and the thickness of the tube are considered to be 250mm, 75mm and 0.8mm respectively. The ratio of the shell diameter to the outer diameter of the tube is taken as 3.93. The radius of the radial fins is considered from the non-dimensional parameters given by Kalapala and Devanuri[29]. The same diameter is considered for spiral fins. The radial distance of longitudinal fins is considered to be equal to the radius of radial fins. Stainless steel is considered for tube and fin material. The fin thickness of radial fins is considered to be 0.8mm and the fin thickness for the spiral is adjusted such that the volume of PCM is the same in every case. Kalapala and Devanuri[42] observed that the influence of the mass flow rate of HTF is negligible. Therefore in the present study, the mass flow rate of the HTF is fixed at 1.4 LPM[29]. The Reynolds number for the considered mass flow rate of HTF is 1710. Lauric acid is considered as the PCM due to its suitability for heat storage applications[133]. The thermophysical properties of lauric acid[134] and nanoparticle-enhanced lauric acid are listed in Table 5.1.

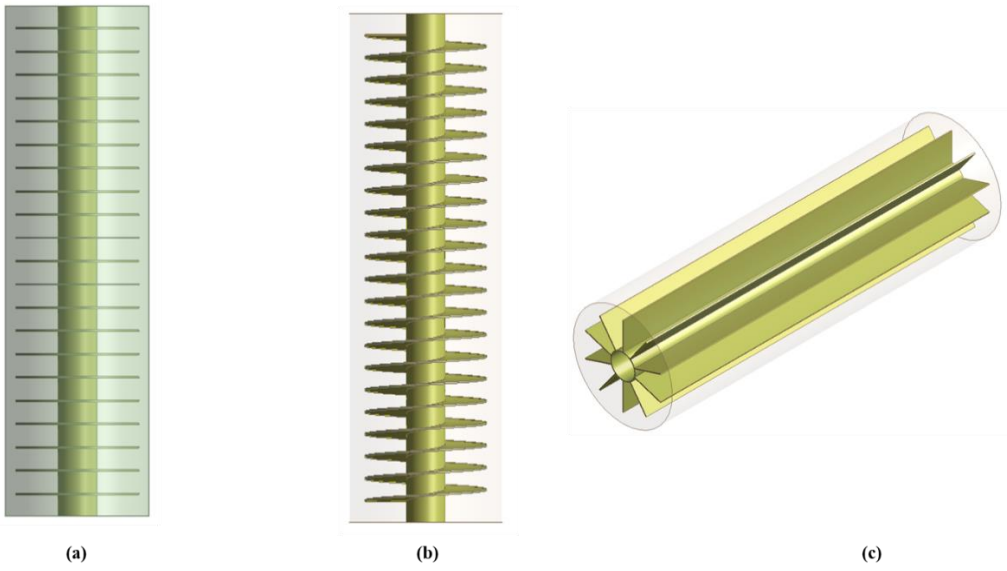

Fig 5.1 Computational domain of LHSS HXs (a) Radial fins (b) Spiral fins (c) Longitudinal fins

Table 5.1 Properties of pure PCM (lauric acid) and NEPCM

	Pure [133]		**0.5% GNP**		**1% GNP**	
	Solid	**Liquid**	**Solid**	**Liquid**	**Solid**	**Liquid**
Solidus temperature (K)	316.46	316.46	316.46	316.46	316.46	316.46
Liquidus temperature (K)	322.94	322.94	322.94	322.94	322.94	322.94
Latent heat (J/kg)	156827	156827	155194.8	154892.2	153580.3	152985.7
Density (kg/m^3)	1051.2	885.04	1056.944	891.61	1062.68	898.189
Thermal conductivity (W/m K)	0.227	0.388	0.374	0.538	0.51	0.687
Specific heat (J/kg K)	1390	1570	1382.226	1558.563	1374.53	1547.294
Thermal expansion coefficient (T^{-1})	_	0.000925	_	0.000914	_	0.000902
Viscosity (kg/m s)	_	0.00435	_	0.004572	_	0.004808

5.3 Numerical methodology

5.3.1 Validation

The finite volume method is considered for the computational domain. For pressure-velocity coupling, the PISO is employed. To handle the pressure PRESTO methodology is used and a second-order upwind scheme is used for the discretization of momentum and energy equations. The convergence criteria for continuity, momentum, and energy equations are kept as 10^{-6}, 10^{-6}, and $10^{-8,}$ respectively. ANSYS FLUENT is used to solve the governing equations.

To make sure that the present numerical results match with realistic phase change process, numerical modeling for the melting and solidification process of NEPCM are compared with the results of Khan et al.[82]. Physical model of Khan et al.[82] is a multi-tube shell

and tube heat exchanger in which the PCM was enhanced with 3% volume Al_2O_3. The present numerical model exhibited a maximum deviation of 4% during melting and 8% during solidification which is shown in Fig.5.2. Thus, it can be concluded that the present numerical model can be used for further investigation.

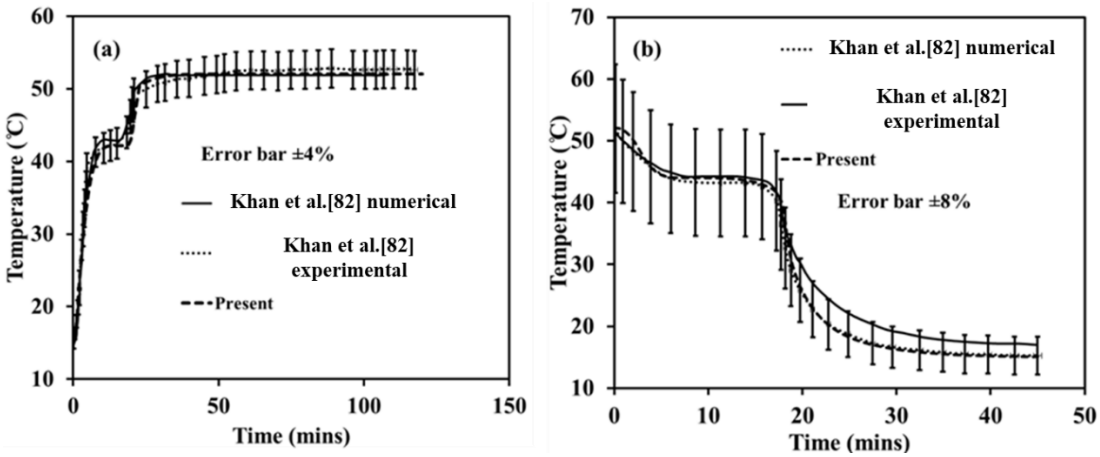

Fig 5.2 Numerical validation for (a) melting (b) solidification [82]

5.3.2 Grid and time independence

For a transient heat transfer phenomenon time step, grid quality, and grid number are very important factors that affect the solution and computational time. For the considered heat exchangers, structured grids are generated as shown in Fig.5.3. Grid and time-independent studies are examined individually for the considered fin configurations by comparing the volume-averaged melt fraction of the PCM in the heat exchanger. Based on the grid independence studies, the grid sizes considered for radial fin, spiral fin, and longitudinal fin heat exchangers are 253195, 391834, and 163284, respectively. Similarly, time-independent studies are carried out with 0.1, 0.2, and 0.3 seconds time steps. Time independence is achieved for 0.2 seconds time step for all the considered fin geometries.

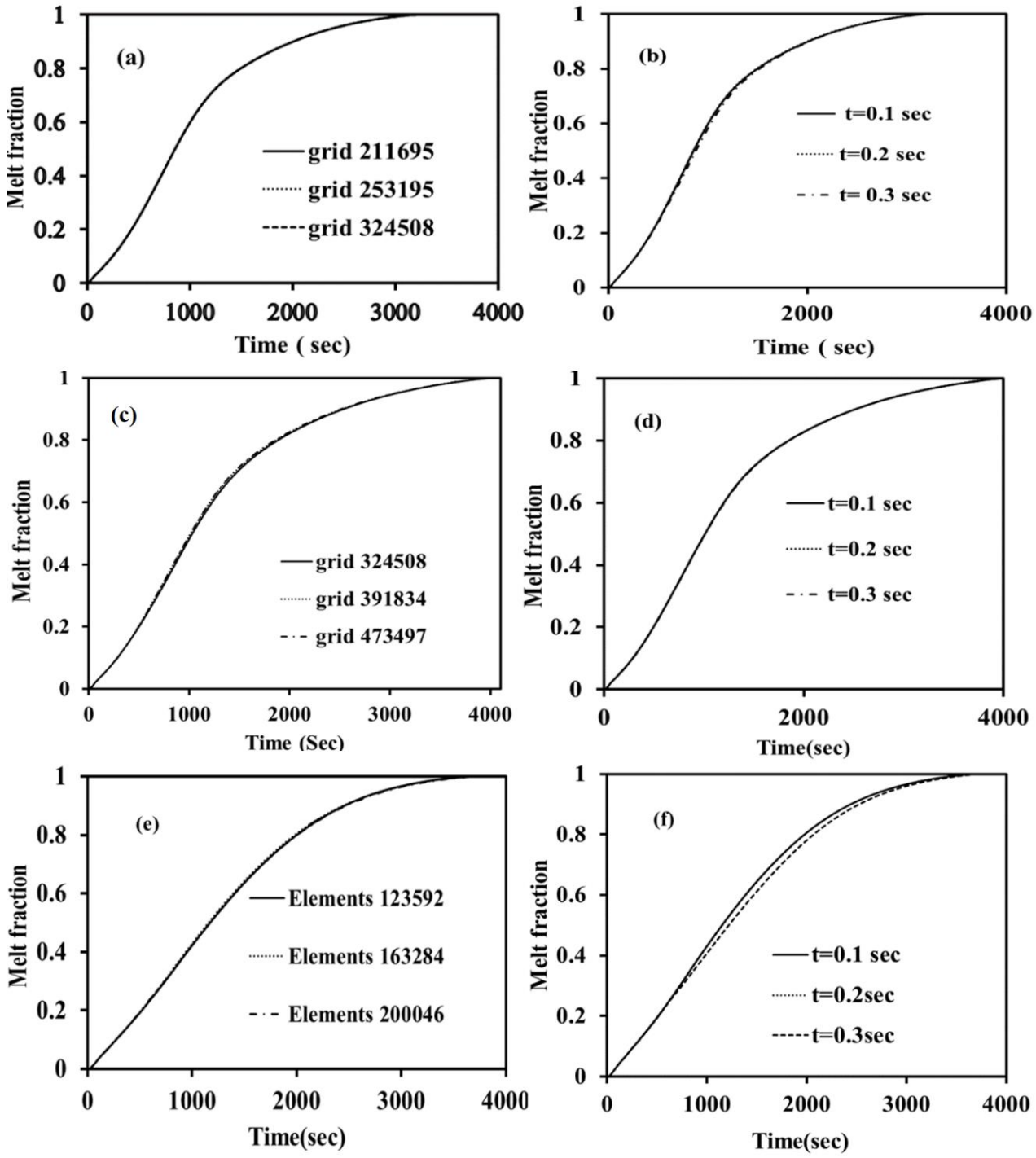

Fig 5.3 Grid independence study for finned HXs:(a)radial (c)spiral (e)longitudinal; Time independence study for finned HXs: (b)radial (d)spiral (f)longitudinal

5.4 Results and discussion

5.4.1 Melting

5.4.1.1 Temperature and melt fraction distribution

Fig.5.4 illustrates the contour profiles of temperature and melt fraction of radial fin LHSS during melting at 1200 seconds. From temperature contours, in the case of the vertically oriented heat exchanger, the uniform temperature is noted throughout the LHSS. This is because, in vertically oriented LHSS with radial fins the melted NEPCM is obstructed by fins to move towards the top portion of the heat exchanger. Whereas in the case of the inclined (45°) and horizontal radial finned LHSS NEPCM temperature at the top portion of the heat exchanger is high, this indicates that melted hot NEPCM is settled at the top portion of the heat exchanger. The temperature at the top portion of the heat exchanger is maximum in the case of the horizontally oriented radial finned heat exchanger. This indicates that the buoyancy effect is maximum in horizontal radial finned heat exchangers because horizontally oriented heat exchanger fins will not obstruct the transport of PCM due to buoyancy force. The effect of the GNP nanoparticles can be noted from the melt fraction contours. For a considered orientation of the heat exchanger shape of the melt front is the same, but the amount of the un-melted portion is noted to be more in pure PCM heat exchanger and less in LHSS with 1% volume GNP nanoparticles NEPCM. This indicates that for a considered orientation of the heat exchanger melting time decreases with an increase in the volume fraction of the GNP nanoparticles.

Fig.5.5 illustrates the contour profiles of the temperature and melt fraction of spiral fin LHSS during melting at 1200 seconds. It can be noted that the profile of temperature and melt fraction contours of spiral finned heat exchanger is similar to that of the radial fin heat exchanger. This is because the geometry of the spiral fins is similar to the radial fins. So the effect of the natural convection and conduction mode of heat transfers will be similar to that of the radial finned heat exchanger. The effect of the orientation and GNP nanoparticles on the spiral finned heat exchanger is similar to the radial finned heat exchanger.

Fig.5.6 illustrates the contour profiles of the temperature and melt fraction of longitudinal finned LHSS during melting at 1200 seconds. From the temperature contours, in the case

of the vertically oriented LHSS, hot melted NEPCM started to form at the top portion of the heat exchanger due to buoyancy force. In the case of longitudinal fin LHSS, in vertical condition fins won't obstruct the hot melted NEPCM to settle at the top portion of the PCM, more over fins provide more surface area along which flow can take place. Whereas in the case of the inclined (45°) and horizontal longitudinal finned LHSS, the temperature at the top section is less, this is due to obstruction of the liquid NEPCM due to fins. Similarly, the radial and spiral fin effect of GNP nanoparticles on the longitudinal finned LHSS can be observed from the melt fraction contours. For a considered orientation of the heat exchanger shape of the melt front is the same but the amount of the un-melted portion is noted to be more in pure PCM heat exchanger and less in LHSS with 1% volume GNP nanoparticles NEPCM. This indicates that for a considered orientation of the heat exchanger melting time decreases with an increase in the volume fraction of the GNP nanoparticles.

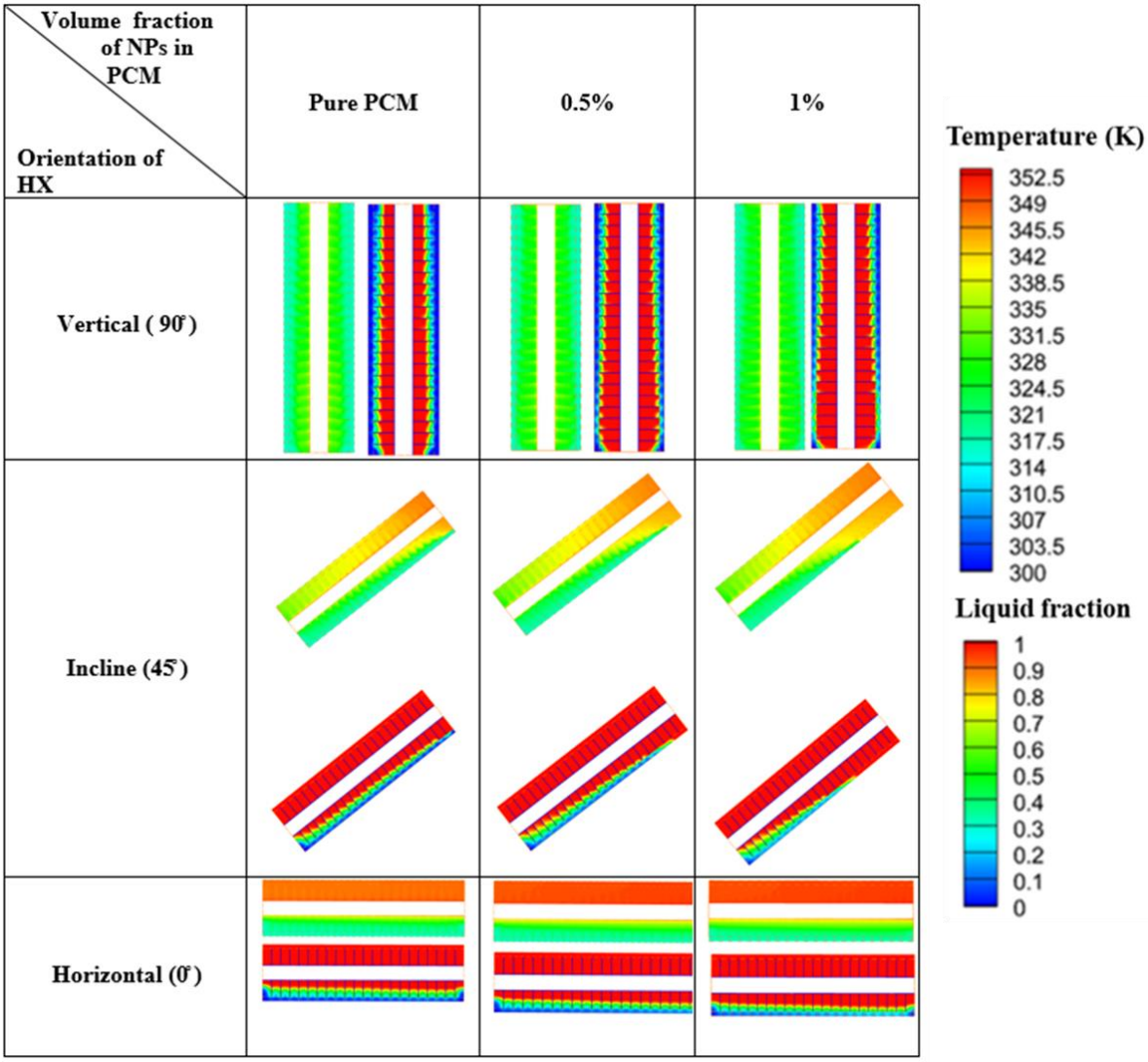

Fig 5.4 Temperature and melt fraction contours of the radial fin heat exchanger at 1200 sec during melting

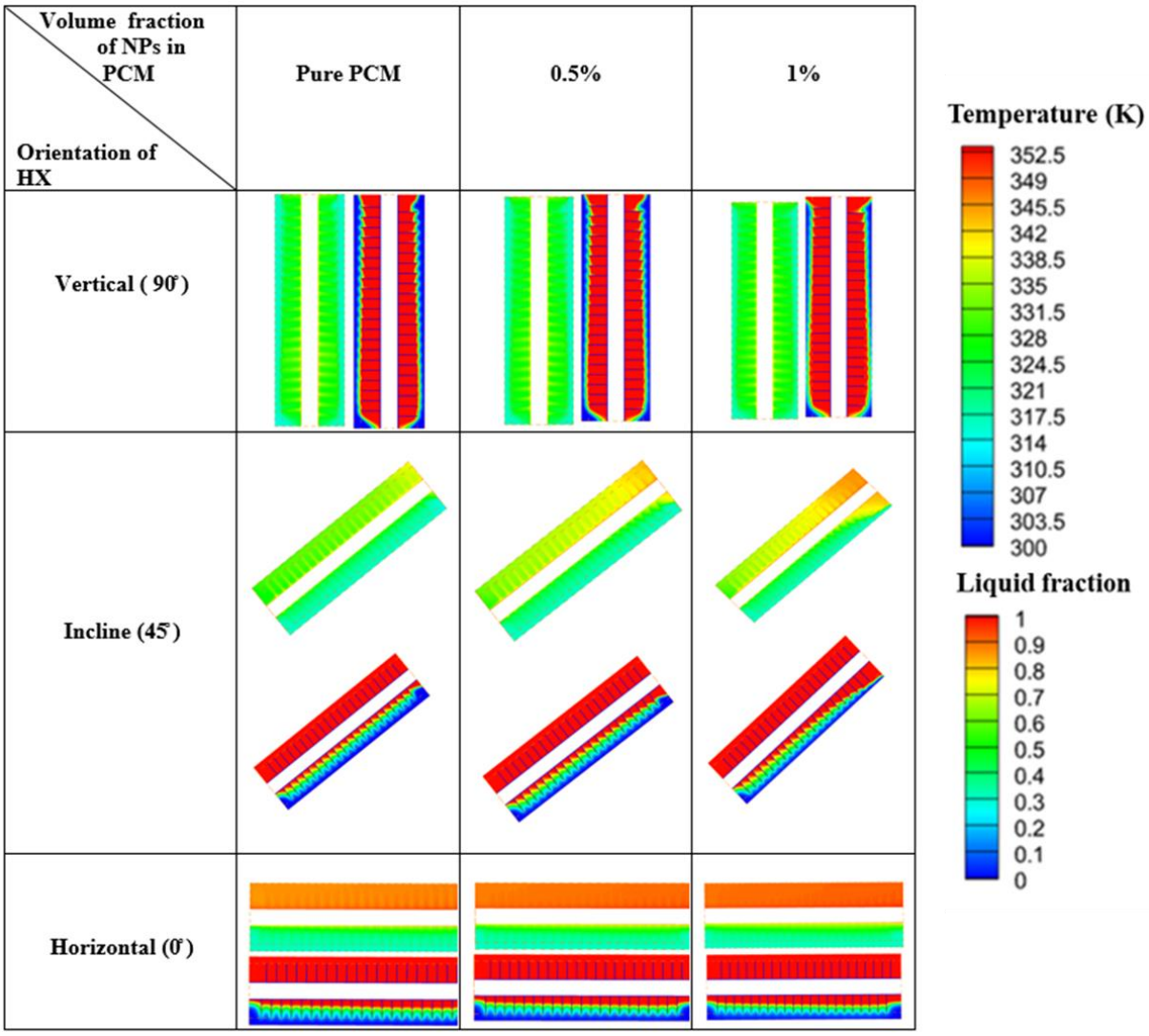

Fig 5.5 Temperature and melt fraction contours of the spiral fin heat exchanger at 1200 sec during melting

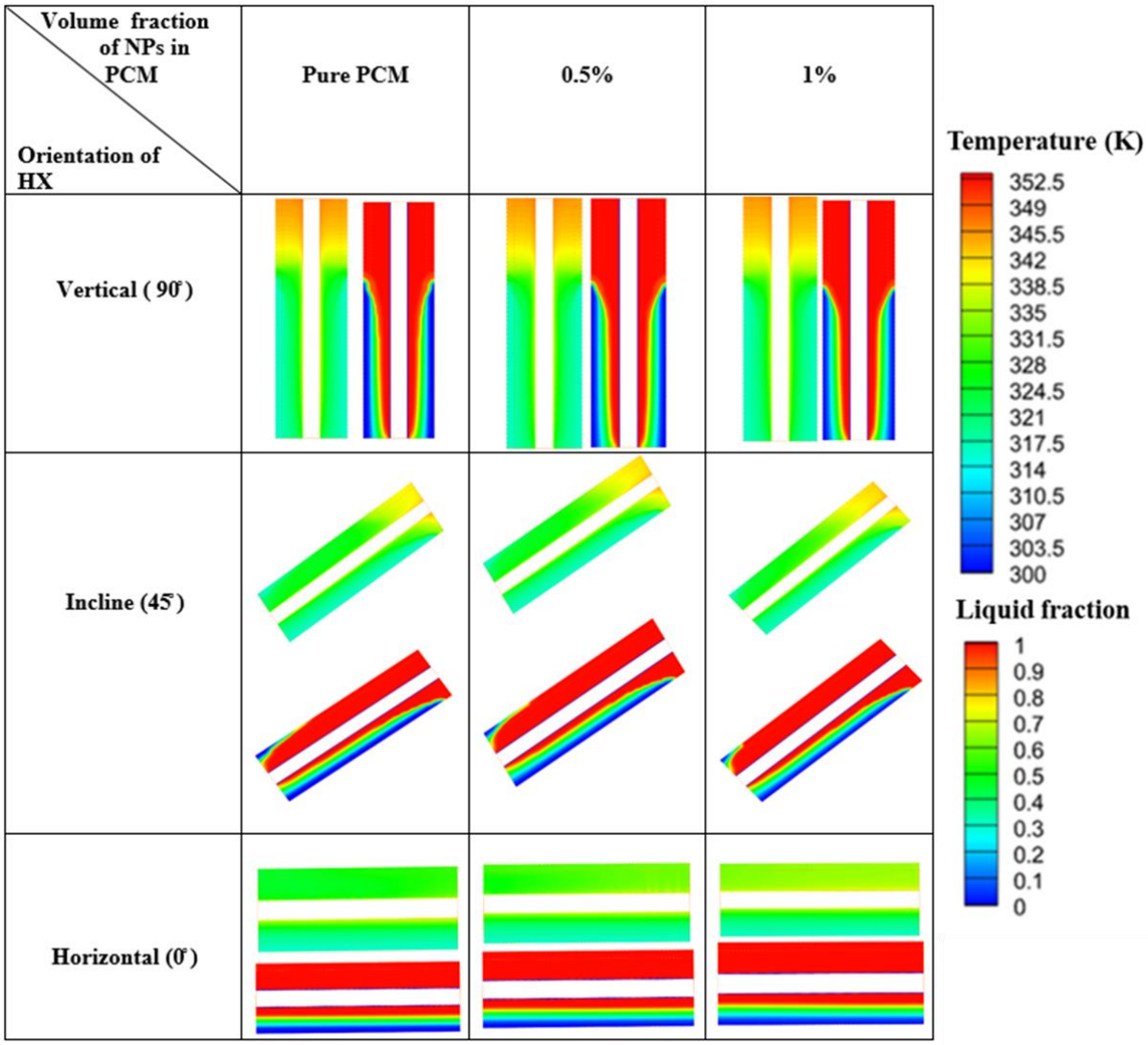

Fig 5.6 Temperature and melt fraction contours of the longitudinal fin heat exchanger at 1200 sec during melting

5.4.1.2 Average temperature

A variation in average temperature during melting is analyzed to gain a better understanding of the effect of orientation, GNP nanoparticles and fin type. Fig.5.7 illustrates the average temperature variation of radial fin shell and tube LHSS heat exchangers during melting. From Fig.5.7 (a), (b), and (c) it can be noted that irrespective of orientation, variation in the average temperature at the initial stage of melting is similar. This is because, at the earliest stage, the heat transfer is predominated by conduction. As time progresses it is noted that the average temperature in the horizontal case is more than that of the inclined followed by vertical oriented heat exchanger irrespective of the volume

fraction of the GNP nanoparticles. This is due to the high strength of buoyancy force which results in hot melted NEPCM, which is nearly at the temperature of HTF getting settled at the top portion of the heat exchanger during the intermediate stage of melting. This amount of NEPCM decreased with an increase in the inclination angle of the radial finned heat exchanger. On further melting a sharp rise in average temperature is noted in the case of the vertically inclined LHSS. This is because at this stage the melt front of NEPCM crossed the finned zone, this gives a provision to melted NEPCM to move to the top portion of the LHSS and reach a temperature nearly equal to HTF temperature. A similar trend can be noted in inclined heat LHSS, but the rate of increase in the temperature is less than that of the vertical case. Although the addition of GNP nanoparticles resulted in an increase in the effective thermal conductivity of the PCM, their effect on the melting mechanism is less when compared with the orientation effect. They have shown the effect on the variation of the magnitude of average temperature. In radial fin LHSS, the maximum average temperature at the end of melting is 352.5 K in pure PCM LHSS inclined at 45° and the minimum average temperature at the end of melting is 338.3 K in 1% volume GNP LHSS oriented vertically.

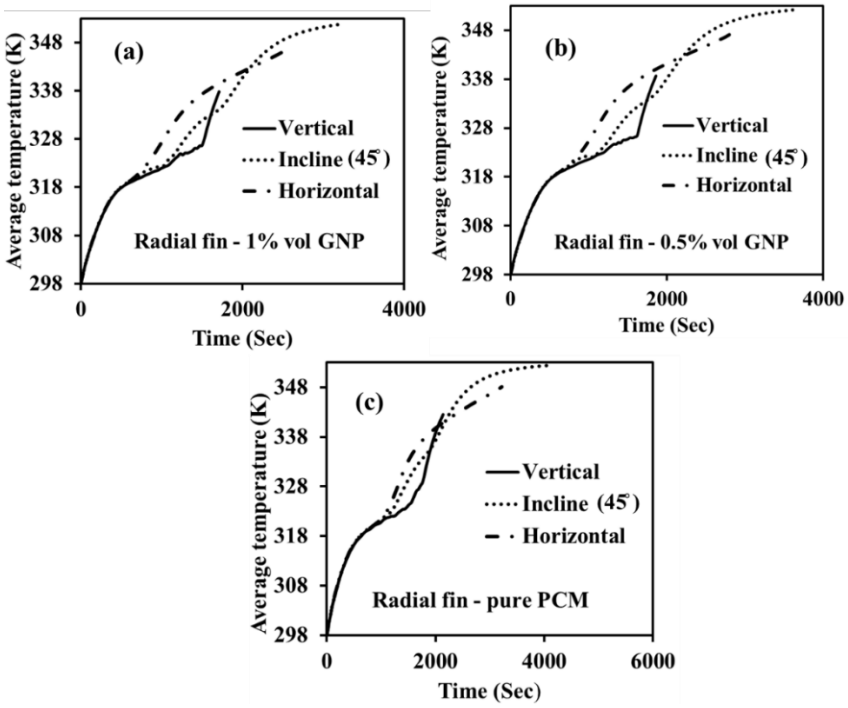

Fig 5.7 Average temperature evolution for radial fin heat exchangers during melting (a) 1% volume GNP (b) 0.5% volume GNP and (c) pure PCM

Fig.5.8 illustrates the average temperature variation of spiral fin shell and tube LHSS heat exchangers during melting. Similarly to that of melt fraction and temperature contours the average temperature trends are similar to that of the radial finned LHSS. In spiral fin LHSS maximum average temperature at the end of melting is 352.4 K in pure PCM LHSS inclined at 45° and the minimum average temperature at the end of melting is 346.5 K in 1% volume GNP LHSS oriented vertically.

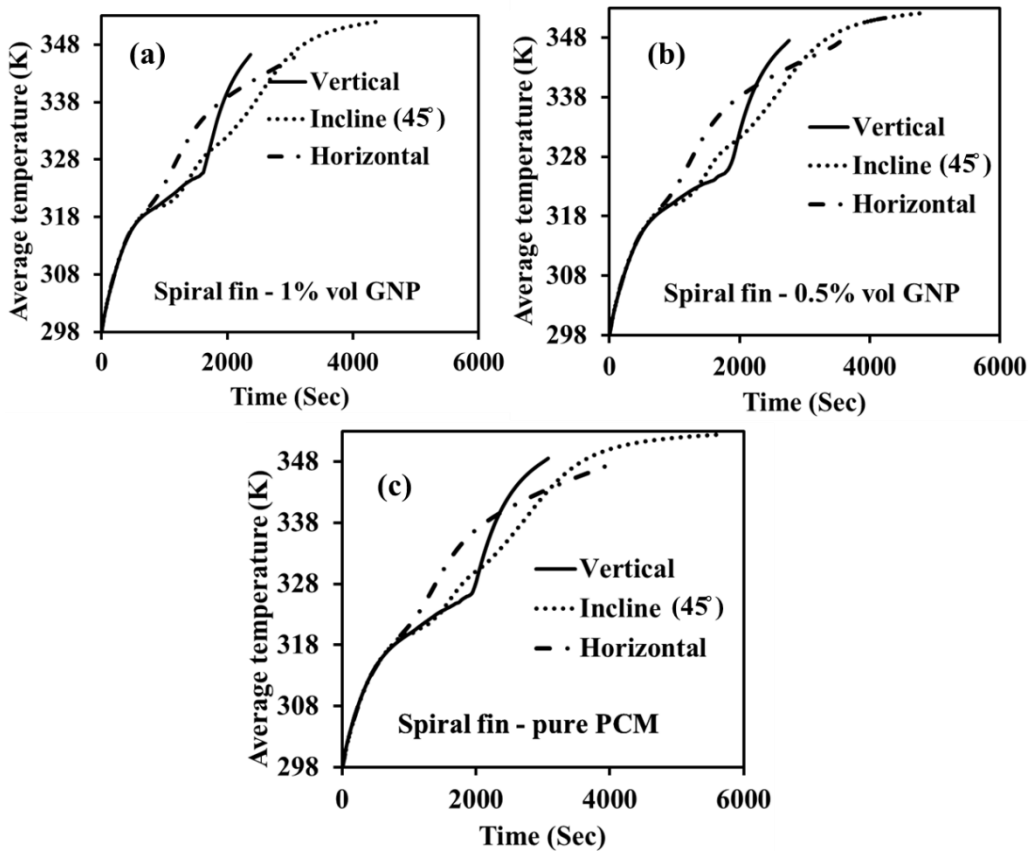

Fig 5.8 Average temperature evolution for spiral fin heat exchangers during melting (a) 1% volume GNP (b) 0.5% volume GNP and (c) pure PCM

Fig.5.9 illustrates the average temperature variation of longitudinal fin shell and tube LHSS heat exchangers during melting. Similarly to that of radial and spiral finned LHSS during the initial stage of melting irrespective of orientation, variation in the average temperature at the initial stage of melting is similar due to the conductive mode of heat transfer during the initial stage of melting. On further melting a little variation is observed in the average temperature of the longitudinal finned heat exchanger due to variation in the orientation of the LHSS. Due to the addition of GNP nanoparticles, variation in the average

temperature is noted similarly to that of the radial and spiral finned heat exchanger. In longitudinal fin LHSS, the maximum average temperature at the end of melting is 352.3 K in pure PCM LHSS inclined at 45° and the minimum average temperature at the end of melting is 346.8 K in 1% volume GNP LHSS oriented horizontally.

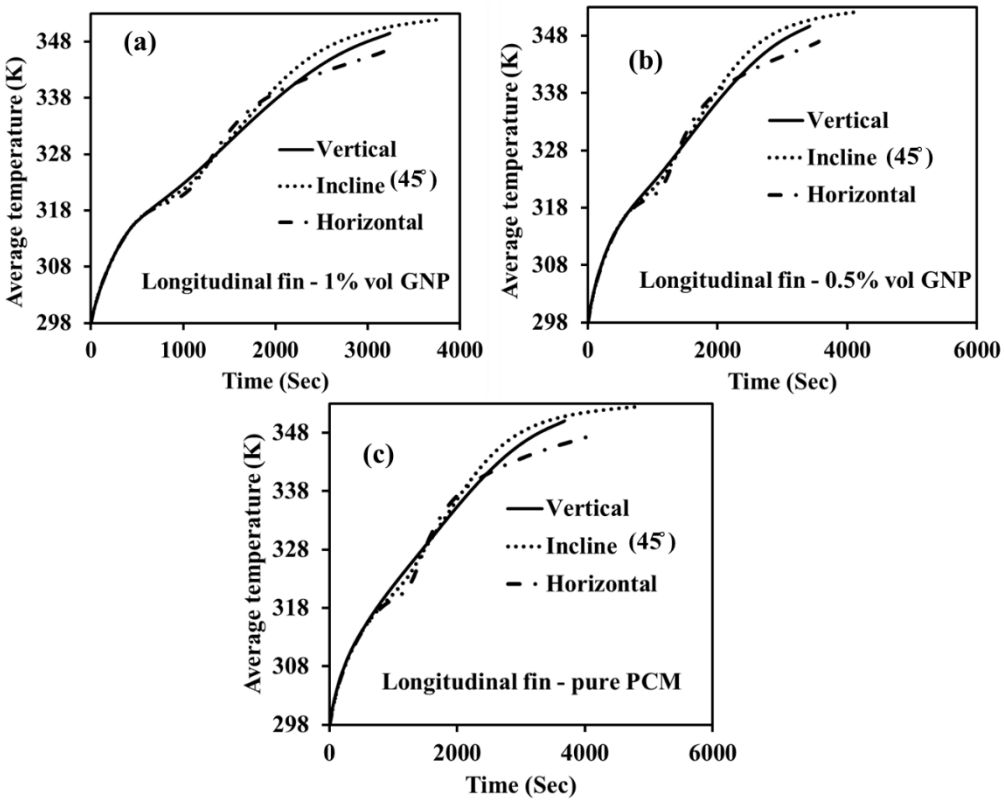

Fig 5.9 Average temperature evolution for longitudinal fin heat exchangers during melting (a) 1% volume GNP (b) 0.5% volume GNP and (c) pure PCM

5.4.1.3 Melting time

Fig.5.10, 5.11, and 5.12 shows the melting time taken to an increment of 0.25 melt fraction for radial, spiral, and longitudinal finned LHSS till the end of the phase change process during melting. During the initial stage of melting time to attain a melt fraction from 0 to 0.25 is higher than the time to attain a melt fraction from 0.25 to 0.5. This is because during the initial stage of melting some amount of energy is stored due to sensible heat, during which NEPCM absorbs energy without melting. Further from a 0.5 melt fraction time taken to melt for every 0.25 melt fraction increases due to a drop in the temperature difference between HTF and the average temperature of the NEPCM. It can be noted that

at all the intervals of melting, melting time decreased with an increase in the volume fraction of the GNP nanoparticles. For a considered heat exchanger with the same volume fraction of the GNP nanoparticles, the radial finned heat exchanger has the least melting time. During melting the maximum melting time of 5680 seconds is observed in spiral finned pure PCM LHSS oriented at 45° and a minimum melting time of 1710 seconds is observed in radial finned 1% GNP LHSS oriented vertically. In comparison with pure PCM shell and tube heat exchanger which has minimum melting time, a minimum of 12.68% and a maximum of 73.71% reduction in melting time is noted.

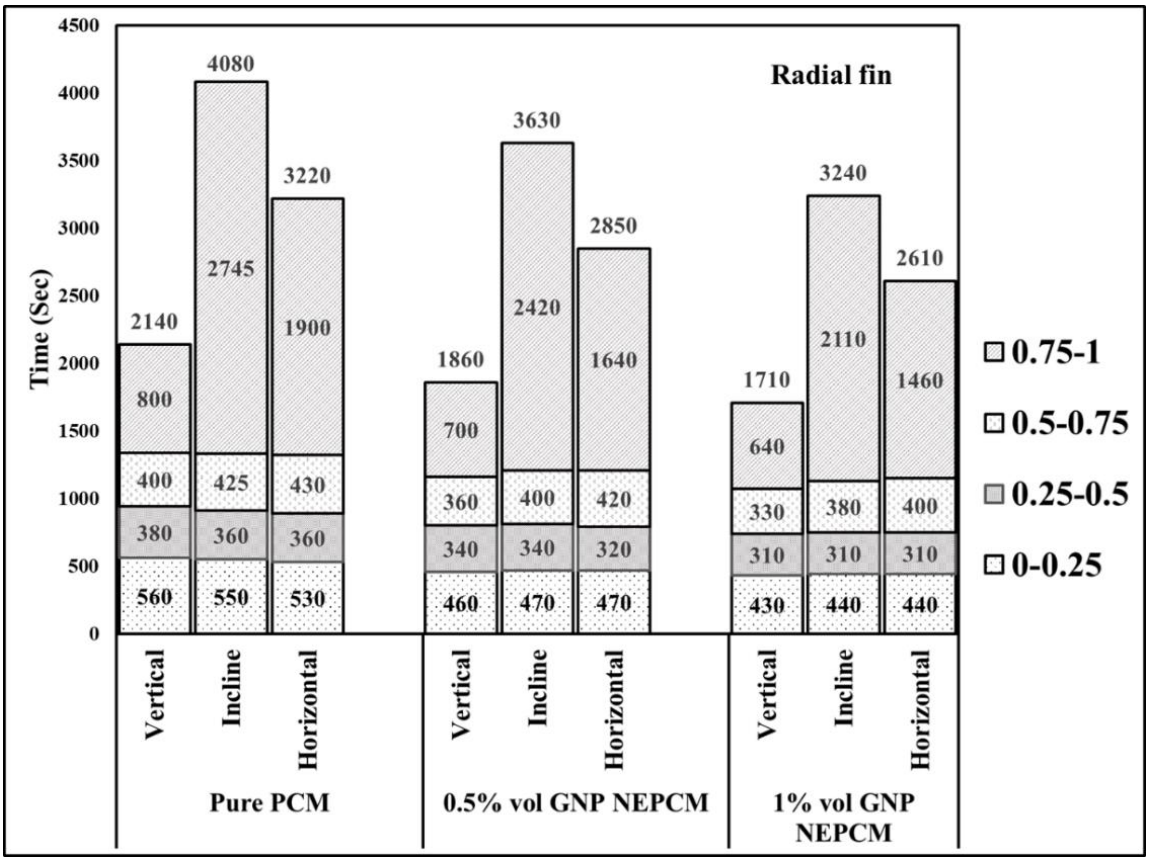

Fig 5.10 Time taken to reach melt fraction with an interval of 0.25 during melting for radial fin heat exchanger

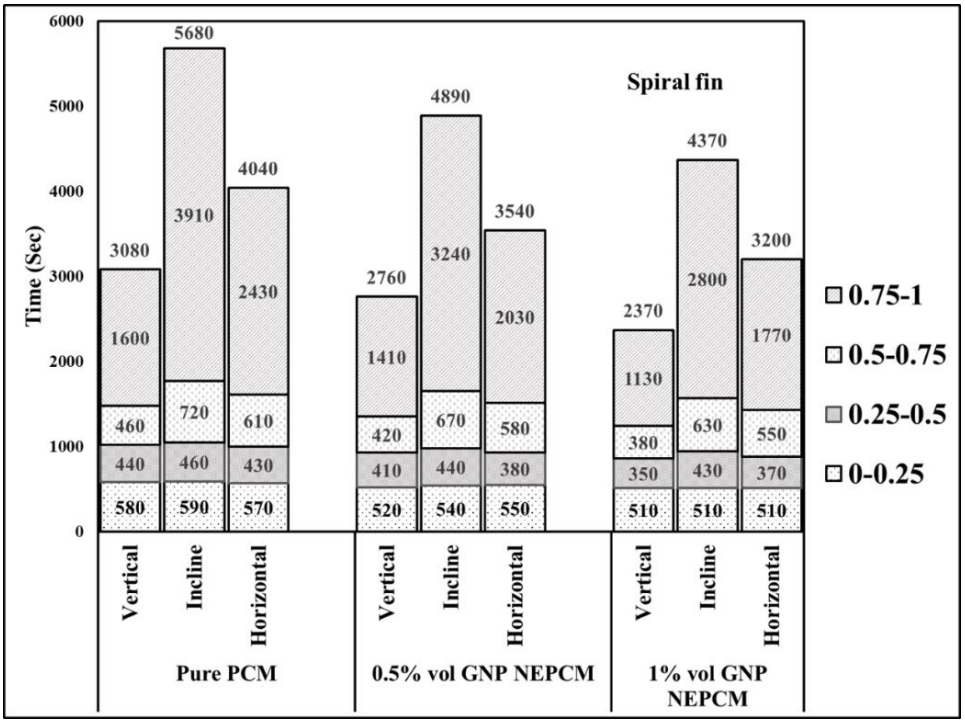

Fig 5.11 Time taken to reach melt fraction with an interval of 0.25 during melting for spiral fin heat exchanger

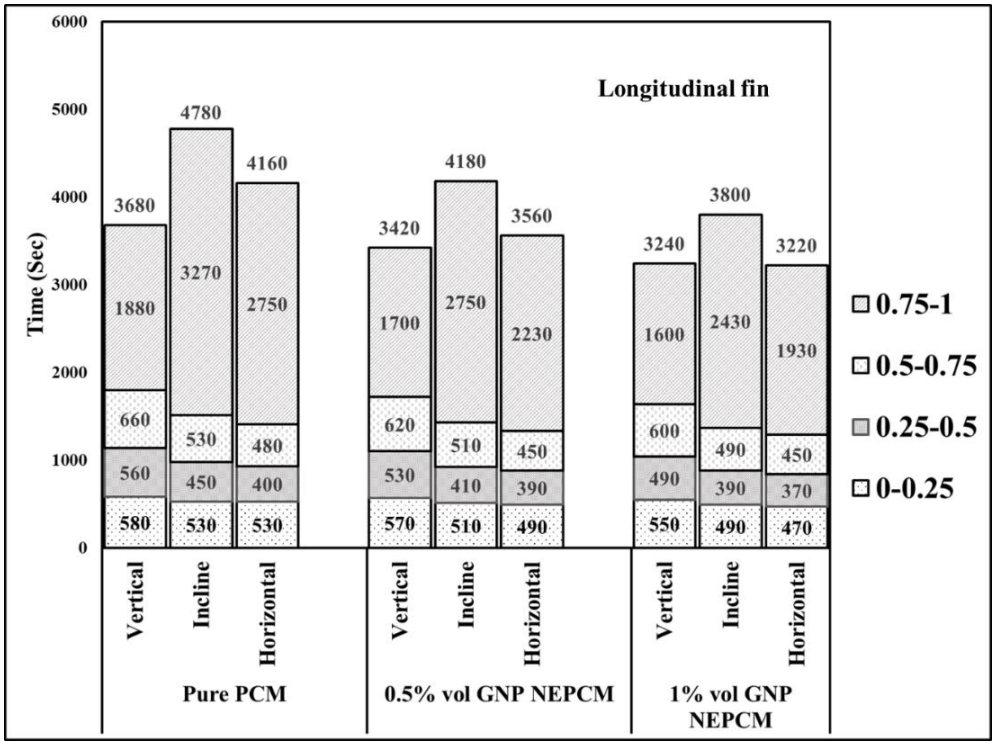

Fig 5.12 Time taken to reach melt fraction with an interval of 0.25 during melting for longitudinal fin heat exchanger

5.4.1.4 Energy storage ratio

The stored energy by NEPCM is directly proportionate to the variation of initial and instantaneous average NEPCM temperature. The energy storage ratio during melting is defined as the energy absorbed by NEPCM to the maximum quantity of energy that NEPCM can absorb. Fig.5.13, 5.14 and 5.15 illustrates how the energy storage ratio varies among the radial, spiral and longitudinal fin heat exchangers. From Fig.5.13, 5.14 and 5.15 it is possible to divide the energy storage ratio into three stages. It is sensible heat that absorbs energy during the initial stages. The material's latent heat capacity absorbs the energy during the second stage. The temperature changes very little during this stage despite absorbing a huge amount of energy. The third stage of solidification releases sensible heat and the temperature increase at a slower rate during this stage, which results in a slower rate of energy absorption. From Figs. 5.13, 5.14 and 5.15 it can be viewed that the energy ratio is significantly affected by the fin type and the inclination of the heat exchanger. The energy storage ratio during melting is high for a 45° inclined heat exchanger irrespective of the type of the fin and volume fraction of GNP nanoparticles. During melting the maximum energy storage ratio of 0.996 is observed in radial finned pure PCM LHSS oriented at 45° and the minimum energy storage ratio of 0.898 is observed in radial finned 1% GNP LHSS oriented vertically. On comparison with pure PCM shell and tube heat exchanger which has a maximum energy storage ratio, a maximum improvement of 0.4% and maximum reduction of 10.28% in energy storage ratio is noted.

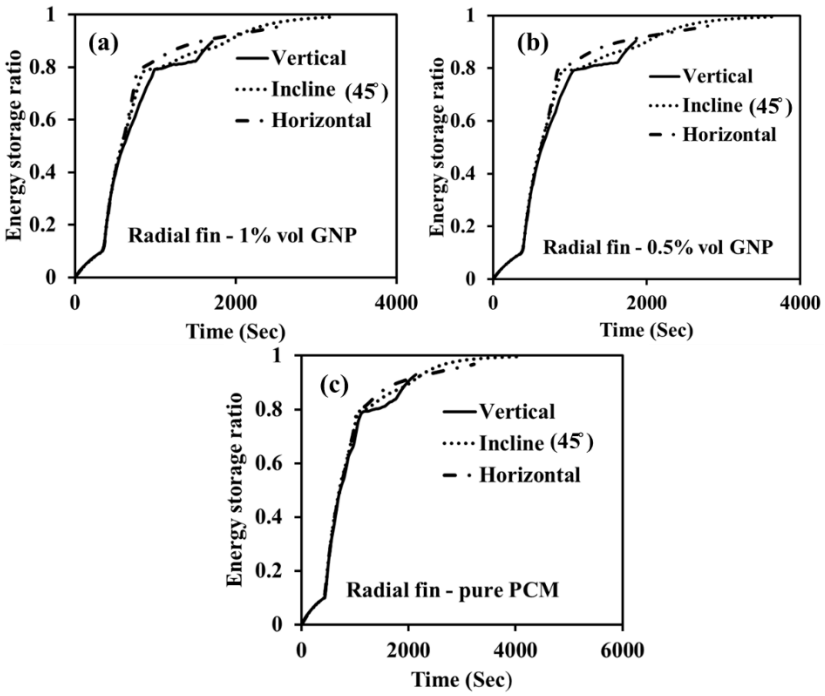

Fig 5.13 Energy storage ratio of radial fin heat exchangers during melting (a) 1% volume GNP (b) 0.5% volume GNP (c) pure PCM

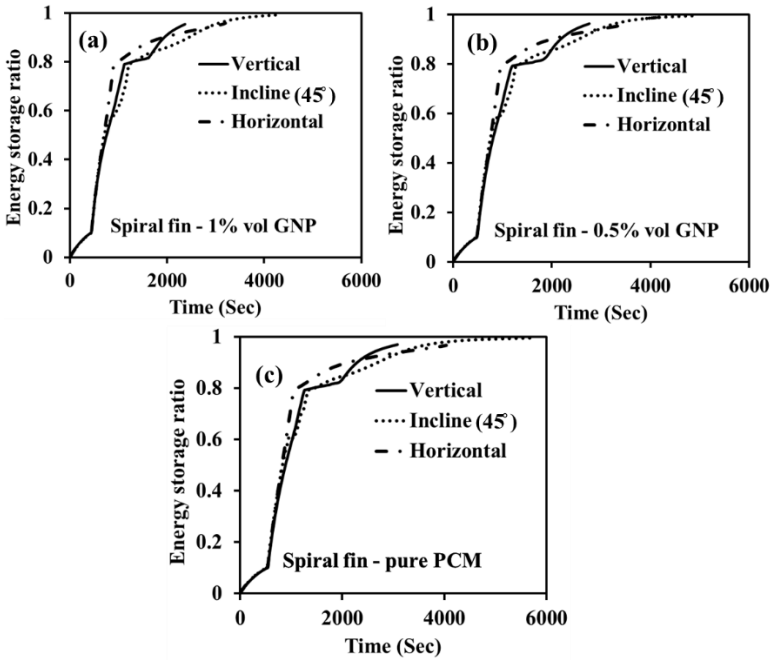

Fig 5.14 Energy storage ratio of spiral fin heat exchangers during melting (a) 1% volume GNP (b) 0.5% volume GNP (c) pure PCM

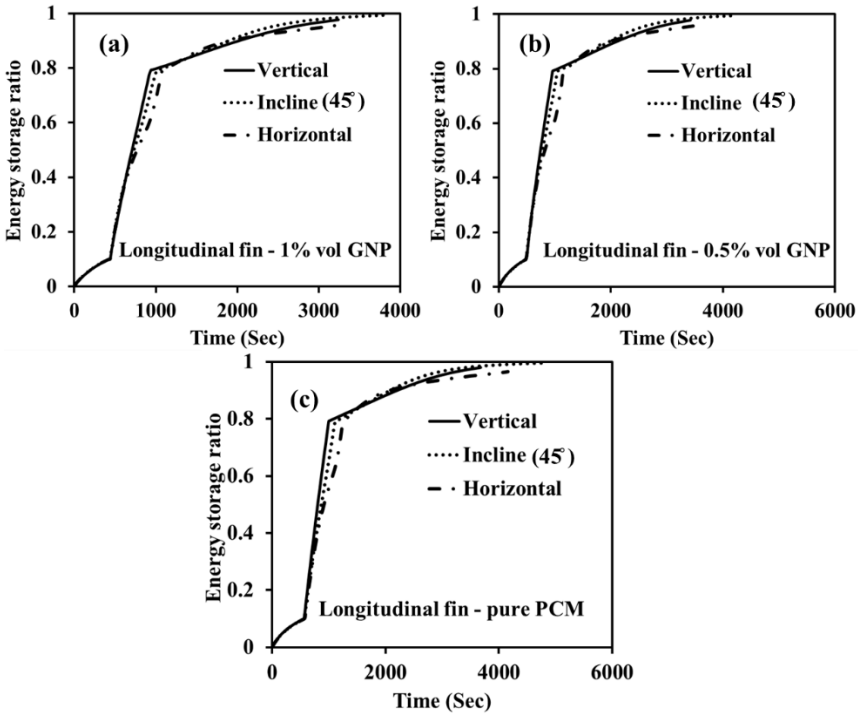

Fig 5.15 Energy storage ratio of longitudinal fin heat exchangers during melting (a) 1% volume GNP (b) 0.5% volume GNP (c) pure PCM

5.4.1.5 Exergy efficiency

The available energy is termed exergy. Its efficiency gives an overview of the quality of energy. It relies on the inlet and outlet HTF temperatures and the average NEPCM temperature. Fig.5.16, 5.17 and 5.18 illustrates the radial, spiral and longitudinal fin heat exchanger exergy efficiency. It can be deduced that the exergy efficiency follows the trend of average NEPCM temperature during melting. This is because as the process of melting progresses the average temperature of NEPCM increases which prompts an increase in the exergy efficiency with time. Throughout the melting process, the difference between the outlet and inlet temperature of HTF is very less, as a result, the exergy efficiency is dependent mostly on the average temperature of the NEPCM. The exergy efficiency at the end of melting depends more on the type of fins and orientation of the LHSS heat exchanger and less on the volume of GNP nanoparticles. The average exergy efficiency during melting is high for 45° inclined heat exchangers and least for vertical heat exchangers irrespective of the type of the fin and volume fraction of GNP nanoparticles. This is because in the case of 45° inclined heat exchanger, the heat exchanger is maintained at a higher temperature for a long time and by the time of complete melting of NEPCM,

the average temperature of LHSS reaches near the inlet temperature of HTF. Whereas in the case of the vertically oriented heat exchanger, the complete melting of NEPCM is finished before NEPCM average temperature reaches near HTF temperature. During melting the maximum average exergy efficiency of 72.77% is observed in spiral finned pure PCM LHSS oriented at 45° and the minimum average exergy efficiency of 44.49% is observed in radial finned 1% GNP LHSS oriented vertically.

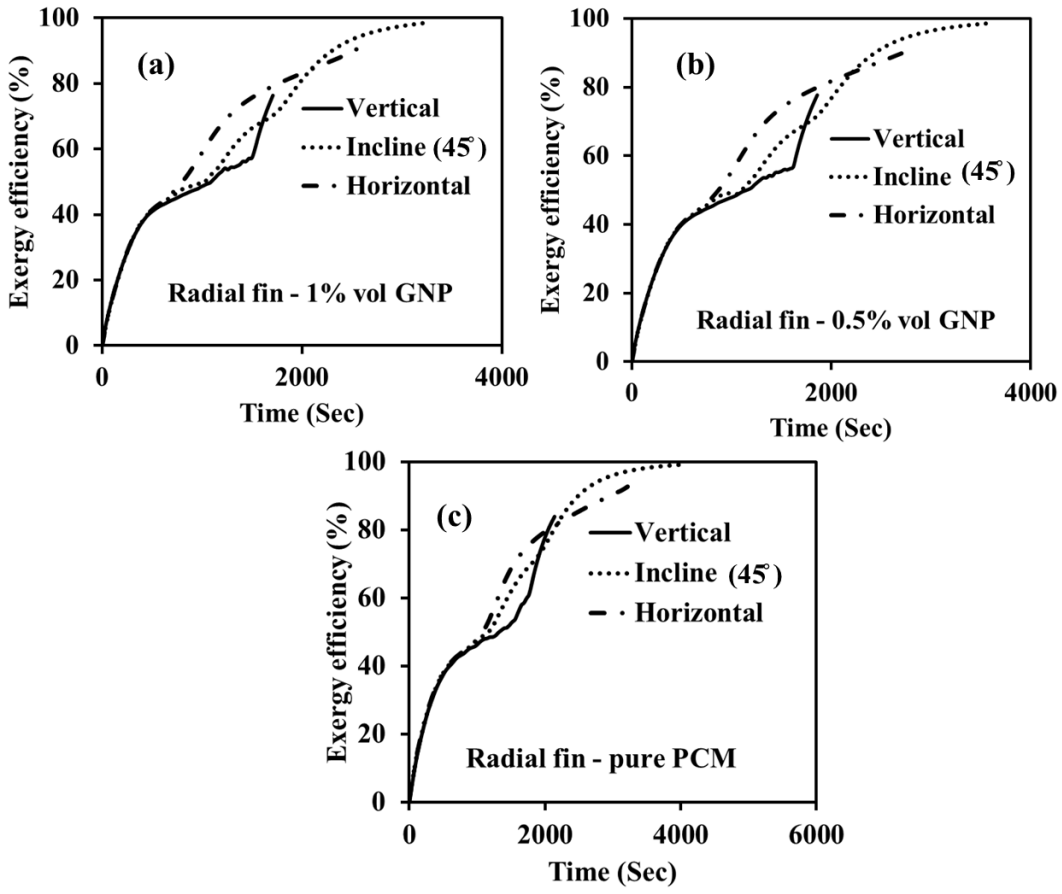

Fig 5.16 Exergy efficiency of radial fin heat exchanger during melting (a) 1% volume GNP(b) 0.5% volume GNP(c) pure PCM

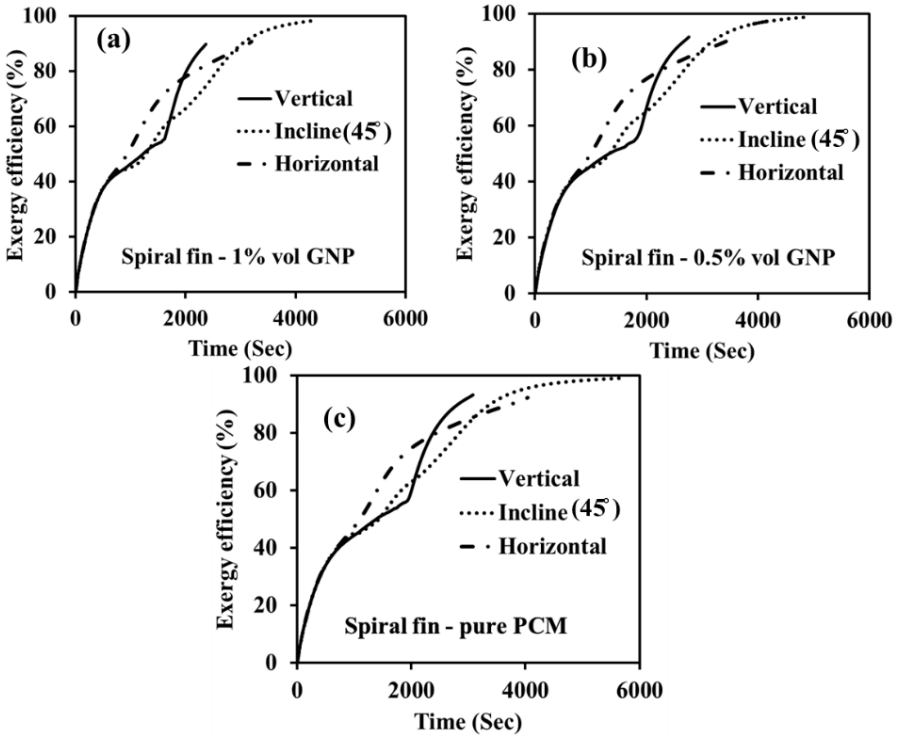

Fig 5.17 Exergy efficiency of spiral fin heat exchanger during melting (a) 1% volume GNP(b) 0.5% volume GNP(c) pure PCM

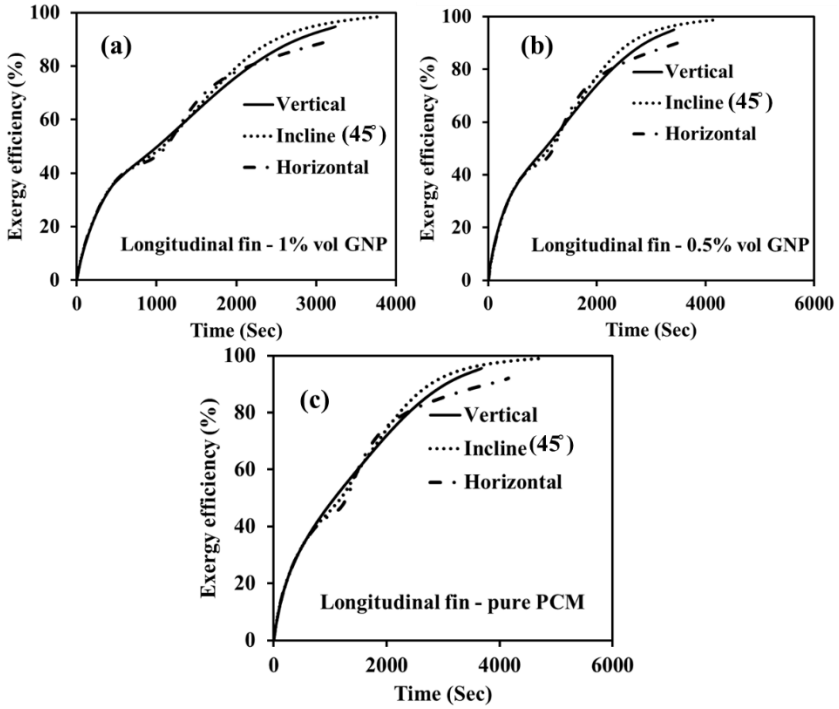

Fig 5.18 Exergy efficiency of longitudinal fin heat exchanger during melting (a) 1% volume GNP(b) 0.5% volume GNP(c) pure PCM

5.4.2 Solidification

5.4.2.1 Temperature and melt fraction distribution

Fig.5.19, 5.20 and 5.21 displays the contour profiles of temperature and melt fraction of radial, spiral and longitudinal fin shell and tube LHSS during solidification at 1800 seconds. The distribution of temperature along the tube is nearly uniform irrespective of the orientation of LHSS, the volume fraction of GNP nanoparticles and the type of fins used because solidification is dominated by conduction. But from melt fraction contours it can be viewed that a little amount of liquid NEPCM is settled on the top portion of all the heat exchangers considered. For a considered orientation and volume fraction of the GNP nanoparticles, the amount of unsolidified NEPCM settled at the top portion of the LHSS is more in spiral and longitudinal fin heat exchanger. Based on this behavior a conclusion can be drawn that longitudinal and spiral fin heat exchangers solidify at a slower rate than radial fin heat exchangers for a considered orientation and volume fraction of GNP nanoparticles. The effect of GNP nanoparticles can be observed from melt fraction contours. For a particular type of fin and orientation of the heat exchanger, it can be observed that with an increase in the volume fraction of GNP nanoparticles, the amount of unsolidified NEPCM settled at the top portion of LHSS is decreasing. This indicates that with an increase in the volume fraction of the GNP nanoparticles, the rate of solidification increases. The effect of the orientation could not be interrupted by the melt fraction and temperature contours.

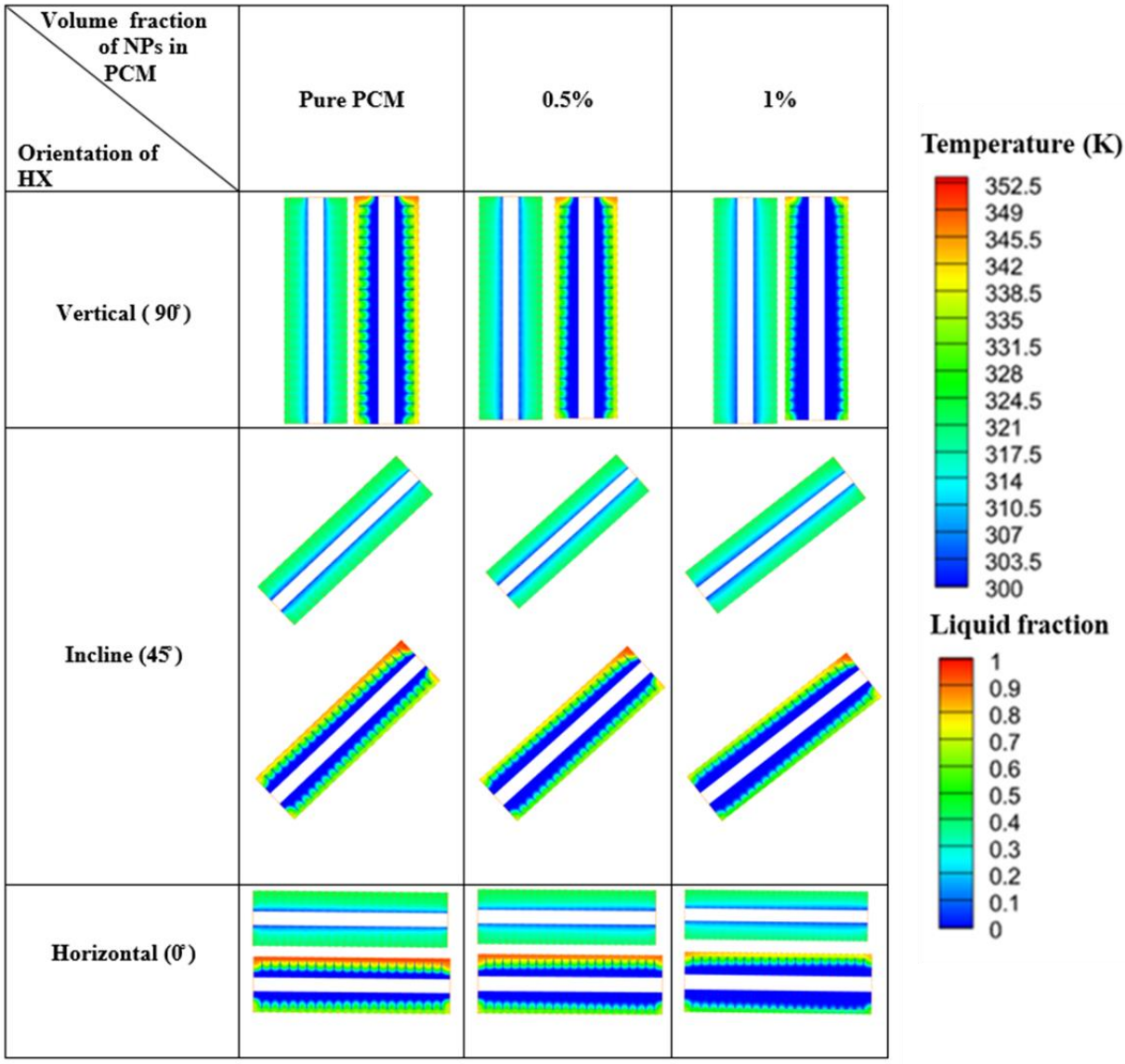

Fig 5.19 Temperature and melt fraction contours of thee radial fin heat exchanger at 1800 sec during solidification

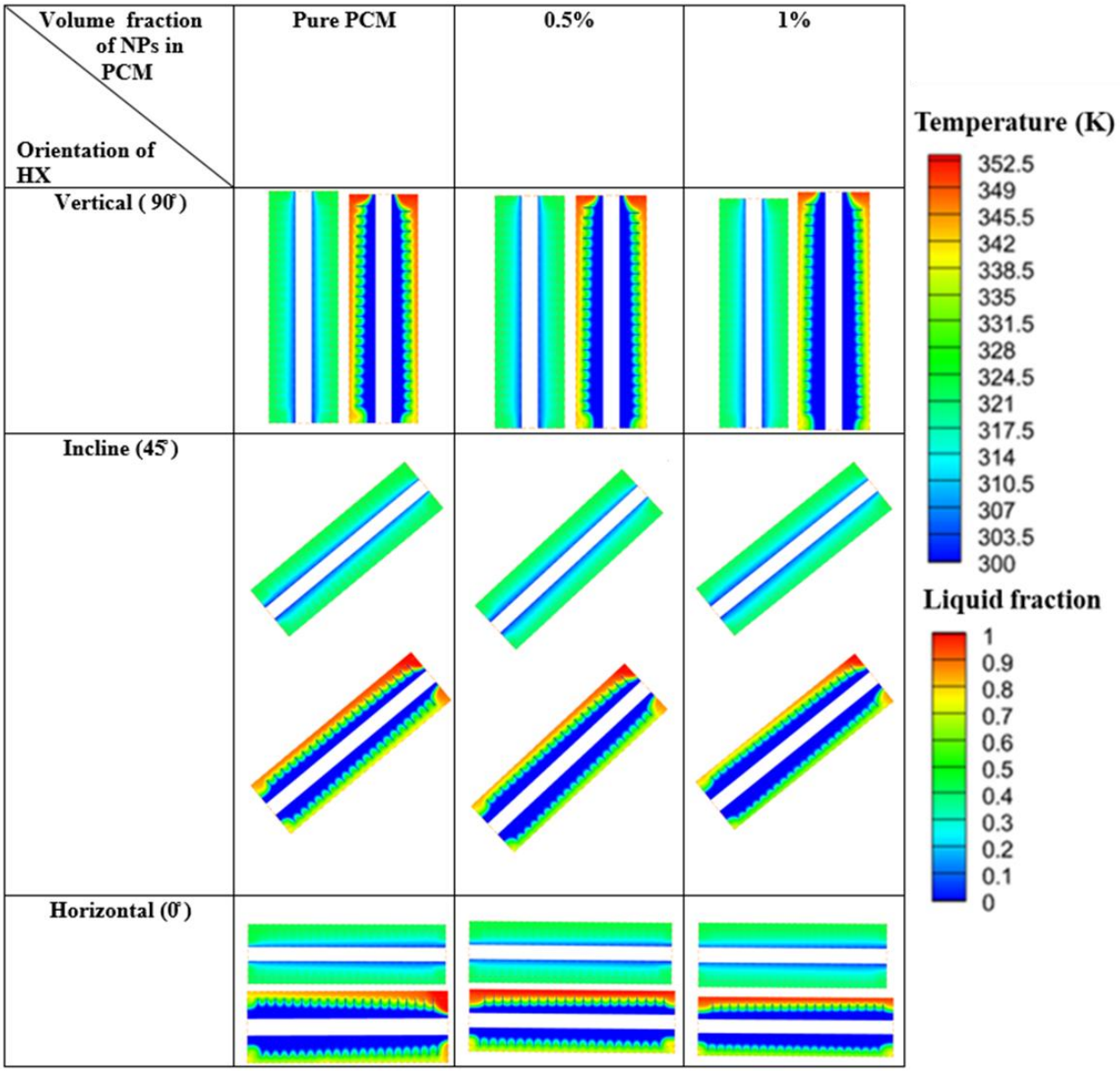

Fig 5.20 Temperature and melt fraction contours of the spiral fin heat exchanger at 1800 sec during solidification

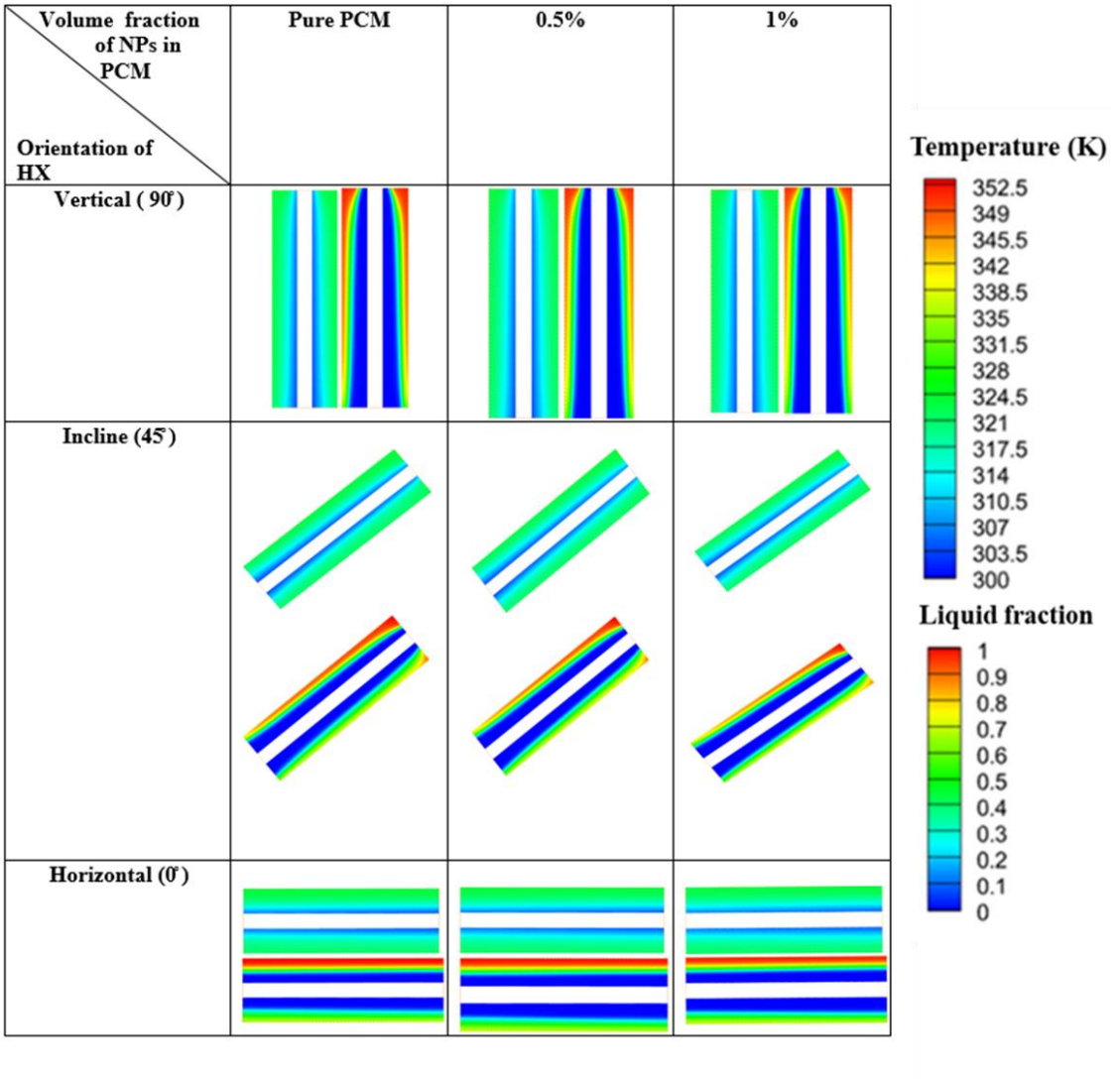

Fig 5.21 Temperature and melt fraction contours of the longitudinal fin heat exchanger at 1800 sec during solidification

5.4.2.2 Average temperature

Variation in average temperature during solidification is analyzed to gain a deeper understanding of the effect of fin type, orientation and volume fraction of GNP nanoparticles. Fig.5.22, 5.23 and 5.24 displays the behavior of average temperature of radial, spiral and longitudinal fin shell and tube LHSS. From Fig. 5.22, 5.23 and 5.24 it can be noticed that transient variation in average temperature follows the same trend regardless of the fin type, inclination and volume fraction of GNP nanoparticles of LHSS because of the conduction mode of heat transfer. Among the optimized geometries studied, the spiral fin heat exchanger has the least average temperature and the radial fin heat exchanger has

the highest, the opposite is observed for solidification time. For a particular heat exchanger with the same fin type and orientation of LHSS, with an increase in the volume fraction of GNP nanoparticles, solidification time decreased. The maximum average temperature at the end of solidification is 304.68 K in longitudinal finned 1% volume GNP LHSS oriented horizontally and the minimum average temperature at the end of melting is 300.43 K in spiral finned pure PCM LHSS oriented horizontally.

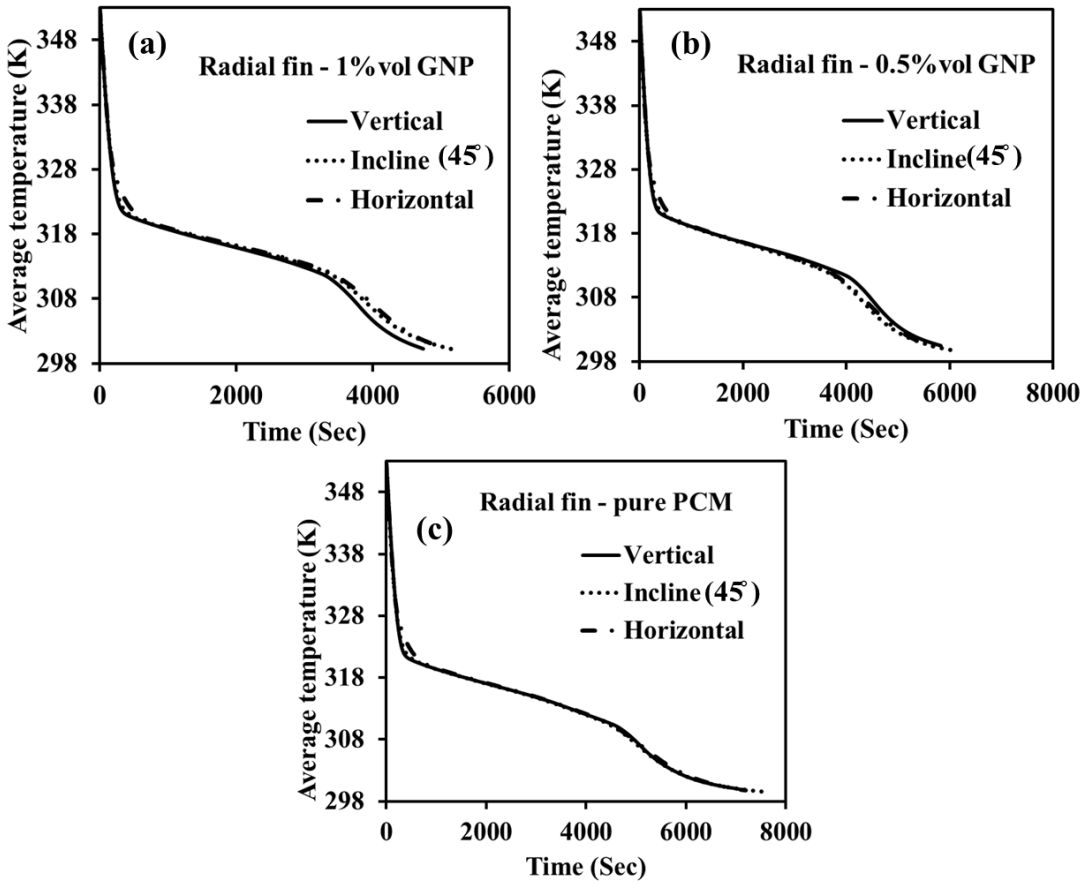

Fig 5.22 Average temperature evolution for radial fin heat exchangers during solidification (a) 1% volume GNP (b) 0.5% volume GNP and (c) pure PCM

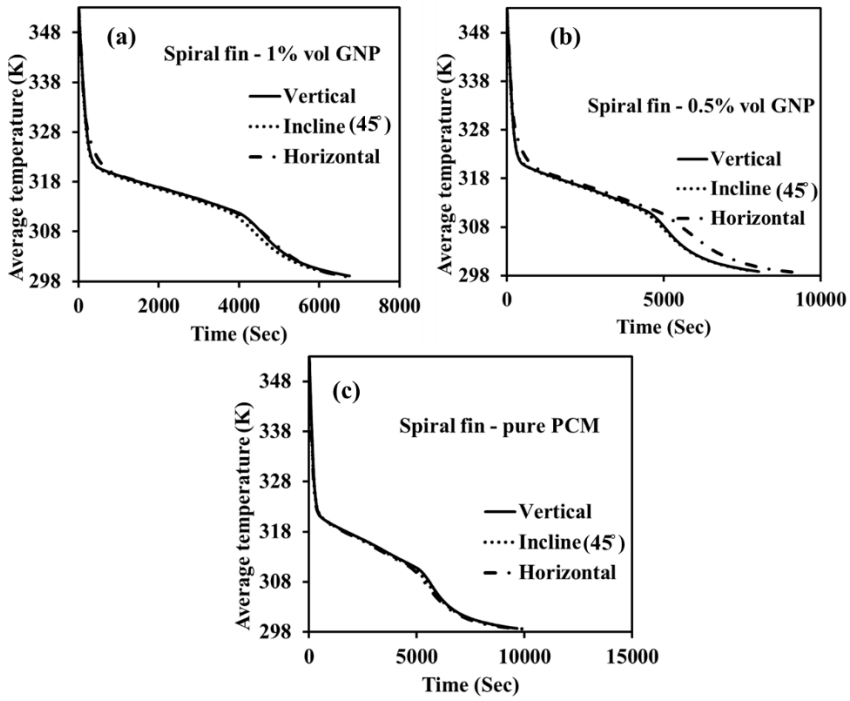

Fig 5.23 Average temperature evolution for spiral fin heat exchangers during solidification (a) 1% volume GNP (b) 0.5% volume GNP and (c) pure PCM

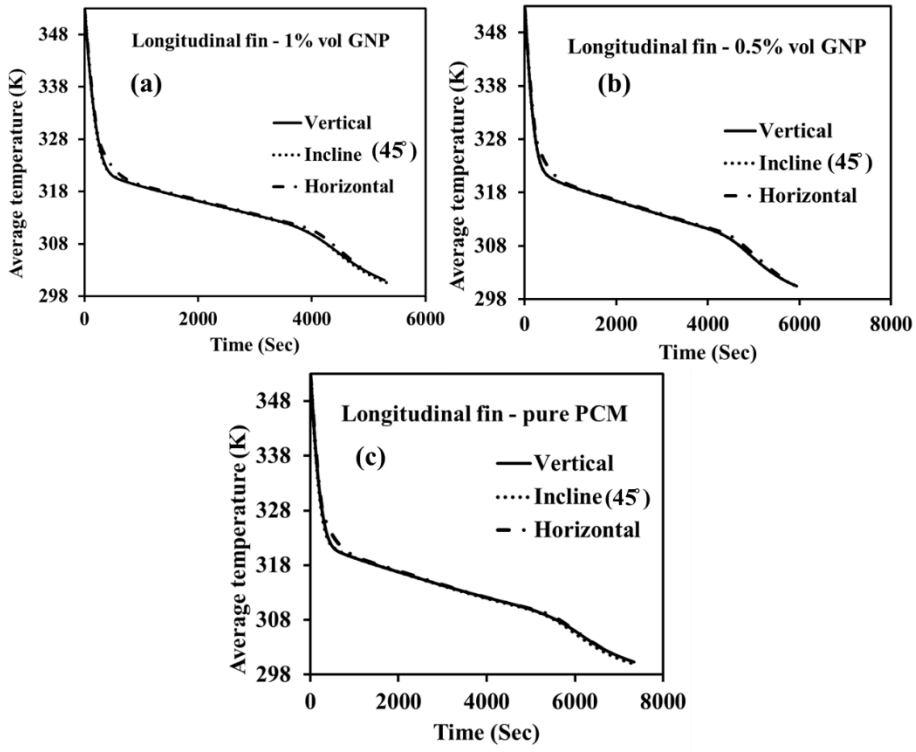

Fig 5.24 Average temperature evolution for longitudinal fin heat exchangers during solidification (a) 1% volume GNP (b) 0.5% volume GNP and (c) pure PCM

5.4.2.3 Solidification time

Fig. 5.25, 5.26 and 5.27 shows the solidification time taken to the reduction of 0.25 melt fraction for radial, spiral and longitudinal finned LHSS till the end of the solidification process. From 0.75 melt fraction time taken to solidify for every 0.25 melt fraction increases due to a drop in the temperature difference between HTF and the average temperature of the NEPCM. It can be noted that at all the intervals of solidification, solidification time decreased with an increase in the volume fraction of the GNP nanoparticles. For a considered heat exchanger with the same volume fraction of the GNP nanoparticles, the spiral-finned heat exchanger has the highest solidification time. It can be observed that in pure PCM LHSS considered, the time taken to solidify up to 0.25 melt fraction is less than the time taken to solidify the final 0.25 melt fraction. During solidification the maximum solidification time of 10380 seconds is observed in spiral finned pure PCM LHSS oriented horizontally and a minimum solidification time of 4740 seconds is observed in radial finned 1% GNP LHSS oriented vertically. On comparison with pure PCM shell and tube heat exchanger which has minimum solidification time, a minimum of 61.08% and a maximum of 82.23% reduction in solidification time is noted.

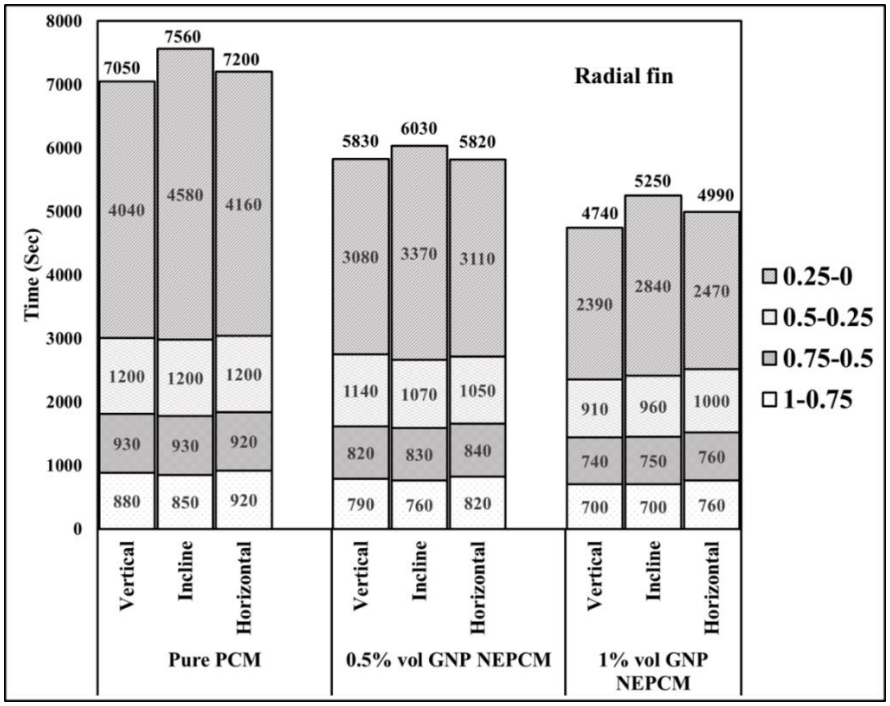

Fig 5.25 Time taken to reach melt fraction with an interval of 0.25 during solidification for radial fin heat exchanger

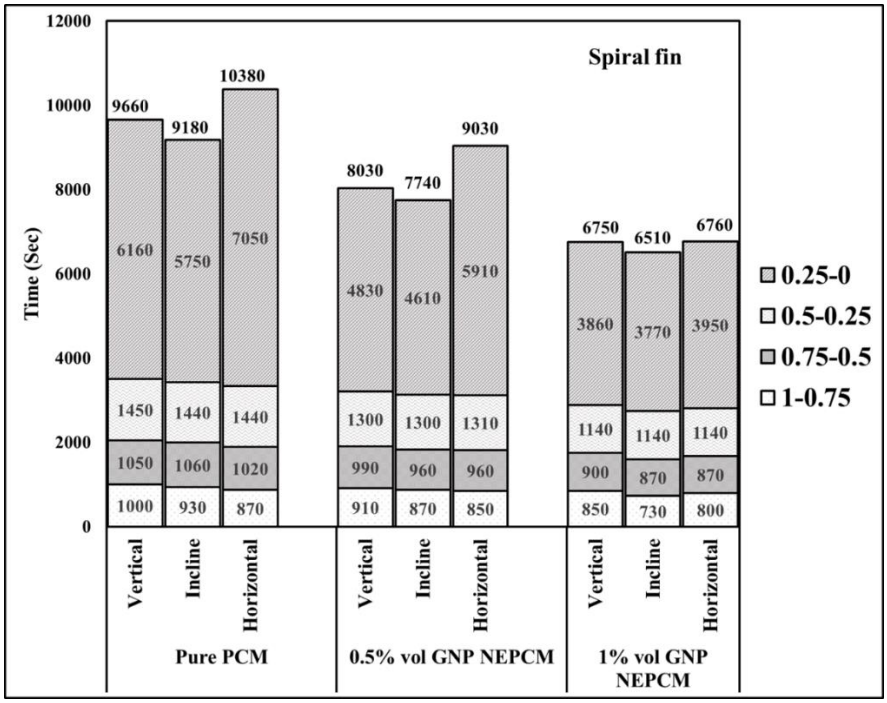

Fig 5.26 Time taken to reach melt fraction with an interval of 0.25 during solidification for spiral fin heat exchanger

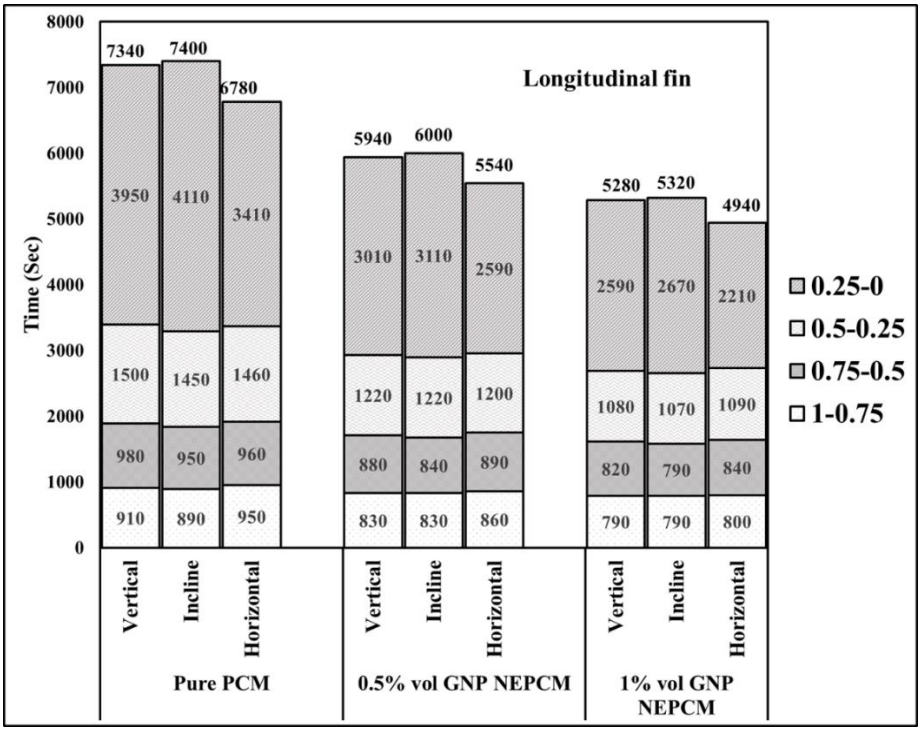

Fig 5.27 Time taken to reach melt fraction with an interval of 0.25 during solidification for longitudinal fin heat exchanger

5.4.2.4 Energy release ratio

The released energy by NEPCM is directly proportionate to the variation of initial and instantaneous NEPCM average temperature. The energy release ratio during solidification is the energy discharged away by the NEPCM to the maximum energy that NEPCM can discharge. Fig.5.28, 5.29 and 5.30 illustrates how the energy ratio varies among the radial, spiral and longitudinal fin heat exchangers considered. From Fig. 5.28, 5.29 and 5.30 it is possible to divide the energy release ratio into three stages irrespective of the type of fins, orientation and volume fraction of GNP nanoparticles. It is sensible heat that releases energy during the initial stages. The material's latent heat capacity releases the energy during the second stage. The temperature changes very little during this stage despite the release of a huge amount of energy. The third stage of solidification releases sensible heat, and the temperature decreases at a slower rate during this stage, which results in a slower rate of energy dissipation. The energy release ratio during solidification is high for a 45° inclined heat exchanger irrespective of the type of the fin and volume fraction of GNP nanoparticles. The maximum energy release ratio of 0.993 is observed in spiral-finned pure PCM LHSS oriented horizontally and the minimum energy release ratio of 0.976 is

observed in longitudinal-finned 1% GNP LHSS oriented horizontally. On comparison with pure PCM shell and tube heat exchanger which has a maximum energy release ratio, a minimum reduction of 0.3%, and a maximum reduction of 2.31% in energy release ratio is noted.

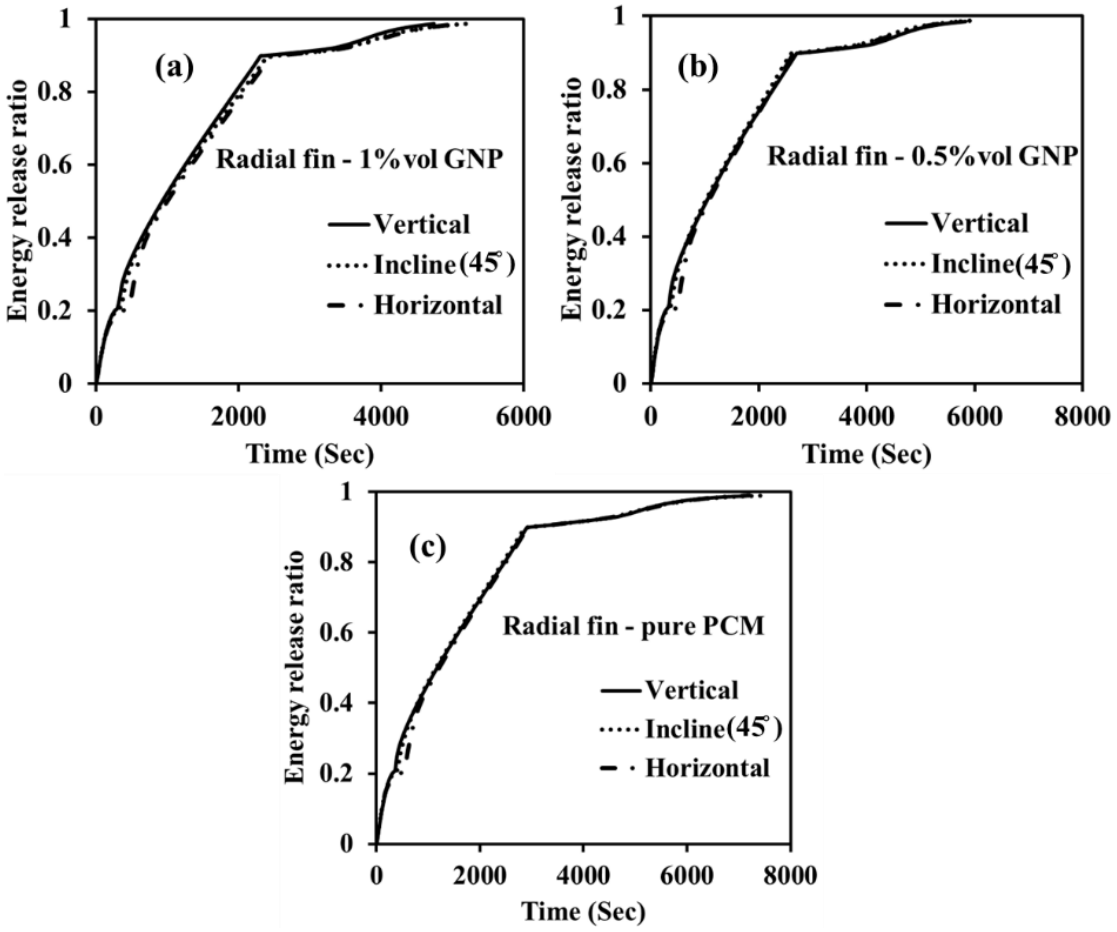

Fig 5.28 Energy release ratio of radial fin heat exchangers during solidification (a) 1% volume GNP (b) 0.5% volume GNP (c) pure PCM

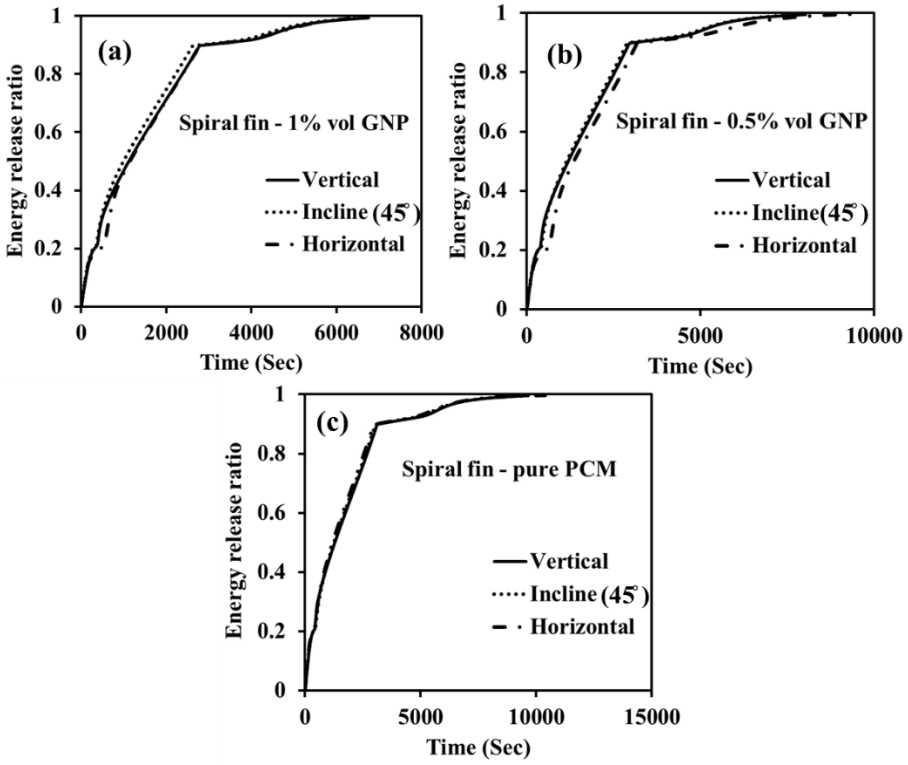

Fig 5.29 Energy release ratio of spiral fin heat exchangers during solidification (a) 1% volume GNP (b) 0.5% volume GNP (c) pure PCM

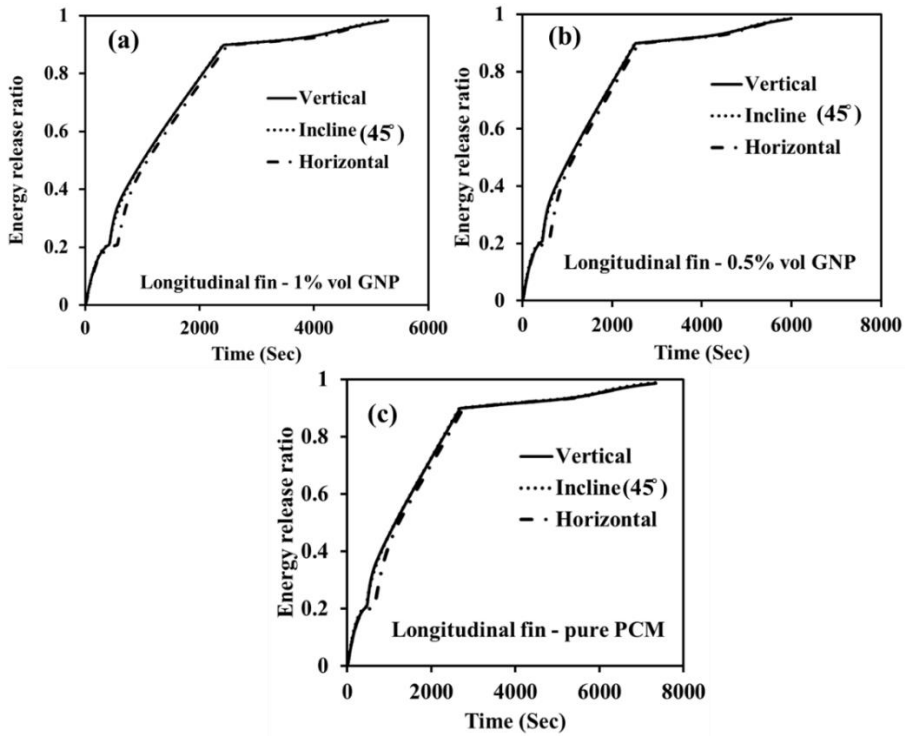

Fig 5.30 Energy release ratio of longitudinal fin heat exchangers during solidification (a) 1% volume GNP (b) 0.5% volume GNP (c) pure PCM

5.4.2.5 Exergy efficiency

An important aspect of solidification is the study of exergy efficiency. Fig.5.31, 5.32 and 5.33 illustrates how exergy efficiency diminishes as solidification progresses in radial spiral and longitudinal fin heat exchangers. During solidification, NEPCM discharges energy at a higher temperature than the HTF's outlet temperature, thus resulting in exergy destruction. At the initial stage of solidification, exergy efficiency is more because of considerable variation in temperatures of HTF at the inlet and outlet. Fig.5.31, 5.32 and 5.33 illustrates that maximum exergy efficiency and average exergy efficiency are high for radial heat exchanger for the considered orientation and volume fraction of GNP nanoparticles. Exergy efficiency during solidification is noted to be high for shell and tube LHSS oriented at 45° for a particular fin and volume fraction of GNP nanoparticles. For a particular fin and orientation of the LHSS exergy efficiency increased with an increase in the volume fraction of GNP nanoparticles. From Fig.5.33 it can be noticed that for the longitudinal finned heat exchanger, exergy efficiency increased at the final stage of solidification. This is because, in the end, the average temperature of the PCM decreases slower than the outlet temperature of the HTF. During solidification, the maximum average exergy efficiency of 4.55% is observed in radial finned 1% GNP LHSS oriented at 45° and the minimum average exergy efficiency of 2.06% is observed in longitudinal finned pure PCM LHSS oriented horizontally.

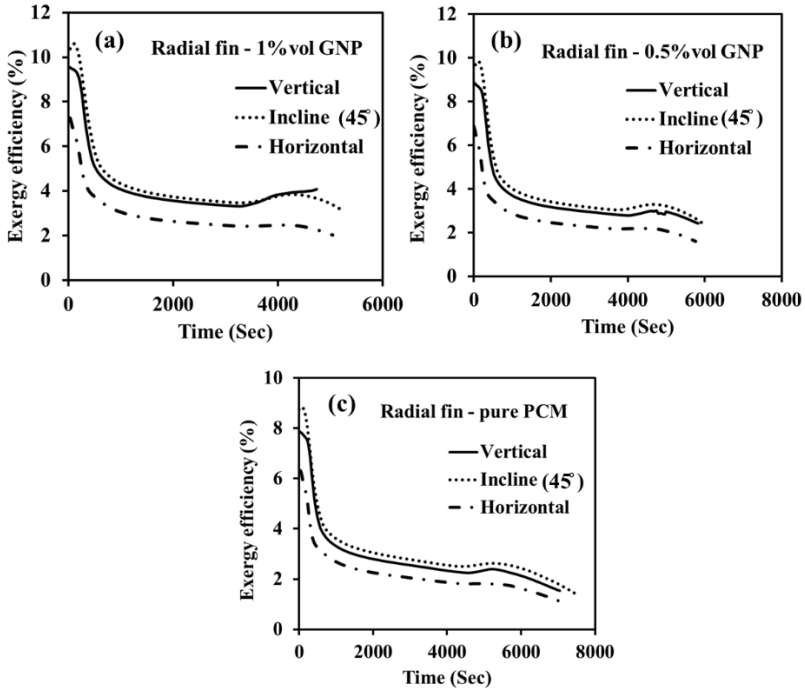

Fig 5.31 Exergy efficiency of the radial fin heat exchanger during solidification (a) 1% volume GNP(b) 0.5% volume GNP(c) pure PCM

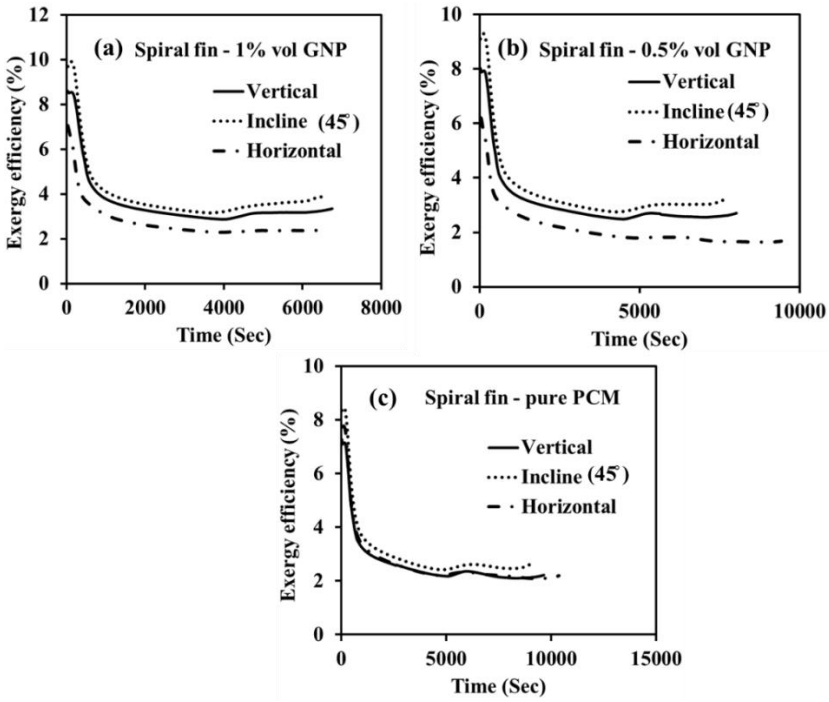

Fig 5.32 Exergy efficiency of the spiral fin heat exchanger during solidification (a) 1% volume GNP(b) 0.5% volume GNP(c) pure PCM

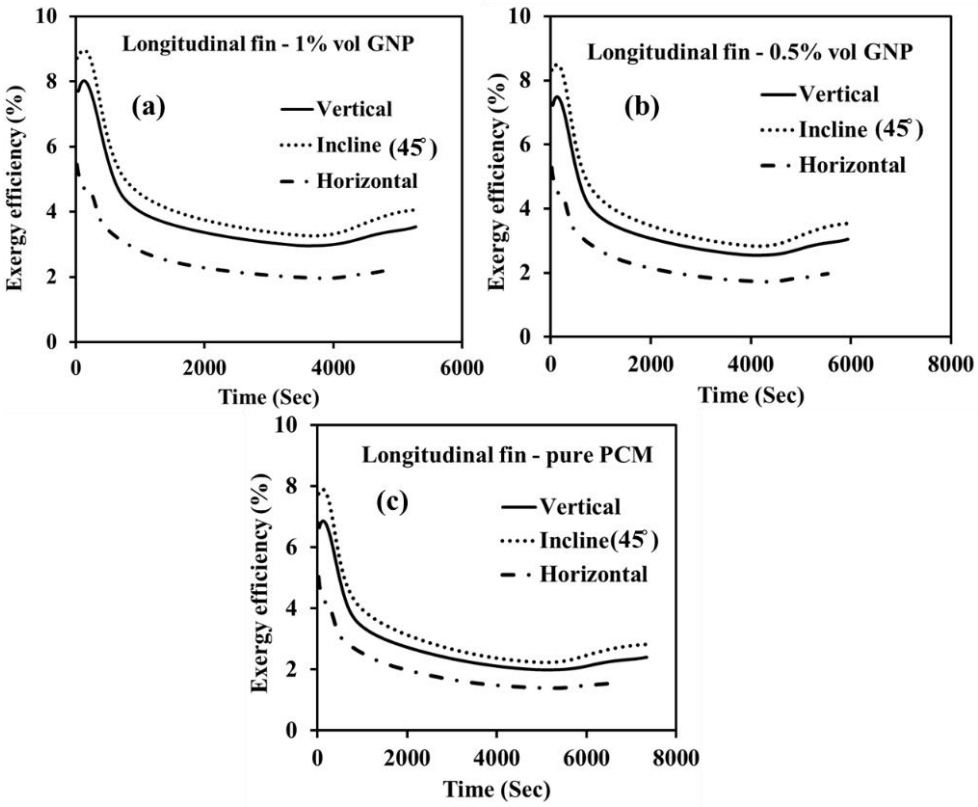

Fig 5.33 Exergy efficiency of the longitudinal fin heat exchanger during solidification (a) 1% volume GNP(b) 0.5% volume GNP(c) pure PCM

5.5 Closure

The thermal performance of the nanoparticle-enhanced phase change materials (NEPCMs) based shell and tube heat exchanger with radial, spiral and longitudinal fins are analyzed considering the orientation effect. The volume fractions of GNP nanoparticles considered are 0, 0.5, and 1%. The orientation angles of the heat exchanger considered are vertical (90̊), inclined (45̊) and horizontal (0̊). The influence of nanoparticles concentration, orientation of heat exchanger and fin type on the thermal performance of heat exchangers is given in terms of average temperature, melt fraction, energy storage/release ratios, and exergy efficiency.

- Both the melting time and solidification time are affected by the addition of the nanoparticles and the type of fins used. Orientation of heat exchangers has shown a significant effect on melting than on solidification. Phase change time decreased with an increase in the volume fraction of the nanoparticles.

- Melting time is least in the case of the vertically oriented radial fin heat exchanger and maximum in the case of the spiral fin heat exchanger oriented at 45° for the considered volume fraction of GNP nanoparticles.
- Solidification time is minimum for radial fin heat exchanger and highest for spiral fin heat exchanger for the considered volume fraction of GNP nanoparticles and orientation of heat exchanger.
- The conductive mode of heat transfer is dominant in radial and spiral fin heat exchangers. Whereas convection is observed to be dominant for longitudinal fin heat exchangers.
- The average temperature and energy release ratio at the end of solidification is almost the same for all the considered heat exchangers.
- On comparison with pure PCM shell and tube heat exchanger, which has minimum melting time, a minimum of 12.68% reduction in melting time on the usage of pure PCM spiral finned heat exchanger inclined at 45° and a maximum of 73.71% reduction in melting time on the usage of 1% volume GNP radial finned heat exchanger positioned vertically is noted.
- On comparison with pure PCM shell and tube heat exchanger, which has minimum solidification time, a minimum of 61.08% reduction in solidification time on the usage of pure PCM spiral finned heat exchanger positioned horizontally and a maximum of 82.23% reduction in solidification time on the usage of 1% volume GNP radial finned heat exchanger positioned vertically is noted.
- On comparison with pure PCM shell and tube heat exchanger which has maximum energy storage ratio, a maximum 0.4% improvement in energy storage ratio on the usage of radial finned pure PCM LHSS oriented at 45° and a maximum of 10.28% reduction in energy storage ratio on the usage of 1% volume GNP radial finned heat exchanger positioned vertically is noted.
- On comparison with pure PCM shell and tube heat exchanger which has a maximum energy release ratio, a minimum of 0.3% reduction in energy release ratio on the usage of spiral-finned pure PCM LHSS oriented horizontally and a maximum of 2.31% reduction in energy release ratio on the usage of longitudinal-finned 1% GNP LHSS oriented horizontally is noted.

- During melting, the maximum average exergy efficiency of 72.77% is observed in spiral finned pure PCM LHSS oriented at 45°, and the minimum average exergy efficiency of 44.49% is observed in radial finned 1% GNP LHSS oriented vertically.
- During solidification, the maximum average exergy efficiency of 4.55% is observed in radial finned 1% GNP LHSS oriented at 45° and the minimum average exergy efficiency of 2.06% is observed in longitudinal finned pure PCM LHSS oriented horizontally.
- A common problem among all the heat exchangers considered is that the average exergy efficiency during solidification is very low. The maximum average exergy efficiency value during solidification is observed to be 4.55% for radial fin HX with a 1% volume fraction of GNP nanoparticles inclined at 45°.

Chapter 6

Effect of metal foam– nanoparticles on the thermal performance of latent heat storage system

6.1 Introduction

The utilization of metal foam and nanoparticles has shown significant improvement in the rate of melting and solidification in latent heat storage systems (LHSS). Combined usage of metal foam and nanoparticles further improves the performance of the LHSS. On reviewing the literature, it is found that copper metal foam is the most commonly used metal foam to improve the rate of heat transfer in LHSS and graphene nanoplatelets (GNPs) nanoparticles were found to show better compatibility with PCMs. Inclination studies on LHSS have shown contradicting results. Hence, in the present chapter melting and solidification performance of copper metal in combination with GNP nanoparticle-enhanced phase change materials (NEPCM) in a shell and tube heat exchanger are analyzed and a comparison is made. GNPs are selected as nanoparticles in the present analysis because they lead to a high increase in the thermal conductivity of PCMs.

6.2 Physical model

Optimized geometric parameters from the literature are considered for the heat exchanger design. Reviewing existing literature on latent heat-based shell and tube heat exchangers, Kalpala and Devanuri [63] concluded that the tube-to-shell diameter ratio should be nearly 0.25. In the present work, this ratio is considered as 0.254. The length, inner diameter of the shell, and the tube thickness of the heat exchanger are considered 250mm, 75mm, and 0.8mm respectively. The schematic of the heat exchanger is shown in Fig.6.1. Analysis of PCM-based shell and tube heat exchanger was carried out by Kalpala and Devanuri [42] noted that varying mass flow rate of heat transfer fluid has an insignificant effect on the behaviour of heat exchanger, the flow rate of heat transfer fluid is fixed at 1.4 LPM [29]. Compatibility studies of organic PCMs with different metals carried out by Gaddala and Devanuri [133] reviled that stainless steel exhibited good resistance towards corrosion so tube material was considered to be stainless steel. Since lauric acid is suitable for heat storage applications [133], it was considered in the study. From the literature it is observed

that copper foam metal foam PCM heat exchangers have shown better performance, so copper is selected as the metal foam material.

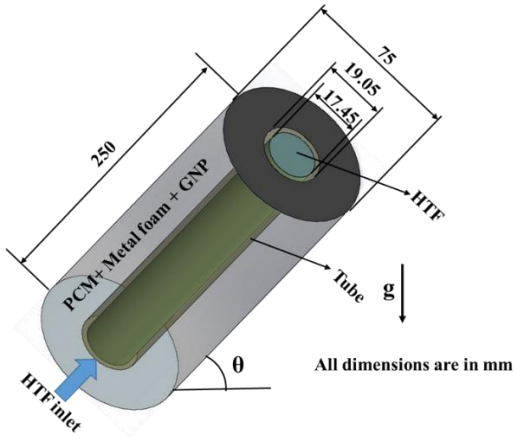

Fig 6.1 Schematic of metal foam + nanoparticles LHSS

6.3 Numerical methodology

6.3.1 Validation

Non-thermal equilibrium approach is used to model the heat transfer interaction between NEPCM and metal foam. The finite volume method is considered for the computational domain. For pressure-velocity coupling, the PISO is used. To handle the pressure, PRESTO methodology is used and a second-order upwind scheme is used for the discretization of momentum and energy equations. The convergence criteria for continuity, momentum, and energy equations are kept as 10^{-6}, 10^{-6}, and $10^{-8,}$ respectively. ANSYS FLUENT is used to solve the governing equations.

To verify the accuracy of the present numerical model, numerical results are compared with the experimental results of Zhao et al.[84] and with the numerical results of Mahdi et al.[123][136] .These results are presented in Figs.6.2 and 6.3. The maximum error is within the reasonable range.

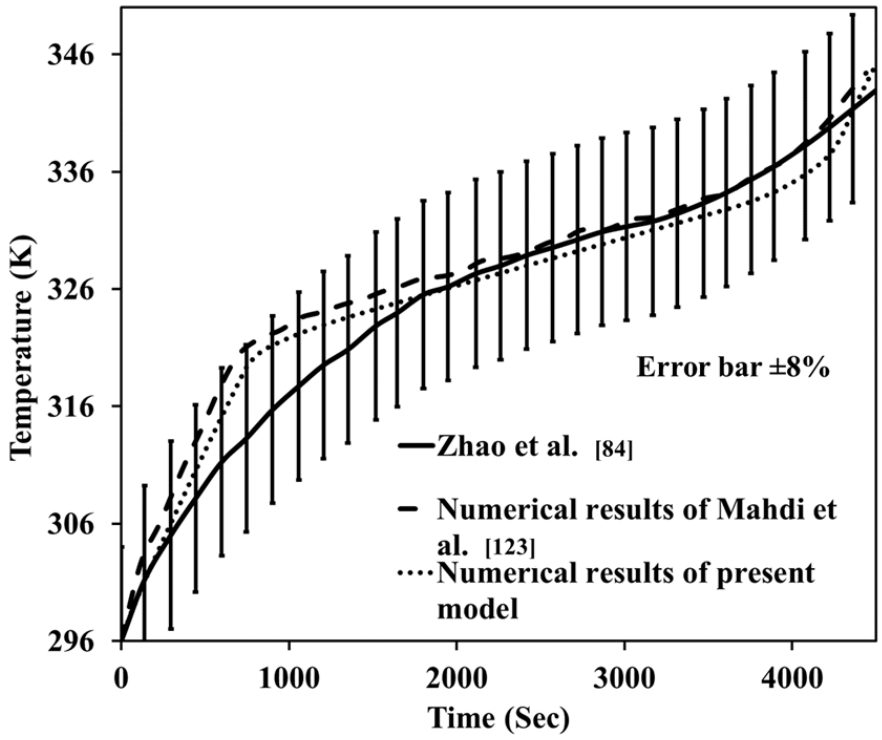

Fig 6.2 Numerical validation with experimental results of Zhao et al.[84]

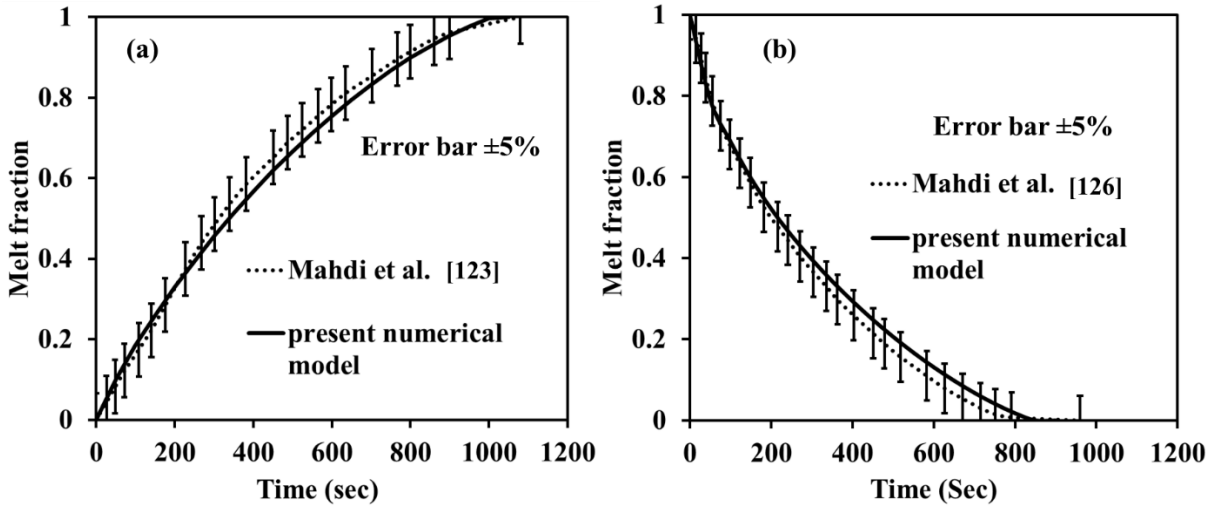

Fig 6.3 Numerical validation for (a) melting (b) solidification

6.3.2 Grid and time independence

A structured grid for considered heat exchanger is created as shown in Fig.6.4. Grid and time independence studies are examined by comparing the volume-averaged melt fraction

of the PCM. Grid sizes considered are 183231, 294963, and 389450. Likewise, time-independent analysis is carried out with time step sizes of 0.3, 0.5, and 0.7 seconds. From Fig.6.5 it can be noted that grid independence is achieved for 294963 elements and time independence is achieved for 0.5 seconds.

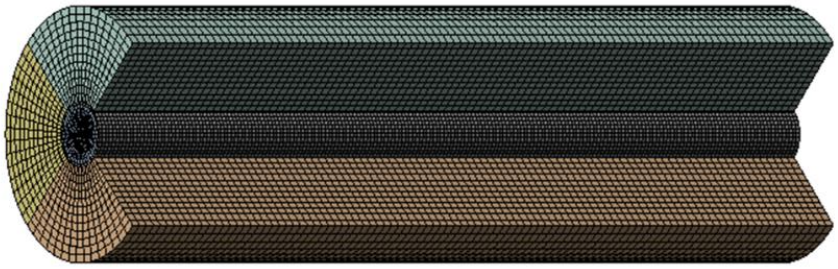

Fig 6.4 Grid structure of computational domain

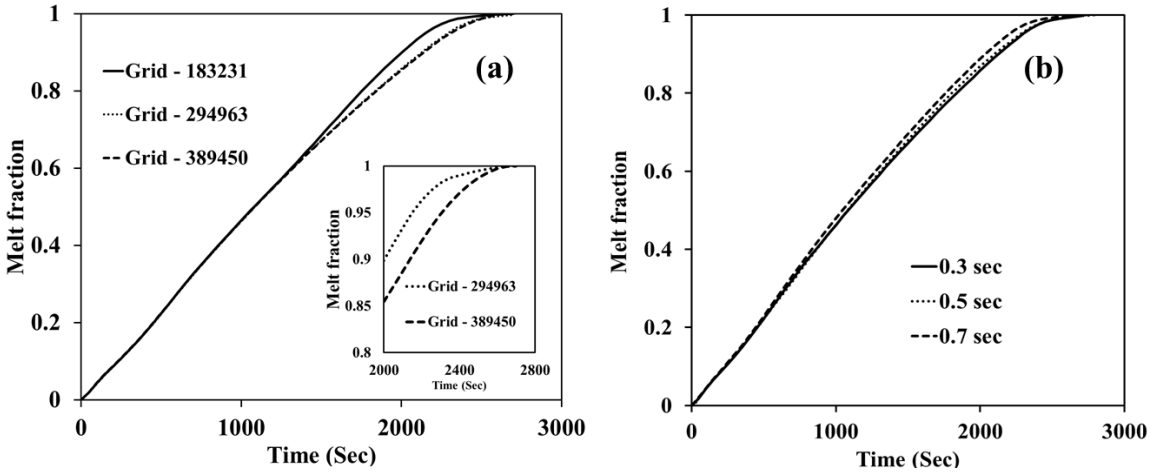

Fig 6.5 (a) Grid and (b) time independence studies

6.4 Results and discussion

6.4.1 Melting

6.4.1.1 Temperature and melt fraction distribution

Figs.6.6, 6.7 and 6.8 shows the temperature and melt fraction distribution contours of 0.97, 0.95 and 0.93 metal foam porosity LHSS at center planes during melting at 1200 sec. From Figs.6.6, 6.7 and 6.8 it can be noted that the amount of melted NEPCM is more in the heat

exchanger with 0.93 porosity metal foam and less in the heat exchanger with 0.97 porosity metal foam. Significant variation in liquid fraction and temperature contours in heat exchangers is noted in Fig.6.6, 6.7 and 6.8 based on the porosity of metal foam. Similarly to the melt fraction of the LHSS, the maximum temperature near the HTF tube tends to increase with a decrease in the porosity of metal foam. This is because, with a decrease in the porosity of metal foam, the effective thermal conductivity of NEPCM increases. From Figs.6.6,6.7 and 6.8, it can be noted that unlike in pure PCM heat exchangers, [42][79] hot PCM is not settled at the top portion of the heat exchanger. Most of the hot PCM is near to HTF tube. Non-uniform melting in the radial direction when kept in 45° orientation and horizontally can be observed in melt fraction contours, this is due to the natural convection effect. But this effect is observed to reduce with a decrease in the porosity of metal foam, this indicates that with a decrease in the porosity of metal foam convective effect decreases. But increase in overall heat transfer indicates that the conductive mode of heat transfer increases with a decrease in metal foam porosity. From Fig.6.6 for 0.97 porosity metal foam LHSS effect of GNP nanoparticles can be noted from melt fraction contours, for a particular orientation of the heat exchanger with increase in the volume fraction of GNP nanoparticles melt fraction tends to decrease. The effect of GNP nanoparticles could not be interpreted from temperature and melt fraction contours in 0.95 and 0.93 porosity metal foam heat exchanger.

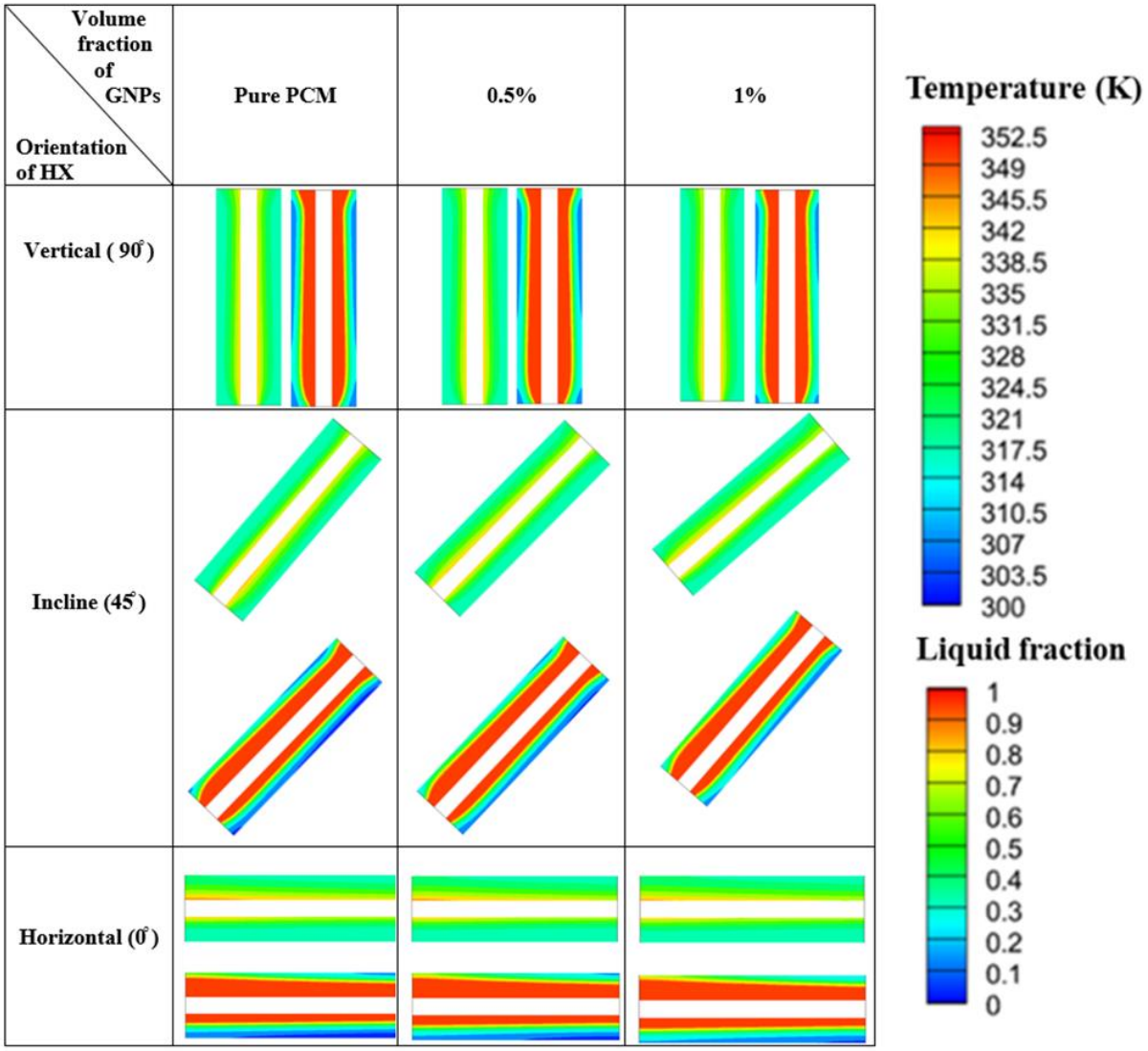

Fig 6.6 Temperature and melt fraction contours of 0.97 metal porosity heat exchanger at 1200 sec during melting

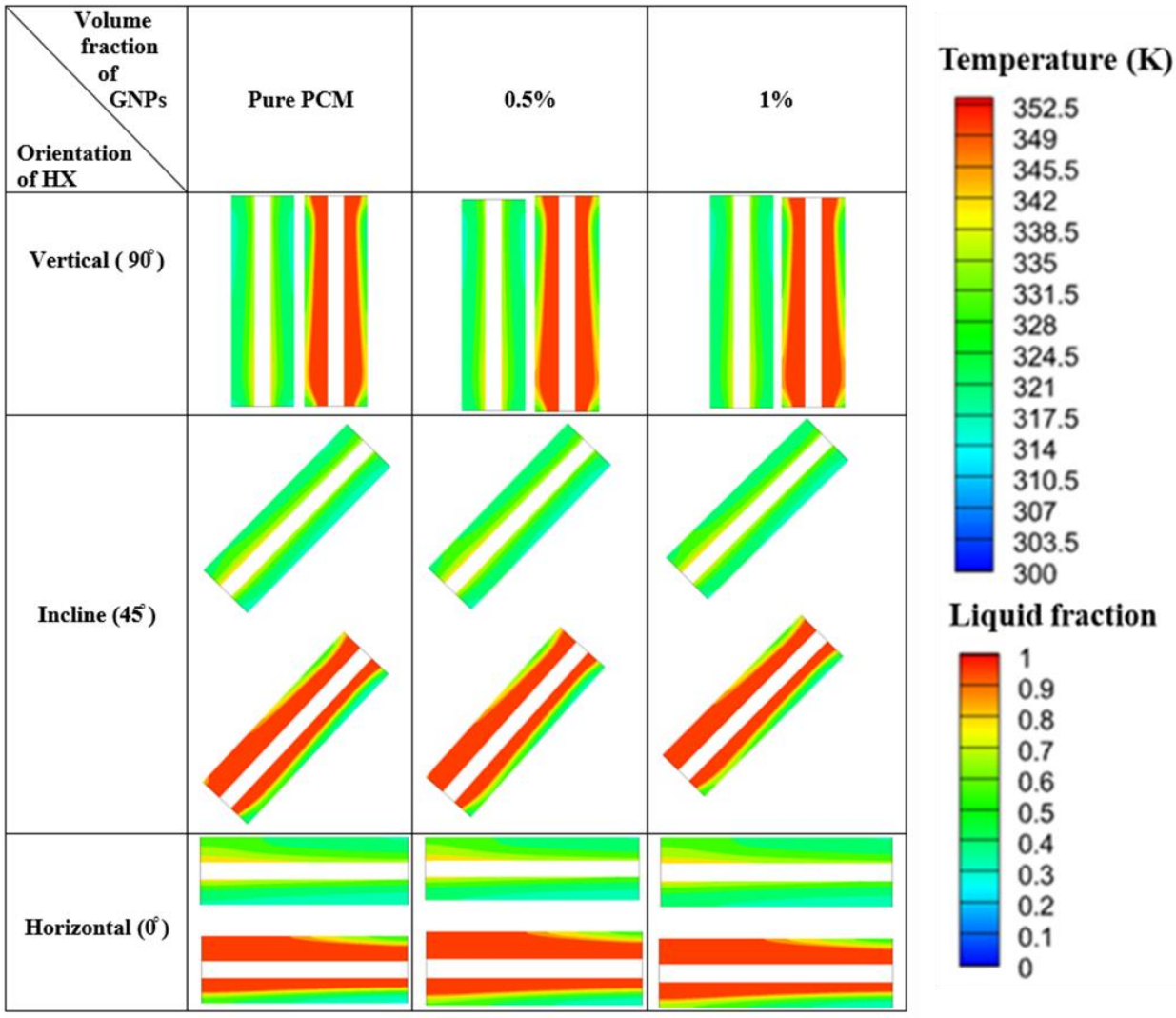

Fig 6.7 Temperature and melt fraction contours of 0.95 metal porosity heat exchanger at 1200 sec during melting

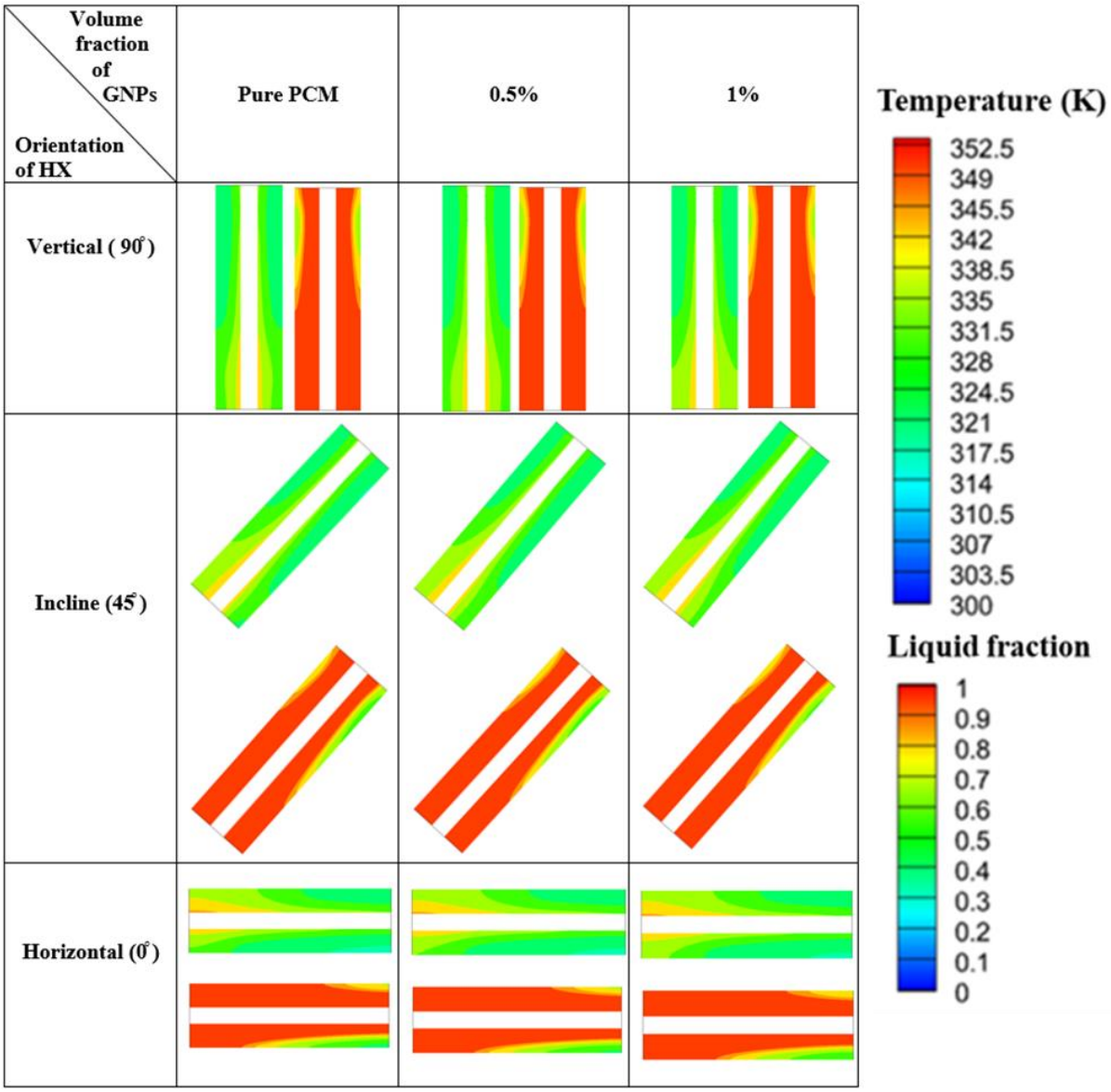

Fig 6.8 Temperature and melt fraction contours of 0.93 metal porosity heat exchanger at 1200 sec during melting

6.4.1.2 Average Temperature

Figs.6.9, 6.10 and 6.11 displays the average temperature variation with respect to time for pure PCM, 0.5% volume GNP and 1% volume GNP LHSS considered. In all the heat exchangers during the early stage of melting a rapid increase in the temperature is noted. This is because energy is stored due to sensible heat. In the second stage of melting a sudden depletion in the rate of temperature is because energy is stored due to latent heat capacity. At the third and final stage again a rapid rise in the temperature is noted this is

because at this stage energy is again stored due to sensible heat capacity. Throughout the melting process irrespective of the volume fraction of GNP nanoparticles and orientation of the heat exchanger temperature increase rate in 0.95 porosity metal foam heat exchanger is more than 0.97 porosity metal foam heat exchanger. This is because of the high effective thermal conductivity due to 0.95 porosity metal foam than that of 0.97 porosity metal foam. The rate of increase in temperature variation is also noted in the case of heat exchanger with 0.93 porosity metal foam when compared with 0.95 porosity metal foam heat exchanger, but this change is less when compared with the change in 0.97 to 0.95 porosity metal foam heat exchanger. This is because the increase in the effective thermal conductivity is more in the case of metal foam with a porosity of 0.97 to 0.95 rather than in the case of 0.95 to 0.93. But a decrease in porosity from 0.95 to 0.93 resulted in high suppression of convective effects than that of from 0.97 to 0.95. At the end of melting, the maximum temperature of 343.5K is observed in pure PCM + 0.97 porosity metal foam LHSS inclined at 45°, minimum temperate of 335K is noted in 1% volume GNP+0.93 porosity metal foam LHSS positioned vertically.

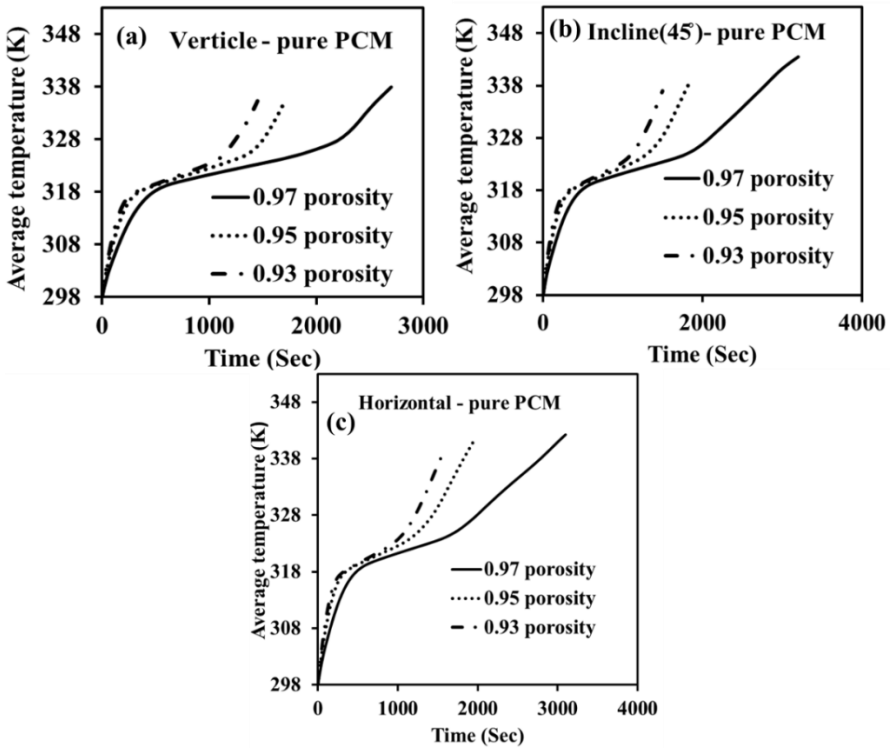

Fig 6.9 Average temperature evolution for pure PCM metal foam heat exchangers during melting (a) vertical (b) incline (45°) and (c) horizontal

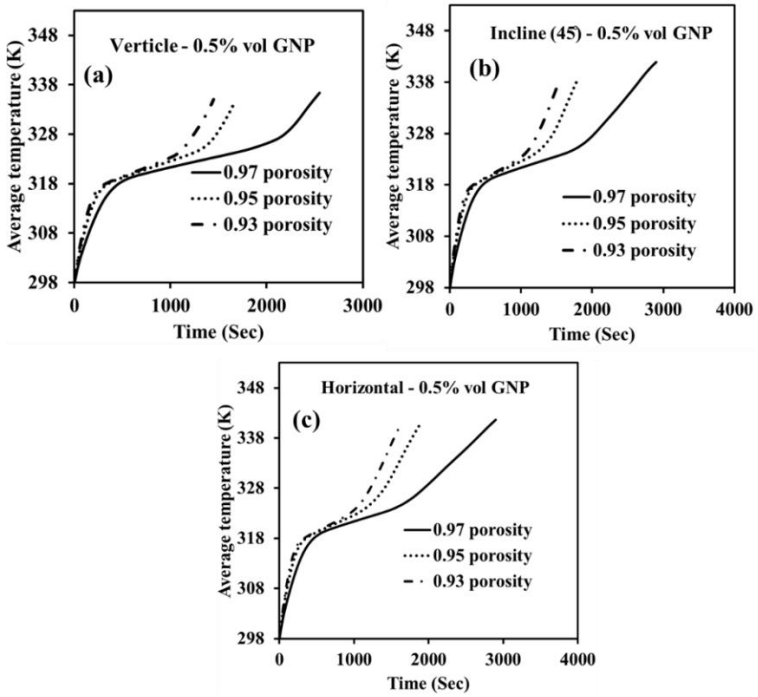

Fig 6.10 Average temperature evolution for 0.5% volume GNP metal foam heat exchangers during melting (a) vertical (b) incline (45°) and (c) horizontal

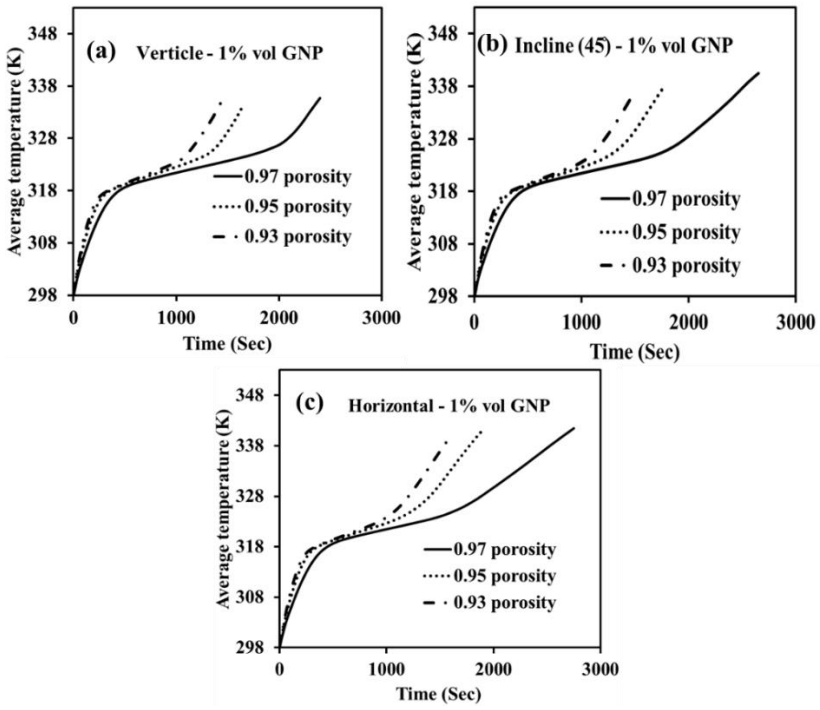

Fig 6.11 Average temperature evolution for 1% volume GNP metal foam heat exchangers during melting (a) vertical (b) incline (45̊) and (c) horizontal

6.4.1.3 Melting time

Figs. 6.12, 6.13 and 6.14 shows the melting time taken to an increment of 0.25 melt fraction of 0.97, 0.95 and 0.93 metal foam porosity LHSS till the end of the phase change process during melting. During the initial stage of melting time to attain a melt fraction from 0 to 0.25 is higher than the time to attain a melt fraction from 0.25 to 0.5. This is because during the initial stage of melting some amount of energy is stored due to sensible heat, during which NEPCM absorbs energy without melting. Further from a 0.5 melt fraction time taken to melt for every 0.25 melt faction increases due to a drop in the temperature difference between HTF and the average temperature of the NEPCM. It can be noted that at all intervals of melting for a particular volume fraction of GNP nanoparticles and orientation of LHSS, melting time is minimum for LHSS with 0.93 porosity metal foam LHSS. It can be noted that at all the intervals of melting variation in the melting time is more in the case of heat exchangers with 0.95 and 0.97 porosity metal foam than that of variation in the melting time of heat exchangers with 0.95 and 0.93 porosity metal foam. This is because the rate of increase in the effective thermal conductivity of NEPCM from 0.97 porosity metal foam to 0.95 porosity metal foam is greater than 0.95 porosity metal

foam to 0.93 porosity metal foam. A considerable variation in the rate of melting is noted among the heat exchanger with 0.97 porosity metal foam with varying volume fractions of GNP nanoparticles, this indicates that the effect of GNP nanoparticles is felt only in the presence of metal foam with 0.97 porosity. In the case of 0.95 and 0.93 porosity metal foam heat exchanger increase in effective thermal conductivity due to GNP, nanoparticles is very less when compared with metal foam. When the volume fraction of GNP nanoparticles are kept constant, the effect of orientation is felt for all the considered metal foam porosities. This effect decreases with a decrease in the porosity of metal foam. As with a decrease in the porosity of metal foam, the effect of the convective mode of heat transfer decreases. During melting the maximum melting time of 3200 seconds is observed in pure PCM + 0.97 porosity metal foam LHSS oriented at 45° and a minimum melting time of 1410 seconds is observed in 1% volume GNP + 0.93 porosity metal foam LHSS oriented vertically. In comparison with pure PCM shell and tube heat exchanger which has minimum melting time, a minimum of 50.8% and a maximum of 78.32% reduction in melting time is noted.

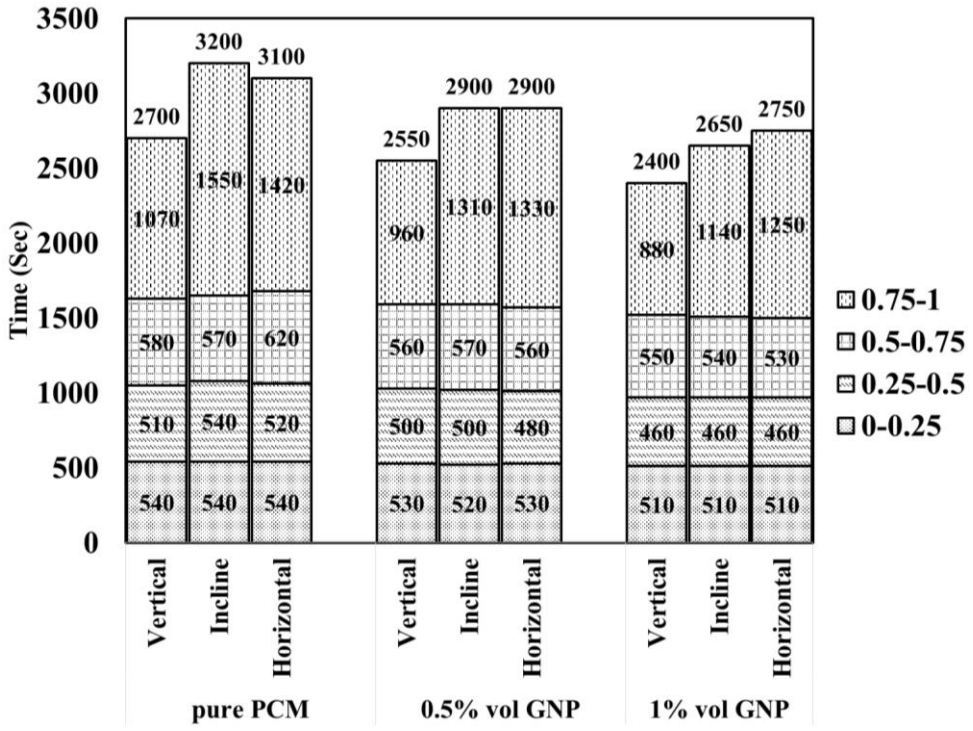

Fig 6.12 Time taken to reach melt fraction with an interval of 0.25 during melting for 0.97 porosity metal foam LHSS

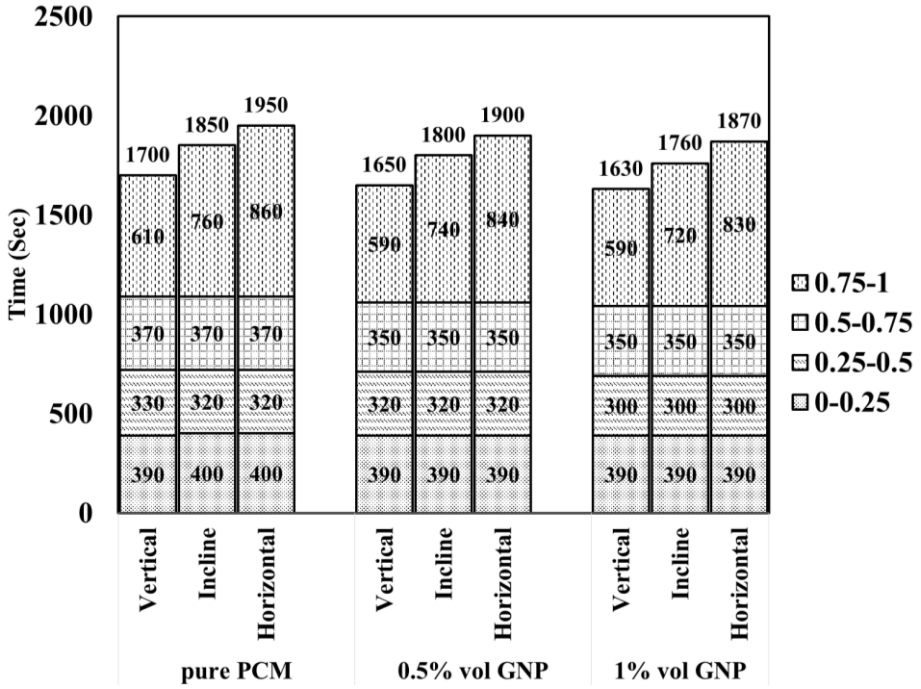

Fig 6.13 Time taken to reach melt fraction with an interval of 0.25 during melting for heat 0.95 porosity metal foam LHSS

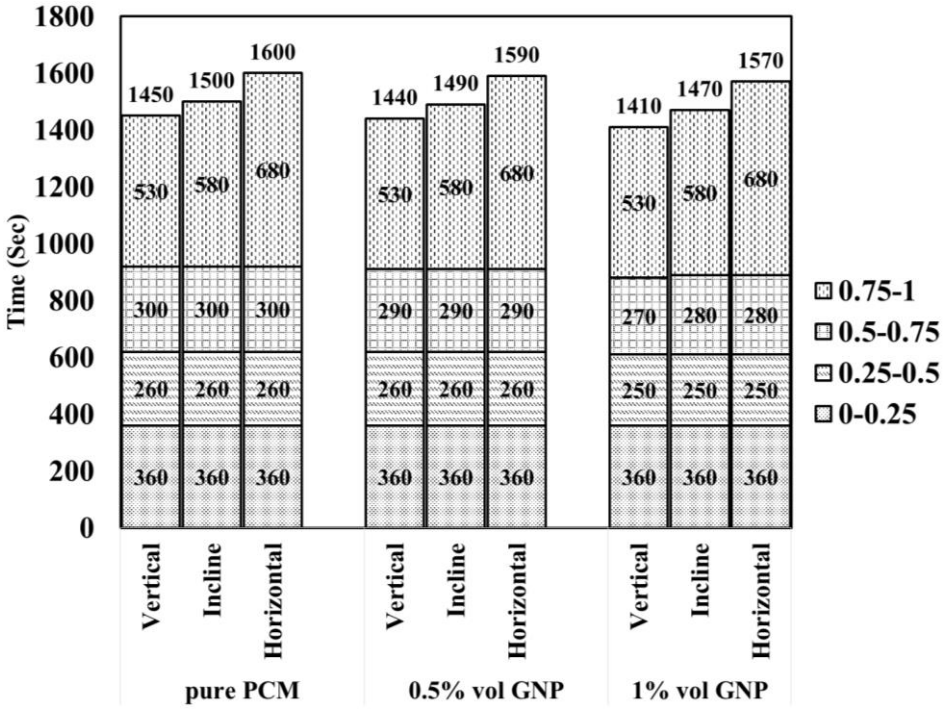

Fig 6.14 Time taken to reach melt fraction with an interval of 0.25 during melting for heat 0.93 porosity metal foam LHSS

6.4.1.4 Energy storage ratio

Figs. 6.15, 6.16 and 6.17 displays the energy storage ratio of pure PCM, 0.5% and 1% volume fraction GNP nanoparticles LHSS during melting. As discussed in section 4.2.1 procedure of energy storage is divided into 3 stages. The initial stage during which changes in temperature is very high for less energy absorbed. In the second stage, energy is stored due to latent heat capacity. During this stage rate of rise in the energy storage ratio is very high when compared to the other two stages, this can be noted from Figs .6.15, 6.16 and 6.17. In the final stage again energy is stored due to specific heat capacity, as a result, the rate of energy effectiveness is reduced. At the final stage rate of increase in energy storage ratio is less than that of the initial stage because of the drop in temperature difference between HTF and NEPCM. It can also be noted that trend in the energy storage ratio depends mostly on the porosity of the metal foam used in the heat exchanger rather than the volume fraction of GNP nanoparticles and orientation of the heat exchanger. During melting the maximum energy storage ratio of 0.93 is observed in pure PCM + 0.97 porosity metal foam LHSS inclined at 45° and the minimum energy storage ratio of 0.88 is observed in 1% volume GNP+0.93 porosity metal foam LHSS positioned vertically. In comparison with pure PCM shell and tube heat exchanger which has a maximum energy storage ratio, a minimum reduction of 6.25% and a maximum reduction of 11.29% in energy storage ratio is noted.

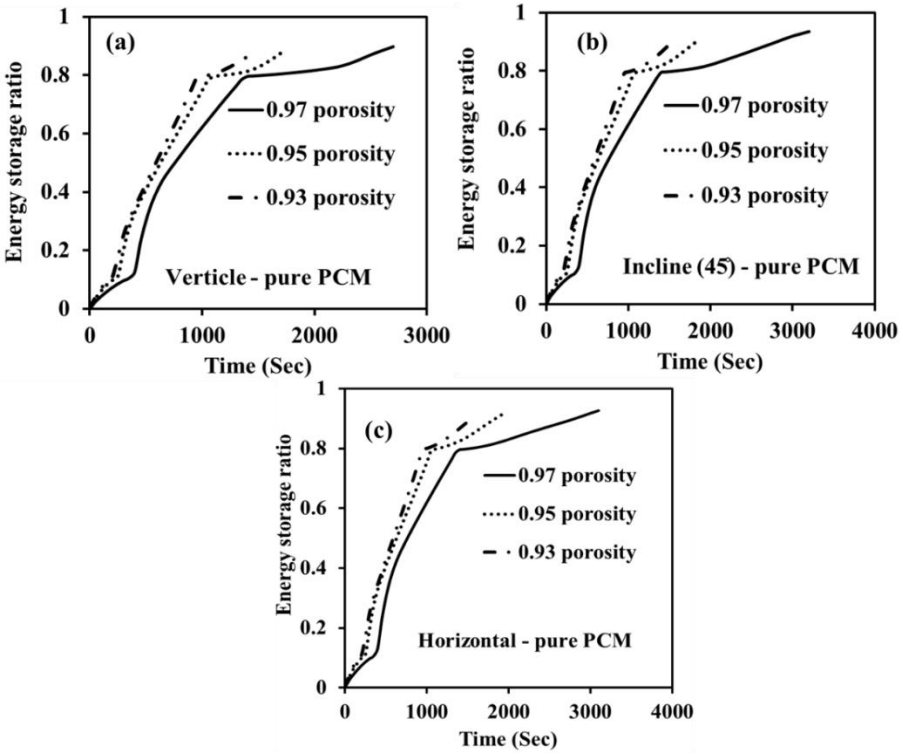

Fig 6.15 Energy storage ratio of pure PCM metal foam heat exchangers during melting (a) vertical (b) incline (45) and (c) horizontal

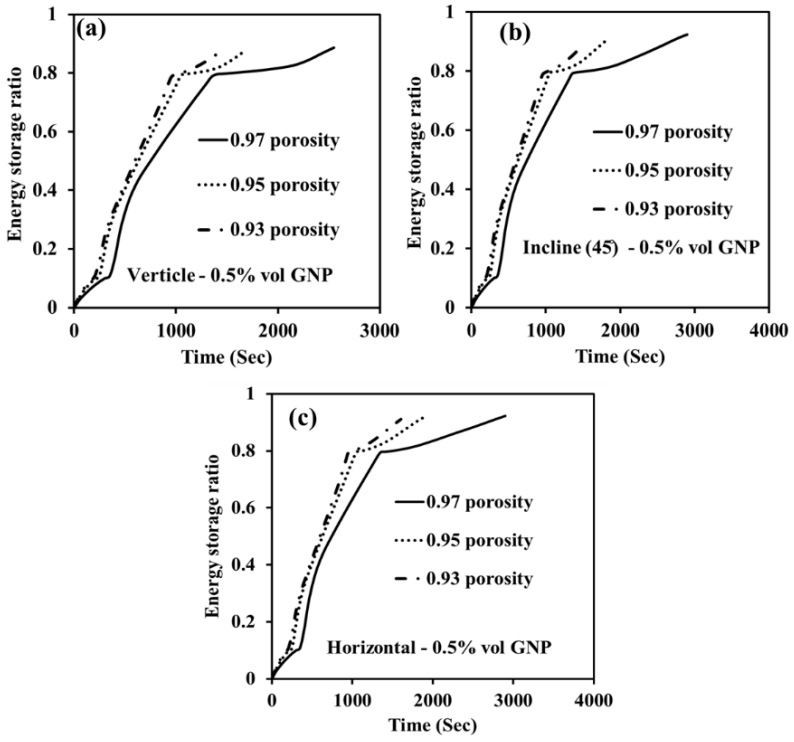

Fig 6.16 Energy storage ratio of 0.5% volume GNP metal foam heat exchangers during melting (a) vertical (b) incline (45) and (c) horizontal

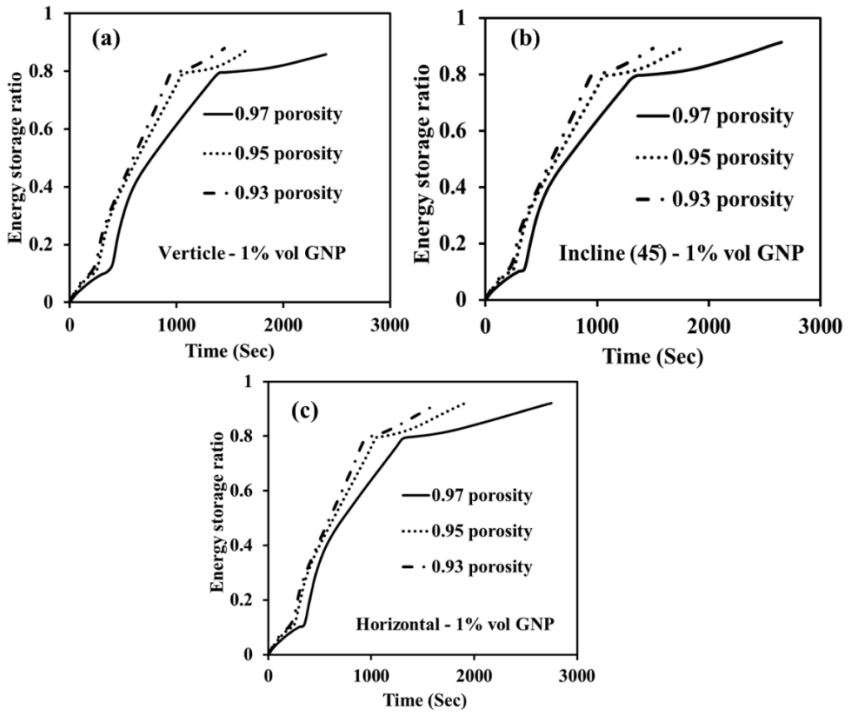

Fig 6.17 Energy storage ratio of 1% volume GNP metal foam heat exchangers during melting (a) vertical (b) incline (45°) and (c) horizontal

6.4.1.5 Exergy efficiency

Figs.6.18, 6.19 and 6.20 displays the exergy efficiency of pure PCM, 0.5% and 1% volume fraction GNP nanoparticles LHSS during melting. Exergy efficiency depends upon the NEPCM average temperature, exit and entrance temperature difference of HTF. The variation in temperature of entrance and exit of HTF is less, thus it depends significantly on average NEPCM temperature during melting. As NEPCM average temperature increases exergy efficiency of LHSS increases. It can be concluded from Figs.6.18, 6.19 and 6.20 that the exergy efficiency of heat exchangers follows the same trend as the average temperature of NEPCM during melting. As the average temperature of NEPCM tends to reach the inlet temperature of HTF exergy efficiency tends to increase. During melting the maximum average exergy efficiency of 54.13% is observed in pure PCM + 0.97 porosity metal foam LHSS oriented at 45° and the minimum average exergy efficiency of 46.28% is observed in 1% volume GNP + 0.93 porosity metal foam LHSS oriented vertically.

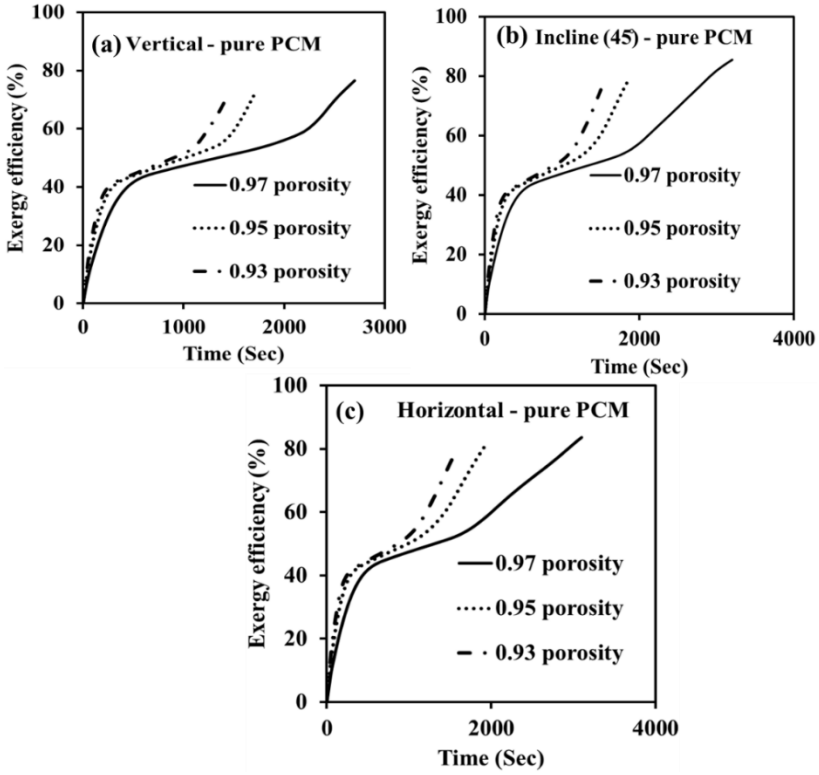

Fig 6.18 Exergy efficiency of pure PCM metal foam heat exchangers during melting (a) vertical (b) incline (45) and (c) horizontal

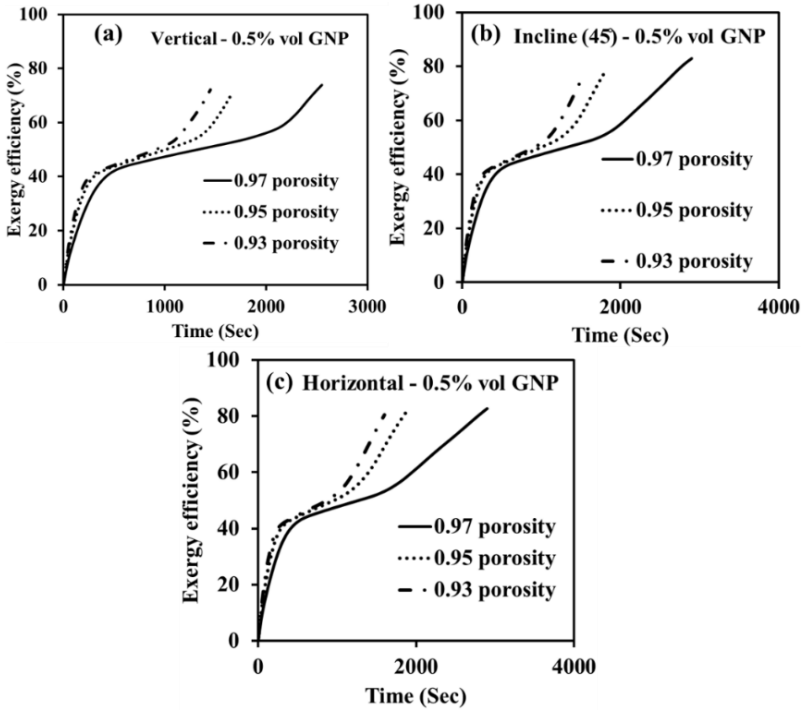

Fig 6.19 Exergy efficiency of 0.5% volume GNP metal foam heat exchangers during melting (a) vertical (b) incline (45) and (c) horizontal

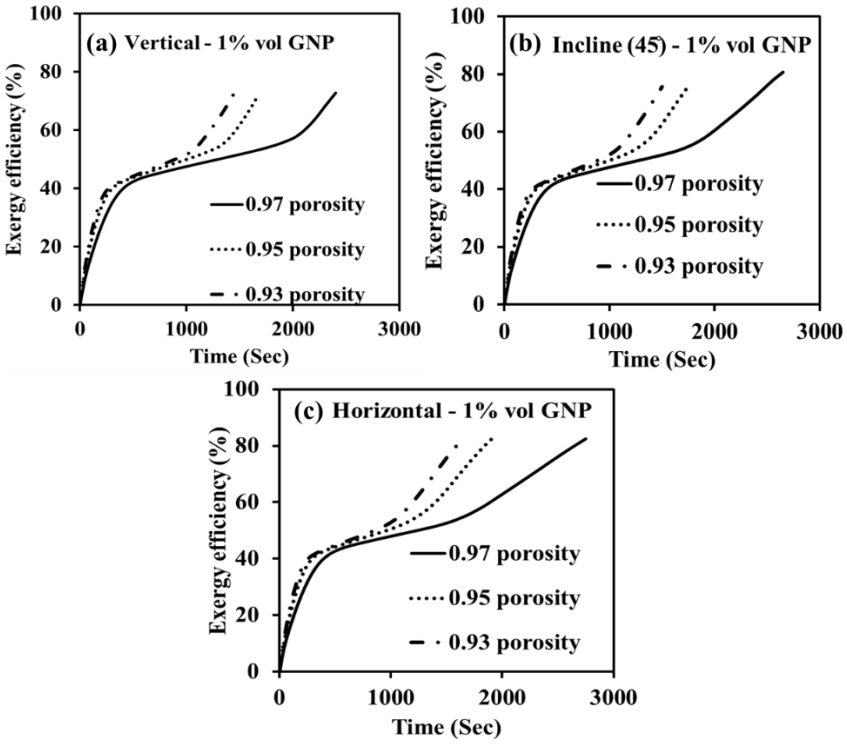

Fig 6.20 Exergy efficiency of 1% volume GNP metal foam heat exchangers during melting (a) vertical (b) incline (45̊) and (c) horizontal

6.4.2 Solidification

6.4.2.1 Temperature and melt fraction distribution

Figs.6.21, 6.22 and 6.23 shows the temperature and melt fraction distribution contours of 0.97, 0.95 and 0.93 metal foam porosity LHSS at center planes during melting at 1800 sec. From Fig.6.21, 6.22 and 6.23 it can be noted that the amount of solidified NEPCM is more in the heat exchanger with 0.93 porosity metal foam and less in the heat exchanger with 0.97 porosity metal foam. This is because the effective thermal conductivity of NEPCM increased with a decrease in the porosity of metal foam. A significant variation in melt fraction contours with varying porosity of metal foam is observed, but from Figs.6.21, 6.22 and 6.23 variation in the temperature contours is insignificant. Irrespective of the angle of orientation uniformity in temperature and melt fraction contours is noted because the solidification process is conduction dominant. From Figs.6.21, 6.22 and 6.23 the effect of the GNP NPs could not be interpreted.

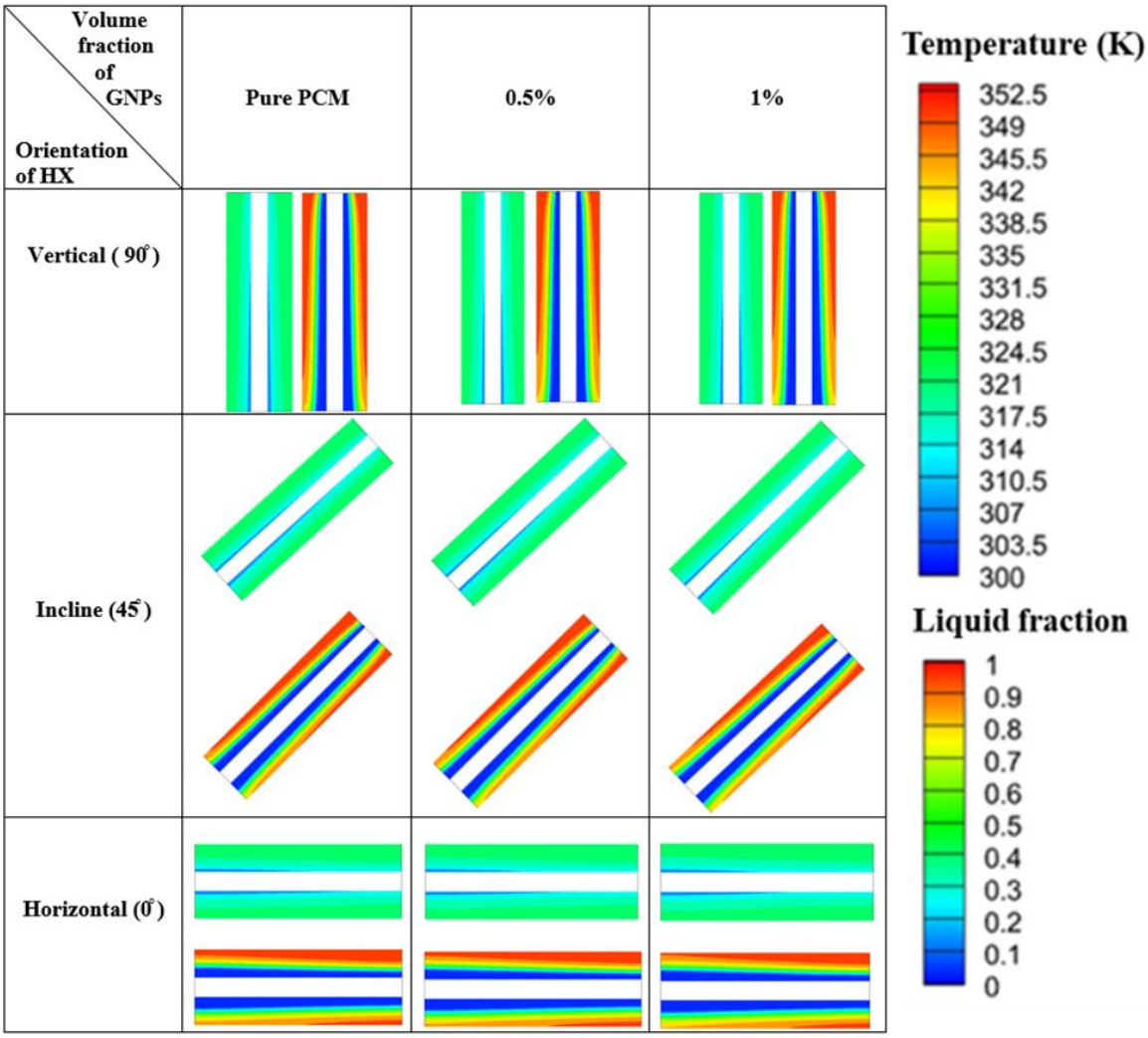

Fig 6.21 Temperature and melt fraction contours of 0.97 metal porosity heat exchanger at 1800 sec during solidification

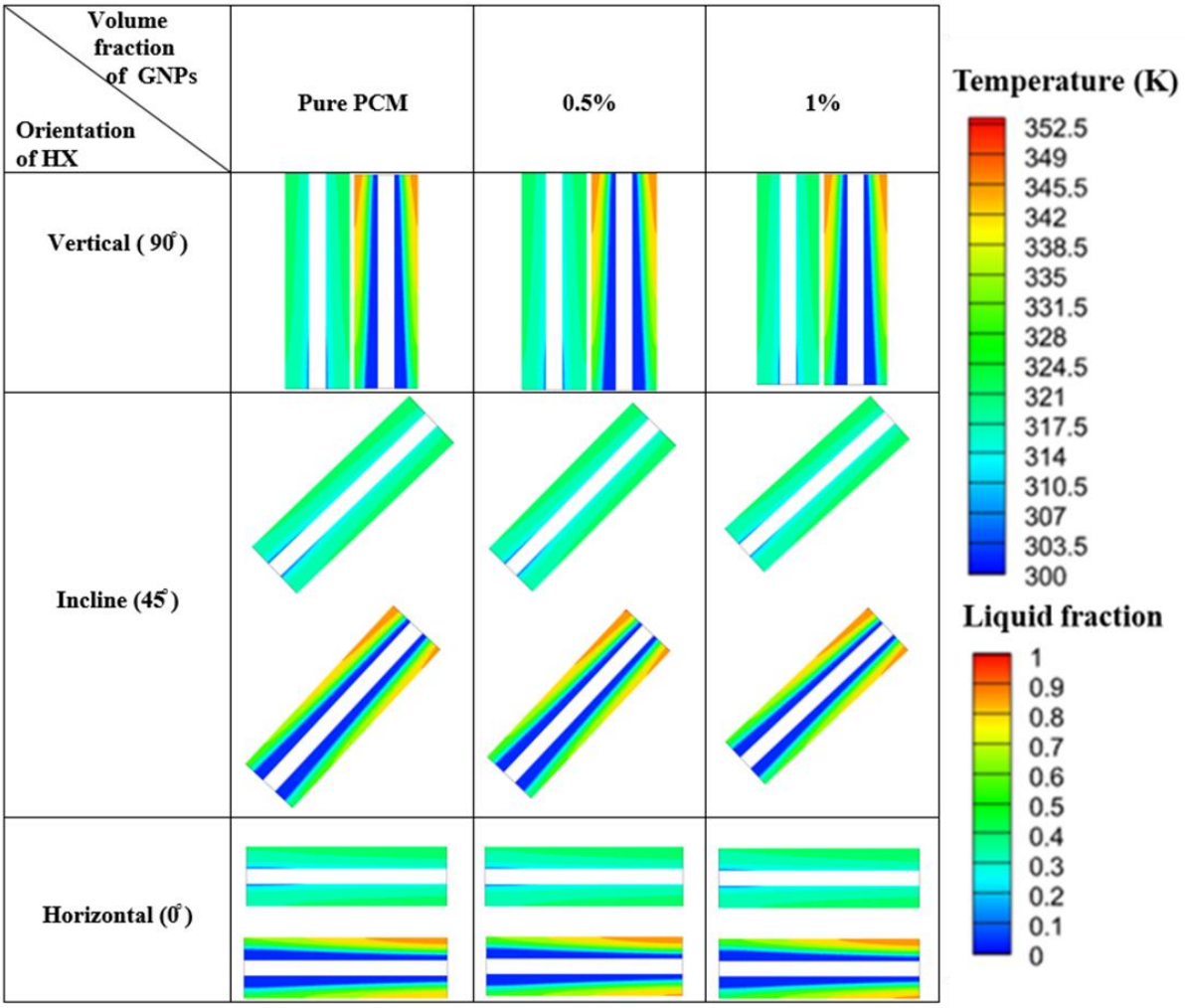

Fig 6.22 Temperature and melt fraction contours of 0.95 metal porosity heat exchanger at 1800 sec during solidification

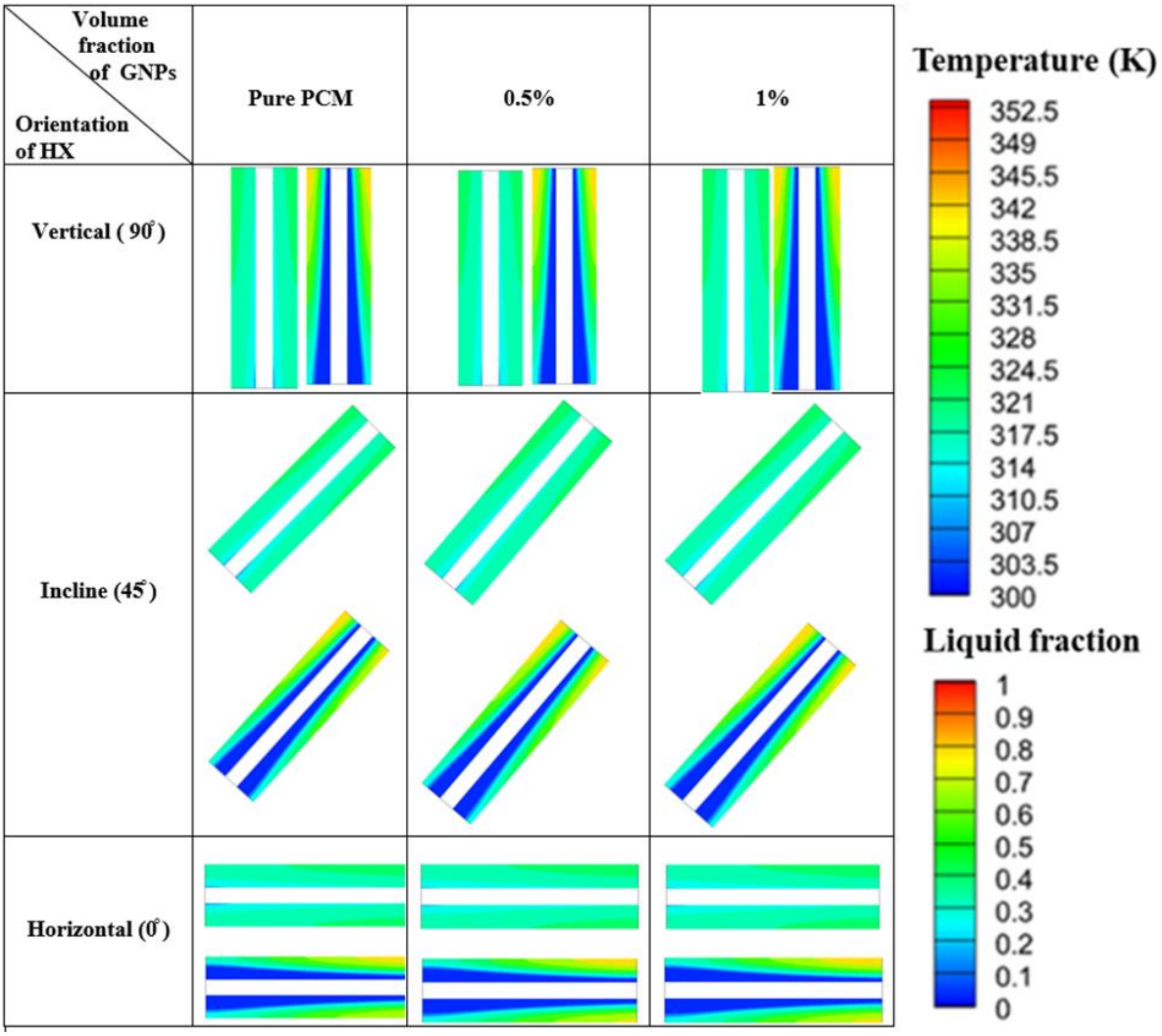

Fig 6.23 Temperature and melt fraction contours of 0.93 metal porosity heat exchanger at 1800 sec during solidification

6.4.2.2 Average Temperature

Figs.6.24, 6.25 and 6.26 displays the variation of average temperature with respect to time and till the end of the phase change process during solidification. During solidification trends of average temperature are the same as during melting, except that during solidification temperature is decreasing. Even in solidification decrease in temperature can be divided into three stages. This is because of the same mechanism of energy release as that of the melting process. The trend in the average temperature is noted to depend more on the metal foam porosity. It is due to an increase in the effective thermal conductivity with a decrease in the metal foam porosity. During the solidification process even in the

case of 0.97 porosity metal foam heat exchanger effect of GNP nanoparticles and orientation is insignificant. At the end of solidification, the maximum temperature of 306.73K is observed in pure PCM + 0.97 porosity metal foam LHSS positioned vertically, minimum temperate of 304.7K is noted 1% volume GNP+0.93 porosity metal foam LHSS inclined at 45°.

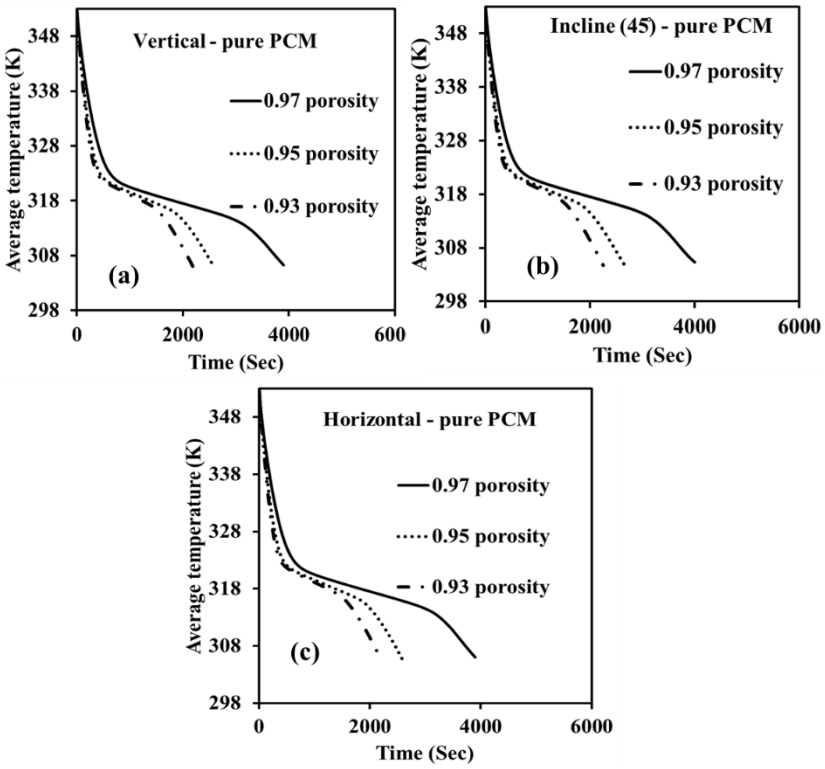

Fig 6.24 Average temperature evolution for pure PCM metal foam heat exchangers during solidification (a) vertical (b) incline (45°) and (c) horizontal

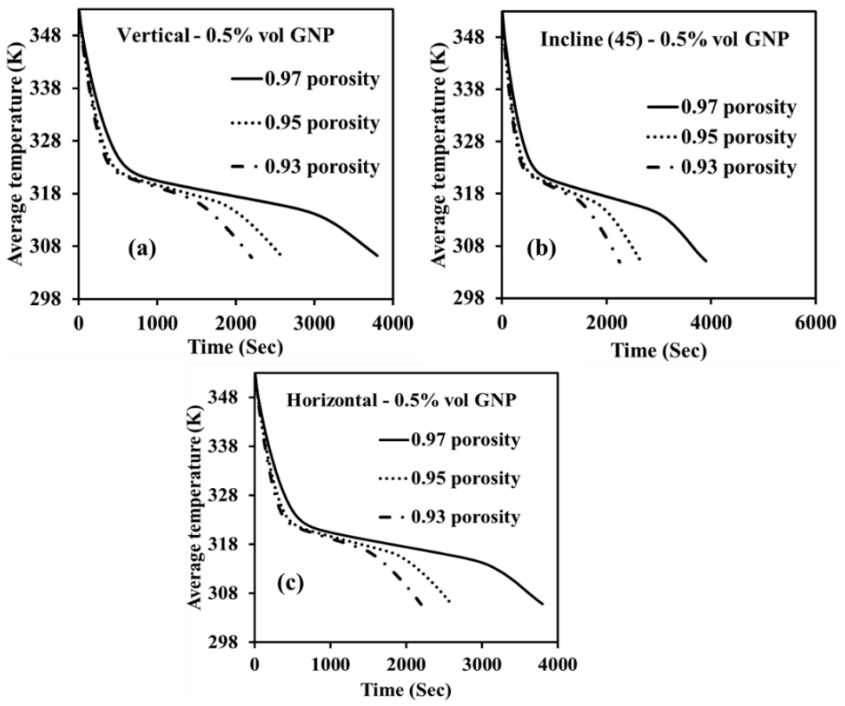

Fig 6.25 Average temperature evolution for 0.5% volumr GNP metal foam heat exchangers during solidification (a) vertical (b) incline (45°) and (c) horizontal

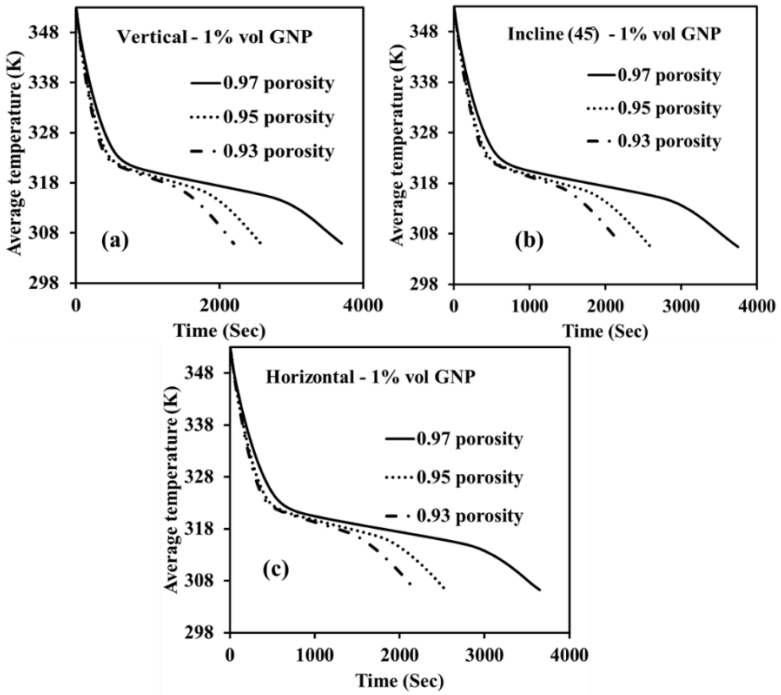

Fig 6.26 Average temperature evolution for 1% volume GNP metal foam heat exchangers during solidification (a) vertical (b) incline (45°) and (c) horizontal

6.4.2.3 Solidification time

Figs.6.27, 6.28 and 6.29 shows the solidification time taken for reduction of 0.25 melt fraction of 0.97, 0.95 and 0.93 metal foam porosity LHSS till the end of the phase change process during solidification. During the initial stage of solidification time to attain a melt fraction from 1 to 0.75 is higher than the time to attain a melt fraction from 0.75 to 0.5. This is because, during the initial stage of solidification, some amount of energy is released due to sensible heat, during which NEPCM releases energy without solidification. Further from a 0.5 melt fraction time taken to solidify for every 0.25 melt faction increases due to a drop in the temperature difference between HTF and the average temperature of the NEPCM. It can be noted that at all intervals of melting for a particular volume fraction of GNP nanoparticles and orientation of LHSS, solidification time is minimum for LHSS with 0.93 porosity metal foam LHSS. It can be noted that at all the intervals of solidification variation in the solidification time is more in the case of heat exchangers with 0.95 and 0.97 porosity metal foam LHSS than that of variation in the solidification time of heat exchangers with 0.95 and 0.93 porosity metal foam. This is because the rate of increase in the effective thermal conductivity of NEPCM from 0.97 porosity metal foam to 0.95 porosity metal foam is greater than 0.95 porosity metal foam to 0.93 porosity metal foam. A considerable variation in the rate of solidification is noted among the heat exchanger with 0.97 porosity metal foam with varying volume fractions of GNP nanoparticles, this indicates that the effect of GNP nanoparticles is felt only in the presence of metal foam with 0.97 porosity. In the case of 0.95 and 0.93 porosity metal foam heat exchangers, the increase in the effective thermal conductivity due to GNP nanoparticles is very less when compared with metal foam. Unlike in melting effect of orientation is not felt during the solidification process. During solidification, the maximum solidification time of 4000 seconds is observed in pure PCM + 0.97 porosity metal foam LHSS oriented at 45° and independent of volume fraction of GNP nanoparticles and ordination of LHSS, minimum melting time of around 2200 seconds is observed in 0.93 porosity metal foam LHSS. In comparison with pure PCM shell and tube heat exchanger which has minimum solidification time, a minimum of 85% and a maximum of 91.75% reduction in solidification time is noted.

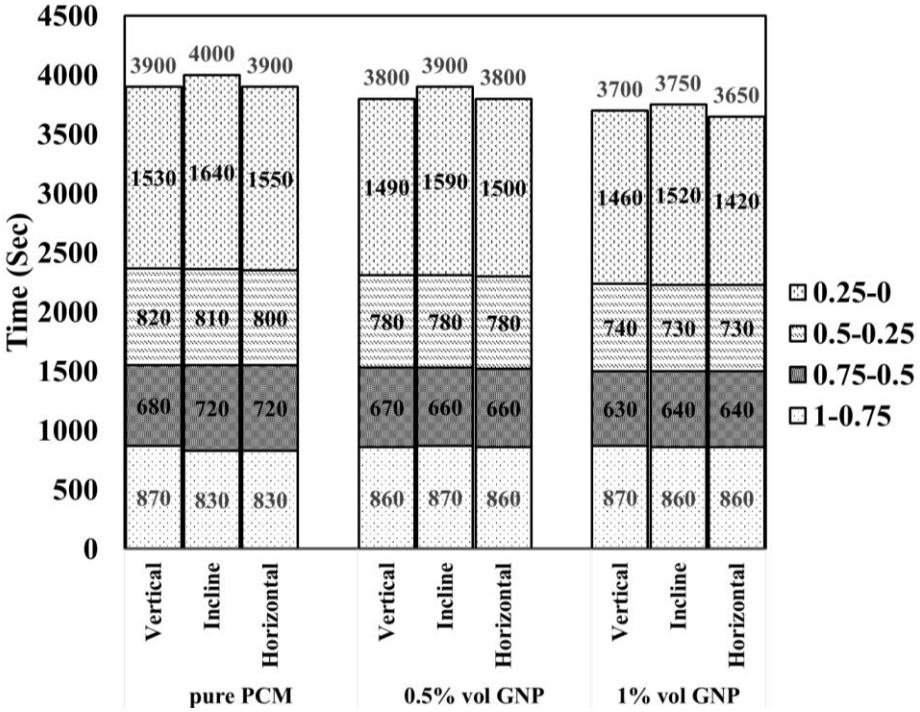

Fig 6.27 Time taken to reach melt fraction with an interval of 0.25 during solidification for 0.97 porosity metal foam LHSS

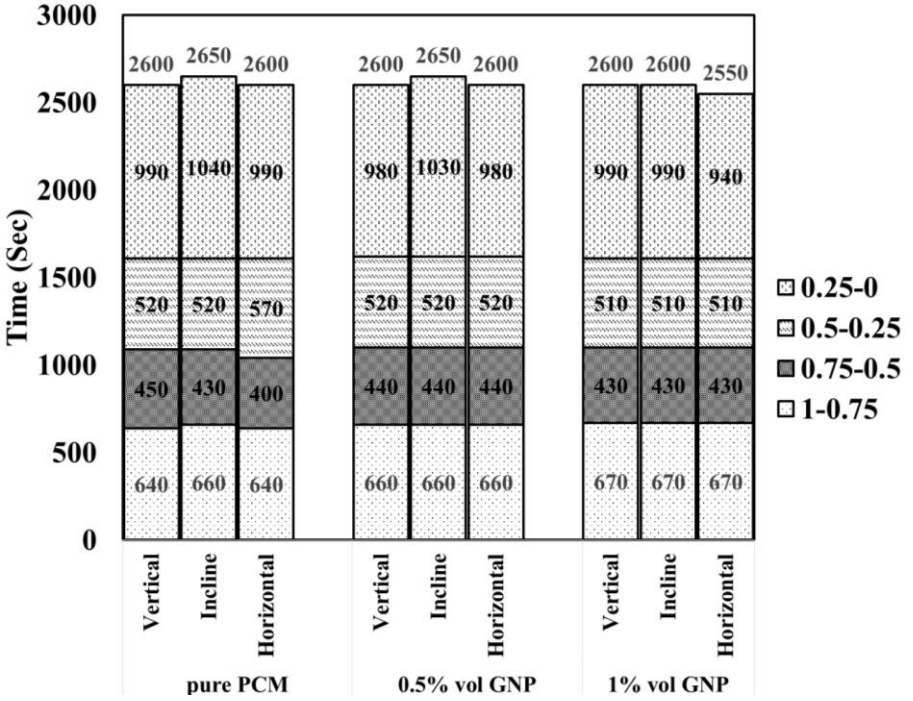

Fig 6.28 Time taken to reach melt fraction with an interval of 0.25 during solidification for 0.95 porosity metal foam LHSS

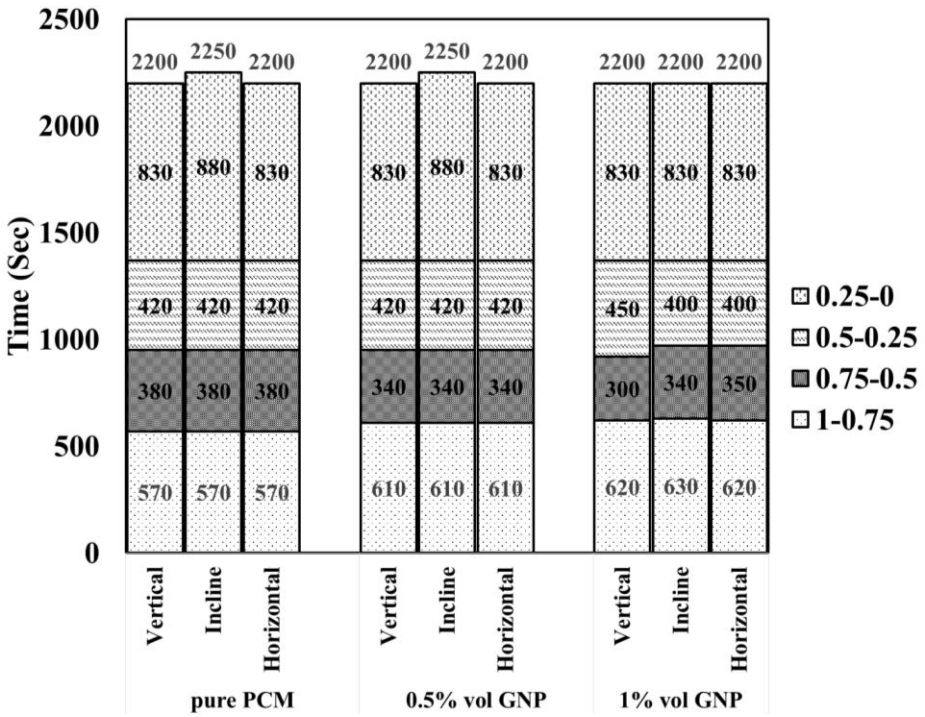

Fig 6.29 Time taken to reach melt fraction with an interval of 0.25 during solidification for 0.93 porosity metal foam LHSS

6.4.2.4 Energy release ratio

Figs.6.30, 6.31 and 6.32 displays the energy release ratio of pure PCM, 0.5% and 1% volume fraction GNP nanoparticles LHSS during solidification. It can be noted that the energy release ratio has a similar trend to the energy storage ratio. The three stages in energy release are the same as that during the melting i,e initial stage during which energy is released due to sensible heat capacity followed by energy release due to latent heat in the second stage and final stage energy is released due to sensible heat capacity. It is observed that variation in the rate of energy release ratio depends upon the porosity of the metal foam used. A minimum energy release ratio of 0.95 is observed in pure PCM + 0.97 porosity metal foam LHSS positioned vertically, maximum energy release ratio of 0.959 is noted in 1% volume GNP+0.93 porosity metal foam LHSS inclined at 45̊. In comparison with pure PCM shell and tube heat exchanger which has a maximum energy release ratio, a minimum reduction of 3.22% and a maximum reduction of 4.13% in energy release ratio is noted.

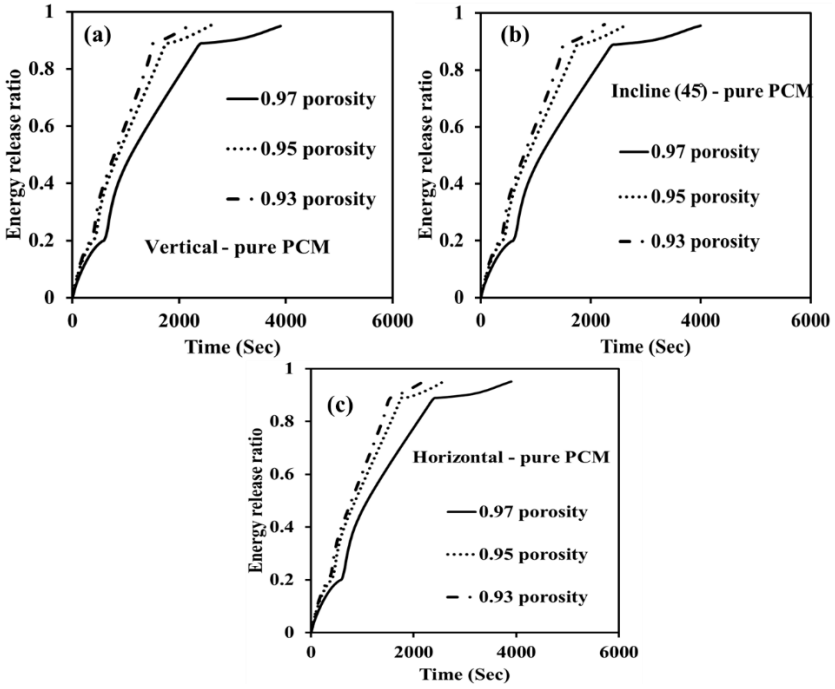

Fig 6.30 Energy release ratio of pure PCM metal foam heat exchangers during solidification (a) vertical (b) incline (45°) and (c) horizontal

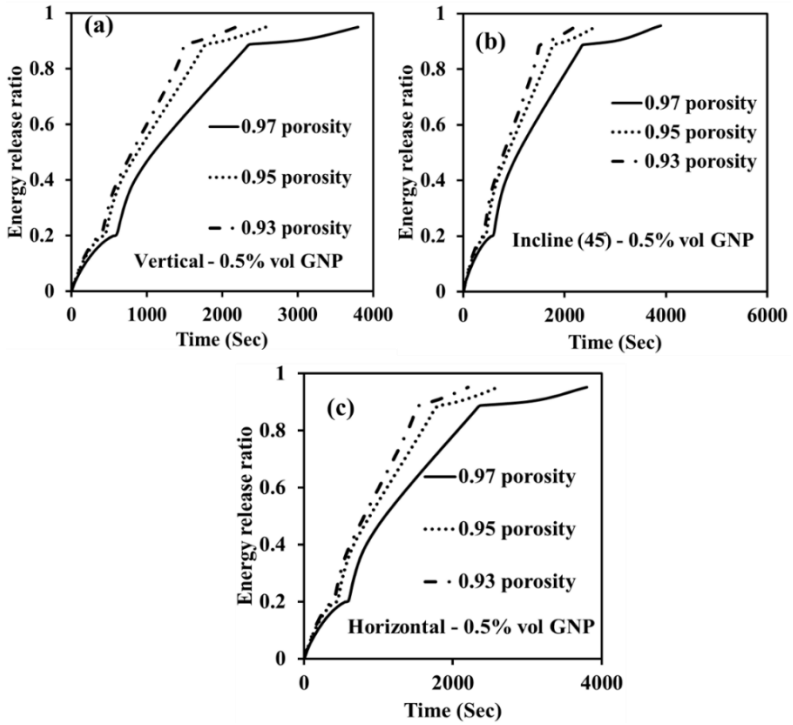

Fig 6.31 Energy release ratio of 0.5% volume GNP metal foam heat exchangers during solidification (a) vertical (b) incline (45°) and (c) horizontal

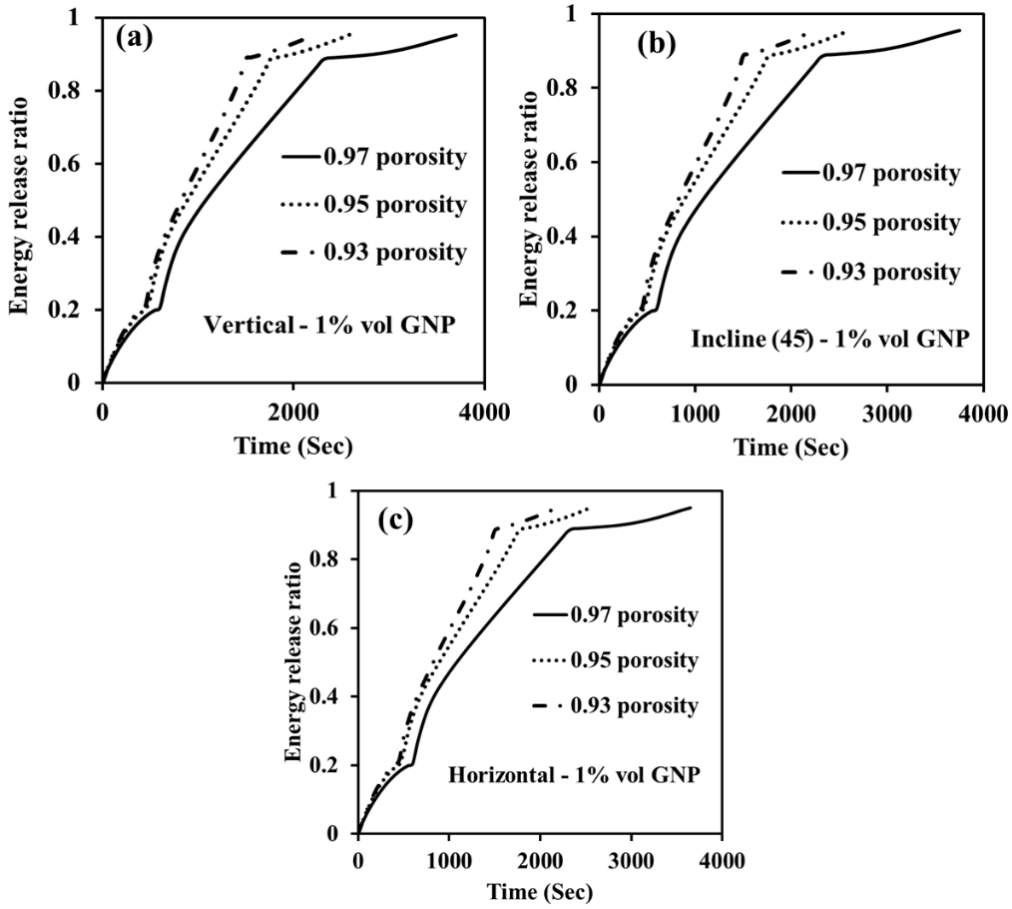

Fig 6.32 Energy release ratio of 1% volume GNP metal foam heat exchangers during solidification (a) vertical (b) incline (45˚) and (c) horizontal

6.4.2.5 Exergy efficiency

Figs.6.33, 6.34 and 6.35 displays the exergy efficiency of pure PCM, 0.5% and 1% volume fraction GNP nanoparticles LHSS during solidification. It can be noted that, unlike the variation in average temperature, melt fraction and energy release ratio trend of exergy efficiency during solidification is not similar to the exergy efficiency during melting. At the initial stage, exergy efficiency is high because the variation in entrance and exit temperatures of HTF is considerably large. As time progresses exergy efficiency decreases because NEPCM releases energy at a higher temperature when compared to HTF exit temperature, thus leading to exergy destruction. On further solidification exergy efficiency increases since NEPCM average temperature decreases at a slower rate than HTF outlet temperature decreases. It can be noted that in the heat exchangers with the same porosity of metal foam and volume fraction of GNP nanoparticles, a 45˚ oriented heat exchanger has

higher exergy efficiency. For the same orientation and volume fraction of GNP nanoparticles, a heat exchanger with 0.93 porosity metal foam has high exergy efficiency. During solidification, the maximum average exergy efficiency of 10.5% is observed in 1% volume GNP + 0.93 porosity metal foam LHSS oriented at 45° and the minimum average exergy efficiency of 4.13% is observed in pure PCM + 0.97 porosity metal foam LHSS oriented horizontally.

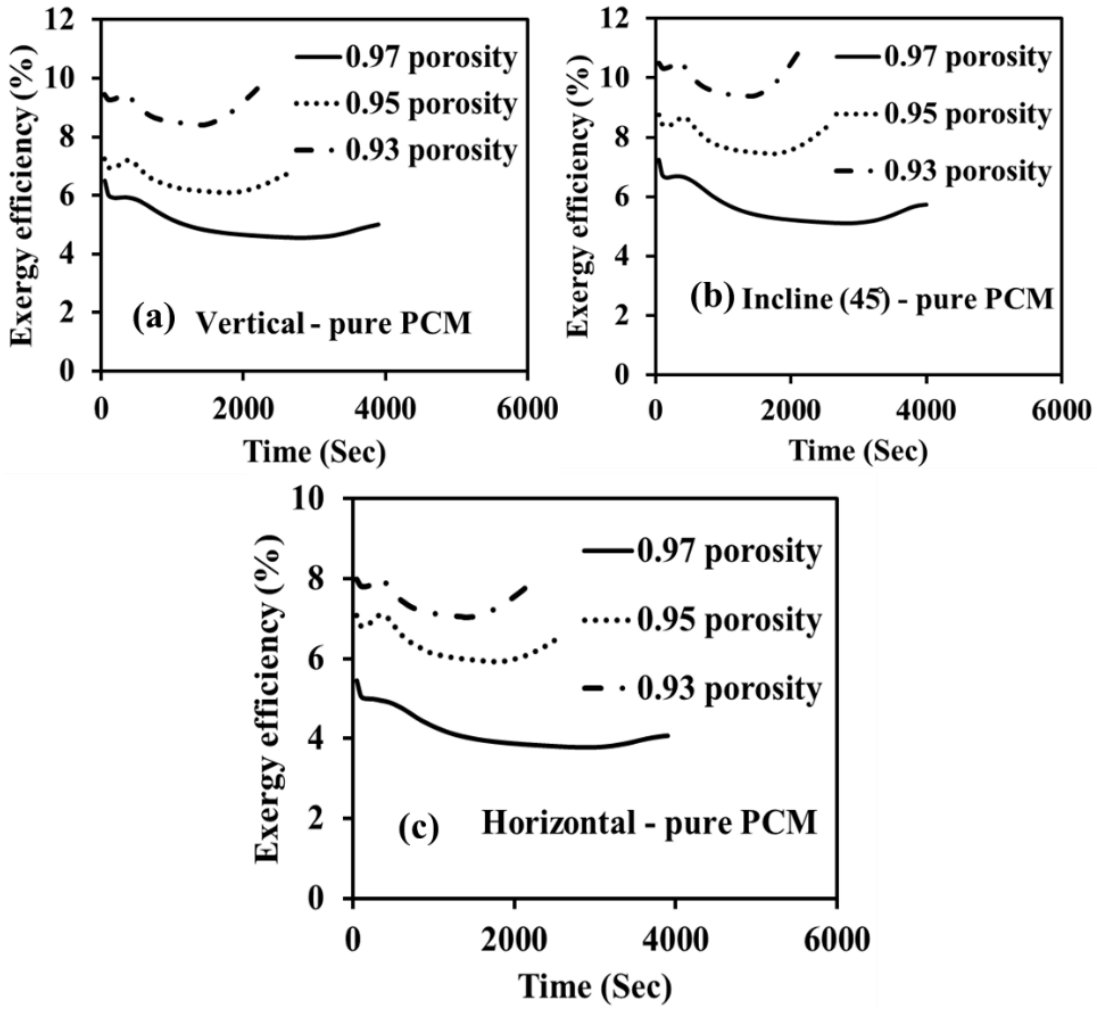

Fig 6.33 Exergy efficiency of pure PCM metal foam heat exchangers during solidification (a) vertical (b) incline (45°) and (c) horizontal

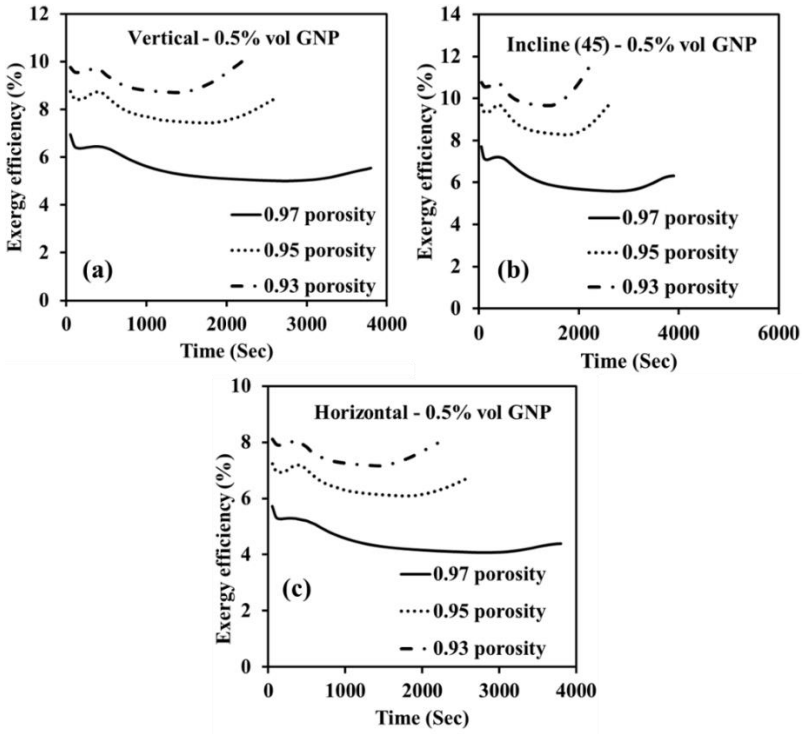

Fig 6.34 Exergy efficiency of 0.5% volume GNP metal foam heat exchangers during solidification (a) vertical (b) incline (45) and (c) horizontal

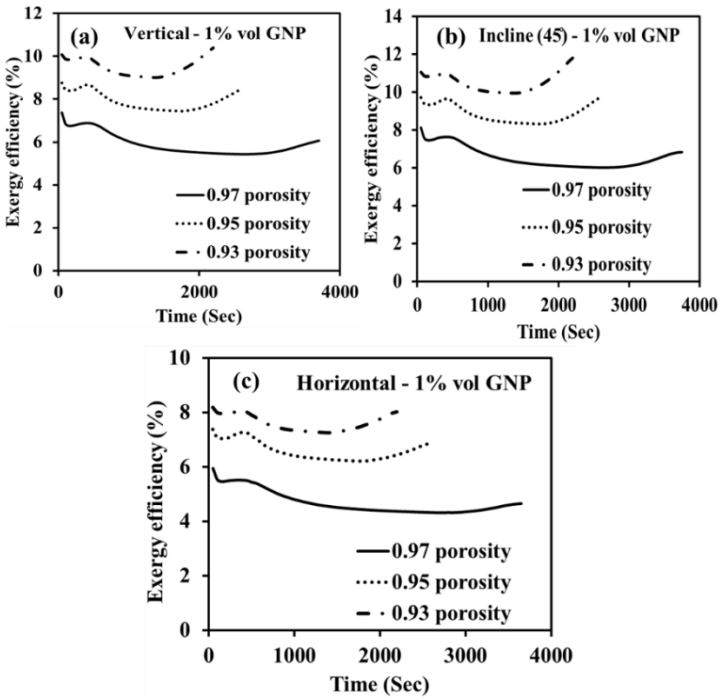

Fig 6.35 Exergy efficiency of 1% volume GNP metal foam heat exchangers during solidification (a) vertical (b) incline (45) and (c) horizontal

6.5 Closure

In the present study, numerical analysis of nanoparticles enhanced PCM shell and tube heat exchanger with copper metal foam is carried out considering orientation effect. Numerical analysis is carried out for both the melting and solidification process. The performance of the heat exchanger is compared by considering phase change time, energy effectiveness, and exergy efficiency during melting and solidification.

- A decrease in the porosity resulted in a decrease in both melting time and solidification time. The decrease in phase change time is more when compared with the variation in porosity of metal foam from 0.97 to 0.95 than the variation in porosity of metal foam from 0.95 to 0.93.
- The energy storage ratio and exergy efficiency during melting decreased with the decrease in the porosity of the metal foam.
- Exergy efficiency during solidification increased with a decrease in the porosity of metal foam. The orientation effect has also shown a significant effect on the exergy efficiency during solidification. 45° oriented heat exchangers have shown better exergy efficiency during solidification.
- Among the porosity of metal foam, the orientation of the heat exchanger and volume fraction of the nanoparticle's performance of the heat exchanger significantly depends upon the porosity of metal foam.
- Heat exchangers with 0.93 porosity metal foam and 1% volume GNP nanoparticles oriented at 45° have shown better performance than other heat exchangers considered.
- On comparison with pure PCM shell and tube heat exchanger which has minimum melting time, a minimum of 50.8% reduction in melting time on usage of pure PCM + 0.97 porosity metal foam LHSS oriented at 45° and a maximum of 78.32% reduction in melting time on usage of 1% volume GNP + 0.93 porosity metal foam LHSS oriented vertically is noted.
- On comparison with pure PCM shell and tube heat exchanger which has minimum solidification time, a minimum of 85% reduction in solidification time on usage of pure PCM + 0.97 porosity metal foam LHSS oriented at 45° and a maximum of 91.75% reduction in solidification time on usage of 0.93 porosity metal foam LHSS is noted.

- On comparison with pure PCM shell and tube heat exchanger which has maximum energy storage ratio, a minimum of 6.25% reduction energy storage ratio on usage of pure PCM + 0.97 porosity metal foam LHSS inclined at 45° and a maximum of 11.29% reduction in energy storage ratio on usage of 1% volume GNP + 0.93 porosity metal foam LHSS positioned vertically is noted.
- On comparison with pure PCM shell and tube heat exchanger which has maximum energy release ratio, a minimum of 3.22% reduction in energy release ratio on usage of pure PCM + 0.97 porosity metal foam LHSS positioned vertically and a maximum of 4.13% reduction in energy storage ratio on usage of 1% volume GNP+0.93 porosity metal foam LHSS inclined at 45° is noted.
- During melting the maximum average exergy efficiency of 54.13% is observed in pure PCM + 0.97 porosity metal foam LHSS oriented at 45° and the minimum average exergy efficiency of 46.28% is observed in 1% volume GNP + 0.93 porosity metal foam LHSS oriented vertically.
- During solidification, the maximum average exergy efficiency of 10.5% is observed in 1% volume GNP + 0.93 porosity metal foam LHSS oriented at 45° and the minimum average exergy efficiency of 4.13% is observed in pure PCM + 0.97 porosity metal foam LHSS oriented horizontally.

Chapter 7

Effect of cascaded metal foam on the thermal performance of latent heat storage system

7.1 Introduction

The usage of metal foam has shown a significant improvement in the melting and solidification of phase change materials (PCM). Studying the effect of cascaded metal foam can help in improving the performance of the latent heat energy storage systems (LHSS). On reviewing the literature, it is found that copper metal foam is the most commonly used metal foam to enhance the rate of heat transfer in LHSS. The present study analyses 0.97, 0.95 and 0.93 porosity copper metal foams cascaded in a radial and linear direction in shell and tube heat exchangers. Inclination studies on LHSS have shown contradicting results. Hence, the present chapter analyzes the influence of inclination on melting and solidification performance of radial and linearly cascaded metal foam in shell and tube heat exchangers.

7.2 Physical model

Geometric parameters of the heat exchanger are selected considering the optimized geometric parameters in the literature. Reviewing the literature on latent heat-based shell and tube heat exchangers [63] concluded that the tube-to-shell diameter should be nearly 0.25. Therefore, in the present work, this ratio is considered 0.254. The heat exchanger length, shell diameter and tube thickness are regarded as 250mm, 75mm, and 0.8mm, respectively. The arrangement of the cascaded metal foams is shown in Fig.7.1. [42] noted that varying volume flow rate of HTF has an insignificant effect on the performance of the heat exchanger due to which the volume flow rate of heat transfer fluid is taken constant and fixed at 1.4 LPM[29]. Compatibility studies of organic PCMs with different metals carried out by [133] revealed that stainless steel exhibited better compatibility with the PCM. So tube material is considered stainless steel. Since Lauric acid is suitable for heat storage applications, it is considered for the study. Copper is used as the metal foam material.

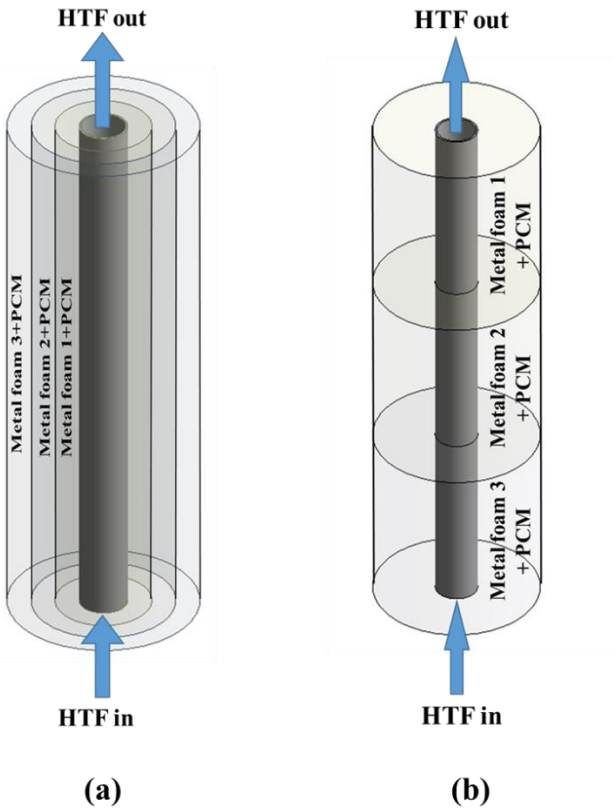

Fig 7.1 Schematic of (a) radial arrangement and (b) linear arrangement of metal foams in PCM heat exchanger

7.3 Numerical methodology

7.3.1 Validation

Non-thermal equilibrium approach is used to model the heat transfer interaction between NEPCM and metal foam. The finite volume method is considered for the computational domain. For pressure-velocity coupling, the PISO methodology is used. To handle the pressure PRESTO methodology is used and a second-order upwind scheme is used for the discretization of momentum and energy equations. The convergence criteria for continuity, momentum, and energy equations are kept as 10^{-6}, 10^{-6}, and 10^{-8} respectively. ANSYS FLUENT is used to solve the governing equations.

To verify the accuracy of the present numerical model, numerical results are compared with the experimental results of Zhao et al.[84] and with the numerical results of Mahdi et al.[123][136] .These results are presented in Figs.7.2 and 7.3. The maximum error is within the reasonable range.

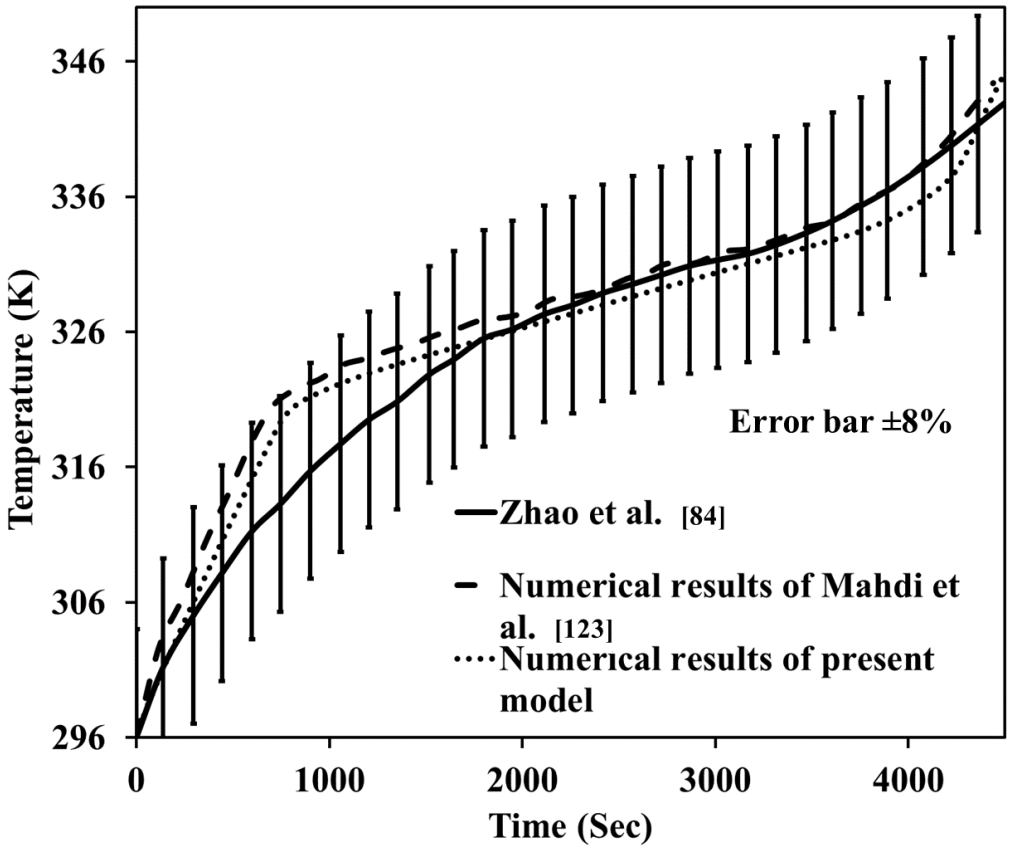

Fig 7.2 Numerical validation with experimental results of Zhao et al.[84]

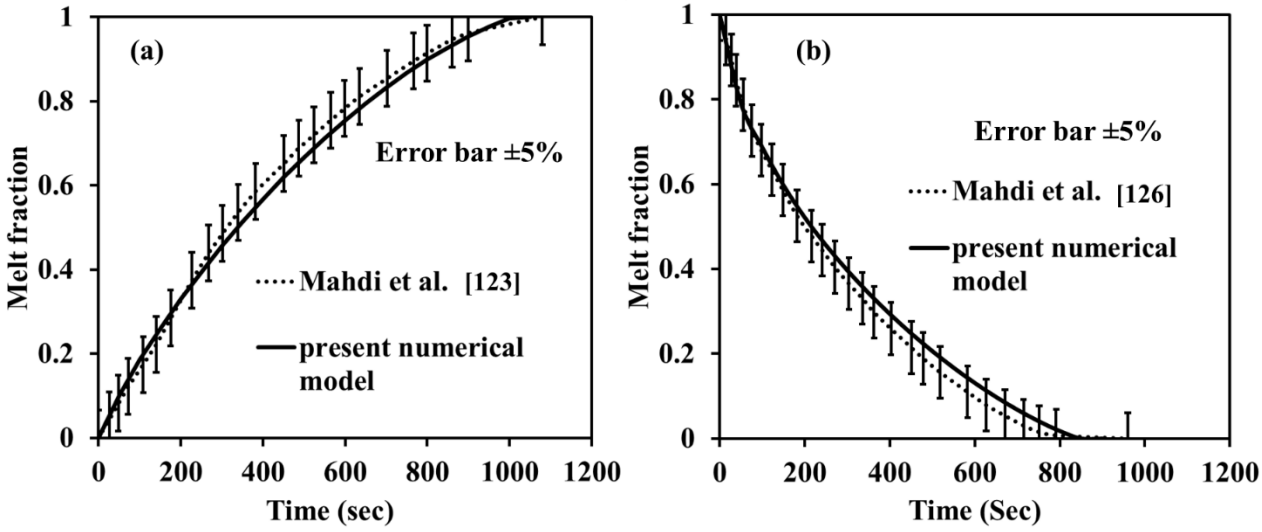

Fig 7.3 Numerical validation for (a) melting (b) solidification

7.3.2 Grid and time independence

Structured grids for radial cascaded and linear cascaded PCM shell and tube heat exchanger are created as shown in Fig 7.4. Grid and time independence studies are examined by considering the volume-average melt fraction of the PCM. The time steps used in time-independent studies are 0.3, 0.5, and 0.7 seconds. From Figs. 7.5(a) and 7.5(c), time independence is achieved at 0.5 sec for both radial and linear cascaded metal foam heat exchangers. Grid numbers considered in the radial cascade heat exchanger are 177062, 230642, and 352403. It can be noted from Fig. 7.5(b) grid independence is achieved for 230642 cells. Similarly, grid numbers for linearly cascaded metal foam heat exchanger are 138439, 188704, and 260819. It can be noted from Fig. 7.5(d) grid independence is achieved for 188704 cells.

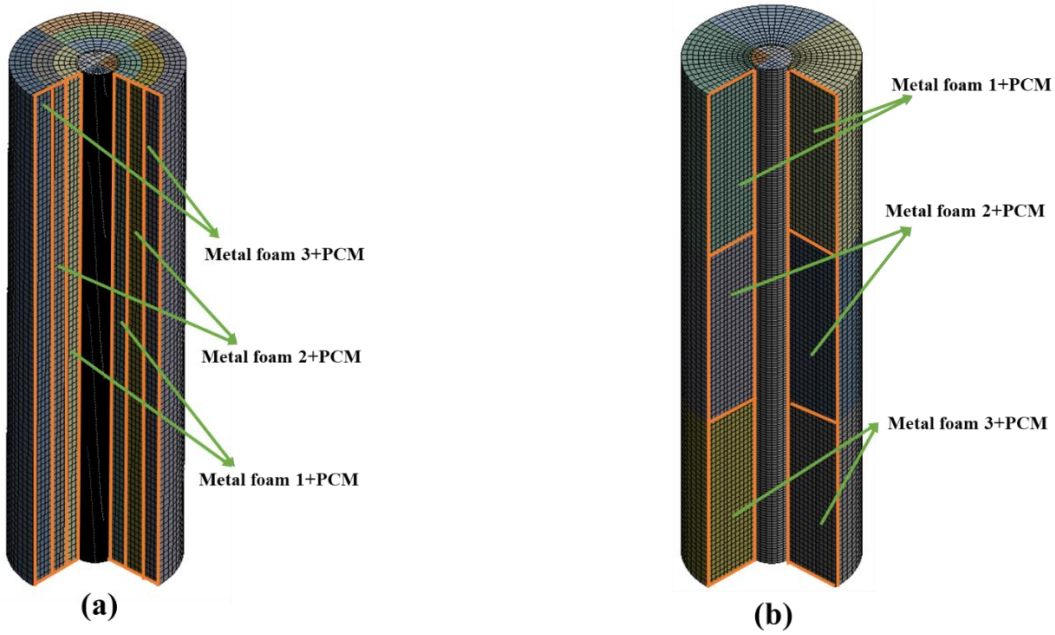

Fig 7.4 Grid for computational domains (a) radial arrangement of metal foam (b) linear arrangement of metal foam

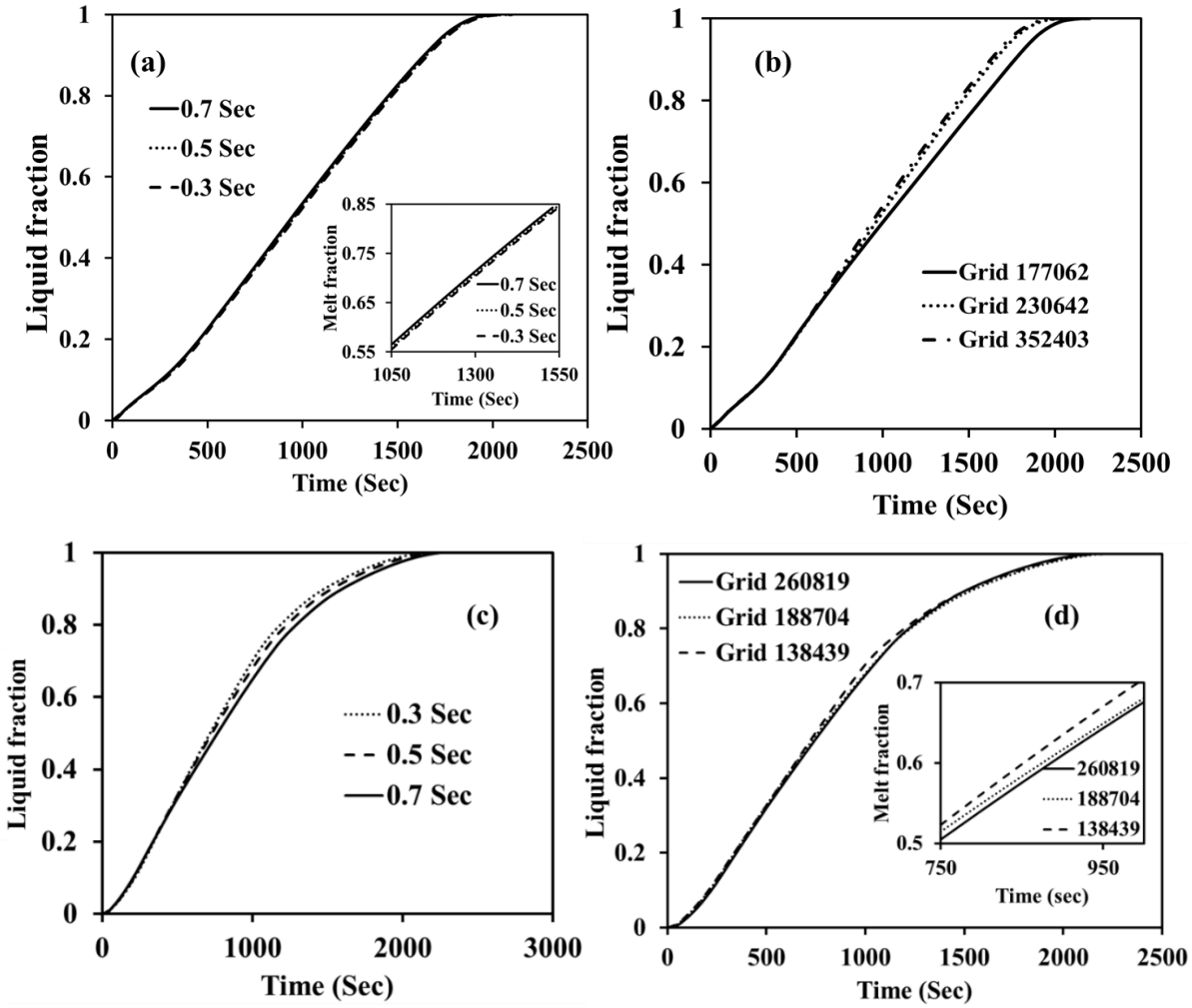

Fig 7.5 Time independence study (a) radial cascaded (c) linear cascaded; Grid independence study (b) radial cascaded (d) linear cascaded

7.4 Results and discussion

7.4.1 Melting

7.4.1.1 Temperature and melt fraction distribution

Figs.7.6 and 7.7 shows the temperature and melt fraction distribution contours of radial and linear cascaded metal foam LHSS at center planes during melting at 1200 sec. It is noted that in the case of the radial arrangement of metal foam, the maximum temperature near the HTF tube decreased when the metal foam with high porosity is placed adjacent to the HTF tube. The uniformity in temperature distribution increased from the bottom to top cross-section in all radially arranged metal foam heat exchangers. In the case of the linearly arranged metal foam heat exchangers, the maximum temperature is noted in the region of

the 0.93 porosity metal foam. This maximum temperature decreased with an increase in the porosity of the metal foam. In linearly arranged metal foam LHSS, more uniformity in temperature distribution is noted in the 0.93 porosity metal foam region, and this effect is reduced with an increase in the porosity of the metal foam. This behavior can be inferred from the increase in the effective thermal conductivity of PCM with a decrease in metal foam porosity. The effect of inclination could not be clearly inferred from the temperature distribution contours.

Melt fraction distribution gives more insight into the impact of cascaded metal foam on thermal transport. In the case of radial cascaded metal foam LHSS, melt fraction is more in the heat exchanger when 0.93 porosity metal foam is used near the HTF tube and observed to decrease with an increase in the metal foam porosity near the HTF tube. The decrease in thermal resistance with the reduction in the metal foam porosity near the HTF tube enables to transfer of more heat from the HTF to PCM. For a considered orientation of LHSS, the effective thermal resistance is lowest for radially cascaded 0.93-0.95-0.97 and highest for linearly cascaded 0.93-0.95-0.97 LHSS. For considered radially cascaded metal foam heat exchangers, the melt fraction at the top portion is more than the bottom portion, and this is due to the effect of natural convection. In the case of the linearly arranged metal foams, it can be noted that the melt fraction is more in the region of 0.93 porosity metal and less in the zone of the 0.97 porosity metal foam. The effect of orientation is clearly observed from melt faction contours. Due to natural convection hot liquid PCM tends to settle at the top portion of the LHSS, thus resulting in uneven melting along the radial direction. The trend of uneven melting increases with decreasing the orientation of the LHSS. The effect of natural convection is noted to be less in the region of 0.93 metal foam porosity and highest in the region of 0.97 porosity. This is because liquid PCM flow obstructions will be more in 0.93 metal foam porosity and less in 0.97 porosity metal foam.

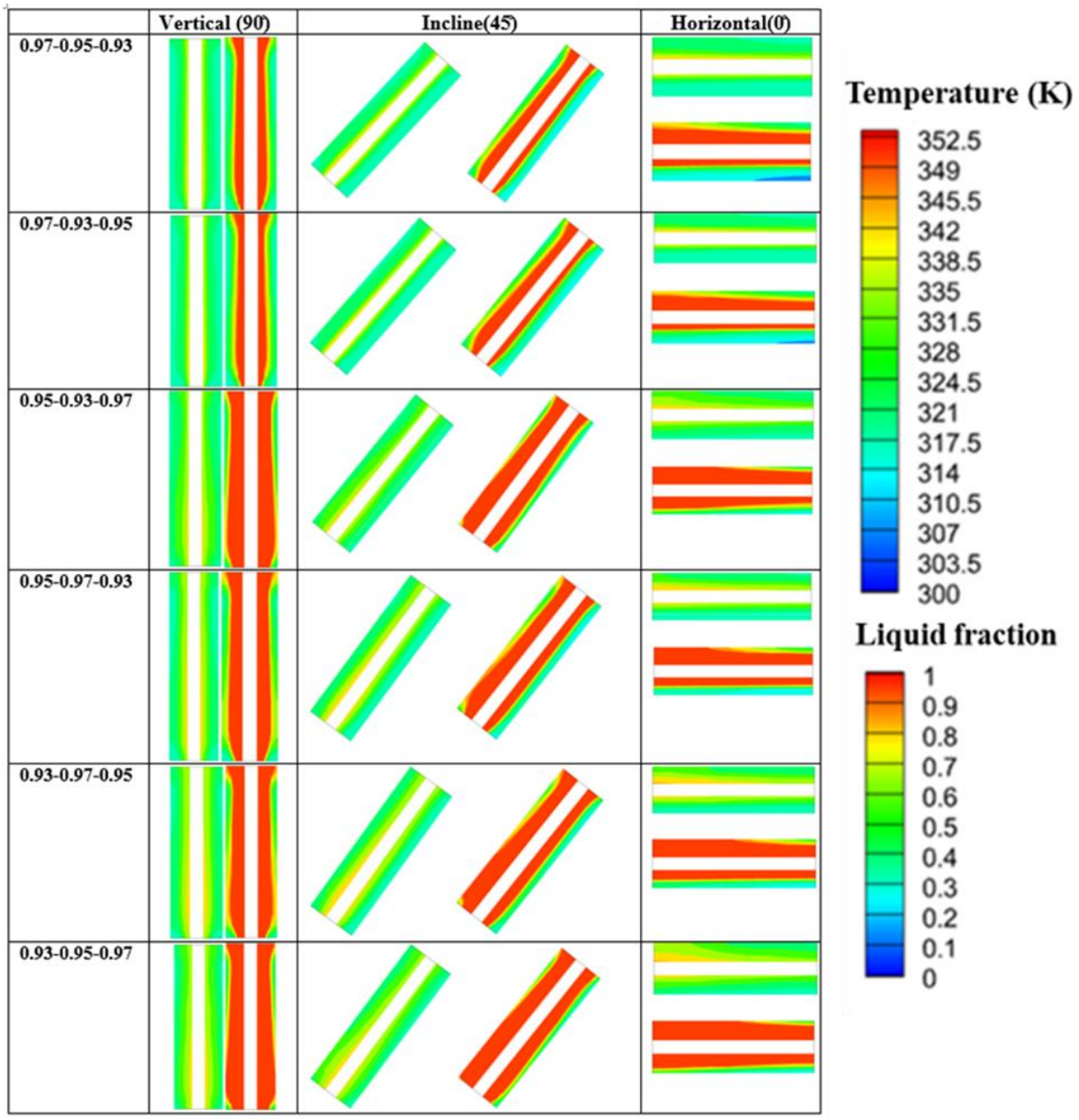

Fig 7.6 Temperature and melt fraction contours of radial cascaded metal porosity heat exchanger at 1200 sec during melting

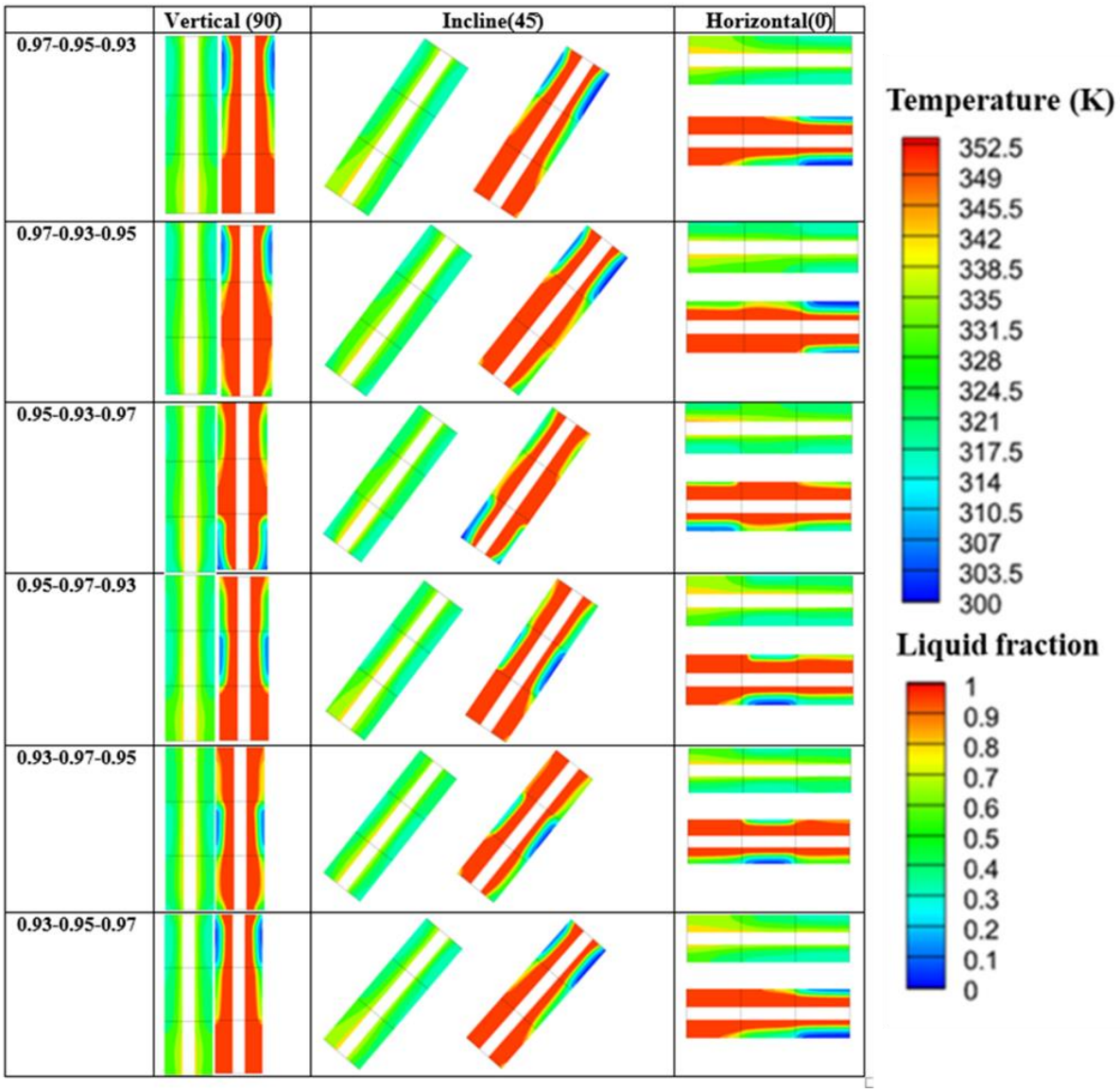

Fig 7.7 Temperature and melt fraction contours of linear cascaded metal porosity heat exchanger at 1200 sec during melting

7.4.1.2 Average temperature

Figs.7.8 and 7.9 illustrates the average temperature variation during melting in radial and linear cascaded metal foam LHSS. At the initial melting stage, a rapid temperature increase is observed. The increase in temperature can be referred to as the absorption of energy due to sensible heat. In the second stage, a decline in the rate of temperature can be observed as the energy is absorbed due to latent heat. At the third and final stage, a rapid temperature increase is noted because energy is again absorbed in the form of sensible heat. From Figs.7.8 and 7.9 for a particular LHSS, it can be noted that trends in average temperature

are independent of LHSS orientation. For radially cascaded metal foam heat exchangers, although the final average temperature is the same in all the cases, the variation in the rate of increase is due to the difference in their overall effective thermal resistance. The linearly cascaded metal foam can be noted to attain nearly the same average temperature. This behavior is observed as the thermal resistance does not vary in the radial direction for the linearly cascaded metal foam. Based on the variation of average temperature, it can be noted that heat transport is dominant in the radial direction. At the end of melting, the maximum average temperature of 347.5K is observed in linearly cascaded 0.95-0.93-0.97 porosity metal foam LHSS inclined at 45°, minimum average temperate of 333.3K is noted radial cascaded 0.95-0.97-0.93 porosity metal foam LHSS positioned vertically.

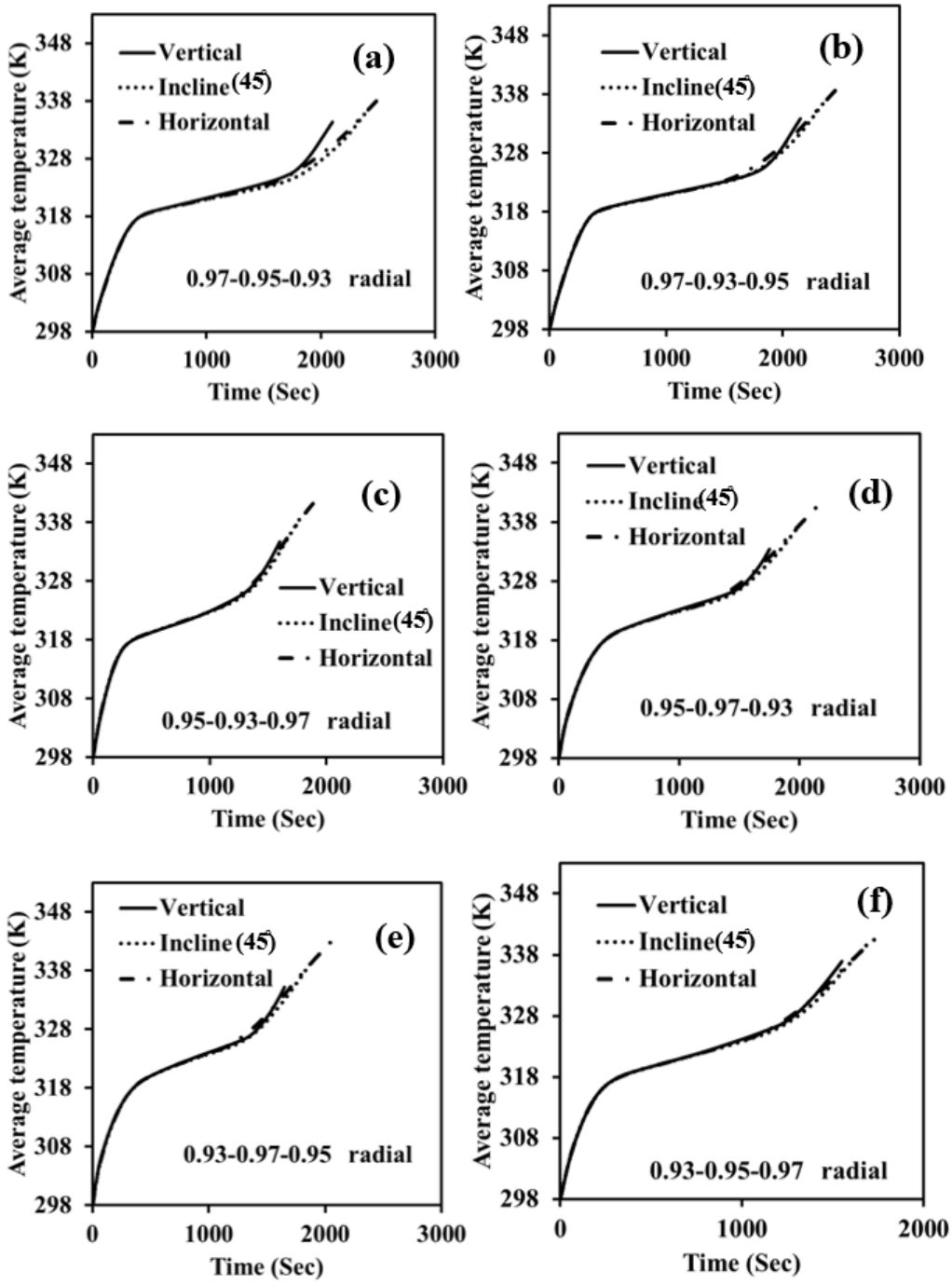

Fig 7.8 Average temperature evolution for radial cascaded metal foam heat exchangers during melting

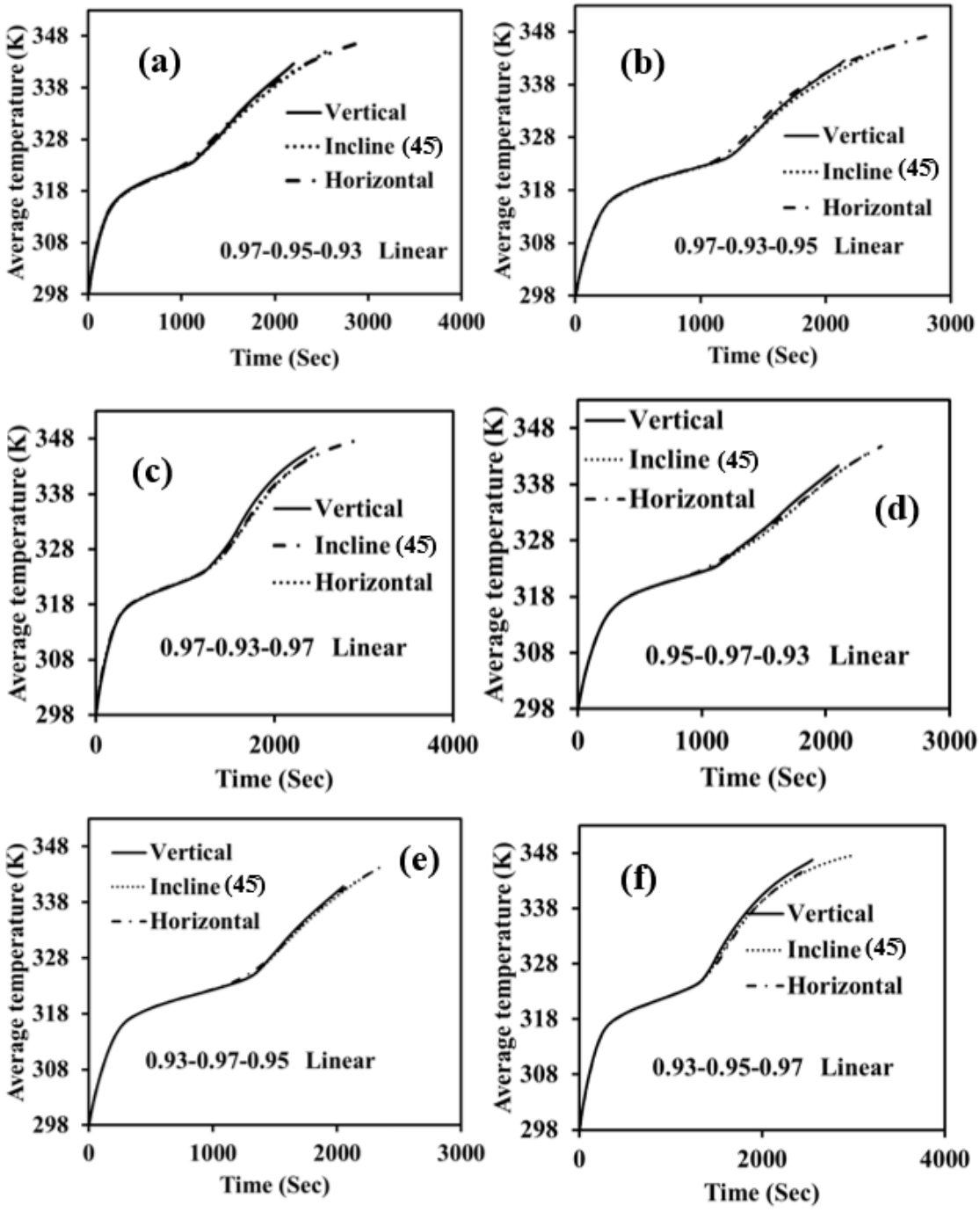

Fig 7.9 Average temperature evolution for linear cascaded metal foam heat exchangers during melting

7.4.1.3 Melting time

Figs.7.10, 7.11 and 7.12 illustrates the melting time for vertical (90°), incline (45°) and horizontal (0°) LHSS at an increment of 0.25 melt fraction until melting is complete. During the initial stage of melting, the time to reach a melt fraction from 0 to 0.25 is higher than the time to attain a melt fraction from 0.25 to 0.5. As energy is absorbed first in the form of sensible heat and after attaining the solidus temperature, the PCM starts melting, so the initial 0.25 melt fraction consumes more time when compared to the later part. Further, from 0.5 melt fraction time taken to melt every 0.25 melt fraction increased due to a decrease in the difference between HTF temperature and average PCM temperature. It can be noted that melting time is less in the case of radially cascaded metal foam heat exchangers, and the least melting time is noted for 0.93-0.95-0.97 metal foam LHSS, where the porosity of metal foam increased in the radial direction. In the case of linearly arranged porous media, although the PCM has melted in the region of 0.93 very early, the melting rate in the 0.97 porosity metal foam region is very low, resulting in an overall increase in the melting time. In radial cascaded LHSS for a considered heat exchanger, the least melting time is noted to be observed in vertically (90°) oriented heat exchanger and highest for horizontally (0°) oriented heat exchanger. In linearly cascade LHSS for a considered heat exchanger, the least melting time is noted to be observed in vertically (90°) oriented heat exchanger and highest for inclined (45°) oriented heat exchanger. During melting the maximum melting time of 3000 seconds is observed in linear cascaded 0.93-0.95-0.97 porosity metal foam LHSS oriented at 45° and a minimum melting time of 1550 seconds is observed in radial cascaded 0.93-0.95-0.97 porosity metal foam LHSS oriented vertically. In comparison with pure PCM shell and tube heat exchanger which has minimum melting time, a minimum of 53.88% and a maximum of 76.17% reduction in melting time is noted.

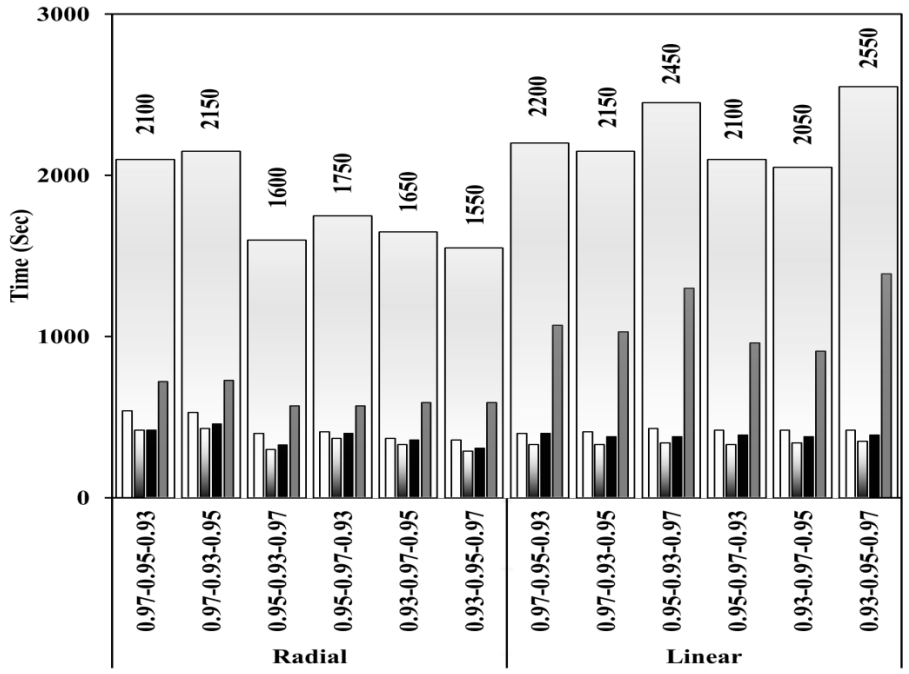

Fig 7.10 Time taken to reach melt fraction with an interval of 0.25 during melting for vertically oriented cascaded metal foam LHSS

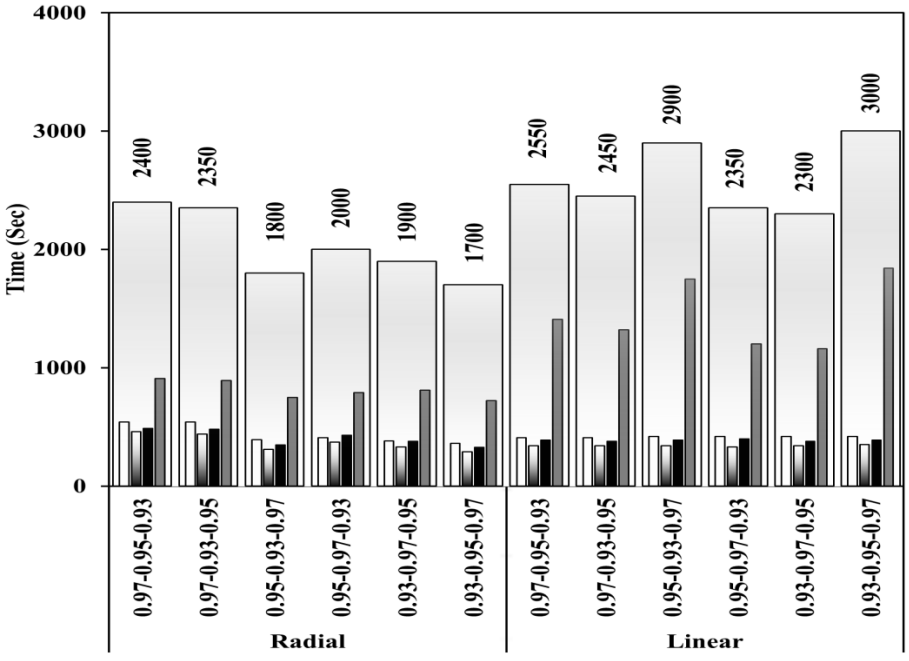

Fig 7.11 Time taken to reach melt fraction with an interval of 0.25 during melting for inclined (45°) cascaded metal foam LHSS

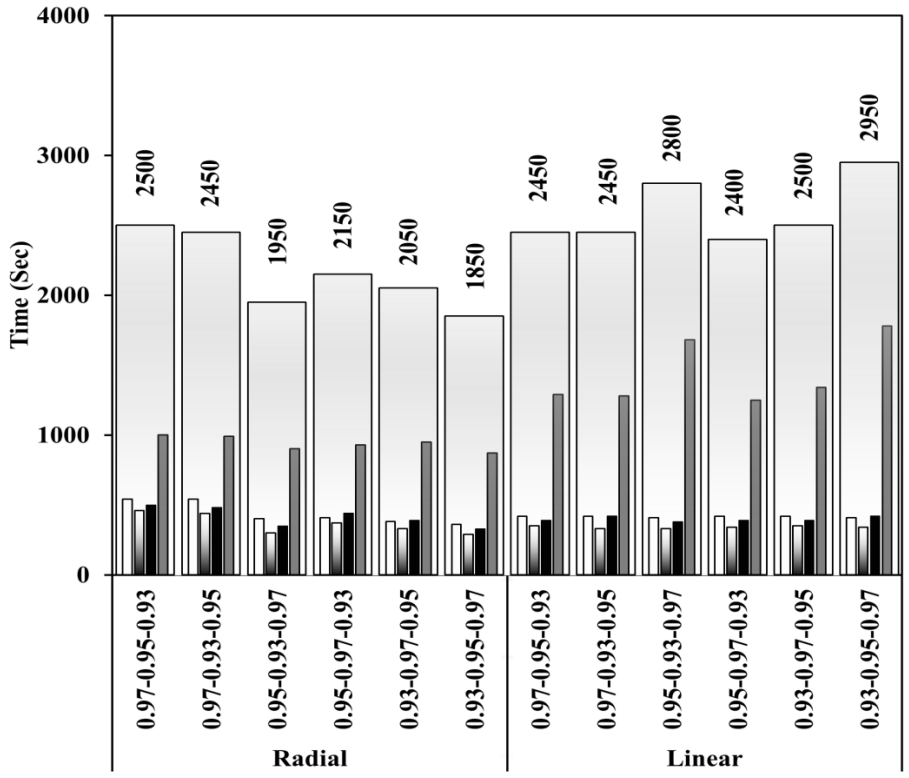

Fig 7.12 Time taken to reach melt fraction with an interval of 0.25 during melting for horizontally oriented cascaded metal foam LHSS

7.4.1.4 Energy storage ratio

Figs. 7.13 and 7.14 shows the energy storage ratio of radial and linear cascaded meal foam heat exchanger during melting. The energy storage ratio depends upon the average temperature of the LHSS, thus it can be observed that trend of the energy storage ratio follows the trend of average temperature. Similar to that of average temperature, the energy storage ratio can also be divided into three stages. The initial stage during which changes in temperature are very high for less energy absorbed. In the second stage, energy is stored due to latent heat capacity. During this stage rate of rise in the energy storage ratio is very high when compared to the other two stages, this can be noted from Figs. 7.13, 7.14 and 7.15. In the final stage again energy is stored due to specific heat capacity, as a result, the rate of energy storage ratio is reduced. The energy storage ratio is less in radial cascaded metal foam heat exchangers because the final average temperature is less in radial cascaded metal foam heat exchangers. It can be noted that the variation in energy storage ratio among the radial cascaded metal foam heat exchangers and linearly cascaded metal foam heat exchangers are less than 5% for the same orientation of heat exchanger; this is due to

less variation in the final average temperature among radial and linearly cascaded heat exchangers. This infers that the energy stored depends on the cascading type rather than the metal foam order. During melting the maximum energy storage ratio of 0.96 is observed in linearly cascaded 0.95-0.93-0.97 porosity metal foam LHSS inclined at 45° and the minimum energy storage ratio of 0.88 is observed in radial cascaded 0.95-0.97-0.93 porosity metal foam LHSS positioned vertically. In comparison with pure PCM shell and tube heat exchanger which has a maximum energy storage ratio, a minimum reduction of 3.22% and a maximum reduction of 11.29% in energy storage ratio is noted.

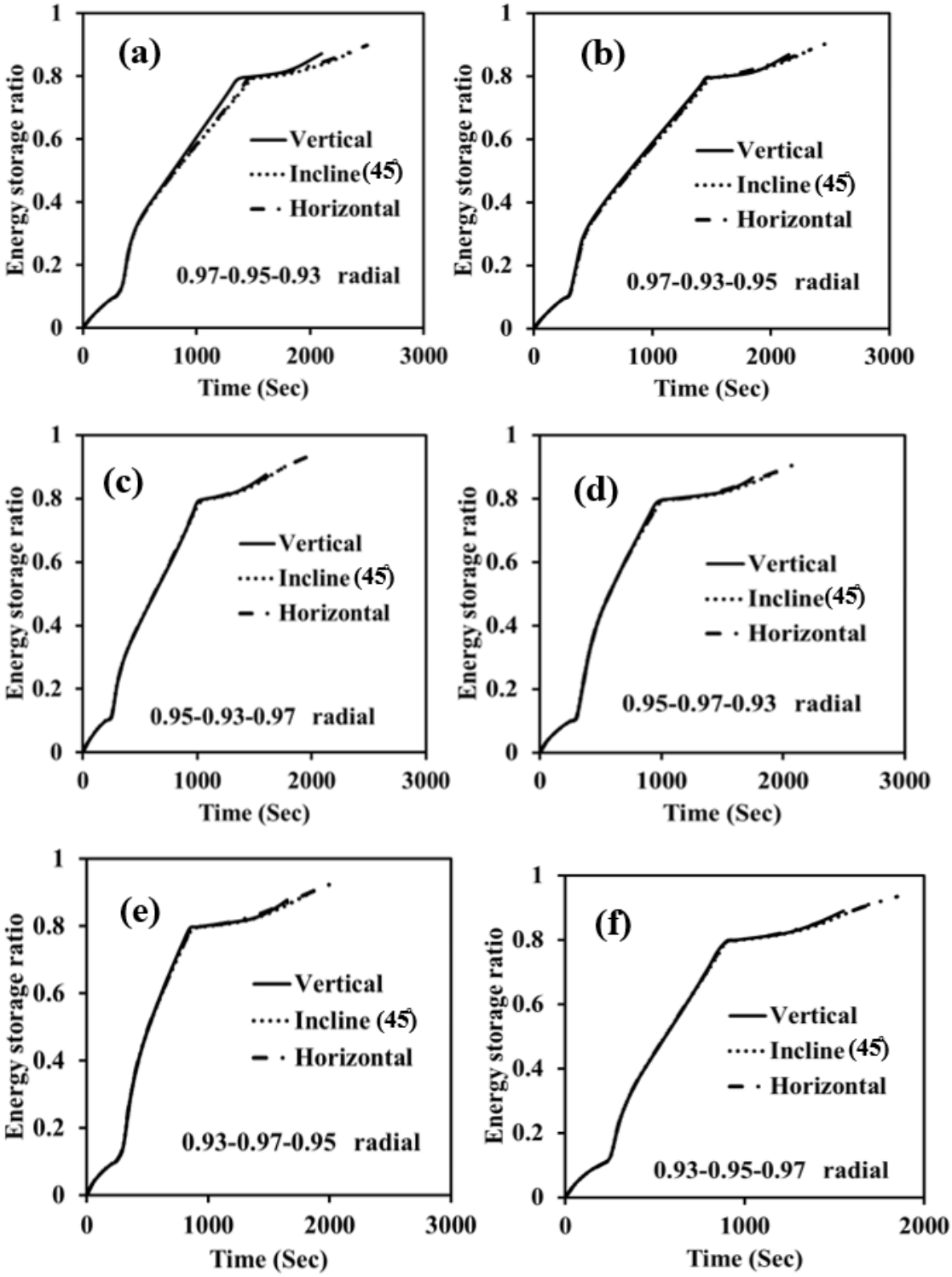

Fig 7.13 Energy storage ratio of radially cascaded metal foam heat exchangers during melting

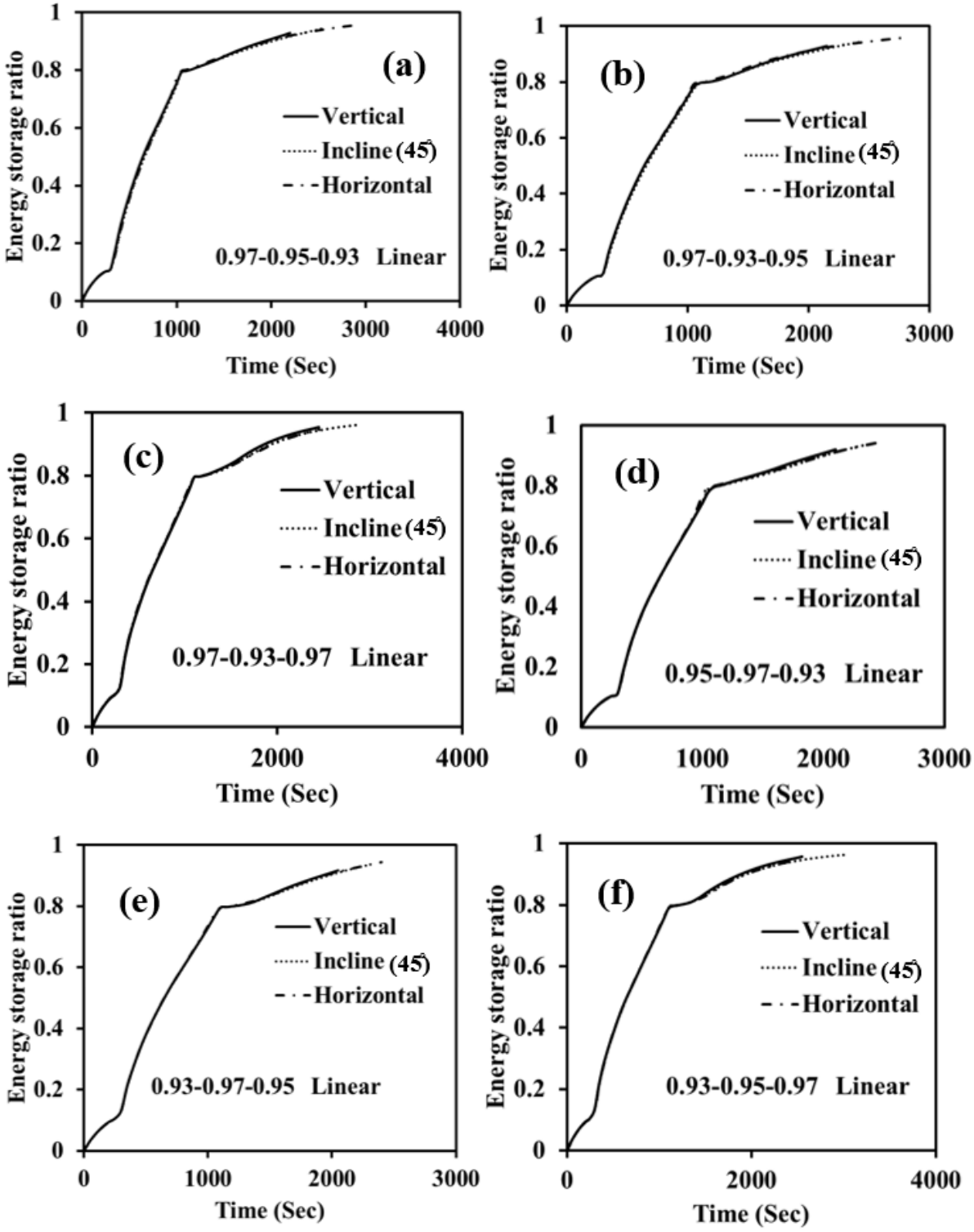

Fig 7.14 Energy storage ratio of linearly cascaded metal foam heat exchangers during melting

7.4.1.5 Exergy efficiency

Figs.7.15 and 7.16 displays the exergy efficiency of radial and linear cascaded LHSS during melting. Exergy efficiency relies upon the PCM average temperature, outlet and inlet temperature difference of the HTF. Since there is less temperature variation between the outlet and inlet of the HTF, the exergy efficiency depends primarily on the PCM's average temperature. Therefore with the increase in PCM average temperature, the exergy efficiency of the heat exchanger increases. From Figs.7.15 and 7.16, it can be viewed that the exergy efficiency of LHSS follows the same trend as the average temperature of PCM. During melting the maximum average exergy efficiency of 62.31% is observed in linearly cascaded 0.93-0.97-0.95 porosity metal foam LHSS oriented at 45° and the minimum average exergy efficiency of 45.04% is observed in radial cascaded 0.97-0.93-0.95 porosity metal foam LHSS oriented vertically.

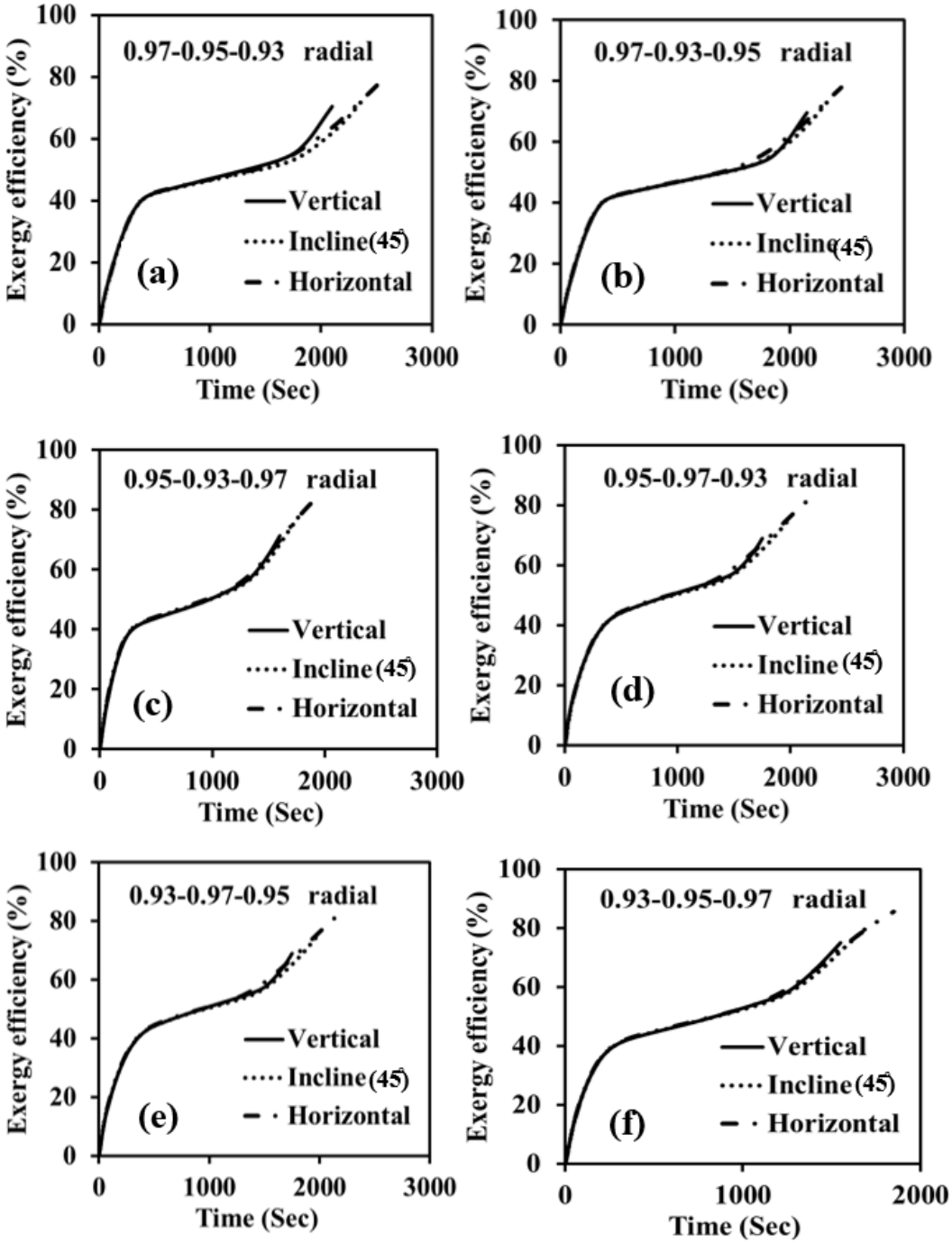

Fig 7.15 Exergy efficiency of radially cascaded metal foam heat exchangers during melting

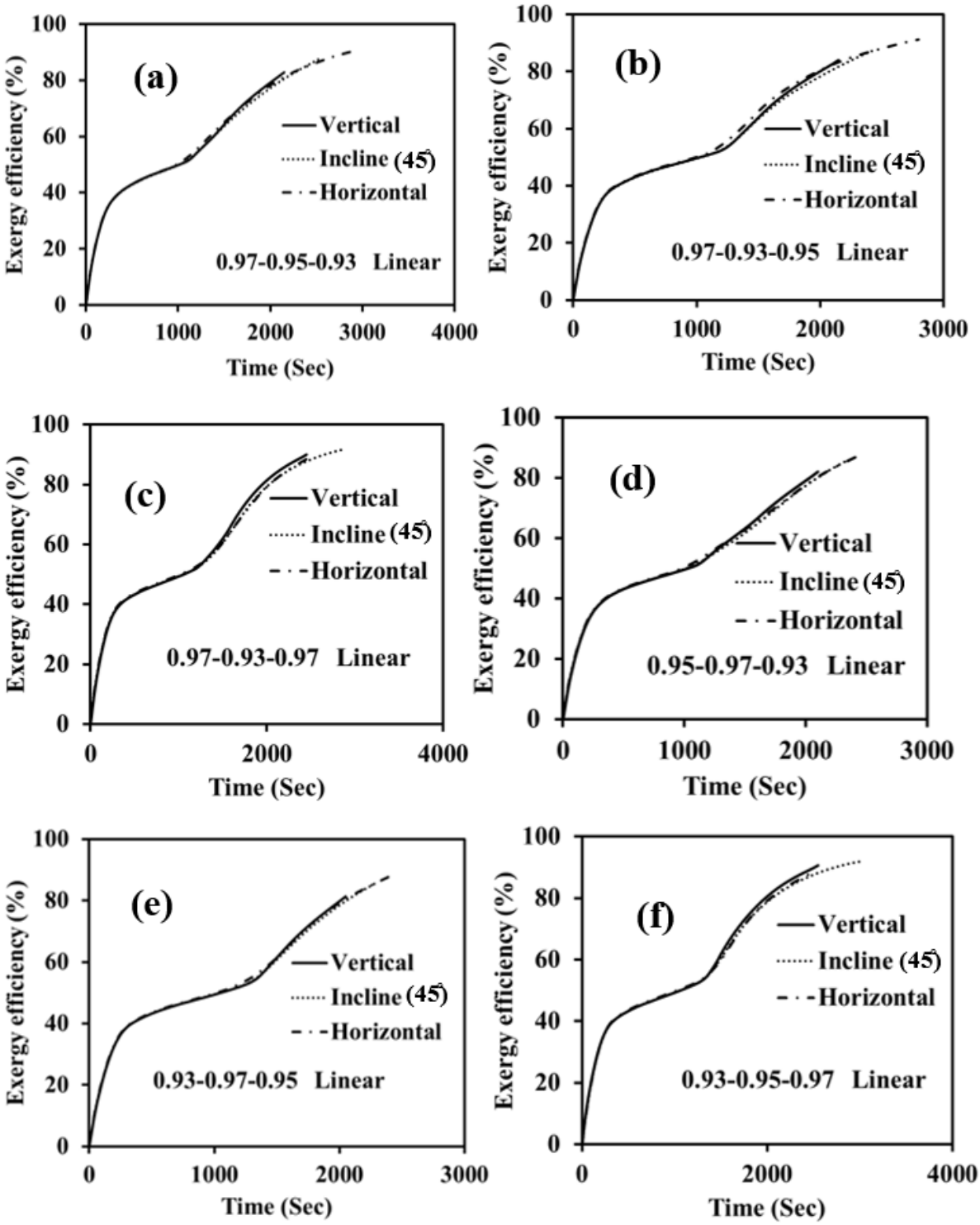

Fig 7.16 Exergy efficiency of linearly cascaded metal foam heat exchangers during melting

7.4.2 Solidification

7.4.2.1 Temperature and melt fraction distribution

Figs.7.17 and 7.18 show the temperature distribution contours of radial and linear metal foam cascaded LHSS at the center plane of the heat exchanger during solidification at 1800 sec. During solidification, the initial temperature of the PCM is considered 353 K, and the HTF at 298 K is made to flow through the tube. Fig.7.17 shows that the temperature is lower for the arrangement with less porosity near the tube. In the case of the linearly arranged metal foam heat exchanger, the temperature contours follow a similar trend and need further investigation to understand the influence of metal foam arrangement along the length of the heat exchanger. For the considered cases, the uniformity in temperature distribution increased from the bottom to the top cross-section. Also, due to a larger temperature gradient between the HTF inlet and PCM at the bottom, a lower temperature is observed at the bottom sections. As this gradient decreases along the length of the heat exchanger, more uniformity is observed in the upper section. The effect of inclination could not be clearly inferred from the temperature distribution contours.

Melt fraction distribution from Figs.7.17 and 7.18 gives more insight into the effect of cascaded metal foam. From the figure, a non-uniformity in melt fraction distribution to the temperature distribution can be noted. In the case of radial cascaded metal foam, melt fraction is less in a heat exchanger with 0.93 porosity metal foam near the HTF tube, and this increased with the increase in the porosity of metal foam near the HTF tube. Due to less thermal resistance near the HTF tube, more heat is transferred from the PCM to the HTF. In all radial cascaded metal foam heat exchangers, the melt fraction at the top portion is more than the bottom portion due to the settlement of the hot PCM at the top portion of the heat exchanger due to buoyancy force. In the case of the linearly arranged metal foams, it is noted that the melt fraction is less in the region of 0.93 porosity metal foam and more in the region of 0.97 porosity metal foam. The increase in effective thermal conductivity with the decrease in porosity improved thermal transport and decreased melt fraction. Although the solidification process is conduction-dominant, the effect of orientation can be noted from melt fraction contours due to the settlement of hot PCM on the top portion of the heat exchanger. Since solidification is conduction-dominant, uneven solidification along the radial direction is very less than uneven melting. The trend of uneven

solidification increased with decreasing the orientation of the LHSS and an increase in the metal foam porosity.

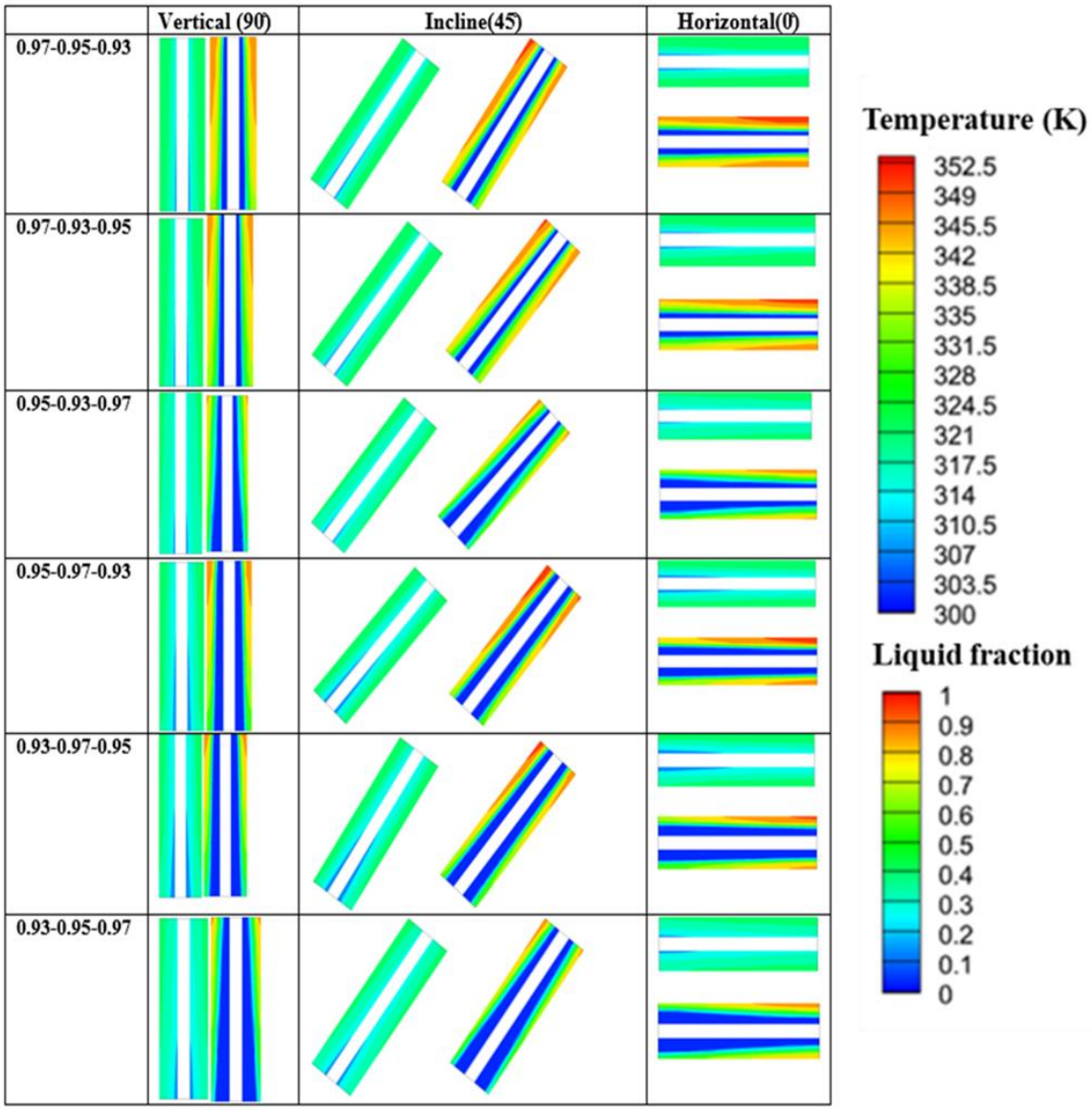

Fig 7.17 Temperature and melt fraction contours of radial cascaded metal porosity heat exchanger at 1800 sec during solidification

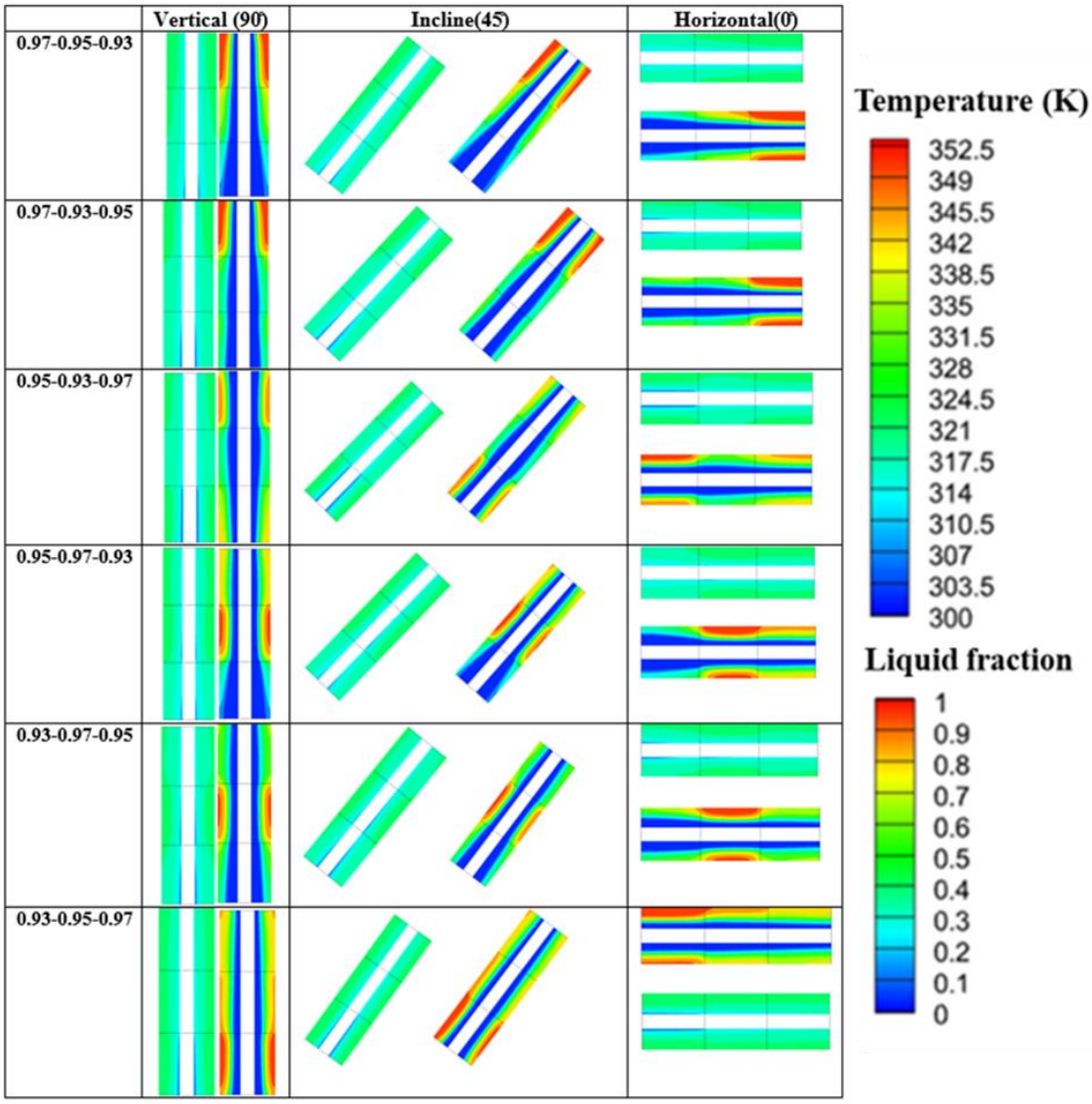

Fig 7.18 Temperature and melt fraction contours of linear cascaded metal porosity heat exchanger at 1800 sec during solidification

7.4.2.2 Average temperature

Figs.7.19 and 7.20 illustrates the average temperature variation of radial and linear cascaded metal foam LHSS with respect to time. During solidification, the trends for average temperature variation are similar to that of melting. The difference is that during the solidification, temperature decreases. For solidification, the temperature decrease can be divided into three stages, similar to the melting process. This is because of the same energy release mechanism as in the melting process. In all the heat exchangers' effect of orientation is not felt until the second stage of solidification. During the final stage of solidification, the hot PCM which is settled at the top gets solidified. This amount of PCM

varies with inclination, thus resulting in variation in average temperature with the orientation of the heat exchanger. At the end of solidification, the maximum temperature of 308K is observed in radial cascaded 0.97-0.93-0.95 porosity metal foam LHSS positioned horizontally, minimum temperate of 302.38K is noted in linearly cascaded 0.93-0.97-0.95 porosity metal foam LHSS inclined at 45°.

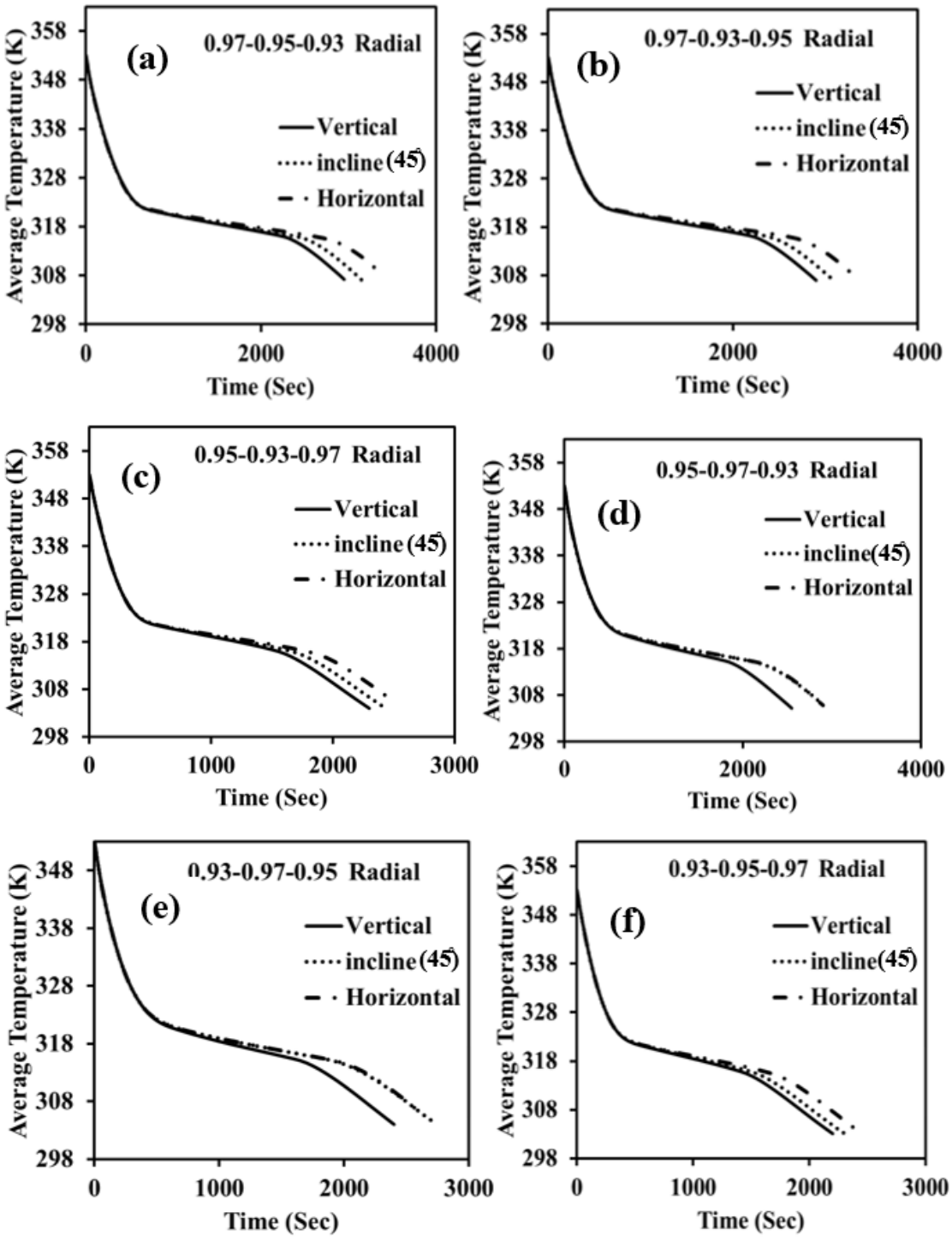

Fig 7.19 Average temperature evolution for radial cascaded metal foam heat exchangers during solidification

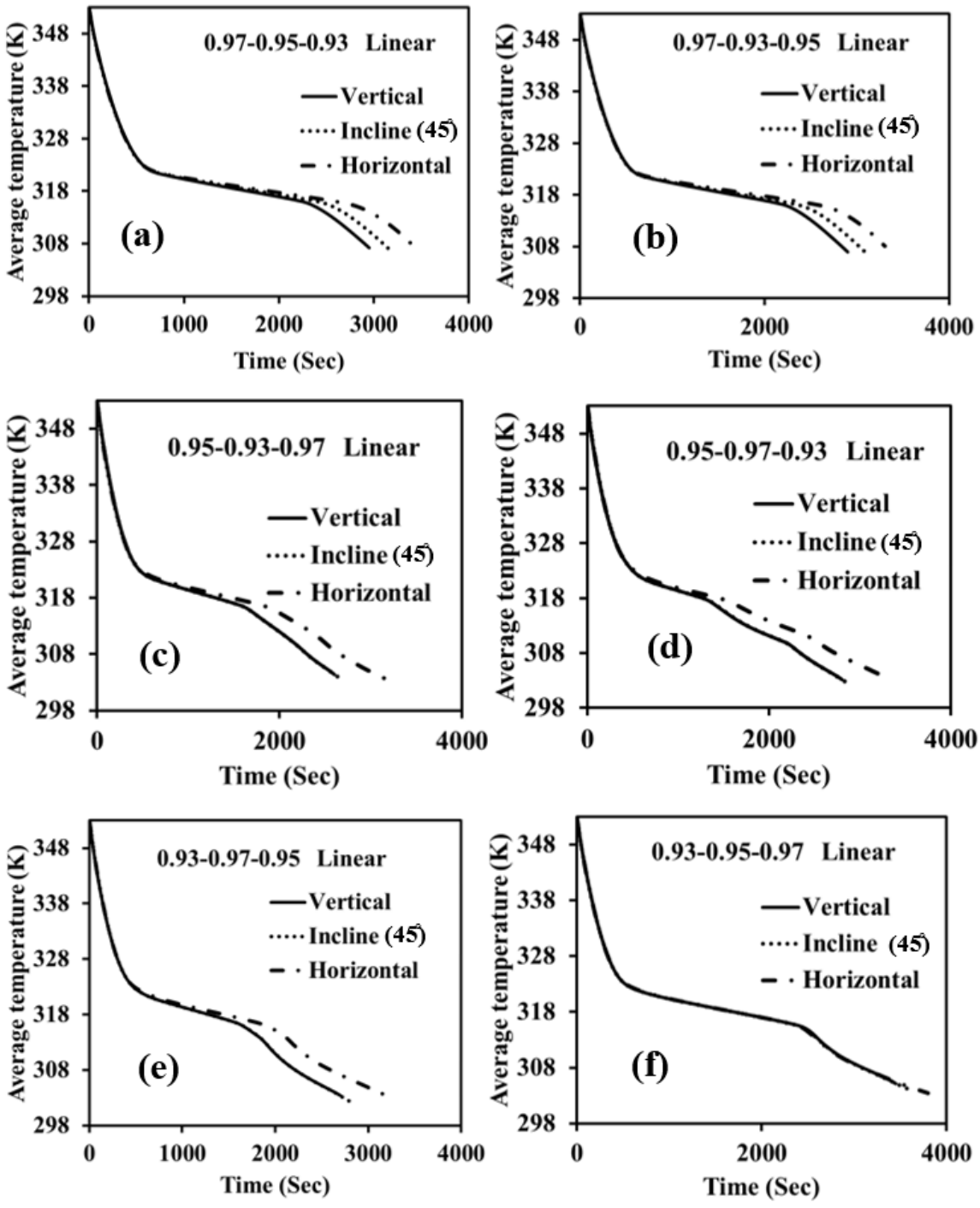

Fig 7.20 Average temperature evolution for linear cascaded metal foam heat exchangers during solidification

7.4.2.3 Solidification time

Figs.7.21,7.22 and 7.23 illustrates the solidification time for the decrease in 0.25 melt fraction interval till the end of solidification of vertical (90°), incline (45°) and horizontal (0°) LHSS. During solidification, the trends for melt fraction variation are similar to that of melting. The difference is that during the solidification, the melt fraction decreases. During the initial stage of solidification, the time to reach a melt fraction from 1 to 0.75 is higher than the time to reach a melt fraction from 0.75 to 0.5. This is because, during the initial stage, some amount of energy is released due to the sensible heat of PCM, where the PCM releases energy without solidification. Further, from 0.5 melt fraction, the time taken to solidify every 0.25 melt fraction increases due to the decrease in the temperature difference between HTF and the average temperature of the PCM. It can be observed that the solidification time is less in the case of radially cascaded metal foam heat exchangers. During solidification, the maximum solidification time of 4000 seconds is observed in linearly cascaded 0.97-0.95-0.93 porosity metal foam LHSS oriented horizontally and a minimum melting time of around 2200 seconds is observed in radial cascaded 0.93-0.95-0.97 porosity metal foam LHSS oriented vertically. In comparison with pure PCM shell and tube heat exchanger which has minimum solidification time, a minimum of 85% and a maximum of 91.7% reduction in solidification time is noted.

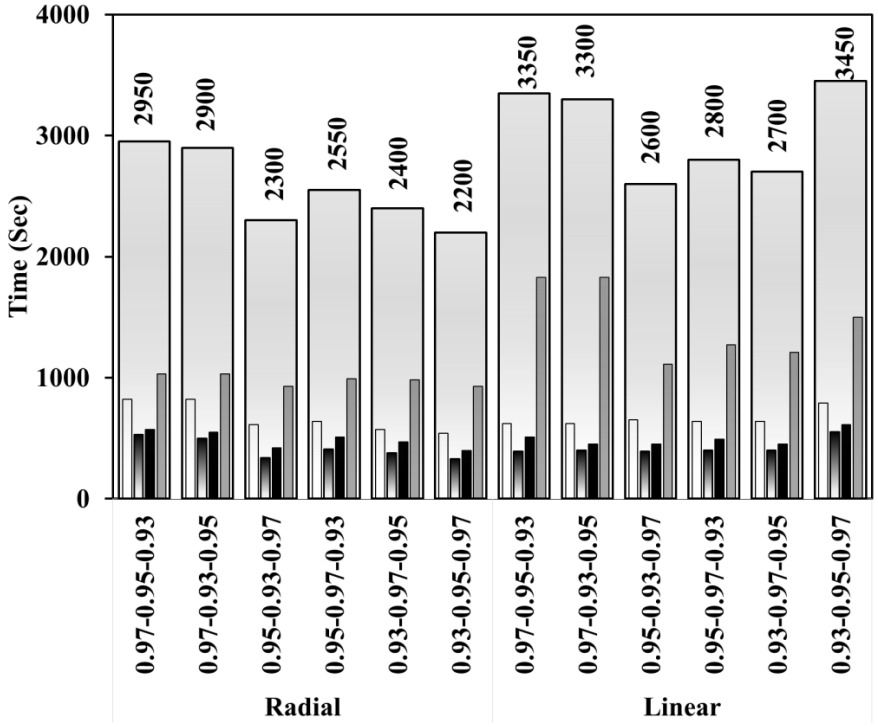

Fig 7.21 Time taken to reach melt fraction with an interval of 0.25 during solidification for vertically oriented cascaded metal foam LHSS

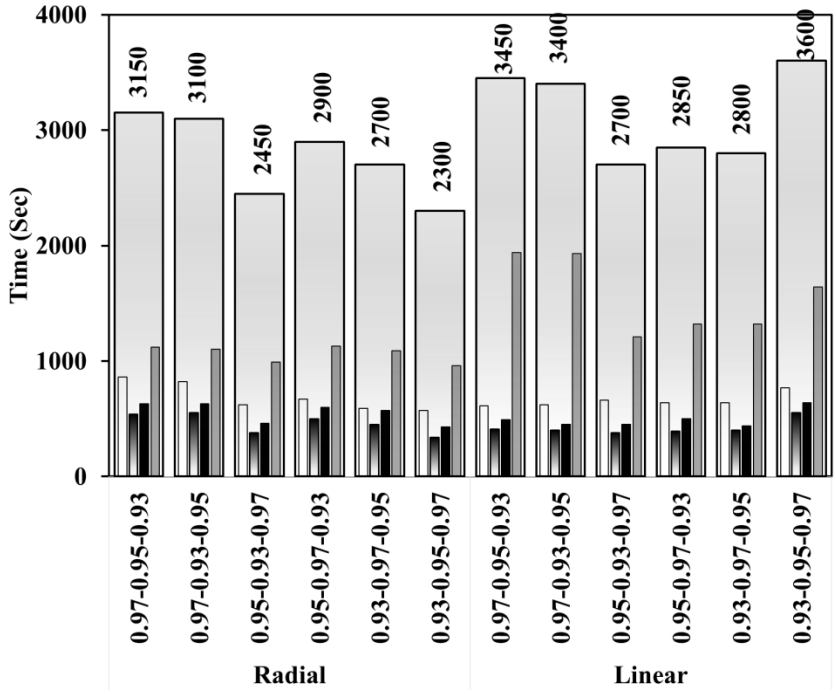

Fig 7.22 Time taken to reach melt fraction with an interval of 0.25 during solidification for inclined (45°) cascaded metal foam LHSS

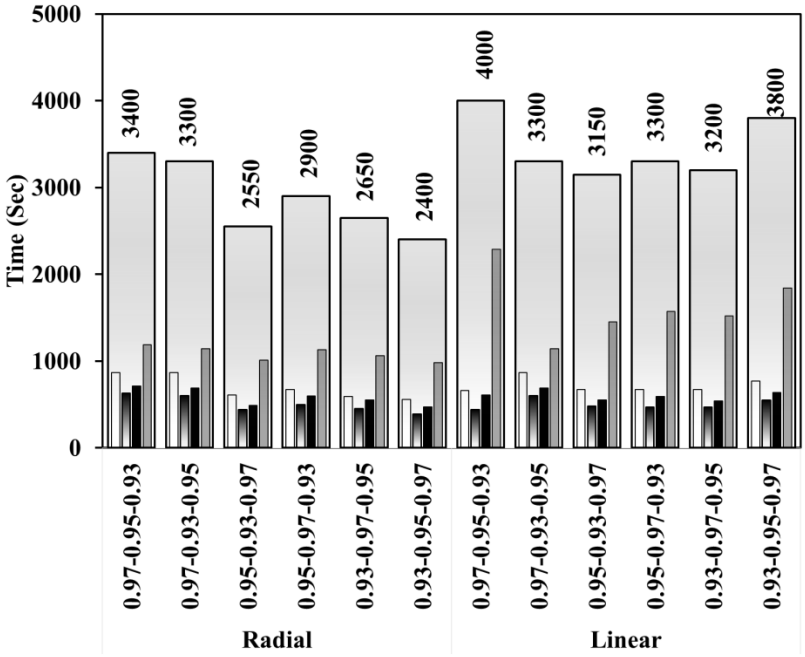

Fig 7.23 Time taken to reach melt fraction with an interval of 0.25 during solidification for horizontally oriented cascaded metal foam LHSS

7.4.2.4 Energy release ratio

Figs.7.24 and 7.25 shows the energy release ratio of radial and linear cascade metal foam heat exchangers during solidification. The energy released depends upon the average temperature of the LHSS. Thus it can be observed that trend of the energy release ratio follows the trend of average temperature. Similarly to that of average temperature, the energy release ratio can also be divided into three stages. The initial stage during which changes in temperature are very high for less energy released. In the second stage, energy is stored due to latent heat capacity. During this stage rate of rise in the energy release ratio is very high when compared to the other two stages, this can be noted from Figs .7.24 and 7.25. In the final stage again energy is released due to specific heat capacity, as a result, the rate of energy release ratio is reduced. It can be noted that the variation in energy release ratio among the radial cascaded and linearly cascaded metal foam heat exchangers is less than 2% for the same orientation. This infers that the energy released has less influence on the metal foam cascading type and placement order. At the end of solidification, a minimum energy release ratio of 0.93 is observed in radial cascaded 0.97-0.93-0.95 porosity metal foam LHSS positioned horizontally, maximum energy release ratio of 0.97

is noted in linearly cascaded 0.93-0.97-0.95 porosity metal foam LHSS inclined at 45°. In comparison with pure PCM shell and tube heat exchanger which has a maximum energy release ratio, a minimum reduction of 2.11% and a maximum reduction of 6.15% in energy release ratio is noted.

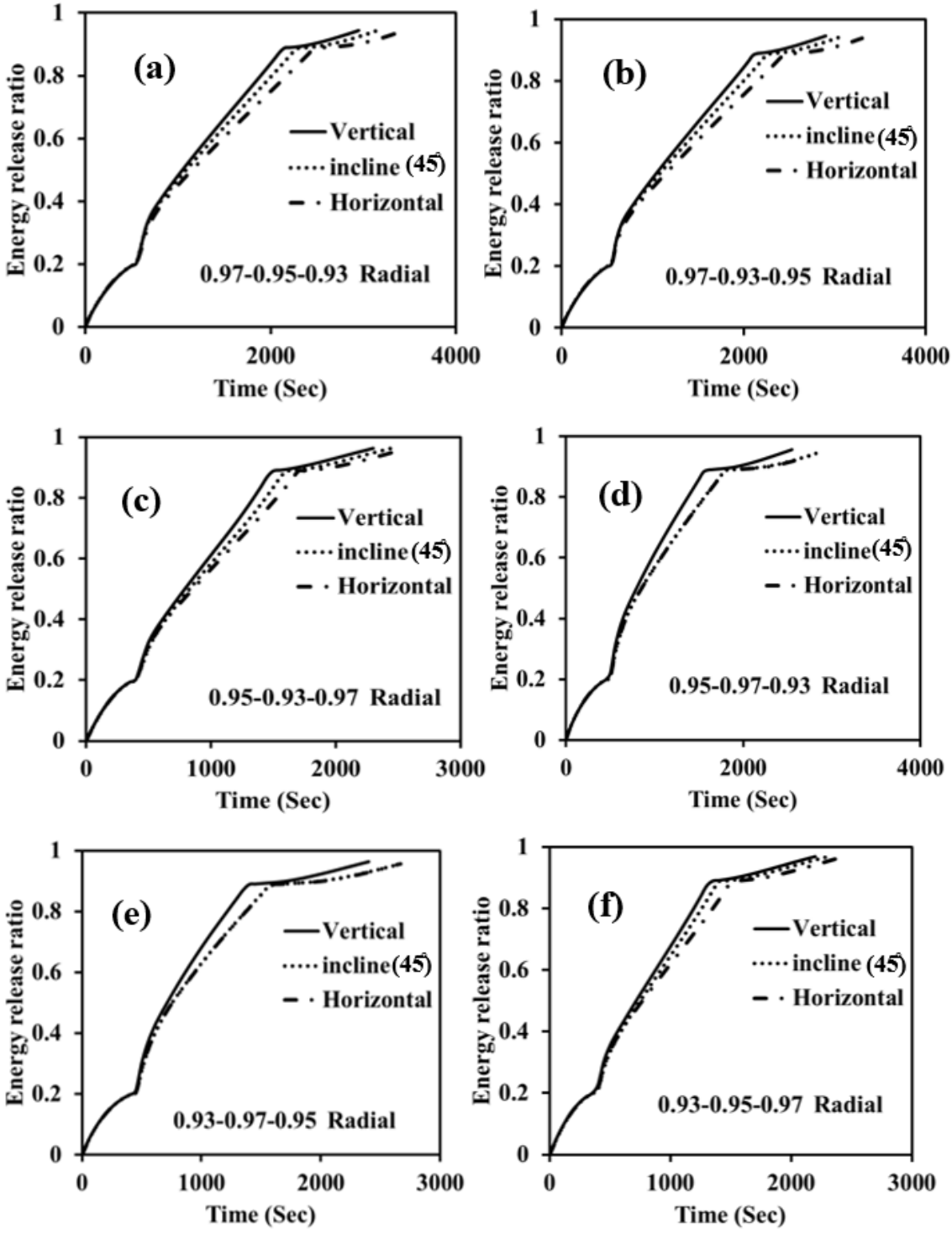

Fig 7.24 Energy release ratio of radially cascaded metal foam heat exchangers during solidification

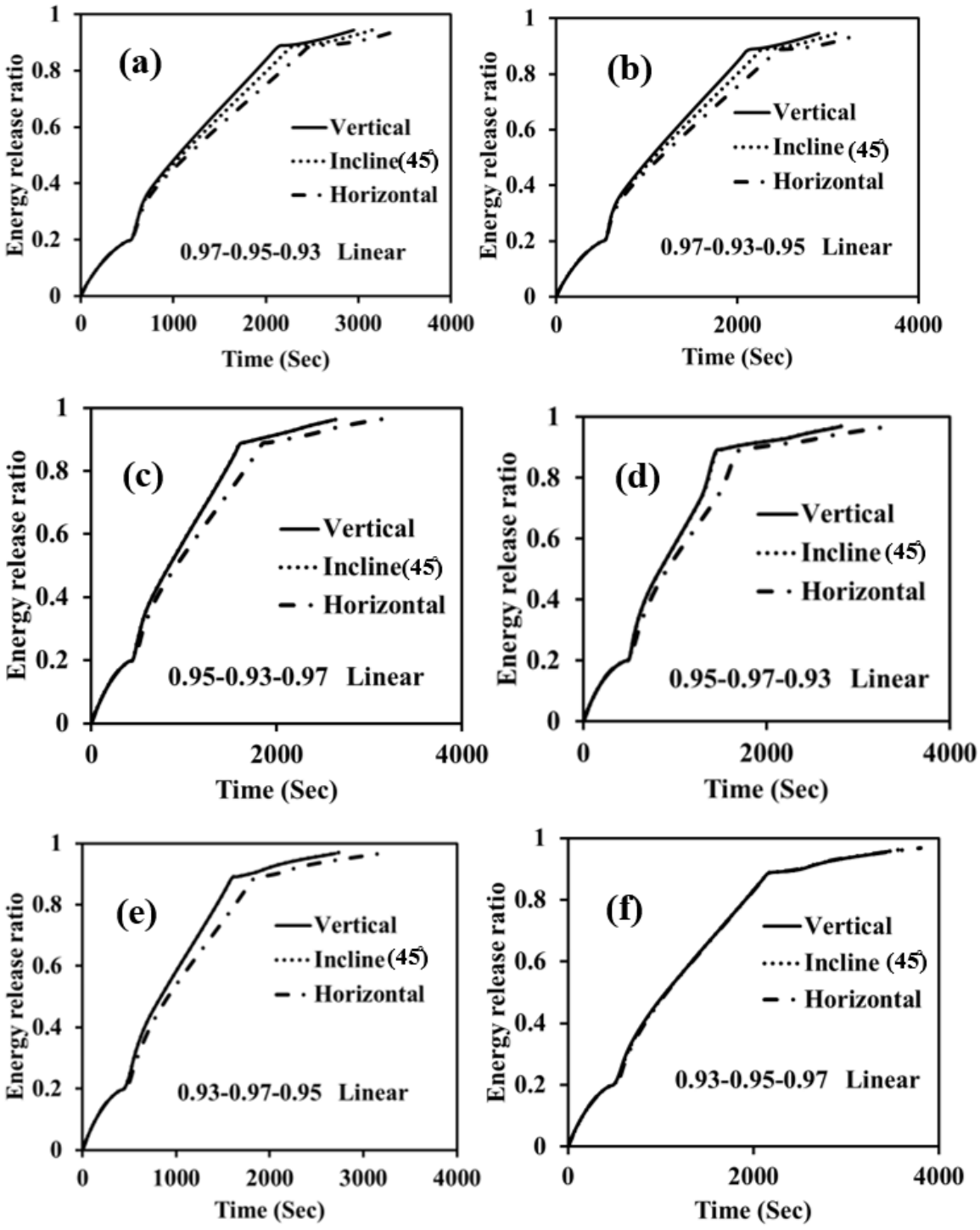

Fig 7.25 Energy release ratio of linearly cascaded metal foam heat exchangers during solidification

7.4.2.5 Exergy efficiency

Fig.7.26 and 7.27 illustrates the exergy efficiency of radial and linear cascaded LHSS during solidification. At the initial stage, exergy efficiency is high as the difference between the inlet and outlet temperatures of the HTF is high. As time progresses, exergy efficiency decreases because PCM releases energy at a temperature higher than the HTF outlet, resulting in exergy destruction. Further, with time the exergy efficiency in linearly cascaded heat exchangers (with 0.97 porosity metal foam near the outlet) and radial cascaded heat exchangers starts increasing due to the increase in the HTF outlet temperature than the average temperature of the PCM. But for other heat exchangers, a rapid decrease in the exergy efficiency can be noted with time during solidification; this is because the increase in HTF's outlet temperature is much less than the average PCM temperature. For radially arranged metal foam heat exchangers, the exergy efficiency is less with 0.97 porosity metal foam near to HTF tube and for linearly cascaded metal foam, the exergy efficiency is minimum for the heat exchanger, with an increase in metal foam porosity from the top to bottom. For a considered heat exchanger, inclined (45°) LHSS has the highest exergy efficiency and horizontal (0°) LHSS has the least exergy efficiency. During solidification, the maximum average exergy efficiency of 9.22% is observed in radial cascaded 0.93-0.95-0.97 porosity metal foam LHSS oriented at 45° and the minimum average exergy efficiency of 4.39% is observed in linear cascaded 0.97-0.95-0.93 porosity metal foam LHSS oriented horizontally.

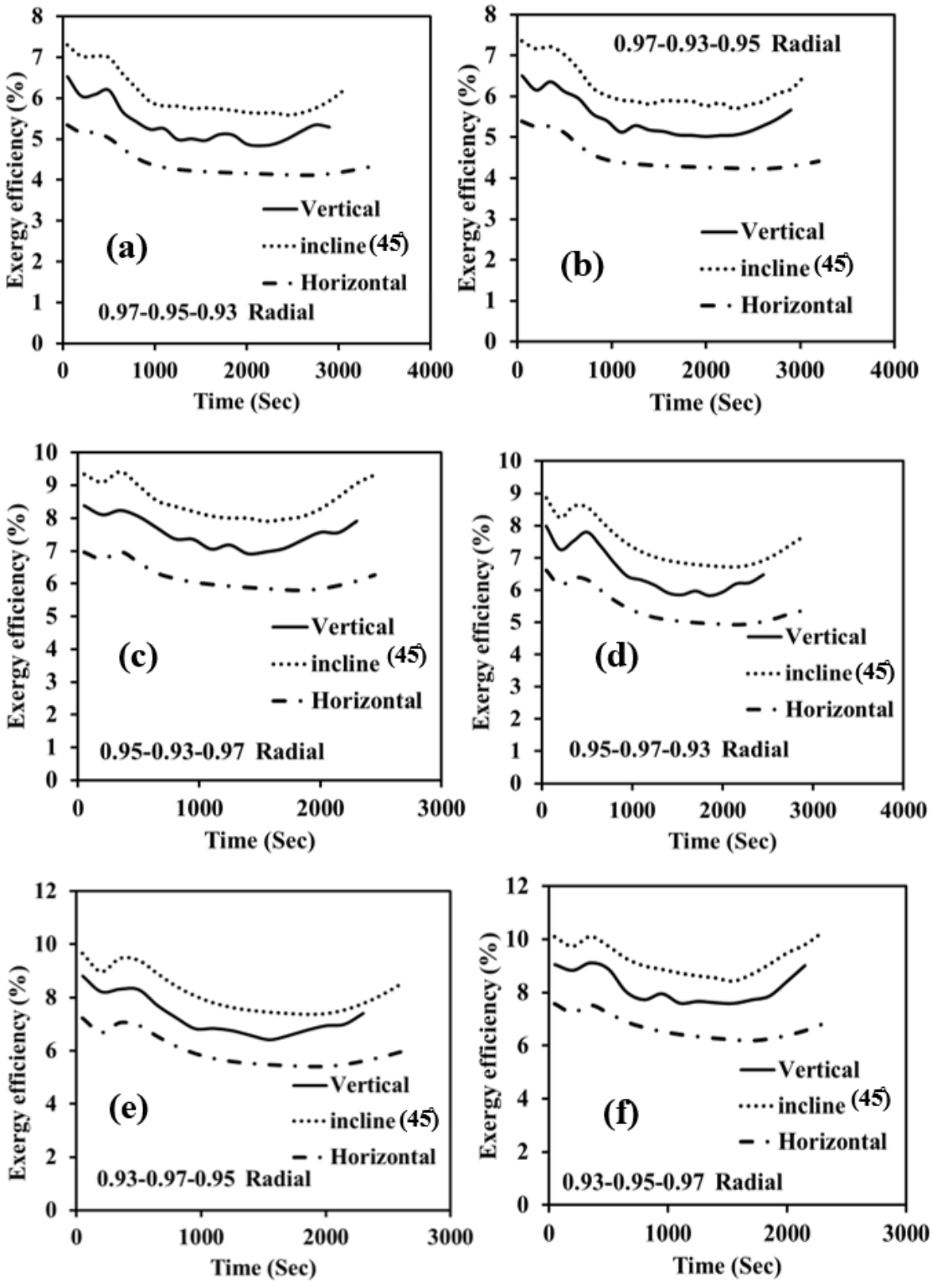

Fig 7.26 Exergy efficiency of radially cascaded metal foam heat exchangers during solidification

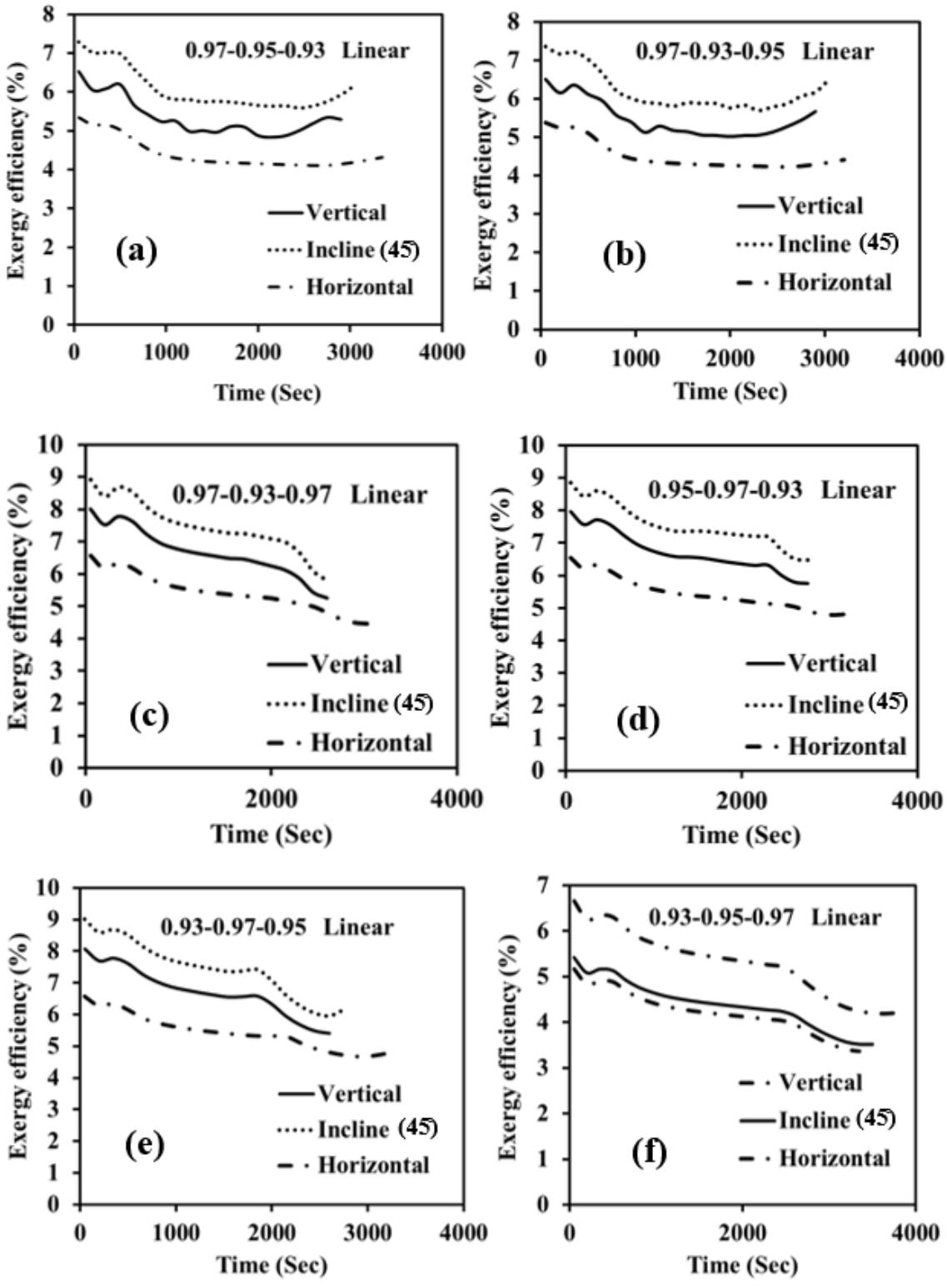

Fig 7.27 Exergy efficiency of linearly cascaded metal foam heat exchangers during solidification

7.5 Closure

In the present study, numerical analysis of phase change material (PCM) based shell and tube heat exchanger with linearly and radially cascaded copper metal foams considering orientation effect is performed. A comparison of the heat exchanger's performance is carried out by considering phase change time, energy stored and released ratios and exergy efficiency. Based on the study, the following conclusions are drawn.

- In radial cascaded metal foam heat exchangers, the heat exchanger oriented vertically in which metal foams are placed in the order of 0.93-0.95-0.97 porosity from HTF to shell has the least melting and solidification duration of 1550 and 2200 seconds, respectively.
- The energy storage ratio depends upon the metal foam cascading type rather than the metal foam order, whereas the energy release ratio is independent of the type of cascading and order of the metal foam.
- During melting linear arrangement of the metal foams has shown better exergy efficiency. The maximum average exergy efficiency of 61.8% is observed for 0.97-0.93-0.95 porosity metal foam placed linearly.
- During solidification, the radial arrangement of the metal foams has given better exergy efficiency. Maximum average exergy of 8.13% is observed for 0.93-0.95-0.97 porosity metal foam placed in a linear manner oriented horizontally.
- On comparison with pure PCM shell and tube heat exchanger which has minimum melting time, a minimum of 53.88% reduction in melting time on linear cascaded 0.93-0.95-0.97 porosity metal foam LHSS oriented at 45° and a maximum of 76.17% reduction in melting time in radial cascaded 0.93-0.95-0.97 porosity metal foam LHSS oriented vertically is noted.
- On comparison with pure PCM shell and tube heat exchanger which has minimum solidification time, a minimum of 85% reduction in solidification time on the usage of radial cascaded 0.93-0.95-0.97 porosity metal foam LHSS oriented vertically and a maximum of 91.7% reduction in solidification time on the usage of linearly cascaded 0.97-0.95-0.93 porosity metal foam LHSS oriented horizontally is noted.
- On comparison with pure PCM shell and tube heat exchanger which has a maximum energy storage ratio, a minimum of 3.22% reduction energy storage ratio on the usage of

linearly cascaded 0.95-0.93-0.97 porosity metal foam LHSS inclined at 45° and a maximum of 11.29% reduction in energy storage ratio in radial cascaded 0.95-0.97-0.93 porosity metal foam LHSS positioned vertically is noted.

- On comparison with pure PCM shell and tube heat exchanger which has a maximum energy release ratio, a minimum of 2.11% reduction in energy release ratio on usage of linearly cascaded 0.93-0.97-0.95 porosity metal foam LHSS inclined at 45° and a maximum of 6.15% reduction in energy release ratio on usage of radial cascaded 0.97-0.93-0.95 porosity metal foam LHSS positioned horizontally is noted.
- During melting, the maximum average exergy efficiency of 62.31% is observed in linearly cascaded 0.93-0.97-0.95 porosity metal foam LHSS oriented at 45° and the minimum average exergy efficiency of 45.04% is observed in radial cascaded 0.97-0.93-0.95 porosity metal foam LHSS oriented vertically.
- During solidification, the maximum average exergy efficiency of 9.22% is observed in radial cascaded 0.93-0.95-0.97 porosity metal foam LHSS oriented at 45° and the minimum average exergy efficiency of 4.39% is observed in linear cascaded 0.97-0.95-0.93 porosity metal foam LHSS oriented horizontally.

Chapter 8

Prediction of transient melt fraction in metal foam - nanoparticle enhanced PCM hybrid shell and tube heat exchanger: A machine learning approach

8.1 Introduction

Machine learning models are used to predict the performance of thermal systems. Melt fraction at any instant in the PCM-based heat exchanger gives a good insight into thermal performance. The prediction of melt fraction during melting and solidification saves a good amount of computational time. Therefore in the present work, transient variation of melt fraction in shell and tube heat exchanger is considered for prediction. On analyzing various hybrid techniques used to enhance the thermal performance of LHSS, it was found that the usage of metal foam + GNP nanoparticles showed better performance. So in the current work, machine learning models are used to predict the melt fraction in metal foam + GNP nanoparticles enhanced shell and tube LHSS. Numerical simulations are carried out on hybrid metal foam and GNP NPs enhanced PCM shell and tube heat exchanger. Orientation angles of 0^o, 30^o, 45^o, 60^o, and 90^o, metal foam with 0.97, 0.95, and 0.93 porosity and 0% (pure PCM), 0.5% volume, and 1% volume GNP NPs are considered in the present work. Numerical simulations are carried out for both melting and solidification. A total of 90 simulations are carried out considering the 3D domain, of which 45 are for melting and 45 are for the solidification process. Data from these simulations are used to train, cross-validate, and test the ML models. Individual ML models are modeled for the melting and solidification processes. In the present study, LR, SVR, K-NN, and XGB algorithms are considered to predict the variation of melt fraction.

8.2 Machine learning methods

In the present study, the melt fraction of PCM enhanced with metal foam and nanoparticles in a shell and tube heat exchanger is predicted using different ML models and their results are compared. The working principles of different ML algorithms are discussed in this section.

8.2.1 Linear Regression (LR):

LR comes under the supervised linear ML predictive model. It is the simplest ML algorithm. The correlation between dependent (y) and independent (x) parameters is represented as follows.

$$y = \propto_0 + \sum_{i=1}^{m} \propto_i x_i \quad (8.1)$$

Where 'm' is the number of independent parameters and 'α_i' are the weights of respective parameters. MSE (mean square error) value is considered as the cost function which has to be minimized to build robust ML models. The error term is given in Eqn.8.2 and the geometric representation of the LR model is shown in Fig.8.1 (a).

$$MSE = \frac{1}{n}\sum_{i=1}^{n}(y_i - y_i^1)^2 \quad (8.2)$$

Where 'n': number of data points, 'y_i': observed value, 'y_i^1': predicted values

8.2.2 Support Vector Regression (SV regression)

Support Vector (SV) regression comes under the supervised linear ML predictive model. Unlike the LR model, the weights of the parameters are not obtained by minimizing the MSE. Here the cost function is the L2-normalization of coefficients of the predicted correlation. This should be minimized simultaneously with the error term. The error term is set to have an absolute value less than or equal to a specified margin. Normalization and error constrain equations are specified in Eqns. 8.3-8.7. The magnitude of the error constraint is the hyperparameter. Fig.8.1 (b) shows the geometric intuition of SV regression.

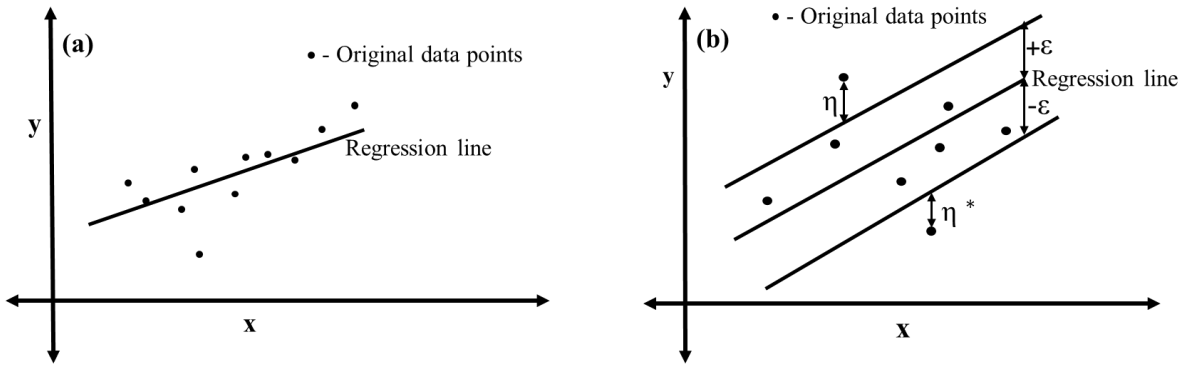

Fig 8.1 Geometric representation of (a) LR model and (b) SVR model

Where 'x' is independent variable and 'y' is dependent variable

$$y = \sum_{i=1}^{n} w_i x_i + b \tag{8.3}$$

The cost function is given as

$$\frac{1}{2}||w||^2 + C\sum_{i=1}^{n}(\eta_i + \eta_i^*) \tag{8.4}$$

Constraints

$$y_i - wx_i - b \leq \varepsilon + \eta_i \tag{8.5}$$

$$wx_i + b - y_i \leq \varepsilon + \eta_i^* \tag{8.6}$$

$$\eta_i \eta_i^* \geq 0 \tag{8.7}$$

'η_i' is the magnitude of deviation from the margin, 'w_i' is the coefficient, 'b' is the y-intercept, 'ε' is the specified margin.

8.2.3 XGBoost (XGB) regression

XGB is a decision tree (DT) ensemble-based ML predictive algorithm. Ensemble models combine several models either by using bagging or boosting techniques. In the bagging method, sample datasets are selected randomly. Using these sample datasets multiple DTs are built. Here boosting weights are assigned to randomly selected data sets. The miscalculated data is given more weight, this enables the model to have more focus on miscalculated values. In gradient boosting instead of assigning weights, the new model is

trained considering the residual error of the previous model. XGB uses gradient-boosted DTs. The flowchart of XGB is shown in Fig.8.2.

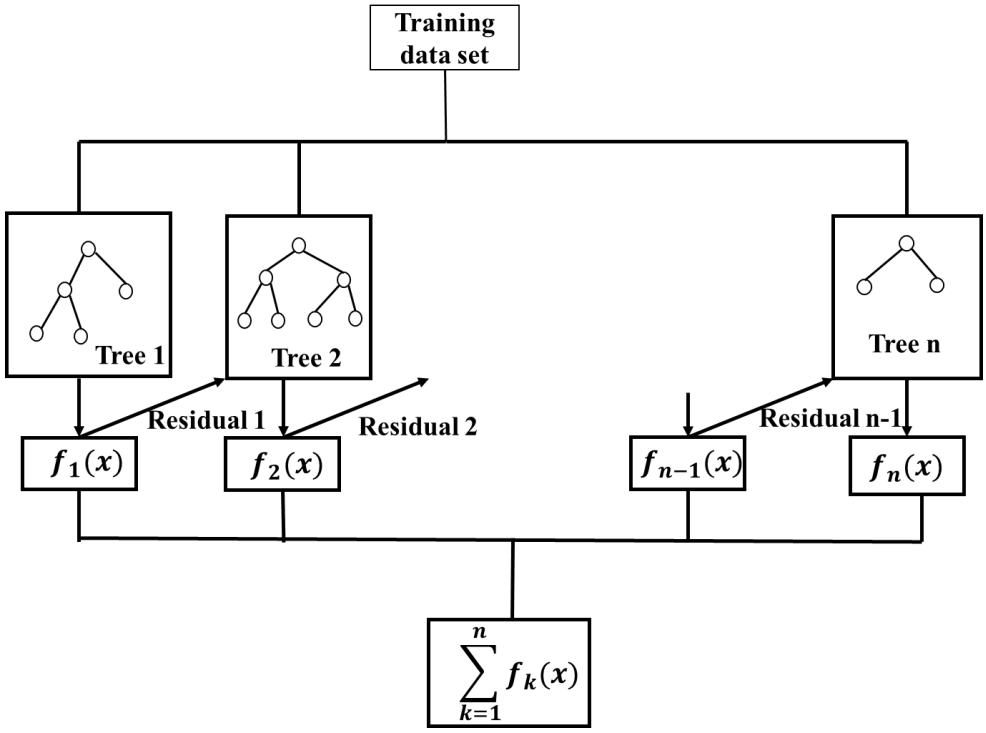

Fig 8.2 Representation of XGB

8.2.4 K Nearest Neighbors (K NN) regression

It is a non-supervised ML algorithm. It stores all the data available and predict the output based on the distance similarity. It is being used in statistics and the recognition of patterns. In this method, the average of K at the nearest neighbors is calculated. In another approach, weights are assigned based on the magnitude of the distance function. The distance functions are given in Eqns.8 and 9. In this predictive model, K is the hyperparameter. A schematic representing the K NN model is given in Fig.8.3.

Manhattan distance between two points is given as

$$\sum_{i=1}^{k} |x_{1i} - x_{2i}| \tag{8.8}$$

Minkowski distance between two points is given as

$$\left(\sum_{i=1}^{k} (|x_{1i} - x_{2i}|)^p\right)^{1/p} \tag{8.9}$$

If p=2 then it is termed Euclidean distance.

Where '*k*' is the dimension of the data set and '*p*' is a positive integer.

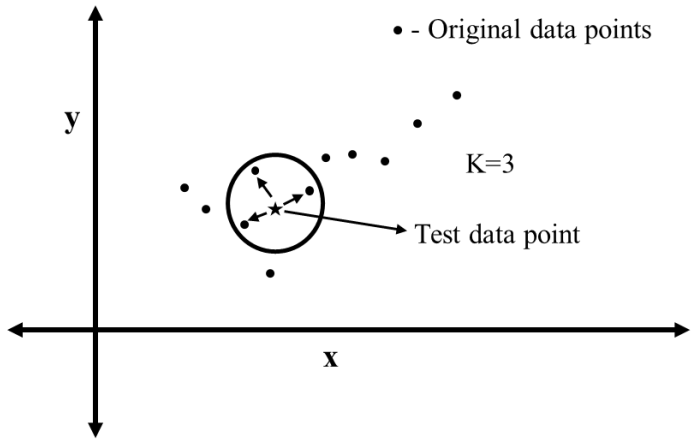

Fig 8.3 Geometric representation of K NN model

8.3 Problem description

8.3.1 Problem geometry

Optimized geometric parameters from the literature are considered for the design of the heat exchanger. On reviewing existing literature (Kalpala and Devanuri [63]) related to latent heat-based shell and tube heat exchanger it is concluded that the ratio of the tube to shell diameter should be nearly 0.25. In the present work, this ratio is considered as 0.254. The dimensions of the shell and tube heat exchanger considered in the present work are given in Table 1. The 3D CAD model of the metal foam + GNP NP heat exchanger is shown in Fig.8.4. Kalpala and Devanuri [42] concluded that varying flow rate of HTF has a negligible effect on the performance of the heat exchanger. On referring to studies carried out by Gaddala and Devanuri [133] tube material is considered to be stainless steel. Since lauric acid is suitable for heat storage applications [133], it is considered in the study. The properties of lauric acid [134] are listed in Table 2. From the literature [137][138] it is observed that copper foam metal foam PCM heat exchangers have shown better performance so in the present study copper is selected as the metal foam material.

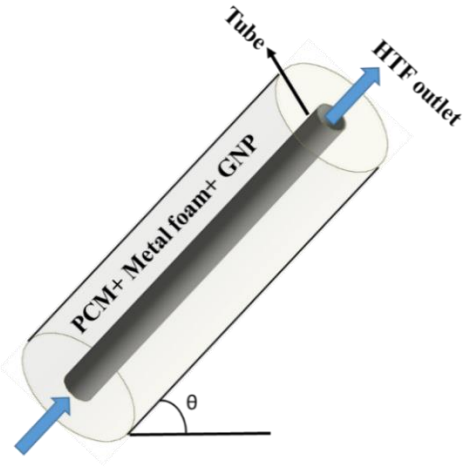

Fig 8.4 Schematic of LHSS

8.4 Results and discussion

To create a good machine learning (ML) model which can predict the melt fraction of the metal foam - NP enhanced PCM shell and tube heat exchanger, 70% of the numerical simulation data is used to train the ML model, 20% of the data is used to cross-validate the results and 10% of the data is used to test the ML model created. LR, SV regression, XGB, and K NN regression ML predictive algorithms are used and their compatibility for the PCM shell and tube heat exchanger problem is compared. Prediction of the transient melt fraction using ML models enables us to save computational time. Data collection, data preparation, and ML model formulation are the three steps involved and are shown in Fig.8.5.

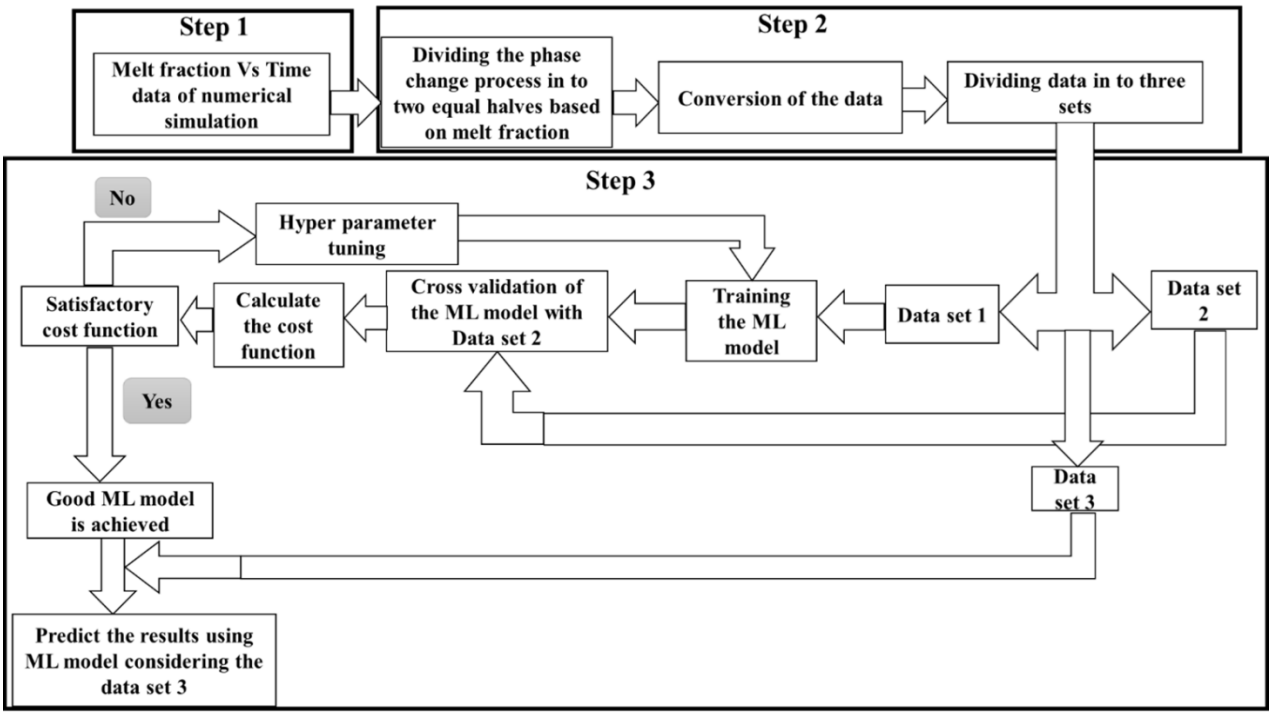

Fig 8.5 Flow chart for the step-by-step procedure of ML model formulation

Step 1: Data is collected by carrying out numerical simulations for melting and solidification of PCM enhanced with the combination of metal foam - NPs in a shell and tube heat exchanger. The porosities of metal foam used in the study are 0.97, 0.95 and 0.93. Volume fractions of the NPs considered are pure PCM (0%), 0.5%, and 1%. The simulations are carried out considering the inclination effect of the heat exchanger (0^o, 30^o, 45^o, 60^o, and 90^o). Here 90^o represents the vertical and 0^o represents the horizontal positions of the heat exchanger. A total of 90 simulations are carried out, of which 45 simulations are for melting and 45 simulations are for solidification. Separate ML models are developed for melting and solidification.

Fig.8.6 illustrates the final melting time of the considered heat exchangers. It can be observed that among the three factors considered porosity of metal foam has a major effect during melting. The usage of metal foam enhances the effective thermal conductivity of PCM, this increases with the decrease in the porosity of metal foam. It can be observed that heat exchanger with 0.93 metal foam has the least melting time. From Fig.8.6 vertically oriented heat exchanger also shows the least melting time for all the considered cases. GNP NPs have a less significant impact in the presence of 0.93 and 0.95 porosity metal foam

when compared to 0.97 metal foam. In the case of 0.97 porosity metal foam with the increase in the volume fraction of GNP NPs melting time decreased. Due to the influence of convective strength, the effect of heat exchanger orientation is felt with 0.97 porosity metal foam.

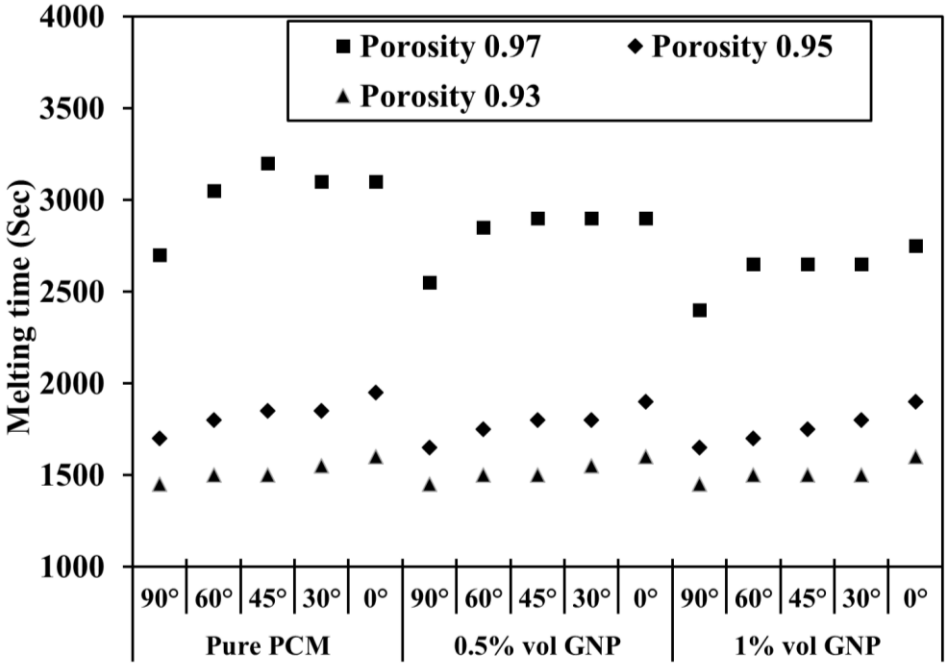

Fig 8.6 Final melting time time of metal foam and GNP nanoparticle heat exchanger

Fig.8.7 shows the final solidification time during solidification in metal foam and GNP NPs enhanced PCM shell and tube heat exchanger. It can be observed that among the three factors considered porosity of metal foam has a major effect on the solidification as noted for melting. The metal foam with 0.93 porosity has less solidification time and the 0.97 porosity metal foam heat exchanger in Pure PCM has the highest solidification time. During solidification, a considerable effect of NPs and inclination can be observed only in the presence of metal foam with 0.97 porosity.

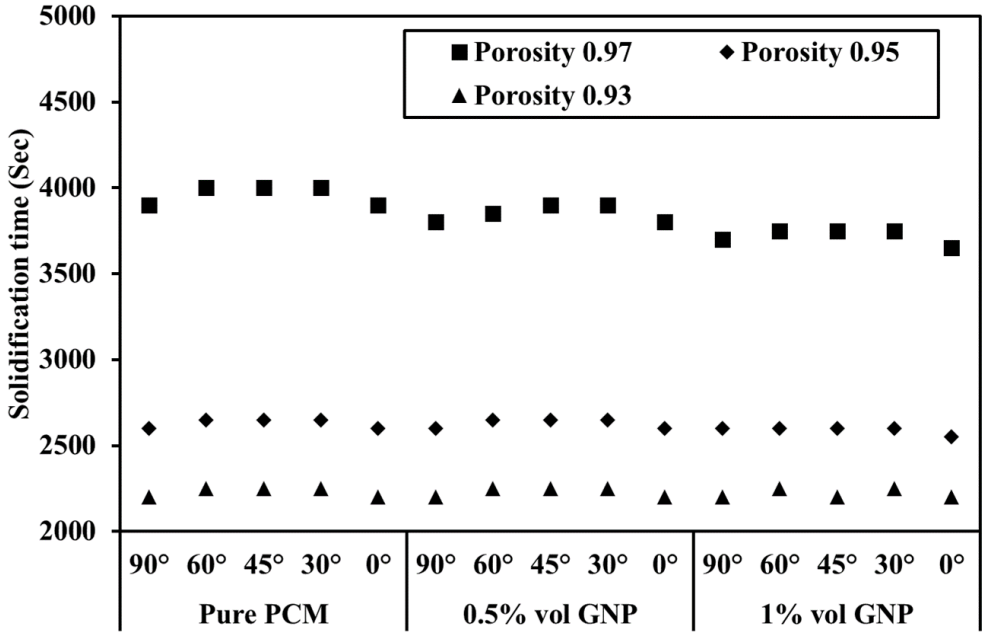

Fig 8.7 Final solidification time of metal foam and GNP nanoparticle heat exchanger

Step 2: The data of each simulation is divided into two parts i.e. input part and the output part based on the melt fraction. During melting the input part is from 0 to 0.3 melt fraction and the output part is from 0.3 to 1 melt fraction. During solidification, the input part is from 1 to 0.7 melt fraction and the output part is from 0.7 to 0 melt fraction. The separation of the data is represented in Figs.8.8 and 8.9.

Using the curve fitting technique two separate third-order equations are generated for the input part and the output part of the melt fraction variation with time for both melting and solidification. During melting the coefficients of the equation for melt fraction variation from 0 to 0.3 are input parameters and during solidification, the coefficients of the equation for melt fraction variation from 1 to 0.7 are input parameters. During melting the coefficients of the equation for melt fraction variation from 0.3 to 1 are output parameters and during solidification, the coefficients of the equation for melt fraction variation from 0.7 to 0 are output parameters. The porosity of the metal foam, the orientation of the heat exchanger, and the volume fraction of GNP NPs are also considered the input parameters of the ML model. The schematic of input and output parameters is represented in Fig.8.10.

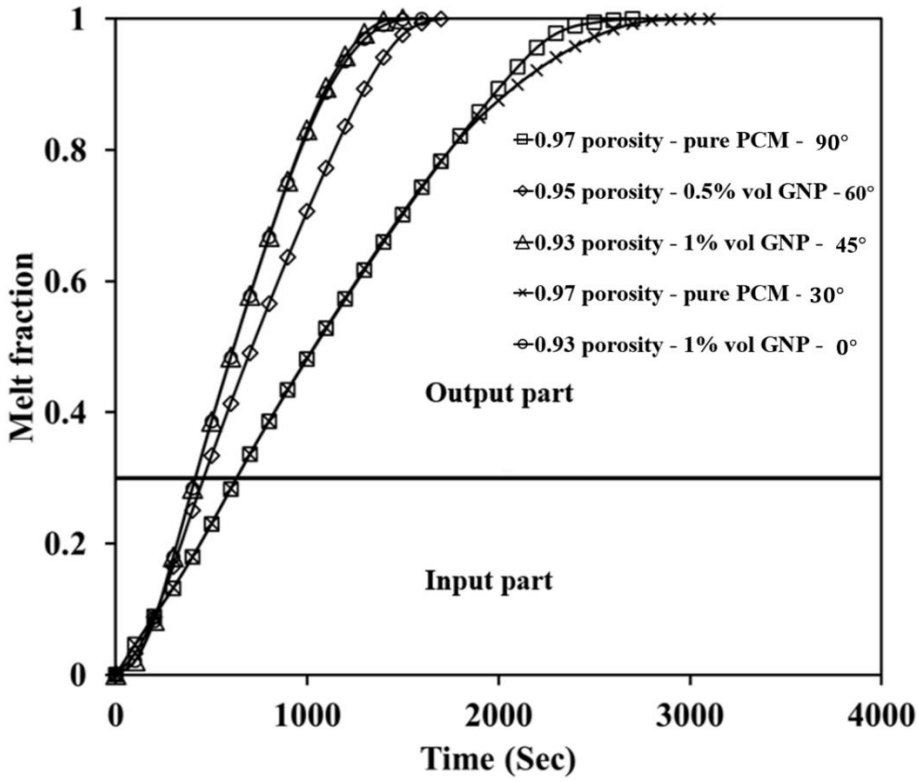

Fig 8.8 Variation of melt fraction with time during melting

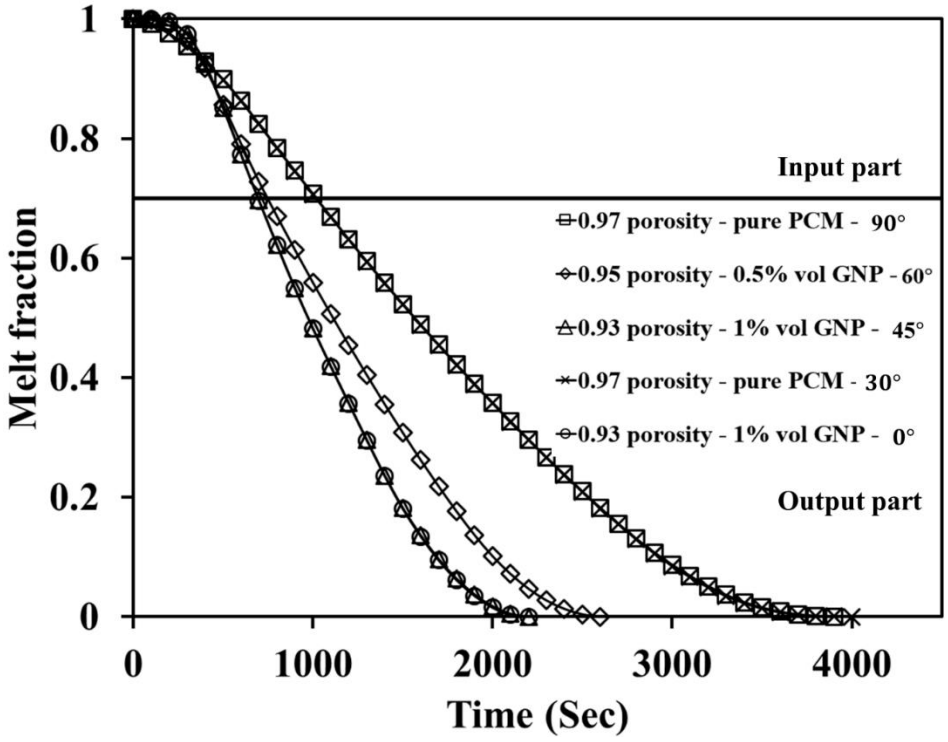

Fig 8.9 Variation of melt fraction with time during solidification

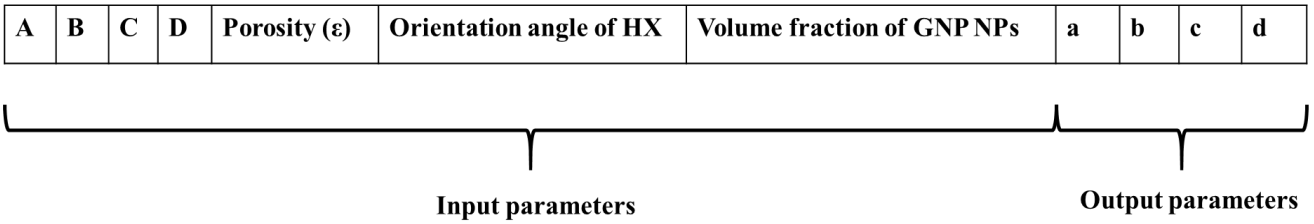

Fig 8.10 Representation of input and output parameters of data

Where

- A, B, C, and D are coefficients of curve fit equations for input data.
- a, b, c and d are the coefficients of the output data equation.

Step 3: The data set is divided into three parts. One part is to train the model which contains 70% of the data and another part which contains 20% of the data is used to cross-validate with the trained model. Rest 10% of the data is used to test the ML model created. The hyperparameters of the ML models have been adjusted such that the cost function of both the training and cross-validation data sets is nearly equal.

Fig.8.11 shows the test data results of the melting process. It can be noted from Fig. 8.11(a) that the XGB ML model has shown the highest deviation, this indicates that the XGB model is exhibiting overfitting. From Figs.8.11 (c) (d) and (e) the results of SV regression is also deviating from the actual regression result. Table 8.1 shows the comparison of the final melting time obtained from ML models with melting time obtained from simulations and the error percentage of the predicted result from ML models with simulations results. LR model is showing reasonable error in all the output cases. A maximum error of 18.8% is observed with the XGB model in the case of 0.97 porosity with 1% volume GNP oriented horizontally. This indicates that model is overfitting, due to this XGB model cannot be used to predict the melt fraction in the shell and tube heat exchanger. Although the predicted results from the K NN models have shown reasonable error, the maximum error in the case of 0.93 porosity with pure PCM oriented vertically is 6.8%. This indicates that the LR model is better than the K NN model. It can be noted that like the XGB model, the SV regression model also exhibited the overfitting problem due to which the maximum error of 10.16% is observed in the case of 0.97 porosity with 1%

volume GNP oriented at 30^{o}. Based on the details it can be concluded that the LR model has predicted better during the melting process.

Fig.8.12 shows the results of the test data for the solidification process. It can be noted from Fig.8.12 (e) that the SV regression ML model has shown the highest deviation. Table 8.2 shows the comparison of the final solidification time obtained from simulations with ML models. Also, the error percentage of the predicted result from the ML model with the results of the simulation is given. During solidification, all the ML models predicted the melt fraction with acceptable error, but the SV model has consistently shown the highest error. This indicates that the SV regression model is suffering from under fitting effect during solidification.

Considering both the melting and solidification process, the LR ML model is not affected either by the overfitting or underfitting effect and predicted the trends of melt fraction with reasonable error. So, the LR model can be considered to be the best ML model to predict the trend of melt fraction and total melting and solidification time for a PCM-based shell and tube heat exchanger with NP and metal foam.

Table 8.1 Final melting time of test cases

HEAT EXCHANGER configuration	**Final melting time (sec) Simulation**	**Final melting time (sec) LR prediction (error)**	**Final melting time (sec) XGB prediction (error)**	**Final melting time (sec) K NN prediction (error)**	**Final melting time (sec) SV regression prediction (error)**
0.97 porosity – 1% vol GNP - 0°	2750	2675 (2.7%)	2232.6 (18.8%)	2698.3 (1.8%)	2611.9 (5.02%)
0.95 porosity - 0.5% vol GNP - 45°	1800	1733.5 (3.69%)	1713.7 (4.7%)	1685.2 (6.3%)	1775.6 (1.3%)
0.93 porosity – pure PCM - 90°	1450	1438.4 (0.8%)	1351.3 (6.8%)	1482.9 (2.2%)	1485.6 (2.4%)
0.97 porosity – 1% vol GNP - 30°	2650	2611.8 (1.4%)	2648.5 (0.05%)	2611.9 (1.4%)	2380.7 (10.1%)
0.93 porosity - 1% vol GNP - 60°	1500	1574.6 (4.9%)	1505.1 (0.3%)	1503.6 (0.2%)	1488.7 (0.7%)

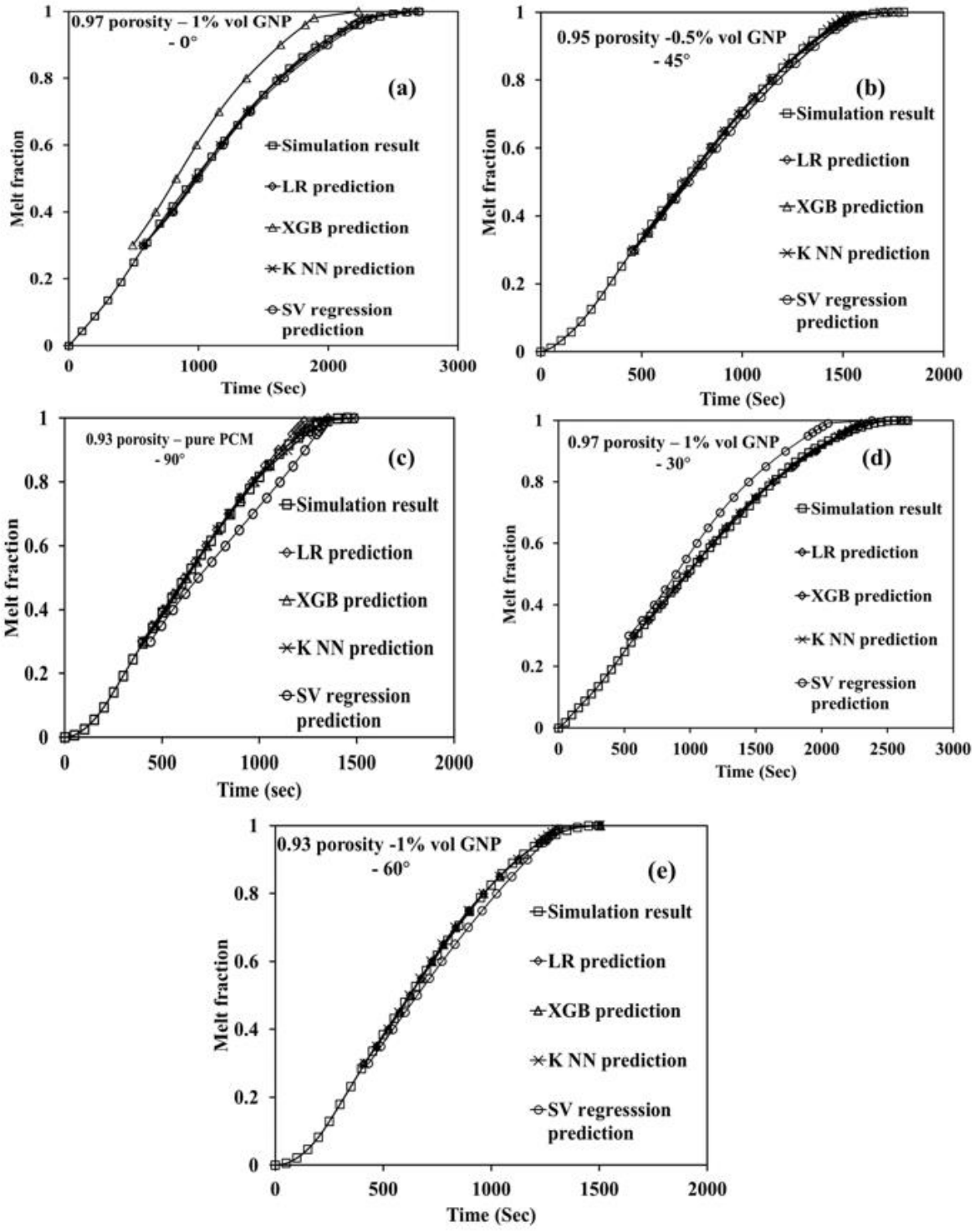

Fig 8.11 Predicted melt fraction trends using ML models during melting

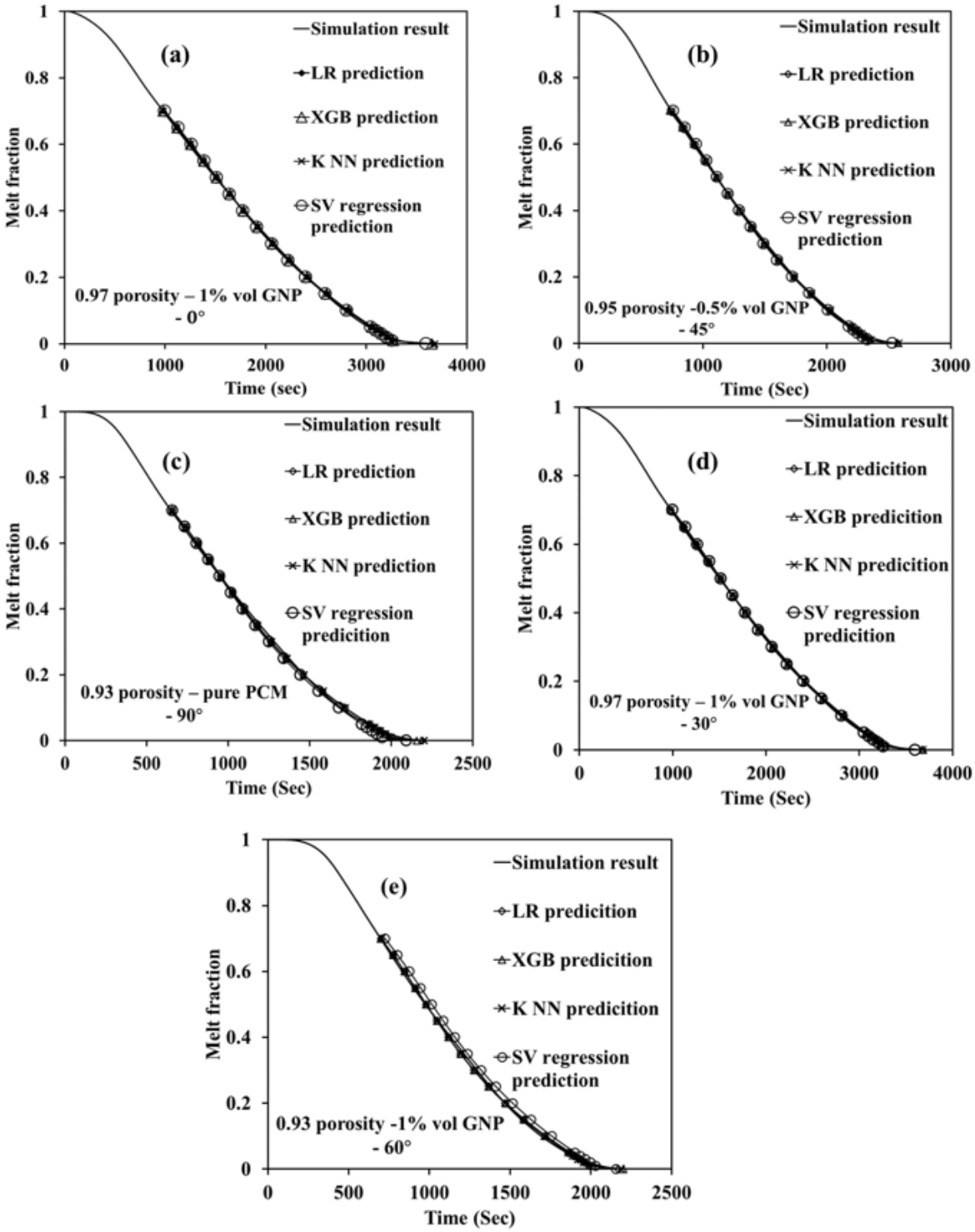

Fig 8.12 Predicted melt fraction trends using ML models during solidification

Table 8.2 Final solidification time of test cases

HEAT EXCHANGER configuration	Final solidification time (sec) Simulation	Final time solidification (sec) LR prediction (error)	Final solidification time (sec) XGB prediction (error)	Final solidification time (sec) K NN prediction (error)	Final solidification time (sec) SV regression prediction (error)
0.97 porosity – 1% vol GNP - 0°	3650	3665.4 (0.4%)	3652.3 (0.06%)	3679.1 (0.7%)	3595.4 (1.4%)
0.95 porosity - 0.5% vol GNP - 45°	2650	2570.7 (2.9%)	2572.8 (2.92%)	2577.1 (2.7%)	2528.9 (4.5%)
0.93 porosity – pure PCM - 90°	2200	2190.1 (0.4%)	2156 (2%)	2200 (0%)	2092.3 (4.8%)
0.97 porosity – 1% vol GNP - 30°	3750	3680.6 (1.81%)	3681.8 (1.82%)	3679.1 (1.8%)	3597.9 (4.05%)
0.93 porosity - 1% vol GNP - 60°	2250	2169.6 (3.5%)	2201.6 (2.1%)	2187.7 (2.7%)	2155.9 (4.1%)

8.5 Closure

- Melting and solidification time got reduced with the reduction in the porosity of the metal foam. The rate of decrease in the melting and solidification is more when the porosity of the metal foam is changed from 0.97 to 0.95 to that of change in porosity from 0.95 to 0.93 for all the volume fractions of the GNP NPs and orientations of the heat exchanger.
- The effect of the GNP nanoparticles is only felt in the presence of 0.97 porosity metal foam for all the considered volume percentages of GNP.
- When both the volume fraction of GNP and porosity of metal foam are kept constant, a vertically oriented heat exchanger has shown less melting time. The

least melting time is noted in the case of a vertically oriented heat exchanger with 1% volume GNP and 0.93 porosity metal foam.

- During solidification, the effect of orientation has the least effect in all heat exchangers and the effect of GNPs is felt in the presence of 0.97 porosity metal foam.
- LR model has predicted the variation of melt fraction with time during both melting and solidification without any underfitting and overfitting effects with a maximum error of 5%. So LR ML model can be used to predict the melt fraction trend in PCM-based shell and tube heat exchangers with nanoparticle and metal foam.

Chapter 9

Effect of geometric parameters on phase change time and exergy efficiency during melting and solidification

9.1 Introduction

The usage of the hybrid techniques resulted in the reduction of phase change time and improved the exergy efficiency during solidification. But exergy efficiency during solidification can be improved further. In the present study effect of geometric parameters on the exergy efficiency of PCM shell and tube heat exchanger during melting and solidification is analyzed. Among the hybrid techniques considered, the combined effect of metal foam and GNP nanoparticles has shown a better effect. So in the present chapter, this technique is considered to enhance the heat transfer in PCM. Effect on phase change time and exergy efficiency is analyzed by varying porosity of metal foam, the volume fraction of GNP nanoparticles, length of the heat exchanger, the inlet temperature of HTF, length to diameter ratio (l/d) of shell and Reynolds number of HTF. Three levels of parameters are considered for each parameter. Taguchi method is used to design the experiments. Grey relational analysis (GRA) is used to rank the heat exchanger based on the performance parameters and to find out the important parameter which affects the phase change time and exergy efficiency of the heat exchanger.

9.2 Physical model

In the present study, the design parameters of the HX are varied to analyze their effect on the phase change time and exergy efficiency. Fig.9.1 shows the geometric representation of the HX. Due to its compatibility, lauric acid is chosen as the PCM (Uma Maheswararao et al., 2022). The properties of lauric acid are given in Table 4.1. The diameter of the tube is kept constant at 19.05mm, and both the length and diameter of the shell are varied such that for all the considered cases volume of PCM is kept the same. The porosities of the copper metal foams analyzed in the present work are 0.97, 0.95 and 0.93, and the volume fractions of GNP NPs are 0.5% and 1%. Reynolds number of HTF is varied between 500 to 4000. The inlet temperature of HTF during melting is varied between 348K to 358K,

and the inlet temperature of HTF during solidification is varied between 293K to 303K. The length-to-shell diameter ratio is varied from 1.19 to 9.22, and the orientation of the heat exchanger is varied from 0° (horizontal) to 90° (vertical).

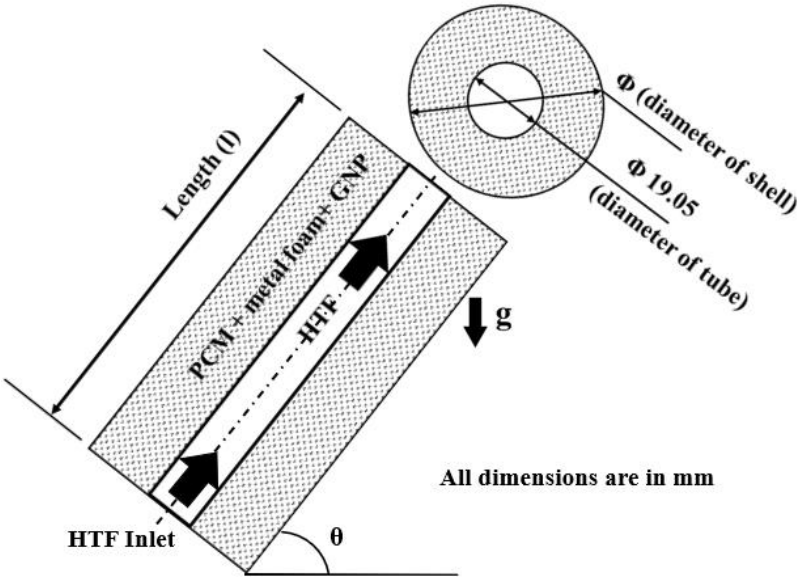

Fig 9.1 Schematic of the heat exchanger

9.3 Grey relational analysis (GRA)

This approach is used to find the relationship among the experiments carried out with the help of gray relational grade (GRG). It is used to find the important parameters by GRG. Following are the steps in the GRA method.

Step 1: The results data is normalized in the initial step. In this process, the whole data is scaled into 0 to 1. In the present study, solidification time is normalized based on the lesser the better, and exergy efficiency is normalized based on the more the better. The higher the better and lesser the better equations are given in Eqns.9.1 and 9.2.

$$x_{i,normalized} = \frac{x_i - x_{min}}{x_{max} - x_{min}} \quad (9.1)$$

$$x_{i,normalized} = \frac{x_{max} - x_i}{x_{max} - x_{min}} \quad (9.2)$$

Using this normalized value deviation value is calculated. The deviation value is calculated using Eqn.9.3

$$x_{i,deviated\ value} = 1 - x_{i,normalized} \quad (9.3)$$

Step 2: Using this normalized data Gray relational coefficient (GRC) was calculated. This represents the correlation between actual and desired values. GRC was calculated using Eqn.9.4

$$\varphi_i = \frac{\Delta_{min} + \psi\Delta_{max}}{\Delta_{o,i} + \psi\Delta_{max}} \quad (9.4)$$

Where $\Delta_{o,i}$ is the difference between x_i and the deviation value of x_i , Ψ is the deviation constant (0.5)

In the present work, individual GRA analysis is carried out for phase change time and exergy efficiency. This gives us the inference of the important parameters influencing the phase change time and exergy efficiency during melting and solidification individually.

9.4. Results and discussion

9.4.1 Taguchi method

Taguchi method consists of an experiment design methodology with a quality loss function. This enables to development of a robust process. Very few experiments can be performed using this method to get the maximum information[140]. The parameters selected in the present study are the porosity of metal foam, the volume fraction of GNP nanoparticles, the length of the heat exchanger, the inlet temperature of HTF, length to diameter ratio of the shell and the Reynolds number of HTF. Each parameter has 3 levels. Process parameters and their levels are shown in Table 9.1. L_{27} orthogonal array is considered depending upon the 6 parameters and 3 levels, this has 27 experiments. These are shown in Table.9.2. Considering these parameters numerical simulations are carried out for the melting and solidification process.

Table 9.1 Parameters and levels

Levels / Parameters	1	2	3
Porosity	0.93	0.95	0.97
GNP vol fraction (%)	0 (pure PCM)	0.5	1
Orientation	0° (horizontal)	45° (incline)	90° (vertical)
HTF inlet temperature (K) (melting/solidification)	348/293	353/298	358/303
l/d ratio	1.19	3.34	9.22
Reynolds number of HTF	500	2000	4000

Table 9.2 L_{27} experimental parameters orthogonal array

Case	Porosity	GNP vol fraction (%)	Orientation	HTF temperature (K) (melting/solidification)	l/d ratio	Reynolds number of HTF
1	0.93	0	0°	348/293	1.19	500
2	0.93	0	0°	348/293	3.34	2000
3	0.93	0	0°	348/293	9.22	4000
4	0.93	0.5	45°	353/298	1.19	500
5	0.93	0.5	45°	353/298	3.34	2000
6	0.93	0.5	45°	353/298	9.22	4000
7	0.93	1	90°	358/303	1.19	500
8	0.93	1	90°	358/303	3.34	2000
9	0.93	1	90°	358/303	9.22	4000
10	0.95	0	45°	358/303	1.19	2000
11	0.95	0	45°	358/303	3.34	4000
12	0.95	0	45°	358/303	9.22	500
13	0.95	0.5	90°	353/293	1.19	2000
14	0.95	0.5	0°	353/293	3.34	4000
15	0.95	0.5	90°	353/293	9.22	500
16	0.95	1	0°	348/298	1.19	2000
17	0.95	1	0°	348/298	3.34	4000
18	0.95	1	0°	348/298	9.22	500
19	0.97	0	90°	353/298	1.19	4000

20	0.97	0	90°	353/298	3.34	500
21	0.97	0	90°	353/298	9.22	2000
22	0.97	0.5	0°	358/303	1.19	4000
23	0.97	0.5	0°	358/303	3.34	500
24	0.97	0.5	0°	358/303	9.22	2000
25	0.97	1	45°	348/293	1.19	4000
26	0.97	1	45°	348/293	3.34	500
27	0.97	1	45°	348/293	9.22	2000

9.4.2 Melting time

Fig.9.2 shows the melt fraction with respect to the time of heat exchangers during melting. For the same porosity of metal foam shell and tube heat exchangers, a clear difference can be observed in melt fraction variation based on the l/d ratio of the heat exchanger. Heat exchangers with an l/d ratio of 9.22 shows the least melting time and heat exchangers with an l/d ratio of 1.19 exhibited the highest melting time. This is because in the presence of metal foam, heat transfer is conduction dominant and with a decrease in the diameter of the shell overall effective thermal resistance decreases. Thus heat transfer increases with a decrease in the diameter of the shell. As the amount of PCM is the same in all heat exchangers, the rate of melting is highest in heat exchangers with an l/d ratio of 9.22. Table 9.3 shows the ranking of the heat exchangers based on the melting time. From Table 9.3 it can be noted that the top three ranked heat exchangers possess an l/d ratio of 9.22 and the bottom three ranked heat exchangers possess an l/d ratio of 1.19. Table 9.3 shows the ranking of the parameters which show the most influence on melting time. From Table 9.4 it can be observed that the l/d ratio of shell and tube heat exchanger has the most significant effect on melting time, melting time decreases with an increase in the l/d ratio of shell and tube heat exchanger. The porosity of metal foam and Reynolds number of HTF has shown a significant effect on the melting time. With the decrease in the porosity of metal foam, the effective thermal conductivity of PCM increases. This results in an increase in the rate of melting. From Table 9.4 it can be noted that with an increase in the Reynolds number of HTF, melting time decreases. This is because, with an increase in the Reynolds number, the heat transfer coefficient increases, thus resulting in increasing in the rate of melting. Effect of volume fraction of GNP nanoparticles, orientation, and HTF inlet

temperature shows an insignificant effect on melting time when compared with porosity of metal foam, l/d ratio of heat exchanger, and Reynolds number of HTF. Least melting time of 300 seconds is exhibited by heat exchanger with metal foam porosity of 0.93, l/d ratio of 9.22 with HTF inlet temperature, and Reynolds number of 358K and 4000 enhanced with 1% volume fraction GNP nanoparticles oriented vertically. Highest melting time of 5150 seconds is exhibited by heat exchanger with metal foam porosity of 0.97, l/d ratio of 1.19 with HTF inlet temperature and Reynolds number of 348K and 4000 enhanced with 1% volume fraction GNP nanoparticles oriented at 45°. For the same amount of PCM considered, a variation of 94.17% in melting time is observed with varying the geometric parameters of shell and tube heat exchanger and input parameters of HTF.

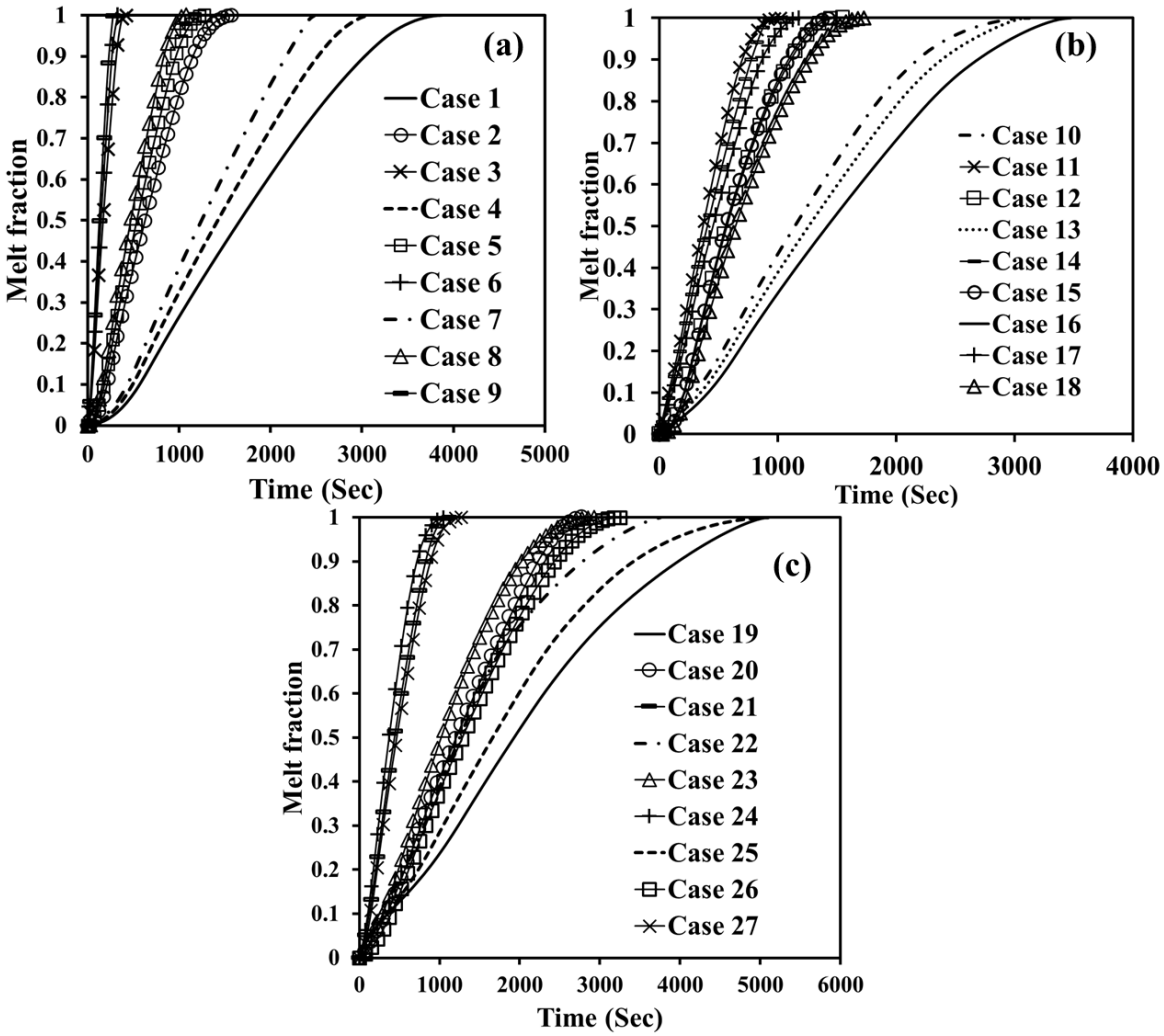

Fig 9.2 Melt fraction variation with time (a) 0.93 porosity metal foam (b) 0.95 porosity metal foam and (c) 0.97 porosity metal foam heat exchanger during melting

Table 9.3 Normalized, deviated and grade of the melting time

Case	Melting time (sec)	Normalized value	Deviation value	Grade	Rank
Case 1	3900	0.257	0.742	0.402	25
Case 2	1600	0.731	0.268	0.651	14
Case 3	450	0.969	0.030	0.941	3
Case 4	3100	0.422	0.577	0.464	18
Case 5	1300	0.793	0.206	0.708	10
Case 6	350	0.989	0.010	0.979	2
Case 7	3500	0.340	0.659	0.431	22
Case 8	1100	0.835	0.164	0.751	6
Case 9	300	1	0	1	1
Case 10	3150	0.412	0.587	0.459	20
Case 11	1050	0.845	0.154	0.763	4
Case 12	1550	0.742	0.257	0.659	13
Case 13	3100	0.422	0.577	0.464	18
Case 14	1050	0.845	0.154	0.763	4
Case 15	1450	0.762	0.237	0.678	12
Case 16	3500	0.340	0.659	0.431	22
Case 17	1200	0.814	0.185	0.729	9
Case 18	1750	0.701	0.298	0.625	15
Case 19	5110	0.008	0.991	0.335	26
Case 20	2800	0.484	0.515	0.492	16
Case 21	1150	0.824	0.175	0.740	8
Case 22	3800	0.278	0.721	0.409	24
Case 23	2950	0.453	0.546	0.477	17
Case 24	1100	0.835	0.164	0.751	6
Case 25	5150	0	1	0.333	27
Case 26	3275	0.386	0.613	0.449	21
Case 27	1300	0.793	0.206	0.708	10

Table 9.4 Response table of parameters for melting time

Levels / Parameters	1	2	3	Max-Min	Rank
Porosity	0.703	0.619	0.521	0.181	2
GNP vol fraction	0.605	0.633	0.606	0.027	5
Orientation	0.602	0.613	0.628	0.026	6
HTF inlet temperature	0.585	0.625	0.634	0.048	4
l/d ratio	0.414	0.643	0.787	0.372	1
Reynolds no	0.520	0.629	0.695	0.175	3

9.4.3 Solidification time

Fig.9.3 shows the melt fraction with respect to the time of heat exchangers during solidification. Similarly to that of melting, for the same porosity of metal foam shell and tube heat exchangers, a clear difference can be observed in melt fraction variation based on the l/d ratio of the heat exchanger during solidification. Heat exchangers with an l/d ratio of 9.22 shows the least solidification time and heat exchangers with an l/d ratio of 1.19 exhibit the highest solidification time. This is because the solidification process is conduction dominant and further using metal foam effective thermal conductivity of PCM increases and with a decrease in the diameter of the shell overall effective thermal resistance decreases. Thus heat transfer increases with a decrease in the diameter of the shell. As the amount of PCM is the same in all heat exchangers, the rate of solidification is highest in heat exchangers with an l/d ratio of 9.22. Table 9.5 shows the ranking of the heat exchangers based on the solidification time. From Table 9.5 it can be noted that the top three ranked heat exchangers have an l/d ratio of 9.22 and the bottom three ranked heat exchangers have an l/d ratio of 1.19 similar to that of melting. Table 9.6 shows the ranking of the parameters which has the most influence on solidification time. Similar to that of the melting process from Table 9.6 it can be observed that the l/d ratio of shell and tube heat exchanger has the most significant effect on solidification time, it decreases with an

increase in the l/d ratio of shell and tube heat exchanger. Similarly to that of the melting process following the l/d ratio of heat exchanger, the porosity of metal foam and Reynolds number of HTF has shown a significant effect on the solidification time. With the decrease in the porosity of metal foam, the effective thermal conductivity of PCM increases. This results in an increase in the rate of solidification. The effect of volume fraction of GNP nanoparticles, orientation, and HTF inlet temperature on solidification time is insignificant when compared with the porosity of metal foam, l/d ratio of heat exchanger, and Reynolds number of HTF. Least solidification time of 400 seconds is exhibited by heat exchanger with metal foam porosity of 0.93, l/d ratio of 9.22 with HTF inlet temperature and Reynolds number of 348K and 4000 pure PCM heat exchanger oriented horizontally. Highest solidification time of 7100 seconds is exhibited by heat exchanger with metal foam porosity of 0.97, l/d ratio of 1.19 with HTF inlet temperature and Reynolds number of 303K and 4000 enhanced with 0.5% volume fraction GNP nanoparticles oriented at 45°. For the same amount of PCM considered, a variation of 94.36% in solidification time is observed with varying geometric parameters of shell and tube heat exchanger and input parameters of HTF.

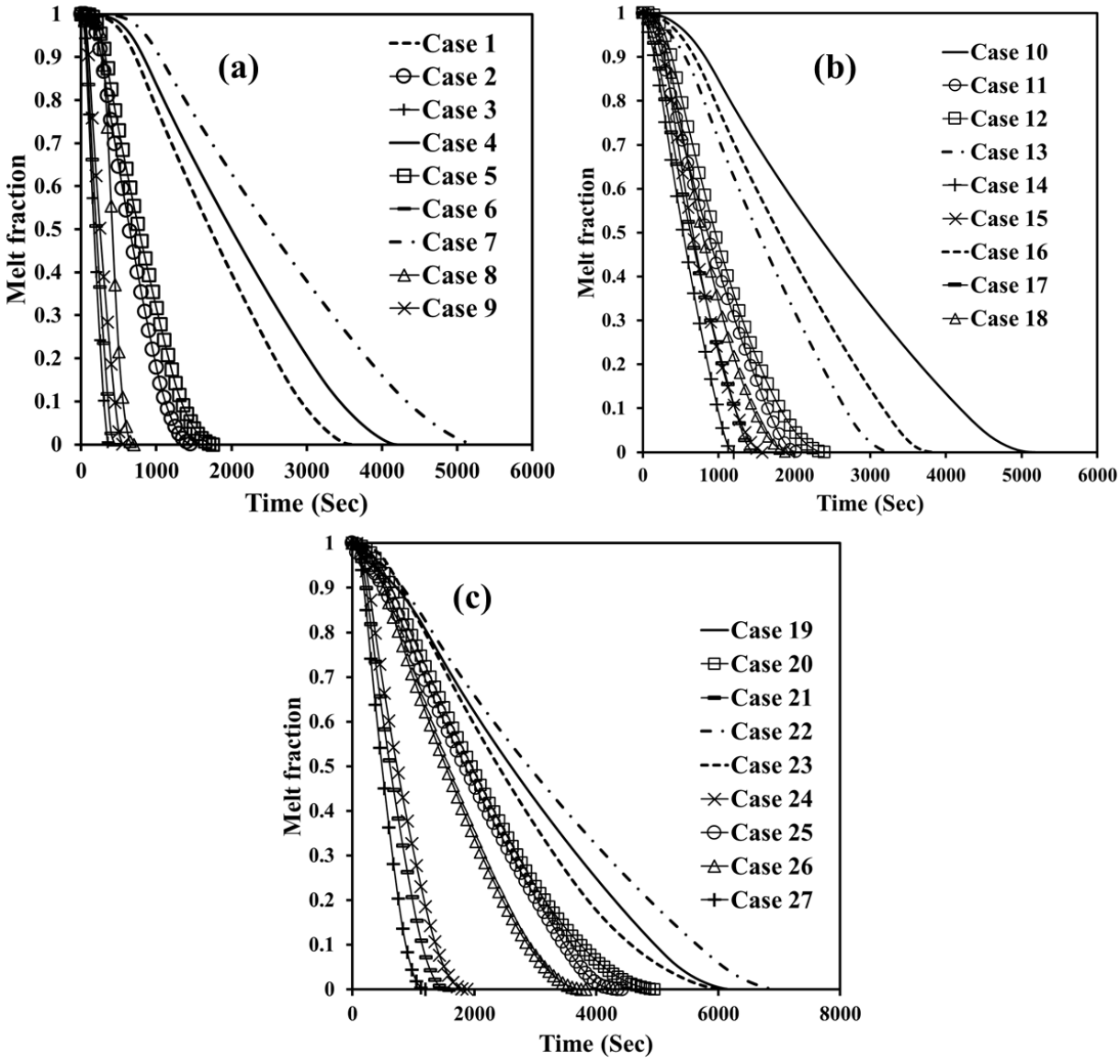

Fig 9.3 Melt fraction variation with time (a) 0.93 porosity metal foam (b) 0.95 porosity metal foam and (c) 0.97 porosity metal foam heat exchanger during solidification

Table 9.5 Normalized, deviated and grade of the solidification time

Case	Solidification time	Normalized value	Deviation value	Grade	Rank
Case 1	3650	0.514	0.485	0.507	17
Case 2	1500	0.835	0.164	0.752	7
Case 3	400	1	0	1	1
Case 4	4250	0.425	0.574	0.465	20
Case 5	1800	0.791	0.208	0.705	11
Case 6	450	0.992	0.007	0.985	2
Case 7	5250	0.276	0.723	0.408	24
Case 8	700	0.955	0.044	0.917	4
Case 9	600	0.970	0.029	0.943	3
Case 10	5200	0.283	0.716	0.411	23
Case 11	2100	0.746	0.253	0.663	14
Case 12	2400	0.701	0.298	0.626	15
Case 13	3300	0.567	0.432	0.536	16
Case 14	1200	0.880	0.119	0.807	5
Case 15	1600	0.820	0.179	0.736	9
Case 16	3900	0.477	0.522	0.489	19
Case 17	1500	0.835	0.164	0.752	7
Case 18	1950	0.768	0.231	0.683	13
Case 19	6225	0.130	0.869	0.365	25
Case 20	5000	0.313	0.686	0.421	22
Case 21	1600	0.820	0.179	0.736	9
Case 22	7100	0	1	0.333	27
Case 23	6250	0.126	0.873	0.364	26
Case 24	1900	0.776	0.223	0.690	12
Case 25	4450	0.395	0.604	0.452	21
Case 26	3850	0.485	0.514	0.492	18
Case 27	1250	0.873	0.126	0.797	6

Table 9.6 Response table of parameters for solidification time

Levels / Parameters	1	2	3	Max-Min	Rank
Porosity	0.742	0.633	0.517	0.225	2
GNP vol fraction	0.609	0.624	0.659	0.050	4
Orientation	0.619	0.622	0.652	0.033	6
HTF inlet temperature	0.658	0.639	0.609	0.0494	5
l/d ratio	0.440	0.653	0.799	0.359	1
Reynolds no	0.522	0.670	0.700	0.177	3

9.4.4 Exergy efficiency during melting

Exergy is a property that enables to determine the work potential of a given amount of energy. For the same amount of energy available, energy at higher temperatures has more exergy. Fig.9.4 illustrates the variation in exergy efficiency with time for the considered heat exchangers. Exergy efficiency in the present study depends on the average temperature of PCM and the inlet and exit temperature of HTF. The initial temperature of the PCM in heat exchangers is 298K which is equal to ambient temperature, as a result, initial exergy efficiency is zero in all the heat exchangers. During melting, with time temperature of the PCM increases, and thus the temperature of energy stored increases. This results in an increase in the exergy efficiency of the heat exchangers. In Fig.9.4 higher exergy efficiency at the end of melting indicates higher average temperature. Table 9.7 infers the ranking of the heat exchangers based on the average exergy efficiency during melting. It can be noted that the top 3 ranked heat exchangers have an inlet HTF temperature of 348K and the bottom 3 raked heat exchangers have an inlet HTF temperature of 358K. This is because during the initial stage and phase change stages of melting average temperature of PCM in all heat exchangers is almost the same, as a result, energy is stored at almost the same temperatures in all heat exchangers. This results in higher exergy destruction in heat exchangers in which the inlet temperature is 358K. Table 9.8 gives the ranking of parameters that influences the exergy efficiency during melting. The inlet temperature of HTF, the orientation of heat exchanger and the porosity of metal foam are showing significant effect on exergy efficiency during melting. Horizontally-

oriented heat exchangers and heat exchangers in which the porosity of metal foam is 0.97 has higher exergy efficiency. Reynolds number of HTF, l/d ratio of heat exchanger and volume fraction of GNP nanoparticles have shown the least effect on exergy efficiency during melting. Although the outlet temperature of HTF varies due to variation in Reynolds number of HTF and keeping the overall rate of energy transfer almost the same, during melting exergy depends more on the average temperature of PCM. Thus Reynolds number of HTF has the least effect on exergy efficiency during melting. Irrespective of the l/d ratio of heat exchanger a gradual increase in the average temperature occurs in all heat exchangers, thus the exergy efficiency increases. The effect of the GNP nanoparticles hinders due to the usage of the metal foam, thus its effect is insignificant on exergy efficiency during melting. The least average exergy efficiency of 40.29% is exhibited by heat exchanger with metal foam porosity of 0.93, l/d ratio of 1.19 with HTF inlet temperature and Reynolds number of 358K and 500 enhanced with 1% volume GNP nanoparticles oriented vertically. The highest average exergy efficiency of 61.29% is exhibited by heat exchanger with metal foam porosity of 0.95, l/d ratio of 9.22 with HTF inlet temperature and Reynolds number of 348K and 500 enhanced with 1% volume GNP nanoparticles oriented horizontally.

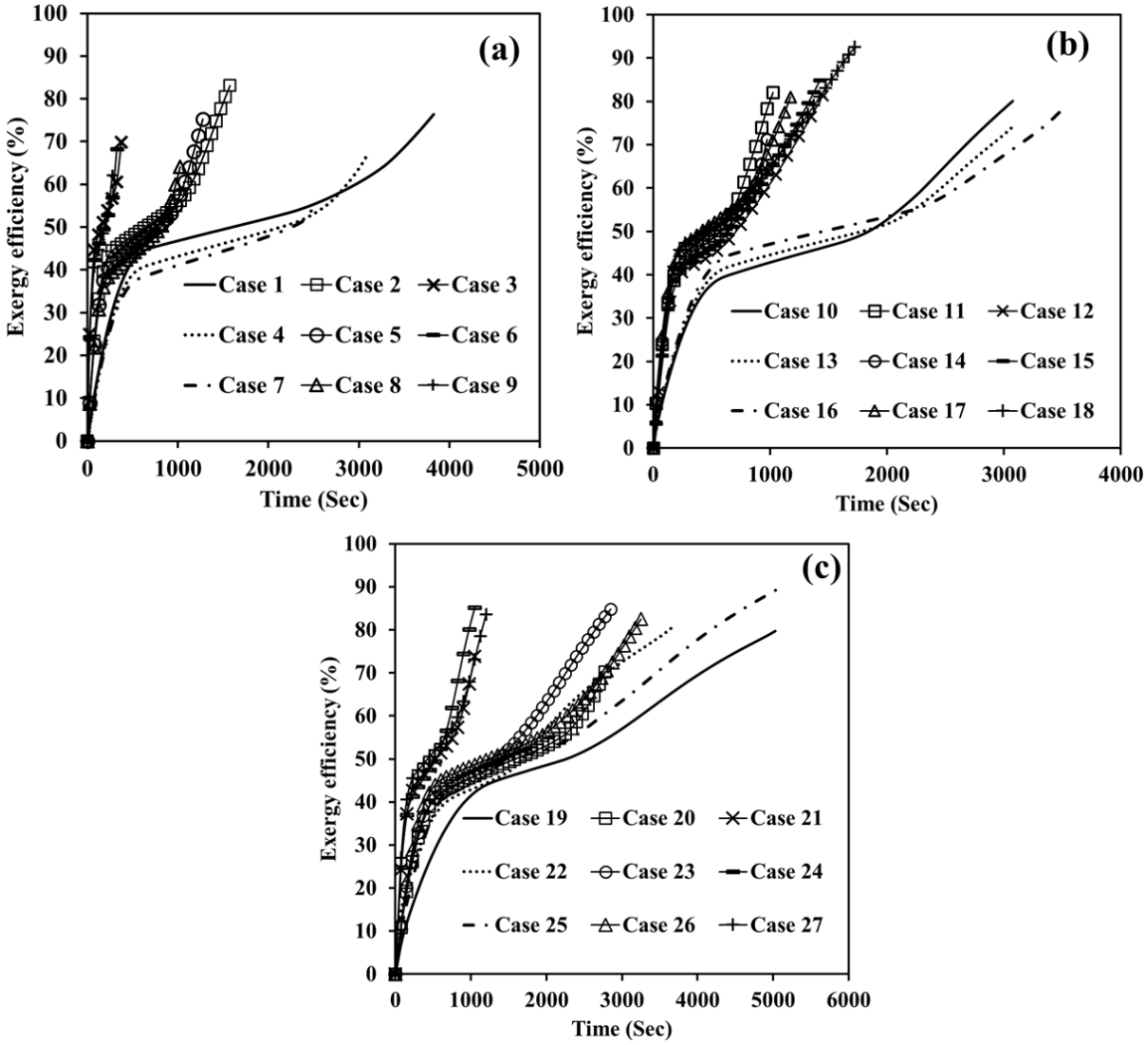

Fig 9.4 Exergy variation with time (a) 0.93 porosity metal foam (b) 0.95 porosity metal foam and (c) 0.97 porosity metal foam heat exchanger during melting

Table 9.7 Normalized, deviated and grade of the exergy during melting

Case	Exergy efficiency (%)	Normalized value	Deviation value	Grade	Rank
Case 1	51.4	0.529	0.470	0.514	14
Case 2	53.3	0.619	0.380	0.567	9
Case 3	50.09	0.466	0.533	0.483	16
Case 4	45.09	0.228	0.771	0.393	24
Case 5	48	0.367	0.632	0.441	20
Case 6	47.49	0.342	0.657	0.432	22

Case 7	40.29	0	1	0.333	27
Case 8	42.83	0.120	0.879	0.362	26
Case 9	44.18	0.185	0.814	0.380	25
Case 10	49.1	0.419	0.580	0.462	18
Case 11	50.58	0.49	0.51	0.495	15
Case 12	52.43	0.578	0.421	0.542	12
Case 13	48.47	0.389	0.610	0.450	19
Case 14	47.94	0.364	0.635	0.440	21
Case 15	54.15	0.66	0.34	0.595	4
Case 16	51.72	0.544	0.455	0.523	13
Case 17	53.51	0.629	0.370	0.574	5
Case 18	61.29	1	0	1	1
Case 19	53	0.605	0.394	0.558	11
Case 20	46.97	0.318	0.681	0.423	23
Case 21	49.46	0.436	0.563	0.470	17
Case 22	53.24	0.616	0.383	0.566	10
Case 23	53.4	0.624	0.375	0.570	7
Case 24	53.34	0.621	0.378	0.569	8
Case 25	59.26	0.903	0.096	0.837	2
Case 26	53.51	0.629	0.370	0.574	5
Case 27	55.02	0.701	0.298	0.626	3

Table 9.8 Response table of parameters for exergy efficiency during melting

Levels / **Parameters**	**1**	**2**	**3**	**Max-Min**	**Rank**
Porosity	0.434	0.564	0.577	0.143	3
GNP vol fraction	0.502	0.495	0.579	0.077	4
Orientation	0.596	0.533	0.446	0.150	2
HTF inlet temperature	0.633	0.467	0.474	0.166	1
l/d ratio	0.515	0.494	0.566	0.072	5
Reynolds no	0.549	0.4970	0.529	0.052	6

9.4.5 Exergy efficiency during solidification

Fig.9.5 illustrates the variation of exergy efficiency with time during solidification. Unlike during melting, exergy efficiency during solidification significantly depends on the outlet temperature of HTF. During solidification energy is carried out by HTF, during this process energy at higher temperatures is converted into lower-temperature energy. This results in exergy destruction. Initially, during solidification, exergy efficiency is higher because of the higher outlet temperature of HTF. As the solidification process progresses exergy efficiency decreases because of higher variation in average temperature of PCM and outlet temperature of HTF. On further solidification, this variation decreases thus resulting in an increase in the exergy efficiency. Table 9.9 illustrates the ranking of the heat exchanger based on the exergy efficiency during solidification. From Table 9.9 it can be noted that all bottom three ranked heat exchangers have 0.97 porosity metal foam with an l/d ratio of 1.19 and HTF Reynolds number of 4000. Table 9.10 infers the ranking of parameters according to the influence on exergy efficiency during solidification. Reynolds number and l/d ratio have shown significant effect on exergy efficiency during solidification. If the flow rate is less, then the outlet temperature of HTF will be higher and for a higher flow rate of HTF, the outlet temperature will be less. Due to this temperature difference, exergy efficiency varies. Higher the outlet temperature of HTF higher the exergy efficiency and vice versa. With a higher l/d ratio length of the heat exchanger increases. This results in higher HTF interaction time, thus enabling HTF temperature to increase. The porosity of metal foam, volume fraction of GNP nanoparticles, orientation and HTF inlet temperature has less effect on exergy efficiency during solidification.

The least average exergy efficiency of 0.53% is exhibited by heat exchanger with metal foam porosity of 0.97, l/d ratio of 1.19 with HTF inlet temperature and Reynolds number of 298K and 4000 pure PCM heat exchanger oriented vertically. The highest exergy efficiency of 23.32% is exhibited by heat exchanger with metal foam porosity of 0.95, l/d ratio of 9.22 with HTF inlet temperature and Reynolds number of 298K and 500 enhanced with 1% volume GNP nanoparticles oriented horizontally.

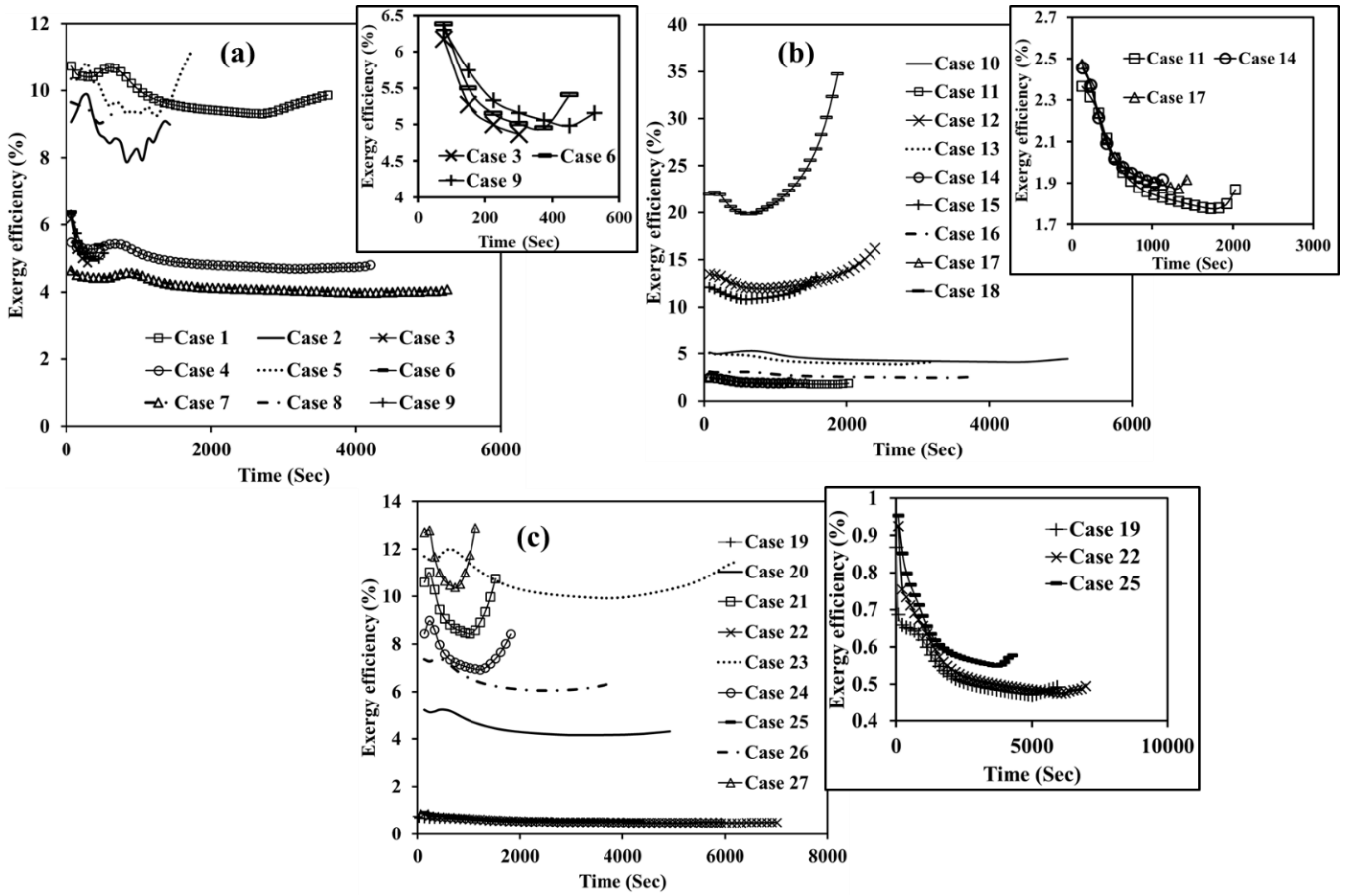

Fig 9.5 Exergy variation with time (a) 0.93 porosity metal foam (b) 0.95 porosity metal foam and (c) 0.97 porosity metal foam heat exchanger during solidification

Table 9.9 Normalized, deviated and grade of the exergy during solidification

Case	Exergy efficiency (%)	Normalized value	Deviation value	Grade	Rank
Case 1	9.79	0.406	0.593	0.457	7
Case 2	8.77	0.361	0.638	0.439	10
Case 3	5.3	0.209	0.790	0.387	15
Case 4	4.92	0.192	0.807	0.382	16
Case 5	9.95	0.413	0.586	0.460	6
Case 6	5.36	0.211	0.788	0.388	14
Case 7	4.16	0.159	0.840	0.372	20
Case 8	9.35	0.387	0.612	0.449	9

Case 9	5.39	0.213	0.786	0.388	13
Case 10	4.46	0.172	0.827	0.376	17
Case 11	1.93	0.061	0.938	0.347	24
Case 12	12.99	0.546	0.453	0.524	2
Case 13	4.24	0.162	0.837	0.373	19
Case 14	2.08	0.068	0.931	0.349	22
Case 15	11.47	0.480	0.519	0.490	4
Case 16	2.65	0.093	0.906	0.355	21
Case 17	2.05	0.066	0.933	0.348	23
Case 18	23.32	1	0	1	1
Case 19	0.53	0	1	0.333	27
Case 20	4.43	0.171	0.828	0.376	18
Case 21	9.41	0.389	0.610	0.450	8
Case 22	0.54	0.0004	0.999	0.333	26
Case 23	10.61	0.442	0.557	0.472	5
Case 24	7.64	0.311	0.688	0.420	11
Case 25	0.62	0.003	0.996	0.334	25
Case 26	6.4	0.257	0.742	0.402	12
Case 27	11.5	0.481	0.518	0.490	3

Table 9.10 Response table of parameters for exergy efficiency during solidification

Levels / **Parameters**	**1**	**2**	**3**	**Max-Min**	**Rank**
Porosity	0.413	0.462	0.401	0.061	5
GNP vol fraction	0.410	0.407	0.460	0.052	6
Orientation	0.468	0.411	0.398	0.070	3
HTF inlet temperature	0.468	0.400	0.409	0.067	4
l/d ratio	0.368	0.405	0.504	0.135	2
Reynolds no	0.497	0.424	0.356	0.140	1

Table 9.11 infers the overall individual ranking of parameters that affects the performance of the PCM shell and tube heat exchanger. ↓ indicates that the lesser value of the chosen parameter will result in the better performance of HX. ↑ indicates that the higher value of the chosen parameter will result in better performance of HX.

Table 9.11 Overall ranking of heat exchanger parameters

Performance factor / Parameters	Melting time	Solidification time	Exergy efficiency (melting)	Exergy efficiency (Solidification)
Porosity	**2 (↓)**	**2(↓)**	**3(↑)**	5
GNP	5	4	4	6
Orientation	6	6	**2(↓)**	**3(↓)**
HTF temp	4	5	**1(↓)**	4
l/d ratio	**1(↑)**	**1(↑)**	5	**2(↑)**
Reynolds no	**3(↑)**	**3(↑)**	6	**1(↓)**

9.5 Conclusions

In the present work, numerical analysis of GNP nanoparticles enhanced metal foam PCM shell and tube heat exchanger during melting and solidification is carried out. The effect of phase change time and exergy efficiency on varying porosity of metal foam, volume fraction of GNP nanoparticles, length of heat exchanger, the inlet temperature of HTF, length to diameter ratio of shell and Reynolds number of HTF is analyzed. GRA is used to rank the heat exchangers based on individual performance factors and to find out the most important operational parameter.

- The effect of GNP nanoparticles is noted to be insignificant in combination with metal foam.
- The porosity of metal foam, l/d ratio of HX and Reynolds number of HTF have shown significant effects on the performance of the HX.
- HXs which have an l/d ratio of 9.22 have shown better performance. Both melting and solidification times decreased with the decrease in the porosity of metal foam. Whereas exergy efficiency during melting decreased with the decrease in the porosity of metal foam.
- A higher HTF Reynolds number favored the phase change time but depreciated the exergy efficiency during solidification.

- For the same amount of PCM considered with the variation of HX parameters, minimum and maximum melting durations of 300 seconds and 5150 seconds are noted. Similarly, minimum and maximum durations of 400 and 7100 seconds are noted during solidification.
- During melting maximum exergy efficiency of 61.29% is noted in ST HX with metal foam porosity of 0.95, l/d ratio of 9.22 with HTF inlet temperature and Reynolds number of 348K and 500 enhanced with 1% volume GNP nanoparticles oriented horizontally.
- During melting minimum exergy efficiency of 40.29% is noted in ST HX with metal foam of 0.93, l/d ratio of 1.19 with HTF inlet temperature and Reynolds number of 358K and 500 enhanced with 1% volume GNP nanoparticles oriented vertically.
- During solidification maximum exergy efficiency of 23.32% is noted in HX with metal foam porosity of 0.95, l/d ratio of 9.22 with HTF inlet temperature and Reynolds number of 298K and 500 enhanced with 1% volume GNP nanoparticles oriented horizontally.
- During solidification, minimum exergy efficiency of 0.53% is exhibited by HX with metal foam porosity of 0.97, l/d ratio of 1.19 with HTF inlet temperature and Reynolds number of 298K and 4000 pure PCM HX oriented vertically.

Chapter 10

Conclusions and scope for future work

The present research work is aimed to analyze the effect of different hybrid techniques on the thermal performance of a latent heat storage unit (LHSS). Lauric acid is chosen as the phase change material (PCM) and shell and tube type heat exchanger is chosen as the heat exchanger. Three hybrid techniques: (1) fins + GNP (graphene nanoplatelets) nanoparticles, (2) metal foam + GNP nanoparticles and (3) cascaded metal foam are used in the present study. Simulations were performed to compare the performance of these three hybrid techniques considering the effect of the orientation of LHSS on its thermal performance. Numerical simulations based on the enthalpy porosity approach are carried out for the proper understanding of the melting and solidification behavior of PCM. To compare the performance of the heat exchangers - phase change time, energy ratio and exergy efficiency during melting and solidification are considered. The performance of the PCM shell and tube heat exchangers with hybrid techniques is compared with pure PCM heat exchangers i.e. without hybrid techniques. From the present numerical investigations, the following conclusions are drawn.

- In a pure PCM heat exchanger, a vertically oriented heat exchanger has the least melting time of 6505 seconds and the highest melting time of 8065 seconds for an inclined (45°) heat exchanger.
- During solidification in a pure PCM heat exchanger horizontal heat exchanger has the least solidification time of 26675 seconds and the highest solidification time of 30775 seconds for an inclined (45°) heat exchanger.
- Among radial, spiral and longitudinal fin heat exchangers, radial fin shell and tube PCM heat exchanger is the least melting and solidification time for the same volume fraction of GNP (Graphene nanoplatelets) nanoparticles and for a particular orientation of heat exchanger.
- With the increase in the volume fraction of GNP nanoparticles, both melting and solidification time decreases.
- The inclined (45°) heat exchanger has the highest melting time irrespective of fin type and nanoparticle volume fraction.

- Orientation of heat exchanger has the least effect on solidification time in GNP nanoparticles enhanced finned shell and tube heat exchanger.
- The decrease in porosity of metal foam resulted in a decrease in melting and solidification time.
- The least melting time of 1410 seconds is noted in 0.93 porosity metal foam enhanced with 1% volume GNP nanoparticles oriented vertically and the highest melting time of 3100 seconds is noted in 0.97 porosity metal foam pure PCM oriented at 45°.
- The least solidification time of 2200 seconds is noted in 0.93 porosity metal foam enhanced with 1% volume GNP nanoparticles. The highest solidification time of 4000 seconds is noted in 0.97 porosity metal foam enhanced with pure PCM heat exchanger oriented at 45°.
- The effect of GNP nanoparticles can be noted only in the presence of metal foam with a porosity of 0.97.
- In the radial cascaded metal foam heat exchanger, the horizontally positioned heat exchanger has the highest melting and solidification time and the vertically oriented heat exchanger has the least melting and solidification time.
- The least melting time of 1550 seconds is noted in radial cascaded 0.93-0.95-0.97 vertically oriented heat exchanger and the highest melting time of 3000 seconds is noted in linearly cascaded 0.93-0.95-0.97 oriented at 45°.
- The least solidification time of 2200 seconds is noted in radial cascaded 0.93-0.95-0.97 vertically oriented heat exchanger and the highest solidification time of 4000 seconds is noted in linearly cascaded 0.97-0.95-0.93 oriented horizontally.
- The energy storage ratio at the end of melting is highest in pure PCM heat exchangers and least in heat exchangers in which the metal foam + GNP nanoparticles hybrid technique is used. But this variation in energy storage ratio is less when compared with the reduction in melting time.
- During solidification energy release ratio is almost the same in all the heat exchangers.
- The average temperature at the end of melting is higher in heat exchangers in which the convective mode of heat transfer dominates. Thus resulting in a higher energy storage ratio and exergy efficiency.

- The highest exergy efficiency of 76.16% is noted in pure PCM heat exchanger oriented at 45° and the least exergy efficiency of 45.40% is noted in radially cascaded 0.97-0.93-0.95 heat exchanger oriented vertically during melting.
- Exergy efficiency during solidification in pure PCM heat exchanger is very less. The highest average efficiency during solidification is 0.715%. This is because of less increase in the outlet temperature of HTF.
- With the increase in the rate of solidification outlet temperature of HTF increases, thus resulting in an increase in exergy efficiency during solidification.
- Heat exchangers in which metal foam+ GNP nanoparticles and cascaded metal foam exhibited the highest exergy efficiency during solidification.
- In metal foam+ GNP nanoparticles hybrid enhanced PCM heat exchanger, exergy efficiency during solidification increased with a decrease in the porosity of metal foam. GNP nanoparticles have an effect in the presence of only 0.97 porosity metal foam.
- During solidification, the least exergy efficiency of 0.715% in pure PCM heat exchanger oriented horizontally is noted, and the highest exergy efficiency of 10.5% in 0.93 porosity metal foam enhanced with 1% volume GNP nanoparticles oriented at 45°.
- Among the hybrid techniques considered metal foam + GNP nanoparticles hybrid technique has shown better performance.
- A machine learning model is developed to predict the transient variation in melt fraction of metal foam+ GNP nanoparticle hybrid enhanced PCM shell and tube heat exchanger.
- The linear regression model has predicted the transient variation of melt fraction during melting and solidification with the highest accuracy.
- On carrying out the parametric analysis by varying the porosity of metal foam, the volume fraction of GNP nanoparticles, length of the heat exchanger, the inlet temperature of HTF, length to diameter ratio (l/d) of shell and Reynolds number of HTF, it is revealed that porosity of the metal foam and l/d ratio of heat exchanger has a significant effect on melting and solidification times.
- The lesser the porosity of metal foam lesser will be the melting and solidification time. The higher the l/d ratio of the heat exchanger lesser will be the melting and solidification time.

- Exergy efficiency during melting depends on HTF inlet temperature and orientation of the heat exchanger. Lesser the HTF inlet temperature lesser will be the exergy destruction, thus resulting in better exergy efficiency.
- Exergy efficiency during solidification significantly depends on the Reynolds number of HTF and the l/d ratio of the heat exchanger. The lesser the Reynolds number better the exergy efficiency and the higher the l/d ratio better the exergy efficiency.

Scope for future work

- Effect of hybrid technique can be analyzed in simultaneous changing and discharging PCM shell and tube heat exchanger.
- Effect of GNP nanoparticles combined with metal foam with gradient porosity can be explored.
- Influence of shell geometry with hybrid techniques on thermal transport can be investigated.
- Thermal hydraulics for a PCM shell and tube heat exchanger with heat transfer fluid tube repleted with metal foam can be examined.

References:

1. Energy BSR of W. Statistical Review. BP Stat Rev World Energy [Internet]. 2019;68. Available from: https://www.bp.com/en/global/corporate/energy-economics/statistical-review-of-world-energy.html

2. Sheikholeslami M, Keshteli AN, Babazadeh H. Nanoparticles favorable effects on performance of thermal storage units. J Mol Liq [Internet]. Elsevier B.V.; 2020;300:112329. Available from: https://doi.org/10.1016/j.molliq.2019.112329

3. Kalapala L, Devanuri JK. Influence of operational and design parameters on the performance of a PCM based heat exchanger for thermal energy storage – A review. J Energy Storage [Internet]. Elsevier; 2018;20:497–519. Available from: https://doi.org/10.1016/j.est.2018.10.024

4. Rathore PKS, Shukla SK. Enhanced thermophysical properties of organic PCM through shape stabilization for thermal energy storage in buildings: A state of the art review. Energy Build. Elsevier B.V.; 2021;236:110799.

5. Zhao Y, Zhang X, Hua W. Review of preparation technologies of organic composite phase change materials in energy storage. J Mol Liq. Elsevier B.V.; 2021;336:115923.

6. Junaid MF, Rehman Z ur, Čekon M, Čurpek J, Farooq R, Cui H, et al. Inorganic phase change materials in thermal energy storage: A review on perspectives and technological advances in building applications. Energy Build. 2021;252.

7. Lin Y, Alva G, Fang G. Review on thermal performances and applications of thermal energy storage systems with inorganic phase change materials. Energy [Internet]. Elsevier Ltd; 2018;165:685–708. Available from: https://doi.org/10.1016/j.energy.2018.09.128

8. Singh P, Sharma RK, Ansu AK, Goyal R, Sarı A, Tyagi V V. A comprehensive review on development of eutectic organic phase change materials and their composites for low and medium range thermal energy storage applications. Sol Energy Mater Sol Cells. Elsevier B.V.; 2021;223:110955.

9. Javadi FS, Metselaar HSC, Ganesan P. Performance improvement of solar thermal systems integrated with phase change materials (PCM), a review. Sol Energy. Elsevier; 2020;206:330–52.

10. Douvi E, Pagkalos C, Dogkas G, Koukou MK, Stathopoulos VN, Caouris Y, et al. Phase change materials in solar domestic hot water systems: A review. Int J Thermofluids. Elsevier Ltd; 2021;10:100075.

11. Salunkhe PB, Jaya Krishna D. Investigations on latent heat storage materials for solar water and space heating applications. J Energy Storage [Internet]. Elsevier Ltd; 2017;12:243–60. Available from: http://dx.doi.org/10.1016/j.est.2017.05.008

12. Luo J, Zou D, Wang Y, Wang S, Huang L. Battery thermal management systems (BTMs) based on phase change material (PCM): a comprehensive review. Chem Eng J. Elsevier B.V.; 2021;430:132741.

13. Shen ZG, Chen S, Liu X, Chen B. A review on thermal management performance enhancement of phase change materials for vehicle lithium-ion batteries. Renew Sustain Energy Rev. Elsevier Ltd; 2021;148:111301.

14. Landini S, Leworthy J, O'Donovan TS. A Review of Phase Change Materials for the Thermal Management and Isothermalisation of Lithium-Ion Cells. J Energy Storage. Elsevier; 2019;25:100887.

15. Jaguemont J, Omar N, Van den Bossche P, Mierlo J. Phase-change materials (PCM) for automotive applications: A review. Appl Therm Eng. Elsevier Ltd; 2018;132:308–20.

16. Katekar VP, Deshmukh SS. A review of the use of phase change materials on performance of solar stills. J Energy Storage [Internet]. Elsevier; 2020;30:101398. Available from: https://doi.org/10.1016/j.est.2020.101398

17. Tyagi V V., Chopra K, Kalidasan B, Chauhan A, Stritih U, Anand S, et al. Phase change material based advance solar thermal energy storage systems for building heating and cooling applications: A prospective research approach. Sustain Energy Technol Assessments. Elsevier Ltd; 2021;47:101318.

18. Faraj K, Khaled M, Faraj J, Hachem F, Castelain C. A review on phase change materials for thermal energy storage in buildings: Heating and hybrid applications. J Energy Storage. Elsevier; 2021;33:101913.

19. Shalaby SM, Bek MA, El-Sebaii AA. Solar dryers with PCM as energy storage medium: A review. Renew Sustain Energy Rev. Elsevier; 2014;33:110–6.

20. Selvnes H, Allouche Y, Manescu RI, Hafner A. Review on cold thermal energy storage applied to refrigeration systems using phase change materials. Therm Sci Eng Prog. Elsevier Ltd; 2021;22:100807.

21. Omara AAM, Mohammed HA, Al Rikabi IJ, Abuelnour MA, Abuelnuor AAA. Performance improvement of solar chimneys using phase change materials: A review. Sol Energy. Elsevier Ltd; 2021;228:68–88.

22. Zaferani SH, Sams MW, Ghomashchi R, Chen Z-G. Thermoelectric Coolers as Thermal Management Systems for Medical Applications: Design, Optimization, and Advancement. Nano Energy. Elsevier Ltd; 2021;90:106572.

23. Farooq AS, Zhang P. Fundamentals, materials and strategies for personal thermal management by next-generation textiles. Compos Part A Appl Sci Manuf. Elsevier Ltd; 2021;142:106249.

24. Sharma SD, Sagara K. Latent Heat Storage Materials and Systems : A Review. 2007;5075.

25. Akeiber H, Nejat P, Majid MZA, Wahid MA, Jomehzadeh F, Zeynali Famileh I, et al. A review on phase change material (PCM) for sustainable passive cooling in building envelopes. Renew Sustain Energy Rev. Elsevier; 2016;60:1470–97.

26. Sharma A, Tyagi V V., Chen CR, Buddhi D. Review on thermal energy storage with phase change materials and applications. Renew Sustain Energy Rev. 2009;13:318–45.

27. Agyenim F, Hewitt N, Eames P, Smyth M. A review of materials, heat transfer and phase change problem formulation for latent heat thermal energy storage systems (LHTESS). Renew Sustain Energy Rev. 2010;14:615–28.

28. Eanest Jebasingh B, Valan Arasu A. A comprehensive review on latent heat and thermal conductivity of nanoparticle dispersed phase change material for low-temperature applications. Energy Storage Mater. 2020;24:52–74.

29. Kalapala L, Devanuri JK. Optimization of Fin Parameters to Reduce Entropy Generation and Melting Time of a Latent Heat Storage Unit. J Sol Energy Eng. 2020;142:1–12.

30. Afsharpanah F, Ajarostaghi SSM, Hamedani FA, Pour MS. Compound Heat Transfer Augmentation of a Shell-and-Coil Ice Storage Unit with Metal-Oxide Nano Additives and Connecting Plates. Nanomaterials. 2022.

31. Afsharpanah F, Pakzad K, Mousavi Ajarostaghi SS, Arıcı M. Assessment of the charging performance in a cold thermal energy storage container with two rows of serpentine tubes and extended surfaces. J Energy Storage [Internet]. Elsevier Ltd; 2022;51:104464. Available from: https://doi.org/10.1016/j.est.2022.104464

32. Duan J, Peng Z. Numerical investigation of nano-enhanced phase change material melting in the 3D annular tube with spiral fins. Renew Energy [Internet]. Elsevier Ltd; 2022;193:251–63. Available from: https://doi.org/10.1016/j.renene.2022.05.014

33. Das N, Takata Y, Kohno M, Harish S. Melting of graphene based phase change nanocomposites in vertical latent heat thermal energy storage unit. Appl Therm Eng [Internet]. Elsevier Ltd; 2016;107:101–13. Available from: http://dx.doi.org/10.1016/j.applthermaleng.2016.06.166

34. Afsharpanah F, Cheraghian G, Akbarzadeh Hamedani F, Shokri E, Mousavi Ajarostaghi SS. Utilization of Carbon-Based Nanomaterials and Plate-Fin Networks in a Cold PCM Container with Application in Air Conditioning of Buildings. Nanomaterials. 2022. p. 1927.

35. Muthya Goud V, Vaisakh V, Joseph M, Sajith V. An experimental investigation on the evaporation of polystyrene encapsulated phase change composite material based nanofluids. Appl Therm Eng [Internet]. Elsevier; 2020;168:114862. Available from: https://doi.org/10.1016/j.applthermaleng.2019.114862

36. Xu HJ, Xing ZB, Wang FQ, Cheng ZM. Review on heat conduction, heat convection, thermal radiation and phase change heat transfer of nanofluids in porous media: Fundamentals and applications. Chem Eng Sci. 2019;195:462–83.

37. Mahdi JM, Lohrasbi S, Nsofor EC. Hybrid heat transfer enhancement for latent-heat thermal energy storage systems: A review. Int J Heat Mass Transf [Internet]. Elsevier Ltd; 2019;137:630–49. Available from: https://doi.org/10.1016/j.ijheatmasstransfer.2019.03.111

38. Cao Y, Faghri A. Performance characteristics of a thermal energy storage module: a transient PCM/forced convection conjugate analysis. Int J Heat Mass Transf. 1991;34:93–101.

39. Khan Z, Khan ZA. An experimental investigation of discharge/solidification cycle of paraffin in novel shell and tube with longitudinal fins based latent heat storage system. Energy Convers Manag. 2017;154:157–67.

40. Khan Z, Khan ZA. Experimental investigations of charging/melting cycles of paraffin in a novel shell and tube with longitudinal fins based heat storage design solution for domestic and industrial applications. Appl Energy. 2017;206:1158–68.

41. Lu B, Zhang Y, Sun D, Yuan Z, Yang S. Experimental investigation on thermal behavior of paraffin in a vertical shell and spiral fin tube latent heat thermal energy storage unit. Appl Therm Eng [Internet]. Elsevier Ltd; 2021;187:116575. Available from: https://doi.org/10.1016/j.applthermaleng.2021.116575

42. Kalapala L, Devanuri JK. Parametric investigation to assess the melt fraction and melting time for a latent heat storage material based vertical shell and tube heat exchanger. Sol Energy [Internet]. Elsevier; 2019;193:360–71. Available from: https://doi.org/10.1016/j.solener.2019.09.076

43. Shakrina G, Rivera-Tinoco R, Bouallou C. Numerical investigation and extensive parametric analysis of cryogenic latent heat shell and tube thermal energy storage system. Therm Sci Eng Prog [Internet]. Elsevier Ltd; 2022;34:101440. Available from: https://doi.org/10.1016/j.tsep.2022.101440

44. Mao Q, Chen K, Li T. Heat transfer performance of a phase-change material in a rectangular shell-tube energy storage tank. Appl Therm Eng [Internet]. Elsevier Ltd; 2022;215:118937. Available from: https://doi.org/10.1016/j.applthermaleng.2022.118937

45. Panisilvam J, Tay NHS, Wang PC. Experimental investigation during the melting process of a vertical and horizontal tube-in-shell Latent Heat Energy Storage System. J Energy Storage [Internet]. Elsevier Ltd; 2022;55:105401. Available from: https://doi.org/10.1016/j.est.2022.105401

46. Nguyen TP, Ramadan Z, Hong SJ, Park CW. Effect of graphite fin on heat transfer enhancement of rectangular shell and tube latent heat storage. Int J Heat Mass Transf

[Internet]. Elsevier Ltd; 2022;194:123018. Available from: https://doi.org/10.1016/j.ijheatmasstransfer.2022.123018

47. Shen Y, Zhang P, Rehman Mazhar A, Chen H, Liu S. Experimental analysis of a fin-enhanced three-tube-shell cascaded latent heat storage system. Appl Therm Eng [Internet]. Elsevier Ltd; 2022;213:118717. Available from: https://doi.org/10.1016/j.applthermaleng.2022.118717

48. Wang WW, Zhang K, Wang LB, He YL. Numerical study of the heat charging and discharging characteristics of a shell-and-tube phase change heat storage unit. Appl Therm Eng [Internet]. Elsevier Ltd; 2013;58:542–53. Available from: http://dx.doi.org/10.1016/j.applthermaleng.2013.04.063

49. Wang Y, Wang L, Xie N, Lin X, Chen H. Experimental study on the melting and solidification behavior of erythritol in a vertical shell-and-tube latent heat thermal storage unit. Int J Heat Mass Transf [Internet]. Elsevier Ltd; 2016;99:770–81. Available from: http://dx.doi.org/10.1016/j.ijheatmasstransfer.2016.03.125

50. Kibria MA, Anisur MR, Mahfuz MH, Saidur R, Metselaar IHSC. Numerical and experimental investigation of heat transfer in a shell and tube thermal energy storage system. Int Commun Heat Mass Transf [Internet]. Elsevier Ltd; 2014;53:71–8. Available from: http://dx.doi.org/10.1016/j.icheatmasstransfer.2014.02.023

51. Avci M, Yazici MY. Experimental study of thermal energy storage characteristics of a paraffin in a horizontal tube-in-shell storage unit. Energy Convers. Manag. 2013. p. 271–7.

52. Hosseini MJ, Rahimi M, Bahrampoury R. Experimental and computational evolution of a shell and tube heat exchanger as a PCM thermal storage system. Int Commun Heat Mass Transf. Elsevier Ltd; 2014;50:128–36.

53. Esen M, Durmus A, Durmus A. Geometric design of soler-aided latent heat store depending on various parameters and phase change materials. Sol Energy. 1998;62:19–28.

54. Malik FK, Khan MM, Ahmed HF, Irfan M, Ahad IU. Performance characteristics of PCM based thermal energy storage system for fluctuating waste heat sources. Case Stud Therm Eng [Internet]. Elsevier Ltd; 2022;34:102012. Available from: https://doi.org/10.1016/j.csite.2022.102012

55. Seddegh S, Joybari MM, Wang X, Haghighat F. Experimental and numerical characterization of natural convection in a vertical shell-and-tube latent thermal energy storage system. Sustain Cities Soc. Elsevier; 2017;35:13–24.

56. Kousha N, Hosseini MJ, Aligoodarz MR, Pakrouh R, Bahrampoury R. Effect of inclination angle on the performance of a shell and tube heat storage unit – An experimental study. Appl Therm Eng. Elsevier Ltd; 2017;112:1497–509.

57. Al Siyabi I, Khanna S, Mallick T, Sundaram S. An experimental and numerical study on the effect of inclination angle of phase change materials thermal energy storage system. J Energy Storage. Elsevier; 2019;23:57–68.

58. Kalapala L, Devanuri JK. Energy and exergy analyses of latent heat storage unit positioned at different orientations – An experimental study. Energy [Internet]. Elsevier Ltd; 2020;194:116924. Available from: https://doi.org/10.1016/j.energy.2020.116924

59. Kalapala L, Devanuri JK. Effect of orientation on thermal performance of a latent heat storage system equipped with annular fins – An experimental and numerical investigation. Appl Therm Eng [Internet]. Elsevier Ltd; 2021;183:116244. Available from: https://doi.org/10.1016/j.applthermaleng.2020.116244

60. Borhani SM, Hosseini MJ, Ranjbar AA, Bahrampoury R. Investigation of phase change in a spiral-fin heat exchanger. Appl Math Model [Internet]. Elsevier Inc.; 2019;67:297–314. Available from: https://doi.org/10.1016/j.apm.2018.10.029

61. Bouzennada T, Mechighel F, Ismail T, Kolsi L, Ghachem K. Heat transfer and fluid flow in a PCM-filled enclosure: Effect of inclination angle and mid-separation fin. Int Commun Heat Mass Transf. Elsevier Ltd; 2021;124:105280.

62. Mahdi MS, Hasan AF, Mahood HB, Campbell AN, Khadom AA, Karim AM em A, et al. Numerical study and experimental validation of the effects of orientation and configuration on melting in a latent heat thermal storage unit. J Energy Storage. Elsevier; 2019;23:456–68.

63. Kalapala L, Devanuri JK. Influence of operational and design parameters on the performance of a PCM based heat exchanger for thermal energy storage – A review. J Energy Storage [Internet]. Elsevier; 2018;20:497–519. Available from: https://doi.org/10.1016/j.est.2018.10.024

64. Trp A, Lenic K, Frankovic B. Analysis of the influence of operating conditions and geometric parameters on heat transfer in water-paraffin shell-and-tube latent thermal energy storage unit. Appl Therm Eng. 2006;26:1830–9.

65. Das N, Kohno M, Takata Y, Patil D V., Harish S. Enhanced melting behavior of carbon based phase change nanocomposites in horizontally oriented latent heat thermal energy storage system. Appl Therm Eng [Internet]. Elsevier Ltd; 2017;125:880–90. Available from: http://dx.doi.org/10.1016/j.applthermaleng.2017.07.084

66. Amudhalapalli GK, Devanuri JK. Synthesis, characterization, thermophysical properties, stability and applications of nanoparticle enhanced phase change materials – A comprehensive review. Therm Sci Eng Prog [Internet]. Elsevier Ltd; 2022;28:101049. Available from: https://doi.org/10.1016/j.tsep.2021.101049

67. Qureshi ZA, Ali HM, Khushnood S. Recent advances on thermal conductivity enhancement

of phase change materials for energy storage system: A review. Int J Heat Mass Transf [Internet]. Elsevier Ltd; 2018;127:838–56. Available from: https://doi.org/10.1016/j.ijheatmasstransfer.2018.08.049

68. Tao YB, He YL. A review of phase change material and performance enhancement method for latent heat storage system. Renew Sustain Energy Rev [Internet]. Elsevier Ltd; 2018;93:245–59. Available from: https://doi.org/10.1016/j.rser.2018.05.028

69. Rehman T ur, Ali HM, Janjua MM, Sajjad U, Yan WM. A critical review on heat transfer augmentation of phase change materials embedded with porous materials/foams. Int J Heat Mass Transf [Internet]. Elsevier Ltd; 2019;135:649–73. Available from: https://doi.org/10.1016/j.ijheatmasstransfer.2019.02.001

70. Darzi AAR, Farhadi M, Sedighi K. Numerical study of melting inside concentric and eccentric horizontal annulus. Appl Math Model [Internet]. Elsevier Inc.; 2012;36:4080–6. Available from: http://dx.doi.org/10.1016/j.apm.2011.11.033

71. Kazemi M, Hosseini MJ, Ranjbar AA, Bahrampoury R. Improvement of longitudinal fins configuration in latent heat storage systems. Renew Energy [Internet]. Elsevier Ltd; 2018;116:447–57. Available from: https://doi.org/10.1016/j.renene.2017.10.006

72. Rozenfeld A, Kozak Y, Rozenfeld T, Ziskind G. Experimental demonstration, modeling and analysis of a novel latent-heat thermal energy storage unit with a helical fin. Int J Heat Mass Transf [Internet]. Elsevier Ltd; 2017;110:692–709. Available from: http://dx.doi.org/10.1016/j.ijheatmasstransfer.2017.03.020

73. Agyenim F, Eames P, Smyth M. A comparison of heat transfer enhancement in a medium temperature thermal energy storage heat exchanger using fins. Sol Energy [Internet]. Elsevier Ltd; 2009;83:1509–20. Available from: http://dx.doi.org/10.1016/j.solener.2009.04.007

74. Tay NHS, Bruno F, Belusko M. Comparison of pinned and finned tubes in a phase change thermal energy storage system using CFD. Appl Energy [Internet]. 2013;104:79–86. Available from: http://dx.doi.org/10.1016/j.apenergy.2012.10.040

75. Caron-Soupart A, Fourmigué JF, Marty P, Couturier R. Performance analysis of thermal energy storage systems using phase change material. Appl Therm Eng [Internet]. Elsevier Ltd; 2016;98:1286–96. Available from: http://dx.doi.org/10.1016/j.applthermaleng.2016.01.016

76. Wang XL, Zhai XQ, Wang T, Wang HX, Yin YL. Performance of the capric and lauric acid mixture with additives as cold storage materials for high temperature cooling application. Appl Therm Eng [Internet]. Elsevier Ltd; 2013;58:252–60. Available from: http://dx.doi.org/10.1016/j.applthermaleng.2013.04.034

77. Luo X, Gu J, Ma H, Xie Y, Li A, Wang J, et al. Numerical study on enhanced melting heat transfer of PCM by the combined fractal fins. J Energy Storage [Internet]. Elsevier Ltd; 2022;45:103780. Available from: https://doi.org/10.1016/j.est.2021.103780

78. Sciacovelli A, Gagliardi F, Verda V. Maximization of performance of a PCM latent heat storage system with innovative fins. Appl Energy [Internet]. Elsevier Ltd; 2015;137:707–15. Available from: http://dx.doi.org/10.1016/j.apenergy.2014.07.015

79. Das N, Takata Y, Kohno M, Harish S. Effect of carbon nano inclusion dimensionality on the melting of phase change nanocomposites in vertical shell-tube thermal energy storage unit. Int J Heat Mass Transf [Internet]. Elsevier Ltd; 2017;113:423–31. Available from: http://dx.doi.org/10.1016/j.ijheatmasstransfer.2017.05.101

80. Parsazadeh M, Duan X. Numerical and statistical study on melting of nanoparticle enhanced phase change material in a shell-and-tube thermal energy storage system. Appl Therm Eng [Internet]. Elsevier Ltd; 2017;111:950–60. Available from: http://dx.doi.org/10.1016/j.applthermaleng.2016.09.133

81. Alomair M, Alomair Y, Tasnim S, Mahmud S, Abdullah H. Analyses of Bio-Based Nano-PCM filled Concentric Cylindrical Energy Storage System in Vertical Orientation. J Energy Storage. 2018;20:380–94.

82. Khan Z, Khan ZA, Sewell P. Heat transfer evaluation of metal oxides based nano-PCMs for latent heat storage system application. Int J Heat Mass Transf. 2019;144.

83. Khan Z, Ahmad Khan Z. Experimental and numerical investigations of nano-additives enhanced paraffin in a shell-and-tube heat exchanger: A comparative study. Appl Therm Eng. 2018;143:777–90.

84. Zhao CY, Lu W, Tian Y. Heat transfer enhancement for thermal energy storage using metal foams embedded within phase change materials (PCMs). Sol Energy. 2010;84:1402–12.

85. Alhusseny A, Al-Zurfi N, Nasser A, Al-Fatlawi A, Aljanabi M. Impact of using a PCM-metal foam composite on charging/discharging process of bundled-tube LHTES units. Int J Heat Mass Transf [Internet]. Elsevier Ltd; 2020;150:119320. Available from: https://doi.org/10.1016/j.ijheatmasstransfer.2020.119320

86. Esapour M, Hamzehnezhad A, Rabienataj Darzi AA, Jourabian M. Melting and solidification of PCM embedded in porous metal foam in horizontal multi-tube heat storage system. Energy Convers Manag [Internet]. Elsevier; 2018;171:398–410. Available from: https://doi.org/10.1016/j.enconman.2018.05.086

87. Sardari PT, Grant D, Giddings D, Walker GS, Gillott M. Composite metal foam/PCM energy store design for dwelling space air heating. Energy Convers Manag [Internet]. Elsevier; 2019;201:112151. Available from: https://doi.org/10.1016/j.enconman.2019.112151

88. Zhang P, Meng ZN, Zhu H, Wang YL, Peng SP. Melting heat transfer characteristics of a composite phase change material fabricated by paraffin and metal foam. Appl Energy [Internet]. Elsevier Ltd; 2017;185:1971–83. Available from: http://dx.doi.org/10.1016/j.apenergy.2015.10.075

89. Xu Y, Ren Q, Zheng ZJ, He YL. Evaluation and optimization of melting performance for a latent heat thermal energy storage unit partially filled with porous media. Appl Energy [Internet]. Elsevier Ltd; 2017;193:84–95. Available from: http://dx.doi.org/10.1016/j.apenergy.2017.02.019

90. Yang X, Yu J, Guo Z, Jin L, He YL. Role of porous metal foam on the heat transfer enhancement for a thermal energy storage tube. Appl Energy [Internet]. Elsevier; 2019;239:142–56. Available from: https://doi.org/10.1016/j.apenergy.2019.01.075

91. Joshi V, Rathod MK. Thermal performance augmentation of metal foam infused phase change material using a partial filling strategy: An evaluation for fill height ratio and porosity. Appl Energy [Internet]. Elsevier; 2019;253:113621. Available from: https://doi.org/10.1016/j.apenergy.2019.113621

92. Huang S, Lu J, Li Y. Numerical study on the influence of inclination angle on the melting behaviour of metal foam-PCM latent heat storage units. Energy [Internet]. Elsevier Ltd; 2022;239:122489. Available from: https://doi.org/10.1016/j.energy.2021.122489

93. Hashem Zadeh SM, Ghodrat M, Ayoubi Ayoubloo K, Sedaghatizadeh N, Taylor RA. Partial charging/discharging of bio-based latent heat energy storage enhanced with metal foam sheets. Int Commun Heat Mass Transf [Internet]. Elsevier Ltd; 2022;130:105757. Available from: https://doi.org/10.1016/j.icheatmasstransfer.2021.105757

94. Sardari PT, Babaei-Mahani R, Giddings D, Yasseri S, Moghimi MA, Bahai H. Energy recovery from domestic radiators using a compact composite metal Foam/PCM latent heat storage. J Clean Prod [Internet]. Elsevier Ltd; 2020;257:120504. Available from: https://doi.org/10.1016/j.jclepro.2020.120504

95. Sardari PT, Giddings D, Grant D, Gillott M, Walker GS. Discharge of a composite metal foam/phase change material to air heat exchanger for a domestic thermal storage unit. Renew Energy [Internet]. Elsevier Ltd; 2020;148:987–1001. Available from: https://doi.org/10.1016/j.renene.2019.10.084

96. Yao Y, Wu H. Pore-scale simulation of melting process of paraffin with volume change in high porosity open-cell metal foam. Int J Therm Sci [Internet]. Elsevier; 2019;138:322–40. Available from: https://doi.org/10.1016/j.ijthermalsci.2018.12.052

97. Chen X, Li X, Xia X, Sun C, Liu R. Thermal Performance of a PCM-Based Thermal Energy Storage with Metal Foam Enhancement. Energies. 2019;

98. Liu G, Xiao T, Guo J, Wei P, Yang X, Hooman K. Melting and solidification of phase change materials in metal foam filled thermal energy storage tank : Evaluation on gradient in pore structure. Appl Therm Eng. Elsevier Ltd; 2022;212:118564.

99. Xu T, Chiu JN, Palm B, Sawalha S. Experimental investigation on cylindrically macro-encapsulated latent heat storage for space heating applications. Energy Convers Manag. Elsevier; 2019;182:166–77.

100. Aziz S, Amin NAM, Abdul Majid MS, Belusko M, Bruno F. CFD simulation of a TES tank comprising a PCM encapsulated in sphere with heat transfer enhancement. Appl Therm Eng. Elsevier; 2018;143:1085–92.

101. He Z, Wang X, Du X, Amjad M, Yang L, Xu C. Experiments on comparative performance of water thermocline storage tank with and without encapsulated paraffin wax packed bed. Appl Therm Eng. Elsevier; 2019;147:188–97.

102. Fang Y, Qu ZG, Fu YD. Experimental study of the thermal characteristics of microencapsulated phase change composite cylinders. Appl Therm Eng. 2017;114:1256–64.

103. Amin NAM, Bruno F, Belusko M. Effectiveness-NTU correlation for low temperature PCM encapsulated in spheres. Appl Energy. 2012;93:549–55.

104. Lee YT, Hong SW, Chung JD. Effects of capsule conduction and capsule outside convection on the thermal storage performance of encapsulated thermal storage tanks. Sol Energy. Elsevier Ltd; 2014;110:56–63.

105. ul Hasnain F, Irfan M, Khan MM, Khan LA, Ahmed HF. Melting performance enhancement of a phase change material using branched fins and nanoparticles for energy storage applications. J Energy Storage. Elsevier Ltd; 2021;38.

106. Wang T, Zhao Y, Diao Y, Ma C, Zhang Y, Lu X. Experimental investigation of a novel thermal storage solar air heater (TSSAH) based on flat micro-heat pipe arrays. Renew Energy. Elsevier Ltd; 2021;173:639–51.

107. Sharifi N, Wang S, Bergman TL, Faghri A. Heat pipe-assisted melting of a phase change material. Int J Heat Mass Transf. Elsevier Ltd; 2012;55:3458–69.

108. Shabgard H, Bergman TL, Sharifi N, Faghri A. High temperature latent heat thermal energy storage using heat pipes. Int J Heat Mass Transf. Elsevier Ltd; 2010;53:2979–88.

109. Nithyanandam K, Pitchumani R. Analysis and optimization of a latent thermal energy storage system with embedded heat pipes. Int J Heat Mass Transf. Elsevier Ltd; 2011;54:4596–610.

110. Motahar S, Khodabandeh R. Experimental study on the melting and solidification of a phase change material enhanced by heat pipe. Int Commun Heat Mass Transf. Elsevier Ltd;

2016;73:1–6.

111. Ebrahimi A, Hosseini MJ, Ranjbar AA, Rahimi M, Bahrampoury R. Melting process investigation of phase change materials in a shell and tube heat exchanger enhanced with heat pipe. Renew Energy. Elsevier Ltd; 2019;138:378–94.

112. Chopra K, Tyagi V V., Pathak AK, Pandey AK, Sari A. Experimental performance evaluation of a novel designed phase change material integrated manifold heat pipe evacuated tube solar collector system. Energy Convers Manag. Elsevier; 2019;198:111896.

113. Song H jie, Zhang W, Li Y qi, Yang Z wei, Ming A bo. Exergy analysis and parameter optimization of heat pipe receiver with integrated latent heat thermal energy storage for space station in charging process. Appl Therm Eng. 2017;119:304–11.

114. Singh RP, Kaushik SC, Rakshit D. Melting phenomenon in a finned thermal storage system with graphene nano-plates for medium temperature applications. Energy Convers Manag [Internet]. Elsevier; 2018;163:86–99. Available from: https://doi.org/10.1016/j.enconman.2018.02.053

115. Singh RP, Xu H, Kaushik SC, Rakshit D, Romagnoli A. Charging performance evaluation of finned conical thermal storage system encapsulated with nano-enhanced phase change material. Appl Therm Eng [Internet]. Elsevier; 2019;151:176–90. Available from: https://doi.org/10.1016/j.applthermaleng.2019.01.072

116. Lohrasbi S, Sheikholeslami M, Ganji DD. Discharging process expedition of NEPCM in fin-assisted Latent Heat Thermal Energy Storage System. J Mol Liq [Internet]. Elsevier B.V.; 2016;221:833–41. Available from: http://dx.doi.org/10.1016/j.molliq.2016.06.044

117. Sheikholeslami M, Lohrasbi S, Ganji DD. Numerical analysis of discharging process acceleration in LHTESS by immersing innovative fin configuration using finite element method. Appl Therm Eng [Internet]. Elsevier Ltd; 2016;107:154–66. Available from: http://dx.doi.org/10.1016/j.applthermaleng.2016.06.158

118. Hosseinzadeh K, Erfani Moghaddam MA, Asadi A, Mogharrebi AR, Jafari B, Hasani MR, et al. Effect of two different fins (longitudinal-tree like) and hybrid nano-particles (MoS2-TiO2) on solidification process in triplex latent heat thermal energy storage system. Alexandria Eng J [Internet]. Faculty of Engineering, Alexandria University; 2021;60:1967–79. Available from: https://doi.org/10.1016/j.aej.2020.12.001

119. Khan Z, Khan ZA. Role of extended fins and graphene nano-platelets in coupled thermal enhancement of latent heat storage system. Energy Convers Manag [Internet]. Elsevier Ltd; 2020;224:113349. Available from: https://doi.org/10.1016/j.enconman.2020.113349

120. Senobar H, Aramesh M, Shabani B. Nanoparticles and metal foams for heat transfer enhancement of phase change materials: A comparative experimental study. J Energy

Storage [Internet]. Elsevier; 2020;32:101911. Available from: https://doi.org/10.1016/j.est.2020.101911

121. Lei J, Yang C, Huang X, Li Z, Zhang Y. Solidification enhancement of phase change materials using nanoparticles and metal foams with nonuniform porosity. J Energy Storage [Internet]. Elsevier Ltd; 2021;44:103420. Available from: https://doi.org/10.1016/j.est.2021.103420

122. Mahdi JM, Mohammed HI, Hashim ET, Talebizadehsardari P, Nsofor EC. Solidification enhancement with multiple PCMs, cascaded metal foam and nanoparticles in the shell-and-tube energy storage system. Appl Energy [Internet]. Elsevier; 2020;257:113993. Available from: https://doi.org/10.1016/j.apenergy.2019.113993

123. Mahdi JM, Nsofor EC. Melting enhancement in triplex-tube latent heat energy storage system using nanoparticles-metal foam combination. Appl Energy [Internet]. Elsevier Ltd; 2017;191:22–34. Available from: http://dx.doi.org/10.1016/j.apenergy.2016.11.036

124. Zhao CY, Wu ZG. Heat transfer enhancement of high temperature thermal energy storage using metal foams and expanded graphite. Sol Energy Mater Sol Cells. 2011;95:636–43.

125. Al-Jethelah M, Ebadi S, Venkateshwar K, Tasnim SH, Mahmud S, Dutta A. Charging nanoparticle enhanced bio-based PCM in open cell metallic foams: An experimental investigation. Appl Therm Eng [Internet]. Elsevier; 2019;148:1029–42. Available from: https://doi.org/10.1016/j.applthermaleng.2018.11.121

126. Li Z, Shahsavar A, Al-Rashed AAAA, Talebizadehsardari P. Effect of porous medium and nanoparticles presences in a counter-current triple-tube composite porous/nano-PCM system. Appl Therm Eng [Internet]. Elsevier; 2020;167:114777. Available from: https://doi.org/10.1016/j.applthermaleng.2019.114777

127. Ghalambaz M, Mehryan SAM, Ayoubloo KA, Hajjar A, Kadri M El, Younis O, et al. Thermal energy storage and heat transfer of nano-enhanced phase change material (NePCM) in a shell and tube thermal energy storage (TES) unit with a partial layer of eccentric copper foam. Molecules. 2021;26.

128. Hassani Soukht Abandani M, Domiri Ganji D. Melting effect in triplex-tube thermal energy storage system using multiple PCMs-porous metal foam combination. J Energy Storage [Internet]. Elsevier Ltd; 2021;43:103154. Available from: https://doi.org/10.1016/j.est.2021.103154

129. Sardari PT, Mohammed HI, Giddings D, walker GS, Gillott M, Grant D. Numerical study of a multiple-segment metal foam-PCM latent heat storage unit: Effect of porosity, pore density and location of heat source. Energy [Internet]. Elsevier Ltd; 2019;189:116108. Available from: https://doi.org/10.1016/j.energy.2019.116108

130. Wang Z, Wu J, Lei D, Liu H, Li J, Wu Z. Experimental study on latent thermal energy storage system with gradient porosity copper foam for mid-temperature solar energy application. Appl Energy [Internet]. Elsevier; 2020;261:114472. Available from: https://doi.org/10.1016/j.apenergy.2019.114472

131. Pu L, Zhang S, Xu L, Ma Z, Wang X. Numerical study on the performance of shell-and-tube thermal energy storage using multiple PCMs and gradient copper foam. Renew Energy [Internet]. Elsevier Ltd; 2021;174:573–89. Available from: https://doi.org/10.1016/j.renene.2021.04.061

132. Kumar M, Krishna DJ. Influence of Mushy Zone Constant on Thermohydraulics of a PCM. Energy Procedia [Internet]. The Author(s); 2017;109:314–21. Available from: http://dx.doi.org/10.1016/j.egypro.2017.03.074

133. Gaddala UM, Devanuri JK. A Hybrid Decision-Making Method for the Selection of a Phase Change Material for Thermal Energy Storage. J Therm Sci Eng Appl. 2020;12:1–11.

134. Maheswararao GU, Krishna DJ. Measurement of thermophysical properties of some potential organic PCMs for low-temperature thermal energy storage systems. ISME J Therm fluids. 2018;04:18–28.

135. Rabienataj Darzi AA, Jourabian M, Farhadi M. Melting and solidification of PCM enhanced by radial conductive fins and nanoparticles in cylindrical annulus. Energy Convers Manag [Internet]. Elsevier Ltd; 2016;118:253–63. Available from: http://dx.doi.org/10.1016/j.enconman.2016.04.016

136. Mahdi JM, Nsofor EC. Solidification enhancement of PCM in a triplex-tube thermal energy storage system with nanoparticles and fins. Appl Energy [Internet]. Elsevier; 2018;211:975–86. Available from: https://doi.org/10.1016/j.apenergy.2017.11.082

137. Joshi V, Rathod MK. Thermal transport augmentation in latent heat thermal energy storage system by partially filled metal foam: A novel configuration. J Energy Storage. 2019;22:270–82.

138. Nedjem K, Teggar M, Hadibi T, Arıcı M, Yıldız Ç, Ismail KAR. Hybrid thermal performance enhancement of shell and tube latent heat thermal energy storage using nano-additives and metal foam. J Energy Storage. 2021;44.

139. Uma Maheswararao G, Jaya Krishna D, John B. Melting and Solidification Behaviour of Some Organic Phase Change Materials Applicable to Low Temperature Heat Storage Applications. Int J Thermophys [Internet]. Springer US; 2022;43:1–24. Available from: https://doi.org/10.1007/s10765-022-03042-9

140. Jaya Krishna D. Operational time and melt fraction based optimization of a phase change material longitudinal fin heat sink. J Therm Sci Eng Appl. 2018;10:1–4.